MEASUREMENT OF STEADY-STATE, SPACE DEPENDENT THERMAL NEUTRON SPECTRA IN BERYLLIUM

A DISSERTATION

Presented to

The Faculty of the Division of Graduate

Studies and Research

by

James Alan Lake

In Partial Fulfillment

of the Requirements for the Degree

Doctor of Philosophy

in the School of Nuclear Engineering

Georgia Institute of Technology

November, 1972

In presenting the dissertation as a partial fulfillment of the requirements for an advanced degree from the Georgia Institute of Technology, I agree that the Library of the Institute shall make it available for inspection and circulation in accordance with its regulations governing materials of this type. I agree that permission to copy from, or to publish from, this dissertation may be granted by the professor under whose direction it was written, or, in his absence, by the Dean of the Graduate Division when such copying or publication is solely for scholarly purposes and does not involve potential financial gain. It is understood that any copying from, or publication of, this dissertation which involves potential financial gain will not be allowed without written permission.

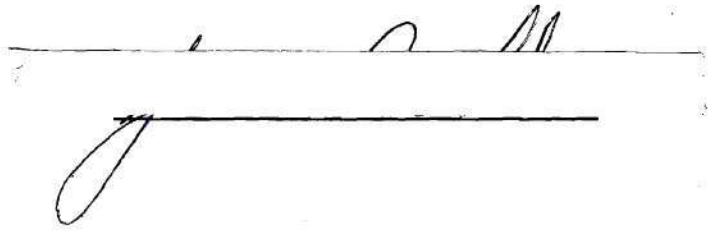

7/25/68

MEASUREMENT OF STEADY-STATE, SPACE DEPENDENT

THERMAL NEUTRON SPECTRA IN BERYLLIUM

Approved:

John M. Kallfelz , Chairman

Geoffrey G. Eichholz

Don S. Harmer

Stephen Spooner

Date approved by Chairman 20 Nov 72

ACKNOWLEDGMENTS

A number of individuals have contributed to the successful completion of this thesis. I wish to take this opportunity to express my gratitude to all concerned.

My adviser, Dr. John M. Kallfelz, has been an integral part of the success of this research. His enthusiasm and close personal contact with the work have proved an invaluable support in times of doubt and confusion. Furthermore, his probing and detailed criticism of this work have stressed perhaps the most valuable lesson to be learned in an undertaking of this type, the painstaking care necessary to ensure that the results of the endeavor will reflect the quality to withstand subsequent meaningful comparison. Additionally, I would like to thank the members of my reading committee, Dr. Geoffrey Eichholz, Dr. Don Harmer, and Dr. Stephen Spooner for taking time from their own busy schedules to follow the progress of the research and to read and improve on the content and style of the thesis draft.

I wish to thank my friend Mr. B. I. Shamasundar for his many probing questions which were invaluable aids in clarifying in my own mind numerous involved aspects of this work. My thanks also to Mr. Ed Chow for his assistance in developing the solution to the detector efficiency equation in Appendix C. I am grateful to Dr. M. M. R. Williams of the University of London, Queen Mary College, whose theoretical work inspired these measurements, for his correspondence and discussion which elucidated

many questions.

Financial support throughout this research has been provided variously by National Science Foundation and U. S. Atomic Energy Commission Traineeships as well as a graduate research assistantship through the School of Nuclear Engineering at Georgia Tech. The beryllium used in these measurements was part of a $100,000 inventory, on loan from the Argonne National Laboratory.

I am indebted to the members of the Georgia Tech Research Reactor staff for their cooperation in carrying out the experimental phases of this research. The reactor supervisors, Mr. Fred Apple and Mr. Robert Kirkland, were very helpful in agreeing to and assisting in the modification of the thermal column to facilitate the experiments. The reactor operators, Messrs. Lamar Bennett, Sam Kirbo, Dean McDowell, John Moon, and Sonny Pruett, were truly a pleasure to work and be associated with. The efforts of the health physics staff, consisting of Messrs. Bob Boyd, Martin Mitchell, Jerry Taylor, and John Wright, at assuring the safe operation of the experiments are appreciated. Finally, Mr. Mike Burke's crackerjack abilities as a machinist have been demonstrated time and again in the construction of various pieces of equipment. More important than the top-notch technical abilities of the aforementioned gentlemen has been their sincere interest in me and their efforts to maintain my good spirits from day to day, for which I am very grateful.

I would like to thank my "family," Mr. and Mrs. Paul Kulcsar, Mr. James H. Lake, and Mr. and Mrs. David Hall, for their heartening and reassuring support during my many years in college. Their love and their

unwavering faith in my abilities have always meant a great deal to me. I owe a special debt of gratitude to my mother for instilling in me a strong drive and desire to succeed, and for teaching me to set my sights high. Whatever success I have achieved or will achieve in the future can be attributed in large part to her efforts early in my education.

My thanks also to Mrs. Lydia Geeslin for a first-rate job of typing the final thesis manuscript.

Finally, my sincerest appreciation to my wife, Sharon, for her untiring efforts at typing and retyping the thesis draft, but especially for her love and encouragement throughout the long ordeal.

TABLE OF CONTENTS

TABLE OF CONTENTS (Continued)

TABLE OF CONTENTS (Concluded)

LIST OF TABLES

LIST OF TABLES (Continued)

LIST OF TABLES (Continued)

LIST OF TABLES (Concluded)

LIST OF ILLUSTRATIONS

LIST OF ILLUSTRATIONS (Continued)

LIST OF ILLUSTRATIONS (Continued)

LIST OF ILLUSTRATIONS (Continued)

LIST OF ILLUSTRATIONS (Continued)

LIST OF ILLUSTRATIONS (Continued)

LIST OF ILLUSTRATIONS (Concluded)

SUMMARY

Neutron scattering phenomena continue to prove an invaluable means by which one is able to investigate the physical structure and characteristics of materials, as well as predict parameters of interest in the design and operation of nuclear reactors. There remain certain aspects of the neutron thermalization problem which are not completely understood. Fundamental questions have arisen concerning the treatment of the neutron field and the establishment of an equilibrium, asymptotic decay mode in the pulsed-source-time-dependent and steady-state-space-dependent diffusion parameter experiments in very small or highly poisoned crystalline moderating systems. Specifically, theory predicts the disappearance of the discrete fundamental mode eigenvalues (decay constants) and eigenfunctions (equilibrium spectra) in systems with bucklings or poisonings above some "critical" value so that the decay in this region is non-asymptotic even at long times after or at large distances from the source, being governed by some non time- or space-energy separable continuum distribution of eigenvalues and eigenfunctions. It is the intent of this thesis to undertake direct experimental verification of the disappearance of the discrete fundamental mode decay and the concurrent existence of the continuum range of eigenvalues and eigenfunctions in the diffusion length problem in small, steady-state crystalline systems with strong transverse leakage effects.

Space dependent angular thermal neutron spectra have been measured

along the longitudinal axes of 25.4 x 25.4 x 50.8 and 35.6 x 35.6 x 50.8 cm beryllium assemblies by the neutron chopper, time-of-flight technique with the thermal column of the Georgia Tech Research Reactor as the steady-state neutron source. The spectra for neutrons moving away from the source were characterized by a progressive build-up of cold neutrons, below the Bragg cut-off, with increasing distance from the source plane; the relative rate of cold neutron build-up increasing with increasing transverse buckling (decreasing transverse dimensions). In both assemblies, the angular spectrum was found to be strongly space dependent and in neither was there any apparent tendency toward an equilibrium or asymptotic distribution out to distances in excess of 40 cm from the source plane. The strong space dependent behavior means that the usual assumption of space-energy separability in the solution of the transport equation is clearly invalid in this buckling range. Furthermore, the complete lack of equilibrium, asymptotic decay conditions means that the coefficients of the usual fit to the decay constant versus buckling expansion are no longer a unique function of the moderator diffusion parameters.

The measured nonequilibrium spatial decay behavior in small beryllium assemblies is in agreement with the published transport theory predictions of the "critical" transverse dimensions for the disappearance of the discrete asymptotic decay mode, but in disagreement with the corresponding diffusion theory results which predict that asymptotic decay conditions should exist in beryllium assemblies as small as 30 x 30 cm. Consequently, it is expected that these experimental results will have significant bearing on the applicability of the transport and diffusion

theory analyses of this and similar problems. In addition, these measured, highly distorted spectra are rich in the physics of neutron scattering and should serve as a sensitive and demanding test situation for theoretical scattering kernels in crystalline systems.

CHAPTER I

INTRODUCTION

Neutron scattering phenomena continue to prove an invaluable means by which one is able to investigate the physical structure and characteristics of materials as well as predict parameters of interest in the design and operation of nuclear reactors. There remain certain aspects of the neutron thermalization problem which are not completely understood. Specifically, questions have arisen concerning the treatment of the behavior of the neutron field and the establishment of an equilibrium distribution in very small or highly poisoned crystalline moderators. Similar anomalies have appeared in the treatment of certain fast reactor physics problems, specifically the prediction of subcriticality effects, such that insight into the neutron transport problem in highly distorted systems can be expected to have relevance to both the thermal and fast reactor fields.

The neutrons in a moderating medium tend to return toward an equilibrium energy distribution after some perturbation in space or time at a rate which is characterized not only by the neutron-nuclear scattering force law, but also by the physical state of the moderator atoms, for neutron energies less than about 1 eV. Thus the scattering kernel, which is a measure of the probability that a neutron moving in a direction $\vec{\Omega}$ with an initial energy E will scatter into a particular solid angle $\vec{\Omega}'$ with a final energy E', is dependent on the nature of the chemical binding of the

moderating atoms.

The final equilibrium neutron energy spectrum in an infinite, non-absorbing medium is a Maxwellian distribution. This is the case regardless of the energy exchange mechanisms at work in the moderator to establish the equilibrium. Thus, in order to obtain any useful information about these moderator-dependent energy exchange mechanisms from the equilibrium spectrum, one must distort the spectrum in some manner from the Maxwellian. This distortion can be accomplished in several ways, one of which, so called diffusion cooling, shifts the spectrum by increasing the number of neutrons with short mean-free-paths as a result of leakage from finite assemblies in the pulsed source, time dependent experiment. Another method, so called diffusion heating, involves shifting the spectrum by increasing the number of neutrons with long mean-free-paths by poisoning the moderator with absorber atoms as in the steady-state diffusion length experiment.

In the case of the time evolution of a pulse of neutrons injected into a finite moderating medium, one expects that the neutron intensity will eventually fall off asymptotically in time like $e^{-\lambda t}$. Similarly, in the case of the space evolution of an initial steady-state distribution of neutrons incident on one face of an essentially infinite half-space of poisoned moderator, one expects the flux to fall away asymptotically in space like $e^{-\kappa z}$ at points sufficiently deep in the assembly. The dependence of the time decay constant, λ, on the size and shape of the moderator assembly, and the dependence of the space decay constant, κ, on absorber concentration, have been the subject of many experiments aimed

at extracting basic diffusion parameters characteristic of the moderating medium. Specifically, one seeks to approximate the variation of measured time or space decay constants with buckling or absorber concentration by a truncated polynomial expansion in B^2 or Σ_a, respectively. The resulting coefficients of this expansion then contain the diffusion coefficient, D, and the diffusion cooling coefficient, C, which is related directly to the scattering law, being inversely proportional to M_2, the mean-squared energy exchanged between the neutrons and scattering atoms in the moderator.[1]

As demands for better neutron physics parameters have increased, these experiments have been pushed to higher values of B^2 or Σ_a, primarily to obtain improved values of the diffusion cooling coefficient, and hence a better understanding of the scattering properties of the moderator, from the curvature of the λ vs B^2 or K vs Σ_a curves. The scatter in the beryllium decay constant data in Figure 1 demonstrates the curious amount of disparity[2] in the data from different laboratories for the crystalline moderators, like beryllium, beryllium oxide, and graphite, with their relatively weak energy transfer characteristics[1] and strongly fluctuating neutron transport mean-free-paths. This disparity has initiated a penetrating investigation into the question of how severely one can distort the neutron energy spectrum by leakage or absorption induced effects in order to improve the accuracy of diffusion parameters, and indeed into the whole realm of the establishment of an equilibrium asymptotic decay mode in very small or highly poisoned moderating systems. The results of these investigations continue to have important ramifications in reactor physics in the areas of determining the thermalizing characteristics of

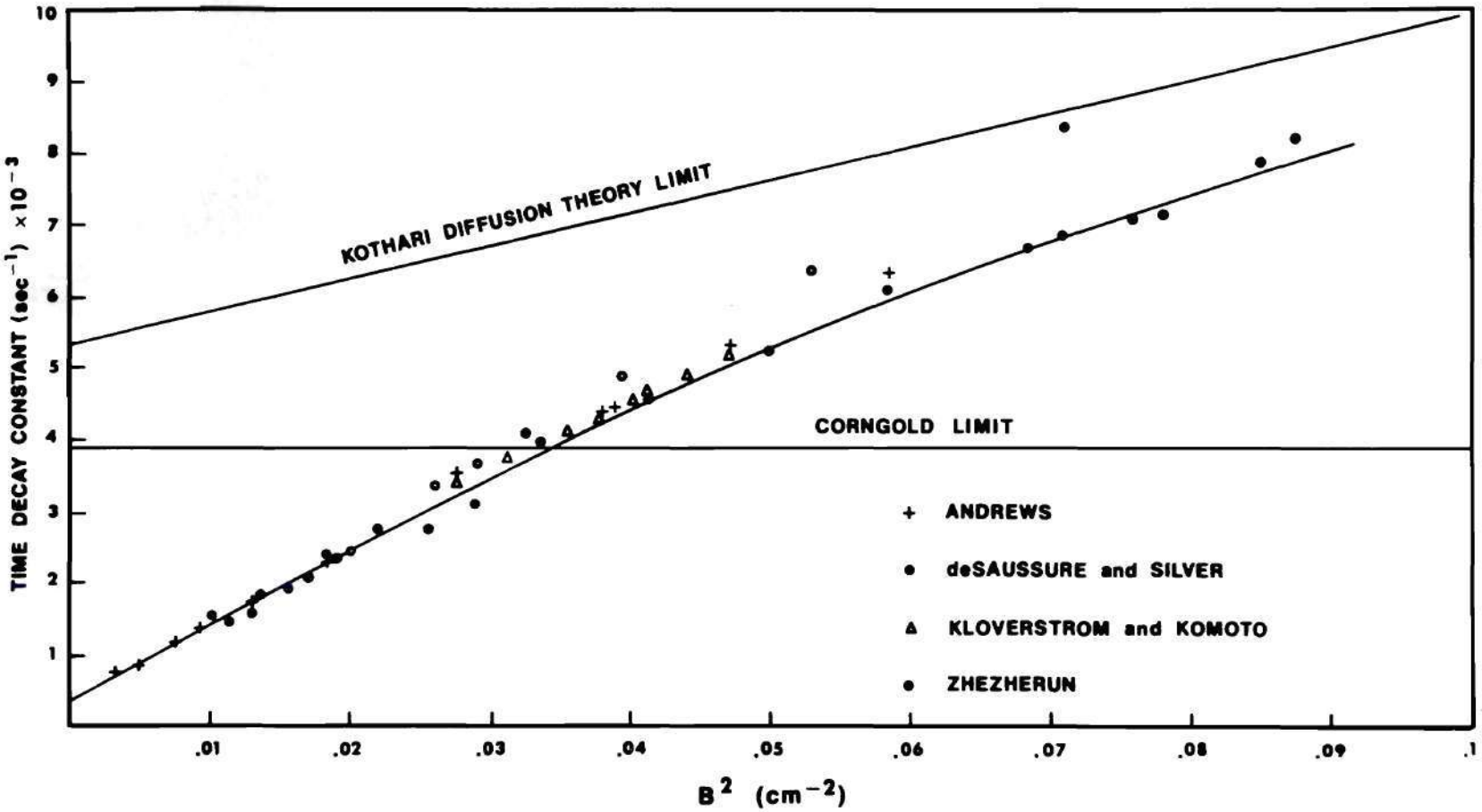

Figure 1. Behavior of the "Fundamental" Time Decay Constant, λ_o, with Geometric Buckling for Polycrystalline Beryllium. (Shown are the relative locations of the Corngold and Kothari limits discussed in the text in connection with equations 10 and 9, respectively. Data from Andrews,[3] deSaussure and Silver,[4] Kloverstrom and Komoto,[5] and Zhezherun.[6] The line through the data points is an eye guide and is not intended to represent any particular theoretical fit.)

crystalline systems through the structure of the scattering kernel and improving on the general methods of solution of the transport equation. In addition, the investigations into the question of the existence of a discrete fundamental mode decay are currently having some important bearing on the problems of fast reactor system subcriticality determinations. Specifically, the interest has centered around the question of under what circumstances one expects discrete eigenvalues (decay constants) and eigenfunctions (neutron energy spectra) to exist in these systems. It has been shown[7,8,9] that the very basic assumption of time- (or space-) energy separability in the solution of the transport equation must be severely restricted under certain circumstances. In addition, there is a limit above which no discrete eigenvalues or eigenfunctions can exist and where the decay is no longer asymptotic at long times or at great distances from the source, being governed by a continuum distribution of eigenvalues. A significant fraction of the measured decay constants in the crystalline moderators have been measured in systems which appear to exceed these limits, casting serious questions as to the interpretability of the results in terms of the usual simple diffusion parameters.

Origin and Discussion of the Limit on the Discrete Asymptotic Decay Mode

Although diffusion theory is certainly inadequate to describe some of the finer points of the thermalization problem, it should suffice here for a general discussion.[10]

Pulsed Neutron Problem

The diffusion equation describing the time evolution of a burst

of neutrons in a finite moderating medium can be written as[1]

$$\frac{1}{v} \cdot \frac{\partial \phi(E,t)}{\partial t} + \Sigma_T(E) \cdot \phi(E,t) + D(E) \cdot B^2 \cdot \phi(E,t) \tag{1}$$

$$= \int_0^\infty \Sigma_s(E' \rightarrow E) \cdot \phi(E',t) \cdot dE' \ ,$$

where the terms have the usual meanings discussed in reference 1 and the customary assumptions have been made to arrive at the buckling approximation for the condition describing neutron leakage. Equation 1 can be turned into an eigenvalue problem by assuming time-energy separability and seeking solutions wherein the flux is given by a superposition of terms of the form

$$\phi_\nu(E,t) = \phi_\nu(E) \cdot e^{-\lambda_\nu t} \ . \tag{2}$$

Equation 2 defines the time eigenvalues, λ_ν, and their associated eigenfunctions, $\phi_\nu(E)$. Substituting into equation 1 and rearranging terms results in

$$\left[\frac{-\lambda_\nu}{v} + \Sigma_T(E) + D(E) \cdot B_\nu^2\right] \cdot \phi_\nu(E) \tag{3}$$

$$= \int_0^\infty \Sigma_s(E' \rightarrow E) \cdot \phi_\nu(E') \cdot dE' \ .$$

It has been generally assumed that, once the eigenfunctions $\phi_\nu(E)$ have been determined from equation 3, the flux $\phi(E,t)$ can then be reconstructed from the eigenfunction expansion according to

$$\phi(E,t) = \sum_{\nu} A_{\nu} \cdot \phi_{\nu}(E,t) \quad , \tag{4}$$

or, substituting equation 2,

$$\phi(E,t) = \sum_{\nu} A_{\nu} \cdot \phi_{\nu}(E) \cdot e^{-\lambda_{\nu} t} \quad , \tag{5}$$

where the A_{ν} are modal weighting functions and the number of decay modes, ν, is as yet undetermined.

Knowing that the eigenvalues, λ_{ν}, are a monotonically increasing set, and assuming for the moment that the eigenfunction expansion 5 is valid and complete, then it follows that, for large t, the lowest order (fundamental) mode will dominate the decay, the higher modes with larger decay constants having fallen off more rapidly in time. Thus, at long times after the injection of the source burst, the flux decay is described according to

$$\phi(E,t) = \phi_{o}(E) \cdot e^{-\lambda_{o} t} \tag{6}$$

where λ_{o} is the fundamental time decay constant and $\phi_{o}(E)$ is the asymptotic, equilibrium neutron energy spectrum.

The fundamental time decay constant is some unknown function of the geometry and dimensions of the moderator assembly which can be approximated by an expansion in powers of the buckling, B^2,

$$\lambda_{o} = \sum_{n=o}^{\infty} a_{n} \cdot (B^2)^{n} \quad . \tag{7}$$

The diffusion parameters of the moderator which determine the absorption and leakage rates, and thus the flux decay rate, are contained in the expansion coefficients, a_n. Specifically, if the expansion 7 is truncated after second order terms in B^2, one obtains

$$\lambda_o = v_o \cdot \Sigma_{ao} + \bar{D}_o \cdot B^2 - C \cdot B^4 \ , \tag{8}$$

where $\bar{D}_o$ is the Maxwellian average of the diffusion coefficient, $D(E)$,

$$\bar{D}_o = \int_o^\infty D(E) \cdot M(E) \cdot dE \Big/ \int_o^\infty \frac{M(E) \cdot dE}{v} \ ,$$

and C is the diffusion cooling coefficient. One varies B^2 by changing the physical dimensions of the moderator assembly and measures the associated fundamental time decay constant, λ_o, in each case. Then, by fitting the measured variation of λ_o with B^2 to an equation of the form 8, as in Figure 1, the diffusion parameters follow from the fitting parameters, a_n. Specifically, the Maxwellian averaged absorption cross section, Σ_{ao}, is proportional to the infinite medium (B^2=0) intercept, the diffusion coefficient $\bar{D}_o$ is the slope of the linear portion of the curve, and the diffusion cooling coefficient, C, may be deduced from the curvature in the dispersion curve at higher bucklings. It is interesting to note that the first two terms in equation 8 depend only on the Maxwellian averaged absorption and transport cross sections, respectively, and are therefore simple functions of the neutronic properties of the moderator nuclei and are predicted by simple one-velocity diffusion theory, whereas the presence of the higher order terms is due to the deviation of the neutron energy spectrum

also goes to zero as v approaches zero, the limit point on the existence of a discrete time decay constant reduces to

$$\lambda_o \leqq \underset{v\to 0}{\text{Limit}} \left\{ v\Sigma_{inel}(E) \right\} . \qquad (9\text{-a})$$

A similar analysis of the transport equation where, among other things, one cannot easily extract the elastic scattering component from the angular and energy dependent scattering kernel, $\Sigma_s(E'\to E, \mu'\to\mu)$, yields the limit

$$\lambda_o \leqq \underset{v\to 0}{\text{Limit}} \left\{ v\Sigma_T(E) \right\} \equiv \lambda^* . \qquad (10)$$

It is interesting to note that, due to the relative 1/v behavior of the low energy inelastic scattering cross section, λ^* reduces to essentially the same value as in equation 9-a at the limit v=0 in this particular case.

Corngold[11] states the limit in terms of a Maximum Buckling Theorem which he proves for an isotropic scattering kernel with a continuously varying cross section model.

Theorem: In the pulsed source experiment there exists a maximum value of B^2, denoted by $(B^*)^2$, corresponding to some minimum system dimensions, such that, for $B^2 > (B^*)^2$, no discrete eigenvalues exist.

This means that, as the size of the system is decreased (buckling increased), the discrete eigenvalues, λ_ν, increase, partly as a result of the increased leakage rate, until at some value of $B^2 = (B^*)^2$ even the lowest order fundamental eigenvalue, λ_o, exceeds the limit in equation 10

and ceases to exist. From this point on, the decay is nonexponential even at long times after the source burst. It should be noted that a more recent theoretical analysis of this same problem by Conn and Corngold[12,13] in the full realm of transport theory and including the effects of Bragg discontinuities in the cross section on the limit point yields a somewhat modified version of the Maximum Buckling Theorem, to be discussed in more detail later.

In mathematical terms, the disappearance of the single-valued exponential decay and the emergence of the non-equilibrium spectrum are equivalent to the disappearance of the discrete eigenvalues and eigenfunctions of the transport equation. The implication is then that the polynomial expansion 5 for the flux in terms of a series of discrete eigenvalues and associated eigenfunctions is no longer a complete set for all bucklings. The general solution should be of the form

$$\phi(E,t) = \sum_{\nu=0}^{\nu_{max}} A_\nu \cdot \phi_\nu(E) \cdot e^{-\lambda_\nu t} + \int_{\lambda^*}^{\infty} A(\lambda) \cdot \phi(E,\lambda) \cdot e^{-\lambda t} \cdot dt \ , \qquad (11)$$

the integral term being a continuum contribution[11,15] which is the only one that can exist for $B^2 > (B^*)^2$. An effect accompanying the disappearance of the discrete eigenvalues and eigenfunctions is that the flux spectrum $\phi(E,t)$, is no longer separable[7,8,16] in time and energy due to the presence of the integral, greatly complicating the subsequent solutions of the transport equation.

The limit on the discrete, fundamental mode decay and the subsequent incompleteness of the expansion 5 are clearly of some considerable importance[2] to the experimentalist, who, in order to obtain improved accuracy

in the higher order diffusion parameters in equation 8, customarily extends his λ vs B^2 measurements over as wide a range of bucklings as is possible. In doing so, however, the limit $(B^*)^2$ may be exceeded, in which case the experiment would not have measured a true discrete eigenvalue, but rather some quasi-exponential contribution from the continuum. The experimental situation is made worse by the fact that the deviation from the discrete exponential decay, at the transition point, $(B^*)^2$, and on into the continuum region may be small, making it difficult[17] in some instances for the experimenter to determine that the decay has in fact become non-fundamental, especially if the strongest spectrum distortion is confined to regions of low neutron intensity as it is in the time dependent experiment. The important thing to realize is that this pseudo-fundamental decay constant from the continuum region does not necessarily bear any simple theoretical resemblance to those discrete decay constants outside the continuum. Specifically, there is no basis to assume that the expansion 7 for the diffusion parameters of the system in terms of the behavior of the discrete, fundamental mode eigenvalue, λ_o, can be extended across the limit $(B^*)^2$ and used to fit the continuum eigenvalues with the same coefficients, a_n, above and below. It is likely that a number of diffusion parameter results reported in the literature, especially for the diffusion cooling coefficient, for which the buckling exceeded $(B^*)^2$, are in error as a result of the inclusion of these continuum eigenvalues in the fit to equation 8.

Diffusion Length Problem

The analysis of the diffusion length problem is closely related to

that for the pulsed source, time-dependent problem in many respects.

The diffusion equation,[1] describing the spatial evolution of an initial distribution of neutrons incident on one face of an essentially infinite half-space of poisoned moderator, is

$$-D(E) \cdot \frac{\partial^2 \phi(E,z)}{\partial z^2} + \Sigma_T(E) \cdot \phi(E,z) = \int_o^\infty \Sigma_s(E' \rightarrow E) \cdot \phi(E',z) \cdot dE' \qquad (12)$$

where terms again have the usual meanings defined in reference 1. Here again, if one assumes space-energy separability, equation 12 can be turned into an eigenvalue problem by seeking solutions of the form

$$\phi_\nu(E,z) = \phi_\nu(E) \cdot e^{-\kappa_\nu z} , \qquad (13)$$

which defines the space eigenvalues, κ_ν, and their associated eigenfunctions, $\phi_\nu(E)$, such that equation 12 becomes

$$\left[\Sigma_a(E) + \Sigma_s(E) - \kappa_\nu^2 \cdot D(E)\right] \cdot \phi_\nu(E) = \int_o^\infty \Sigma_s(E' \rightarrow E) \cdot \phi_\nu(E') \cdot dE' . \qquad (14)$$

The flux, $\phi(E,z)$, can then be reconstructed from the eigenfunctions, $\phi_\nu(E)$, according to

$$\phi(E,z) = \sum_\nu A_\nu \cdot \phi_\nu(E) \cdot e^{-\kappa_\nu z} \qquad (15)$$

where κ_o, the fundamental mode eigenvalue which is presumed to dominate at large distances from the source, is equal to the inverse of the diffusion length, L_o.

In the diffusion length case one expresses the unknown dependence of the fundamental space decay constant on poisoning in the system as a power series expansion in Σ_{ao},

$$\kappa_o^2 = \sum_{n=0}^{\infty} b_n \cdot (\Sigma_{ao})^n \quad , \tag{16}$$

wherein the diffusion parameters are contained in the expansion coefficients, b_n. When the expansion is truncated at second order terms in Σ_{ao},[10,18]

$$\kappa_o^2 = \frac{v_o}{\bar{D}_o} \cdot \Sigma_{ao} - \frac{Cv_o^2}{\bar{D}_o^3} \cdot \Sigma_{ao}^2 \tag{17}$$

where the terms are as defined in conjunction with equation 8. One varies Σ_{ao} by changing the poison concentration in the moderator assembly and measures the associated fundamental space decay constant, κ_o, in each case. Then, by fitting the measured variation of κ_o with Σ_{ao} to an equation of the form 17, the diffusion parameters $\bar{D}_o$ and C follow from the fitting parameters, b_n. The similarity to the pulsed source, time-eigenvalue problem is obvious, with the additional advantage that one is not forced to define an extrapolation distance as precisely.

By arguments identical to those presented in the pulsed source case, the following limit on the discrete fundamental mode space decay eigenvalue, κ_o, can be derived from equation 14.

$$\kappa_o^2 \leqq \left[\frac{\Sigma_a(E) + \Sigma_s(E)}{D(E)}\right]_{min} \tag{18}$$

or, since $\Sigma_a(E) \ll \Sigma_s(E)$ for most moderators, and $D(E) \cong 1/3\ \Sigma_s(E)$, in diffusion theory

$$\kappa_o \leqq 1.7\ \Sigma_s(E)_{min} \ . \tag{19}$$

A more general derivation in the realm of transport theory leads to the limit,

$$\kappa_o \leqq \Sigma_T(E)_{min} \equiv \kappa^* \ . \tag{20}$$

This limit on the discrete fundamental mode space decay constant is controlled by the scattering characteristics of the moderator through the behavior of $\Sigma_T(E)$. A large class of moderators, particularly H_2O and D_2O, have a total cross section which varies smoothly with energy in such a manner that $\Sigma_T(E)$ never drops below the "free atom" value[2] at about 1 eV. However, in the case of the crystalline moderators like beryllium, beryllium oxide and graphite, to mention only a few, $\Sigma_T(E)$ displays sharp fluctuations in the vicinity of Bragg scattering peaks. Figure 2 shows that $\Sigma_T(E)$ in fact drops very sharply below the Bragg cut-off (at about 0.007 eV in beryllium) to a minimum which is relatively much lower than the free atom value. Thus, the limit imposed by equation 20, which occurs at an energy just below the Bragg cut-off, should be substantially more restrictive in crystalline systems than, for example, in the common liquids. It is apparent from examination of the beryllium cross section in Figure 2 that the limit in crystalline systems is very sensitive to the scattering characteristics of the moderator, especially the value and temperature dependence[13,19] of the inelastic scattering cross section, $\Sigma_{inel}(E)$, below the Bragg cut-off.

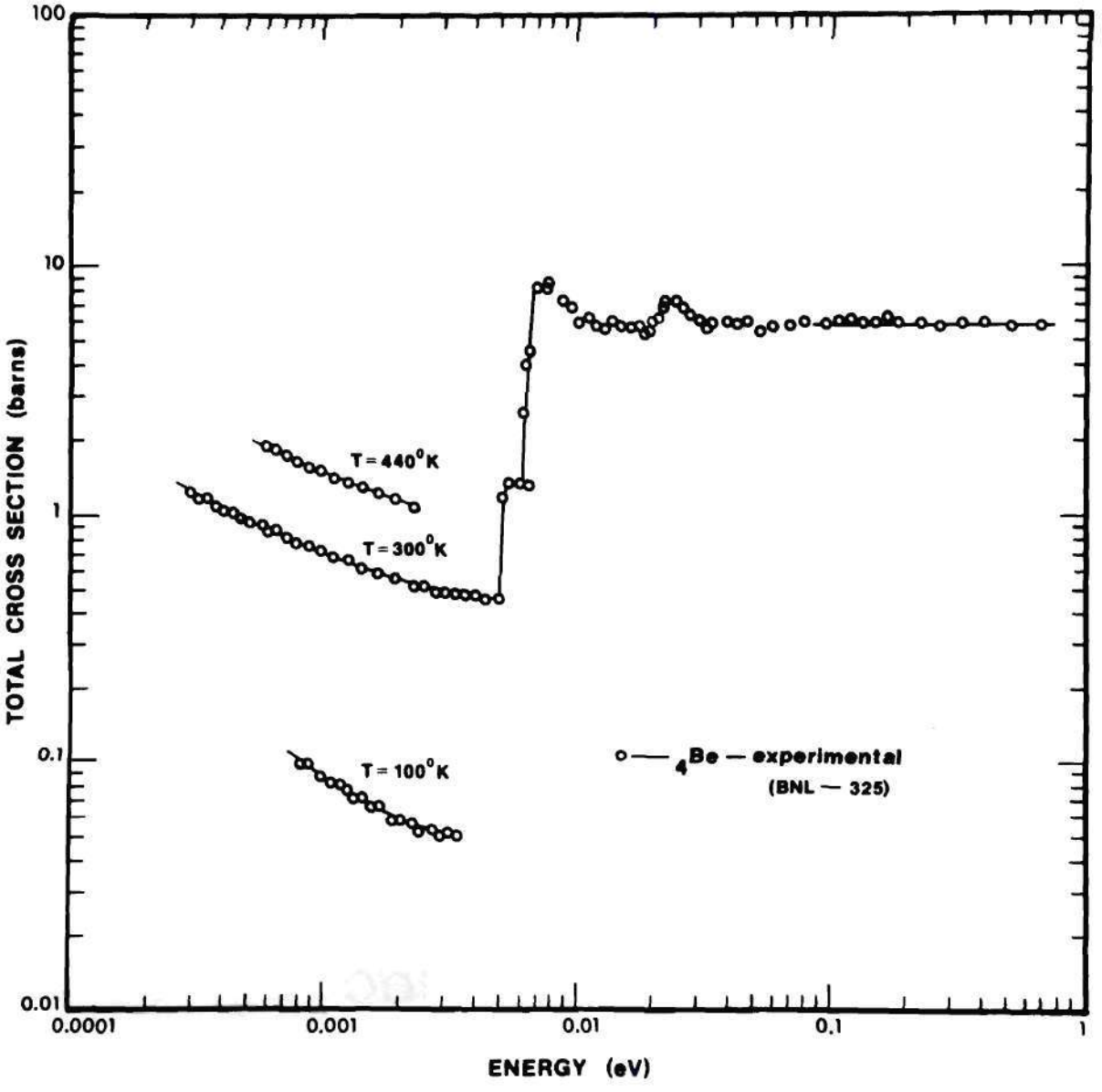

Figure 2. Total Microscopic Cross Section for Beryllium in the Thermal Energy Range. (Data from BNL-325 reference 14.)

Corngold[11] proves the following Maximum Absorption Theorem for the diffusion length case in the realm of transport theory for an isotropic scattering kernel with a continuously varying cross section model, for physically meaningful absorption laws.[20]

Theorem: Let the macroscopic absorption cross section of the poison in a diffusion length experiment be written as $\Sigma_a(v) = N_a\sigma_a(v)$, where $\sigma_a(v)$ is the microscopic cross section. There exists a maximum concentration of absorber, denoted by N_a^*, such that for $N_a > N_a^*$ no discrete eigenvalues exist. In particular, no diffusion length exists.

This means that as the poison concentration in the system is increased, the discrete eigenvalues, κ_ν, increase until, at some poison concentration, N_a^*, even the lowest order fundamental, κ_o, exceeds the limit 20 (which has also increased by the addition of Σ_a to Σ_t, but at a slower rate than the κ_ν) and ceases to exist so that the spatial decay necessarily becomes nonexponential, even at large distances from the source.

An interesting insight into the physical situation that gives rise to the disappearance of the discrete fundamental mode decay can be drawn from the following discussion. As the absorber concentration is increased in the moderating assembly, the effect is to increase the flux decay rate by increasing the space decay eigenvalues, κ_ν, in equation 16. Physically speaking, this increased decay rate results from an increased absorption rate in the poisoned assemblies. If a fundamental asymptotic decay mode is to be attainable, then the energy exchange mechanisms in the moderator must be capable of compensating for the energy and angle

dependent spectrum distortions, resulting from the absorption induced gradients within the assembly, by replenishing the depleted regions in the angular neutron energy spectrum by way of elastic and inelastic scattering interactions. This must be the case since, by definition, an asymptotic decay mode implies that the spectrum has reached some equilibrium distribution where all energy regions decay at the same rate. The equilibrium state explains why an integral parameter like the fundamental decay constant, K_o, which is characteristic of the average behavior of the neutrons throughout the spectrum, can completely describe the decay in an asymptotic mode. The intensity of neutrons in the spectrum at any particular energy, E, cannot decay any faster, on the average, than $e^{-\Sigma_T(E)}$ for $1/\Sigma_T(E)$ is the mean-distance between collisions. Thus, those neutrons in the spectrum, for which Σ_T is a minimum, limit the maximum rate of decay since they correspond to the longest mean-free-paths. When the poison concentration is high enough such that the limit N_a^* (or K^* in equation 20) is exceeded, some regions of the spectrum, those for which $\Sigma_T(E) > (\Sigma_T)_{min}$, will decay faster than $e^{-(\Sigma_T)_{min}}$ and the spectrum will become progressively distorted. Inasmuch as $1/(\Sigma_T)_{min}$ is the maximum mean-free-path for neutrons in some region of the spectrum, the interaction mechanisms in the moderator are unable to make this particular region decay fast enough to keep pace with the other regions in the spectrum, since a neutron obviously cannot change its energy or direction "between" interactions, and no equilibrium distribution can be established even at large distances from the source plane. The progressive spectrum distortion and the disappearance of the asymptotic decay mode mean that a single-valued discrete

decay constant like κ_o cannot possibly completely describe the average behavior of the flux decay at all space points.

Here again, the existence of the limit in equation 20 means that the polynomial expansion 15 for the flux in terms of a series of discrete eigenvalues and eigenfunctions is not a complete set, and the general solution should look like

$$\phi(E,z) = \sum_{\nu=0}^{\nu_{max}} A_\nu \cdot \phi_\nu(E) \cdot e^{-\kappa_\nu z} + \int_{\kappa^*}^{\infty} A(\kappa)\phi(E,\kappa) \cdot e^{-\kappa z} \cdot d\kappa \ , \qquad (21)$$

where the integral term is the continuum contribution which is the only one that can exist for $N_a > N_a^*$. The presence of the integral causes the flux, $\phi(E,z)$ to be space-energy inseparable when the decay is non-fundamental, even at large distances from the source. Once again, the implication of the disappearance of the discrete, fundamental mode decay is that the power series expansions, 16 or 17, for κ_o in terms of the usual diffusion parameters is not valid for $\kappa > \kappa^*$ with the same coefficients above and below the limit.

Recently, Williams[21,22,23] has studied this same diffusion length problem in greater detail and in the physically more realistic situation of a finite medium. That is, his analysis accounts explicitly for neutron leakage out the sides of the system and the problem then is to investigate the existence of a single-valued, fundamental mode decay along the axis of the assembly as a function of both absorption and transverse dimensions. One important result of this analysis is the emergence of an even more restrictive limit than equation 20. Specifically, Williams finds that the limit for a discrete fundamental mode decay, in terms of a

maximum permissible transverse buckling, $(B^*)^2$, is

$$(B^*)^2 \leq \left\{\Sigma_T^2(E)_{min} - \kappa_\nu^2\right\} , \qquad (22)$$

where κ_ν are the previous infinite medium eigenvalues. The minimum dimensions of a rectangular assembly of polycrystalline beryllium with only "natural" absorption, are found[22] to be of the order of 127 x 127 cm at 300°K, corresponding to a "critical" transverse buckling of 1.16×10^{-3} cm^{-2}, for the existence of a discrete fundamental mode decay. By the usual standards, these "critical" dimensions are quite large and well within the range that might earlier have been called "infinite" for purposes of determining diffusion parameters from diffusion-length-type experiments. However, the implications of the Williams theory are quite clear: in systems smaller than the limit in equation 22, the flux decay will necessarily be nonexponential and the energy spectrum which is no longer separable in space and energy, will change continuously with increasing distance from the source plane. In poisoned or low temperature moderators these minimum critical dimensions will be even larger since an increase in absorber will increase κ_ν, whereas a decrease in temperature significantly lowers the value of $\Sigma_T(E)$ below the Bragg cut-off.

Recently, Ahmed, Kothari, and Kumar[24] have presented the results of diffusion theory calculations of the dependence of the diffusion length, $L_o = 1/\kappa_o$, on the transverse dimensions of infinitely long blocks of polycrystalline beryllium. Using an energy-dependent transverse buckling approximation they find that a true discrete spatial decay mode exists for assemblies with transverse dimensions as low as 30 x 30 cm. They also

find the pseudo-equilibrium conditions, governed by the independent decay rate of the sub-Bragg neutrons, are established reasonably fast in assemblies with transverse dimensions less than about 20 x 20 cm. In assemblies of intermediate transverse size, between 20 x 20 and 30 x 30 cm, equilibrium conditions are not predicted out to 100 cm from the source. These "critical" dimensions are substantially lower than those predicted by the Williams theory.[22] Williams[25] has, in fact, attacked the Kothari results on the basis of the questionable justification for the use of diffusion theory for this problem. We shall have more to say about this in the Conclusions.

Current Status of Understanding

Theoretical

It has been predicted theoretically that there exists some upper limit on the discrete, fundamental mode decay constant in poisoned, steady-state diffusion length experiments (with or without transverse leakage), and finite medium, pulsed source experiments. This limit manifests itself in a maximum poison concentration or a maximum geometric buckling, above which the flux decay in the system can no longer be described by a single discrete exponential decay constant, even at large distances from, or long times after, the source insertion. A cursory investigation of the existing experimental data reveals that a substantial number of measured decay constants in the crystalline moderators lie above the limit λ^* or κ^* and extend well into what could be the region of continuum eigenvalues. See, for example, Figure 1 for the pulsed source case in beryllium. (In Figure 1, the limit in equation 10, $(v\Sigma_T(E))_{min}$, is labeled as the "Corngold Limit.") If this limit is, in fact, the

correct one, then some of the experiments have not measured an asymptotic, single-valued exponential decay, but rather some pseudo-exponential decay "constant" from the continuum of eigenvalues. Of course, since the spectrum is continually changing in this region, the measured decay constants will, in fact, not be constants at all, but rather they are in all likelihood some slowly varying functions of space or time, and the value of decay constant reported is dependent on the range of space or time over which the analysis was performed. The slowly changing nature of the measured decay "constants" at high values of Σ_a or high bucklings could lead to rather obvious difficulties in determining the coefficients of equations 17 or 8 and would certainly be responsible for errors in the diffusion parameters derived from these coefficients. This effect offers a possible explanation for the lack of agreement between the reported values of measured diffusion parameters, especially the diffusion cooling coefficient, C, from different laboratories.

There remains the question of why so many experiments seem to be measuring "discrete" decay constants in the buckling or poisoning region above the theoretical limit (for example, see references 3 through 6 and 26 through 29). There is the additional problem that the measured decay constants appear to show no tendency whatsoever to bend over and lie under the bound in equations 10 or 20. If the data are, in fact, correct, that is, if the measured decay constants are representative of a true discrete mode, then Corngold[2] feels that this lack of a limiting tendency "stands in direct contradiction to the rather direct consequences of the Boltzmann equation."

One might look to the experimental situation itself for answers to the aforementioned anomalies. It is reasonable to assume that experiments measuring integral parameters in crystalline moderators with large values of Σ_a or B^2 have a large statistical uncertainty attached to them resulting from a lack of sufficient neutron intensity, due, in part, to the large absorption or leakage rates in these systems and consequently the very high flux decay rates. The associated error limits seemingly make it difficult in some cases for the experiment to distinguish between a pure exponential decay and some slowly changing pseudo-exponential behavior in this situation.[30]

One thing seems clear, however, the error limits are not nearly large enough to obscure any tendency for the measured decay constants to lie under a limit like equations 10 or 20, leading one to conclude that, in fact, this tendency does not exist. In addition, there appeared to be no experimentally detectable transition when crossing the theoretical bound, equations 10 or 20, into what should have been the continuum region of eigenvalues. In the words of one team of experimenters,[31]

> . . . our λ measurements have greatly exceeded this [critical buckling value]. We observed a perfect exponential decay with a single decay constant for each assembly, in the continuum region. The decay constants were obtained with good statistical accuracy and the data had excellent reproducibility. The decay constant curve [λ is B^2] was smooth and continuous.

The situation was then that the experiments in crystalline moderators did appear to be measuring a fundamental mode, exponential decay well into the region where theory predicted that the decay should have been governed by a non single-valued continuum of eigenvalues.

An explanation proposed by Kothari[32,33] for why this was so is

that the value of the Corngold limit, equation 10, may not be quantitatively correct. In a theoretical analysis of the pulsed neutron experiment, Kothari suggests that the observed decay constants in very small systems are eigenvalues of a truncated form of the Boltzmann equation which is bounded away from zero energy. Physically, this implies the assumption that, even though the energy distribution of neutrons is slowly changing with time for B^2 above $(B^*)^2$, this change is confined to those neutrons very close to zero energy. Since, in the pulsed source case, there are very few neutrons in the low energy region below the last Bragg peak in the transport cross section, this change in the neutron energy distribution will remain experimentally undetected in crystalline moderators. Kothari argues that it is therefore unrealistic to consider the absolute minimum of the limit in equation 10 at zero velocity. Rather, he would seek a minimum in the energy region of significant neutron intensity. When the energy region below some arbitrary $E_{cut\text{-}off}$ is excluded from consideration, the limit on the discrete fundamental mode decay constant reverts to equation 9 (in the diffusion approximation), namely

$$\lambda \leqq (v\cdot\Sigma_T(E) + v\cdot D(E)\cdot B^2)_{min} \equiv \lambda_{Kothari} \ . \qquad (9)$$

This limit is labeled the "Kothari Diffusion Theory Limit" in Figure 1. For crystalline moderators, this limit occurs at that energy corresponding to the highest Bragg peak in the transport cross section, just above the Bragg cut-off. The limit correctly reflects the fact that, ultimately, the fundamental mode decay will be governed by those neutrons with short mean-free-paths in the energy region just above the Bragg cut-off

(in the pulsed source case).[30,34] This is the so-called "trapping effect" of deSaussure.[35] It is interesting that deSaussure derives an essentially identical limit on slightly different grounds, starting from a more exact form of the transport equation and employing a variational principle.

The truncation of the Boltzmann equation has the effect of raising the value of the limit in the high buckling range by making it linearly dependent on B^2. Kothari is quick to point out[32] that, whereas a significant fraction of the measured decay constants lies well above the Corngold limit in equation 10, all the points are well within his new limit in equation 9 (see Figure 1). However, this new limit still does little to explain the poor agreement in the diffusion cooling coefficient from decay constant measurements at high bucklings.

Corngold[36] has argued that the Kothari approach does not really offer an explanation for why seemingly discrete eigenvalues exist above the limit $(v\Sigma_T(E))_{min}$ in equation 10 because it rests on the ad hoc assumption that one <u>should</u> truncate the range of neutron energies, whereas there is no real physical principle or experimental constraint that would compel one to do so. Rather, he feels that the phenomenon must be understood through reasoning based on the Boltzmann equation in its full domain of energy.

Wood[17,19,37] has studied this same pulsed neutron problem in small polycrystalline systems, solving the diffusion equation by numerical techniques with a realistic crystalline scattering kernel. He finds that, although there is a noticeable peaking of neutrons just above the Bragg cut-off, the "trapping effect" of deSaussure, it is the pile-up of neutrons near E=0 that prevents a truly asymptotic mode from being attained.

Wood concludes that, unless the experimentalist examines the spectra in this low energy region, he might be led to believe that an asymptotic distribution had been achieved when, in fact, it had not.

Inasmuch as the limit in the theoretically analogous diffusion length case occurs, not at v=0, but at the Bragg cut-off, it appears that the low energy cut-off assumption would have no effect on the value of the limit in equation 20. In addition, the neglect of the lowest energy neutrons in the diffusion length problem is most likely invalid inasmuch as it is these very low energy neutrons, specifically those neutrons below the Bragg cut-off, that control the ultimate existence of an asymtotic spatial flux decay mode due to their very long mean-free-paths.[38] In any case, the steady-state energy spectrum in crystalline moderators is enriched in these cold neutrons at certain angles, and even though the ΔE in this energy region is relatively small in relation to the rest of the spectrum, its neglect is most likely not defensible.

When a moderating system is highly poisoned or very small, no discrete decay constant is predicted to exist, as has been pointed out previously, and the decay should be described in terms of a continuous spectrum of eigenvalues. In this case, the amplitude functions, $A(\lambda)$ or $A(K)$ in equations 11 and 21, are particularly important. For example, $A(\lambda)$ is a weighting function of the density of continuum eigenvalue states lying between λ and $\lambda+d\lambda$, and as such it reflects, to some extent, the scattering properties of the moderator. Using diffusion theory, Corngold and Durgun[39] found that, whereas $A(\lambda)$ varies smoothly when the moderator is an incoherent scatterer, such as one of the common hydrogenous

liquids, it shows considerable oscillation in the case of coherent scattering crystalline moderators due to the Bragg structure of the cross section. Furthermore, a sharp peak in $A(\lambda)$ at some λ_p produces an effect, upon integration, much like that of a "discrete" mode. That is, the high density of eigenvalue states around λ_p makes the flux decay appear to be single-valued of the form $e^{-\lambda_p t}$. One sees that such a pseudo-discrete decay may well be observed in crystalline moderators. Corngold and Durgun have further shown that, for bucklings just slightly larger than $(B^*)^2$, the value of λ_p at which the peak in the weighting function occurs may be very close to λ^*, the transition point where the decay passes from a discrete fundamental mode into being governed by the continuum of eigenvalues. Thus it is easy to see why an experiment might not detect this transition in crossing the limit. It is well to remember that λ_p, while it may dominate the decay of the flux in this region, is in no way connected with a truly fundamental or asymptotic mode. The important conclusion to be drawn from this fact is that it is still <u>not</u> correct to extend one's analysis for diffusion parameters across the limit into the continuum region because the pseudo-fundamental decay constant, λ_p, is not necessarily related to the discrete fundamental mode decay constant, λ_o, by the same expansion 8. Specifically, Wood[40] and others have shown that, whereas λ_o and λ_p are perhaps very nearly the same at the limit point, λ^*, the slope of the λ vs B^2 curve is <u>not</u> the same when approaching the limit from the discrete or continuum sides. This fact seems to be born out in some recent experimental results in BeO by Sohrabpour and Bull.[41] It is this discontinuity in the slope of the λ vs B^2 curve which disallows any sort of analytic continuation of the expansion 8 across the limit, λ^*.

The recent work of Conn and Corngold[12,13,42] refutes at least some of the earlier diffusion theory predictions about the behavior of the eigenvalues above λ^*, although the implications to the experimental situation remain essentially intact. Conn and Corngold's inclusion of discontinuous, Bragg-type cross sections, as well as their explicit use of transport theory has produced some unexpected results. Most important among these is the discovery that discrete eigenvalues with magnitude $|\lambda| > \lambda^*$, that is discrete eigenvalues above the limit in equation 10, <u>can</u> in fact exist in crystalline moderators. These eigenvalues are buried in what is referred to as the "sub-Bragg continuum," that is, a continuum governed by those neutrons with long mean-free-paths in the energy region below the Bragg cut-off, and they are bounded from above by still another limit, $\lambda_{elastic}$,

$$\lambda_{el}(B^2) = \lambda^* + \frac{v_{Bragg} \cdot B^2}{3 \cdot \Sigma_{el}(v_{Bragg})} + O(B^4) \quad , \tag{23}$$

where $O(B^4)$ denotes terms of the order B^4. Exclusive of B^4 terms, it is interesting to note the similarity between λ_{el} and $\lambda_{Kothari}$ in equation 9.

The existence of discrete eigenvalues above λ^* contradicts that part of the "Maximum Buckling" theorem[11] which states that λ^* is an upper bound on the magnitude of <u>any</u> discrete eigenvalues. The discrepancy lies in the fact that, in the proof of the original theorem, it was implicitly assumed that the cross sections were continuous, slowly varying functions of energy, that is, discontinuous Bragg effects were excluded. The revised statement of the theorem proposes a new upper bound, $(B^{**})^2$, above which no isolated discrete eigenvalues are permitted to exist, and an inter-

mediate region between $(B^*)^2$ and $(B^{**})^2$ where the decay is governed by some admixture of sub-Bragg-discrete and continuum eigenvalues. Conn and Corngold find that the discrete exponential in this transition region is not the one that is dominant at long times, but rather, peaks in the continuum, $A(\lambda)$, govern the long-time behavior in the aforementioned manner suggested by Corngold and Durgun.[39] As B^2 increases toward $(B^{**})^2$, the time range over which a "good exponential" decay exists, that is the time range over which the decay is controlled by discrete decay constants buried in the sub-Bragg continuum between λ^* and λ_{el}, becomes progressively smaller[12] until, above $(B^{**})^2$, the theory still predicts that only the continuum eigenvalues above λ_{el} can exist. The existence of the sub-Bragg transition region, bounded by the new limit, λ_{el}, in equation 23, appears to be supported by some pulsed source, time dependent decay measurements in BeO by Rainbow and Ritchie.[26] The contention that decay data above λ^* cannot be used in the usual interpretation of the coefficients of the expansion 8 appears to remain valid in connection with inclusion of discrete sub-Bragg continuum eigenvalues. That is, analytic continuation of equation 8 into the sub-Bragg transition region between λ^* and λ_{el} is still forbidden if the coefficients of equation 8 are to be subsequently interpreted in terms of unique diffusion parameters.

Even though the experimental observations of "quasi-exponential" decay modes above the limit in equation 10, in what should be the continuum region of eigenvalues, now seem to be explained in a way which does not "stand in direct contradiction to the direct consequences of the Boltzmann equation," and without having to resort to any sort of energy cut-off assumption, the exact details of the structure of the continuum eigenvalues

and eigenfunctions, above the limit $(B^{**})^2$ (or Σ_a^{**} presumably) are still not completely understood. The theory of Conn and Corngold[12,13] is quite advanced and at the present time is well ahead of the experimental capabilities. In this light, there appears to be a standing need for improved experimental eigenvalue (decay constants) and eigenfunction (spectra) data both near the limit and on into the continuum region.

Experimental

By far the most popular method of obtaining diffusion parameters has been by way of pulsed source, time decay eigenvalue measurements in finite moderator assemblies. The experiments are relatively straightforward[1] in light of currently available sophisticated electronics, and the necessary equipment is "inexpensive" and available at any number of laboratories throughout the world. To date, many such time eigenvalue measurements have been performed with a significant number of the reported decay constants in crystalline moderators exceeding the theoretical limit for a discrete, fundamental mode decay.

The eigenvalue is by its very nature only an integral parameter describing the average behavior of the energy integrated flux spectrum. This fact is of little consequence where one is interested in the decay of a truly asymptotic, fundamental mode since the energy spectrum fast approaches some equilibrium value and remains in a steady-state thereafter. In this situation, an average parameter is usually sufficient to describe the behavior of the spectrum decay once the initial transients have died out. However, eigenvalue measurements, because of their integral nature, are not a particularly sensitive tool for investigating such questions as

the disappearance of the discrete, fundamental mode decay, and particularly the behavior of the flux spectrum where no fundamental mode exists. The reason for this is that the behavior of the integrated flux may be only weakly influenced by the changes in the neutron energy spectrum (eigenfunction) which take place in the region of low energy Bragg scattering peaks in very small or poisoned crystalline systems. Thus, it is apparent that an integral parameter, like the decay eigenvalue, may tend to obscure some important effects, especially in the buckling or poisoning region around the limit $(B^*)^2$ or Σ_a^*. In support of this contention, one needs only point out that the decay constant measurements have, in general, been unable to detect any significant deviation from a purely single-valued exponential decay until well into the continuum region, whereas the continuum energy spectra should be constantly changing functions of time or space due to the imbalance between leakage or absorption induced distortions and the weakly coupled energy exchange processes taking place within the moderator. Therefore, a better experimental tool for probing the question of the existence of a discrete, fundamental mode decay, and the behavior of that decay within the continuum region, is obviously measurement of the neutron energy spectrum itself. The price one pays for this increased sensitivity is an increasingly complicated experimental situation.

Some time dependent energy spectrum measurements in a small polycrystalline beryllium assembly, reported by Gaerttner et al.,[43] are shown in Figure 3. Their results indicate that the theoretical predictions about the disappearance of the discrete fundamental mode decay in the

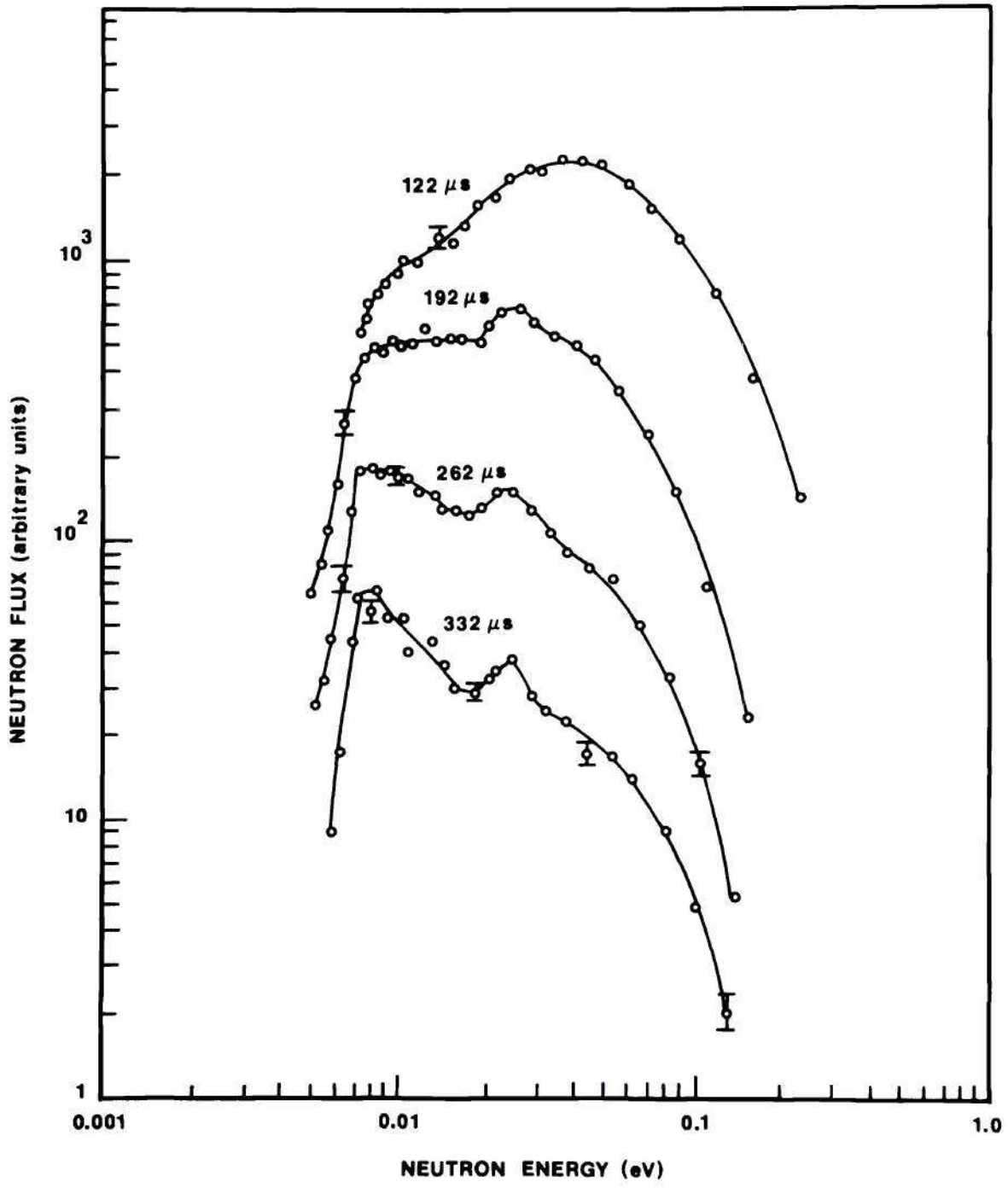

Figure 3. Time Dependence of the Measured Neutron Energy Spectrum in the Center of a Pulsed Beryllium Assembly with Buckling, $B^2 = 0.12\ cm^{-2}$. (Normalization is arbitrary. Error bars are statistical only. Solid lines are an eye guide and relate to no theory. Data from Gaerttner et al.[43])

pulsed source case are at least qualitatively correct. They find that, at a large enough buckling, roughly corresponding to that predicted by some of the simplified theoretical models, an asymptotic spectrum is not established for times up to six mean-decay-times after the source pulse. That is, the spectrum is a constantly changing function of time, governed by a progressive buildup of "trapped" neutrons just above the Bragg cut-off energy without showing any tendency to approach an equilibrium or asymptotic state. These spectra are widely used as bench-mark test cases for comparison with various theoretical treatments of neutron scattering in crystalline moderators.[44,45]

At the present time there exist no published stationary source, diffusion-length-type energy spectrum measurements in crystalline systems comparable to the available pulsed source spectrum data. In particular, the group at Georgia Tech is the only one to have undertaken to verify directly the more restrictive limit in equation 22 on the discrete fundamental mode proposed by Williams[21] for the diffusion length problem in finite moderating systems where leakage as well as absorption effects are important. DeJuren and Swanson[38] have observed that the transverse buckling term, necessary to fit their diffusion length measurements in "small" graphite assemblies to a discrete space decay constant, contained an extrapolated endpoint which was an increasing function of distance from the source plane. This proves, at least by implication, that, in sufficiently small steady-state systems there is a progressive buildup of neutrons with long-mean-free-paths in the spectrum. Thus, even at large distances from the source in small steady-state crystalline systems, the decay may not be describable by a discrete fundamental mode eigenvalue.

One possible reason for the shortage of comprehensive, steady-state experimental data is the relative scarcity of usable, high intensity, steady-state (so-called stationary) neutron sources compared to the propensity of the pulsed sources. Specifically, the two laboratories most prolific in spectrum measurements in the past, Rensselaer Polytechnic Institute and Gulf General Atomic, both have high intensity LINAC pulsed source systems in operation, but neither has ready access to a large research reactor or similar stationary system. If a stationary source is available, the measurement of steady-state, space dependent spectra offers some very distinct advantages over their pulsed source, time dependent counterparts. Most important among these advantages is that, at certain angles, the stationary spectrum exhibits a relative maximum intensity in the energy region below the Bragg cut-off in crystalline systems, whereas the pulsed source spectrum exhibits just the opposite tendency, that is, a relative depression in this same energy region.[10,18,46] Therefore, all other things being equal, the steady-state spectrum permits greatly improved experimental (statistical) accuracy in this energy region. For purposes of studying the existence of a discrete, fundamental mode decay in crystalline moderators the behavior of the spectrum just above and below the Bragg cut-off is of particular importance. As one passes into the region where the decay is governed by the continuum of eigenvalues, the spectrum is no longer in equilibrium, and it in fact changes most drastically in this energy region around the Bragg cut-off. Whereas both the steady-state and pulsed source spectra can have good intensity in the thermal energy region, only the steady-state spectrum has the additional

advantage of intensity and associated experimental accuracy in the energy region of most interest below the Bragg cut-off.

Purpose and Objectives of This Research

It is the intent of this thesis to present the results of a series of comprehensive measurements of space dependent, angular neutron energy spectra from various parallelepiped configurations of polycrystalline beryllium using the thermal column of the Georgia Tech Research Reactor as the steady-state neutron source. This is the (diffusion length) problem with transverse leakage proposed by Williams,[21,22] for which the limit in equation 22 applies. The nature of these measurements is intended to be relevant to the validity of this more restrictive limit on the existence of a discrete fundamental mode decay in small crystalline systems.

Williams[21] has dealt explicitly with the behavior of the angular flux spectrum in the stationary source diffusion length problem in small crystalline systems, extracting a closed form, analytic solution from the integral transport equation for the case of the simple separable kernel. Although he does not claim quantitative agreement for this particular analysis, due to the restrictions on the simple separable scattering kernel, the results do show that, as far as the spectrum is concerned, the most dramatic effects near the limit, $(B^*)^2$, and in the continuum, are to be found in the angular flux distribution. For assemblies with dimensions approaching the limit in equation 22, he finds that the asymptotic angular distribution is highly peaked in the forward, positive "Z", direction for neutrons below the Bragg cut-off energy. As one moves away from the forward direction, this peak rapidly diminishes in intensity, eventually

disappearing altogether and becoming a distinct depression in the reverse direction. These results are summarized in the theoretical (asymptotic) spectra pictured in Figure 4.

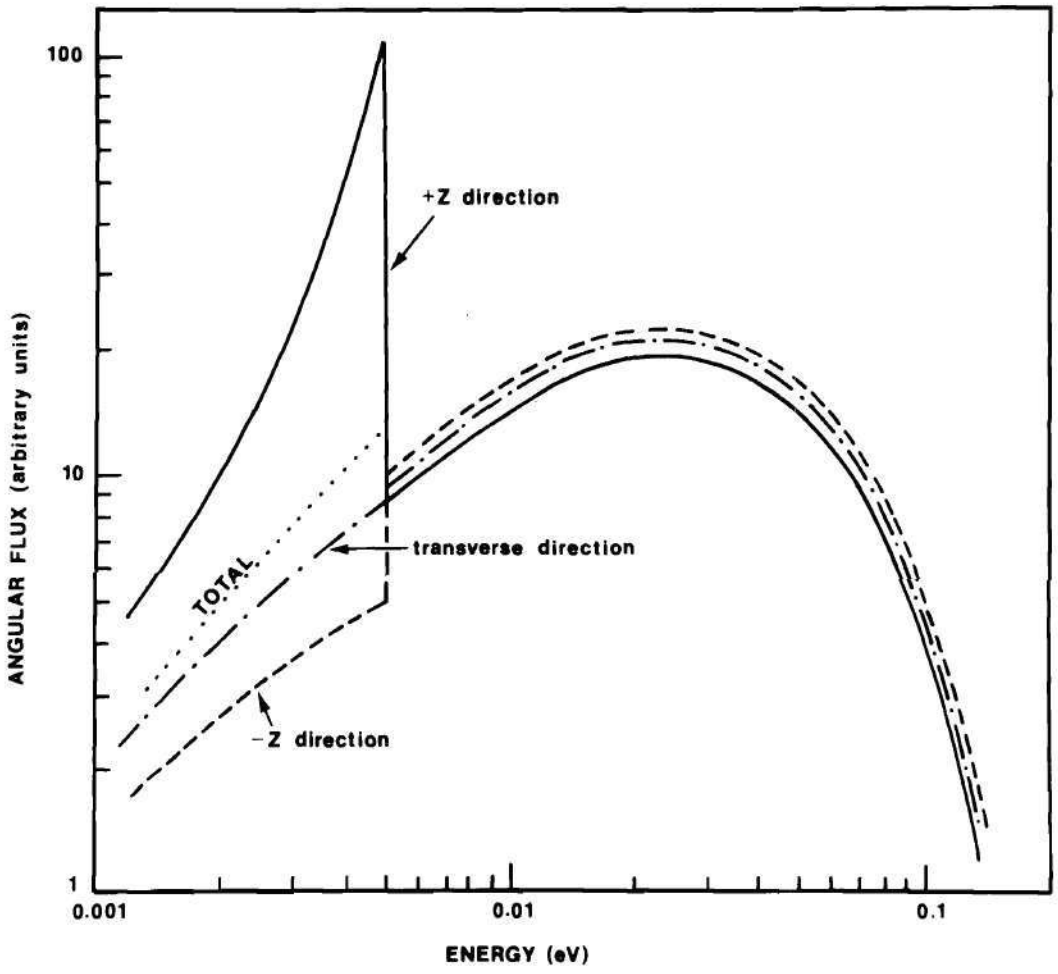

Figure 4. Theoretical, Steady-State, Asymptotic, Angular Neutron Energy Spectra in Beryllium in the (Forward) Positive "Z", Transverse, and (Reverse) Negative "Z" Directions with $B^2 = 0.00035$ cm^{-2}. (Calculations by Williams[21])

When the assembly dimensions are small enough such that the limit in equation 22 is exceeded, there is no equilibrium asymptotic spectrum (and

hence no discrete spatial decay) and the angular flux distribution is governed by the combination of source and continuum "transients." The transient angular distribution is similar in form to the asymptotic except that the relative flux peaking (depression) in the forward (reverse) direction for sub-Bragg neutrons is now a progressively increasing function of distance from the source plane; the rate of change increasing with decreasing system dimensions. As one moves further into the continuum, the forward spectrum, far from the source, approaches a singular beam of neutrons with energies below the Bragg cut-off, this being the familiar crystalline filtering effect.

According to the Williams theory,[21,22] the spectrum measurements reported herein in beryllium assemblies with transverse dimensions of 35.6 x 35.6 and 25.4 x 25.4 cm, respectively, should be well into the region governed by the continuum of eigenvalues, and thus the spectra should be strongly space dependent. However, the aforementioned Kothari[24] diffusion theory analysis puts the limit point for the transition from a discrete asymptotic mode to a continuum decay at 30 x 30 cm, such that the dimensions of the assemblies used in these studies exactly straddle their predicted limit. It is anticipated, then, that these experimental results will have some conclusive bearing on the applicability of the two different theoretical approaches to this problem, as well as verifying directly the disappearance of the discrete fundamental mode decay and the existence of the continuum eigenfunction for the diffusion length problem in small crystalline systems. In addition, sound experimental data on the behavior of the angular neutron energy spectrum in small beryllium assemblies with

strong transverse leakage should further provide a very sensitive and demanding test situation for scattering kernels[34,47,48] and approximate methods of solution of the transport equation.[10,45]

CHAPTER II

INSTRUMENTATION AND EQUIPMENT

Thermal neutron energy spectra in small beryllium assemblies have been measured by the slow chopper, time-of-flight technique using the Georgia Tech Research Reactor (GTRR) thermal column as a steady-state neutron source. The basis for the time-of-flight method is the production of short time duration, polyenergetic neutron bursts by the spinning shutter of a Fermi-type chopper. The neutrons contained in each burst spread out in time according to their velocities while flying along a fixed flight path to a detector where they are recorded in a multi-channel analyzer according to their arrival times. The data in each channel then represents the number of neutrons within a certain time or velocity interval. By suitable techniques, to be described later, one unfolds the measured time distribution of neutrons to produce an energy spectrum.

The equipment and instrumentation necessary to carry out such spectrum measurements can conveniently be divided into the following five major categories:

1. the neutron source,
2. the beryllium assembly,
3. the neutron chopper,
4. neutron detection, and
5. data processing and recording,

each of which will be discussed in turn in the paragraphs that follow.

The Neutron Source

Georgia Tech Research Reactor

The GTRR is a CP5-type heavy water moderated and cooled reactor which is fueled with plates of aluminum-uranium alloy containing approximately 2.25 kilograms of highly enriched U^{235}. The core itself is roughly cylindrical, two feet in diameter by two feet high with provisions for up to 19 fuel element assemblies arranged in a triangular array. The core is surrounded radially by a two foot thick D_2O moderator, a two foot thick graphite reflector, and roughly four feet of high density concrete and lead forming the biological shielding. At present the reactor operates at a maximum power level of 1000 kilowatts and is designed[49] to produce a peak thermal neutron flux in excess of 10^{13} $n/cm^2/sec$.

Thermal Column

The thermal column, located on one face of the reactor, is provided as a branch of the graphite reflector and extends from the reactor D_2O tank face five feet out into the biological shielding. The column is square, five feet on a side, with the central 16 x 16 inch portion consisting of 4 x 4 inch by five foot long removable stringers for the installation of experiments. Access is provided by heavy lead shutters and removable shielding plugs at the outer face. The pneumatically operated shutter doors open, exposing either a 16 x 16 inch access port or a centered 4 x 4 inch beam extraction port.

Neutron intensity considerations suggested that, at a maximum reactor power level of 1000 kilowatts, the neutron flux intensity at the end of the thermal column might be too low, or at best marginal for a

clean experimental situation. It was deemed necessary, therefore, to operate from within the column itself and consequently the last two feet of the five foot long graphite stringers were cut off and removed leaving a 16 X 16 inch by two foot deep cavity at the end of the thermal column into which the beryllium assembly could be placed. The dimensions of the cavity were determined by the maximum transverse dimensions of the fully open thermal column shutter doors, through which the beryllium assembly had to be inserted and removed, and a depth which permitted installation of a relatively long beryllium block for longitudinal space dependent measurements. Sufficient graphite was retained in the thermal column to ensure a highly thermalized neutron source distribution from the reactor core.

The distribution of source neutrons at the base plane of the thermal column cavity was more nearly isotropic and relatively flatter spatially than were the more beam-like characteristics at the normal end of the thermal column and, in addition, calculations indicated a flux intensity increase of roughly a factor of eight at this point. Locating the entire beryllium assembly inside the thermal column and subsequently extracting only a small beam out through the biological shielding for spectrum measurements, rather than endeavoring to effectively shield a much larger source beam, greatly reduced the radiological health hazard from streaming gamma rays. However, the necessity to place the beryllium assembly inside the thermal column cavity prohibited the installation of assemblies wider than the full-open width of the shutter doors, about 14.5 inches (37 cm). This, then, was in effect a physical constraint on

the class of spectrum measurements which could be carried out with this arrangement as will become apparent later.

Beryllium Assembly

A typical assembly used in the spectrum measurements consisted of a 35.6 X 35.6 X 50.8 cm pile of tightly packed 5 X 5 X 10 cm beryllium blocks contained in an open-ended BORAL box. Figures 5 and 6 illustrate the beryllium arrangement in a representative pair of assemblies. The BORAL served both as a structural and as a neutron shielding material to precisely define the physical and neutronic dimensions of the assembly. BORAL is a dispersion of 50 percent, by weight, boron carbide (B_4C) grit and aluminum powders sandwiched between aluminum cladding sheets to form a 1/4 inch thick plate with good structural and physical integrity. Details of the BORAL sandwich construction can be seen in Figures 5 and 6 around the edges of the beryllium assemblies. The exposed edges of the BORAL plates were painted with an epoxy resin to preclude the possibility of boron carbide grit getting out of the sandwich into either the beryllium assembly or into the thermal column graphite where the boron would behave as a neutron absorbing poison. BORAL was chosen as the neutron shielding material, over the seemingly more obvious choice of sheet cadmium, because of its structural strength and because of its ability to absorb neutrons without the production of high energy gamma rays. Hard gamma rays were particularly avoided due to the possibility of the photoneutrons resulting from the (γ, n) interaction of these rays in beryllium (with a 1.67 MeV threshold) contaminating the measurements with a ubiquitous fast neutron background. The open end of the BORAL box served as the source window

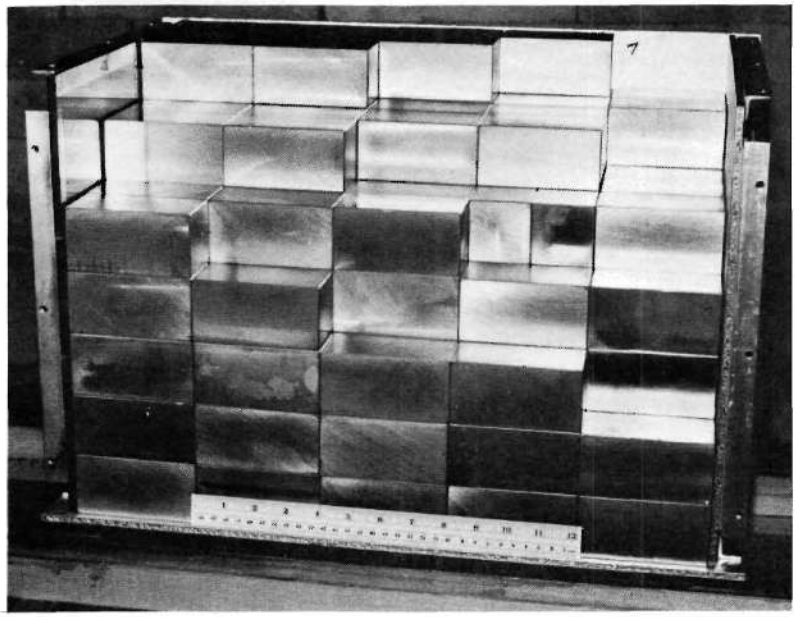

Figure 5. The 35.6 x 35.6 x 50.8 cm Beryllium Assembly. (The top and one side have been removed to reveal the stacking arrangement. The sandwich-like structure of the BORAL plates can be seen along the lower edge and at the extreme right of the assembly.)

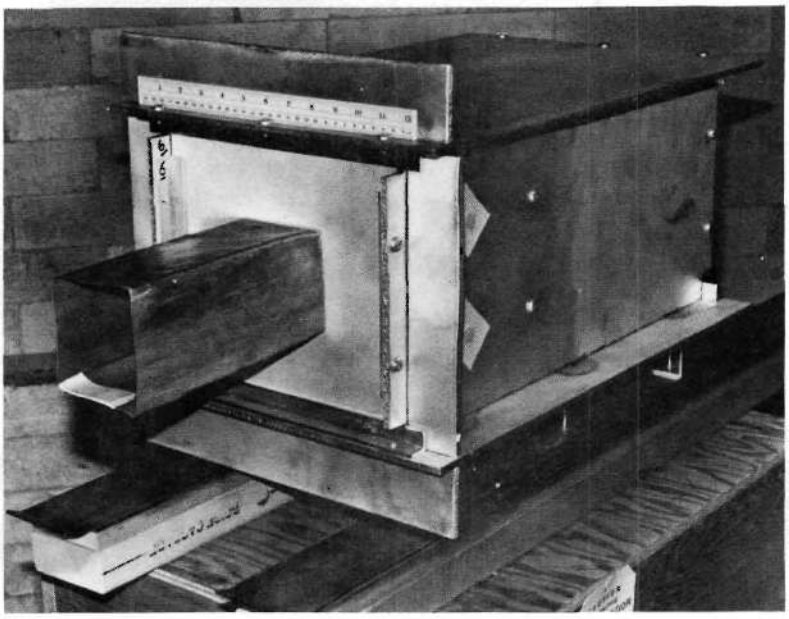

Figure 6. The 25.4 x 25.4 x 50.8 cm Beryllium Assembly. (The location of the BORAL skirts and cadmium beam shielding collar, employed for background neutron suppression, are shown.)

and was covered with a 1/4 inch thick plexiglass plate. The purpose of the plexiglass, other than to add strength to the end of the assembly, was to help wash out the small Bragg peaks in the low energy tail of the graphite leakage spectrum by multiple scattering these neutrons in the hydrogenous plastic material. The resulting energy spectrum, which served as the planar neutron source to one end of the beryllium assembly, is illustrated in Figure 7. The distribution is very nearly Maxwellian in nature with an average (effective) temperature of 334 $^{\circ}$K. The slight heating effect can be attributed to the longitudinal spatial flux decay gradient within the plexiglass source plate.

Reactor-grade beryllium shapes are manufactured by hot pressed, powder fabrication techniques, wherein a fine mesh beryllium powder is pressure compacted at elevated temperatures under vacuum conditions.[50] The fabricated material is generally rather impure, containing[51,52] a maximum 0.2 percent metallic impurities, primarily iron, and, more important, as much as 0.9 percent beryllium oxide (BeO) tied up primarily on the block surfaces. The vacuum hot-pressed shapes have a desirable fine-grained structure which is randomly oriented to give a more or less isotropic polycrystalline material.[53] The density of typical samples of the blocks used in these measurements has been determined to be 1.85 g/cm^3, indicating that they are practically free of porosity. The surfaces of the hot pressed blocks have been machined to tolerances, and within a few hours the as-machined surfaces oxidized to form a tough, nonporous BeO film. When the oxide layer reached a depth of the order of 100 Angstroms,[53] further oxidation was halted by the non permeability of the film itself,

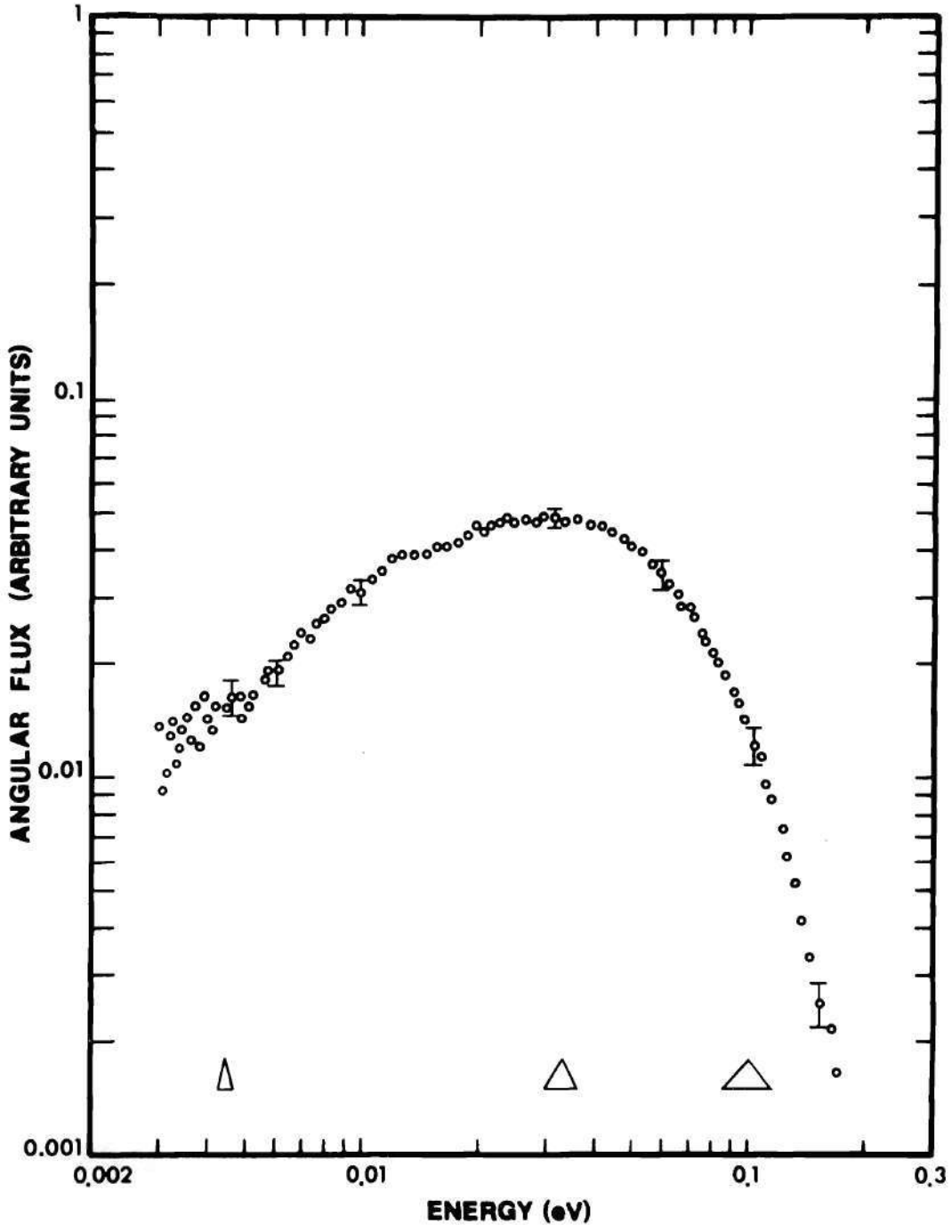

Figure 7. Measured Energy Distribution of Source Neutrons in the Positive "Z" Direction from the Thermal Column. (The spectrum is characteristic of a slightly heated Maxwellian. The origin of the error bars and energy resolution triangles is discussed in Chapter VI. Normalization is arbitrary.)

and the blocks were ready for use. Each of the blocks used in the spectrum measurements was cleaned thoroughly with isopropyl alcohol several times during the course of the experiments, and subsequently handled only with plastic gloves to minimize difficulties with surface contaminants.

The quantity of beryllium on hand at Georgia Tech for these measurements represented a $100,000 inventory loan from the Argonne National Laboratory where the blocks were previously used as part of a mock-up beryllium reflector for the now defunct Argonne Advanced Research Reactor (A^2R^2). A large number of regular parallelepiped shapes were obtained to allow for a certain amount of flexibility in putting together various assembly configurations. As a rule, the 5 × 5 × 10 cm pieces have been used in the spectrum measurements.

Neutron Chopper

The function of a neutron chopper is to modulate a continuous beam of polyenergetic neutrons into short bursts from which a time-of-flight analysis can be performed. The action of the rotor is that of a spinning neutron shutter that alternately transmits and blocks off the beam.

Neutron choppers can be grossly classified into at least two groups, fast and slow choppers, according to the neutron energy range in which they are designed to work. The slow, or thermal neutron chopper is a relatively straightforward mechanical device originally designed and operated by Fermi et al.[54,55] at Argonne National Laboratory to measure energy dependent thermal neutron cross sections. The early Fermi-type choppers consisted of a multi-layered sandwich of cadmium and aluminum

sheets contained in a hollow steel cylinder. The aluminum sheets, due to their low neutron cross section, acted as the "slits" allowing neutrons to pass through only when they were aligned parallel to the beam. The rotor was belt driven by a small electric motor, producing two neutron bursts of a few degrees duration per revolution. The early slow choppers proved to be extremely versatile devices and many of the original thermal neutron cross sections were measured in chopper-based, time-of-flight experiments.[14]

Rotor Construction

The Georgia Tech Neutron Chopper, pictured in Figures 8 and 9, was modeled after the Brookhaven slow chopper[56,57] with some changes and improvements to tailor the device to the specific needs of our measurements and to reflect advances in the current technology, especially in the area of electronic timing. The rotor consists of 33, 3-1/2 × 4-3/4 × 0.015 inch thick, stainless steel blades, electroplated with 0.002 inches of cadmium on each side. The 0.069 inch slit spacing between the blades is accomplished by five rows of narrow aluminum strips running parallel to the incident neutron beam direction (perpendicular to the rotor spin axis). The blade stack is held flat by upper and lower steel shaper plates, and the entire sandwich structure is held together by 15 cadmium plated steel bolts running through the spacers. The assembly is enclosed in a 1/16 inch thick aluminum cylinder which serves to reduce wind friction and as a safety feature to restrain fragments should breakage occur at high rotation speeds. After final assembly, the rotor was carefully dynamically balanced to preclude the possibility of extreme vibration-

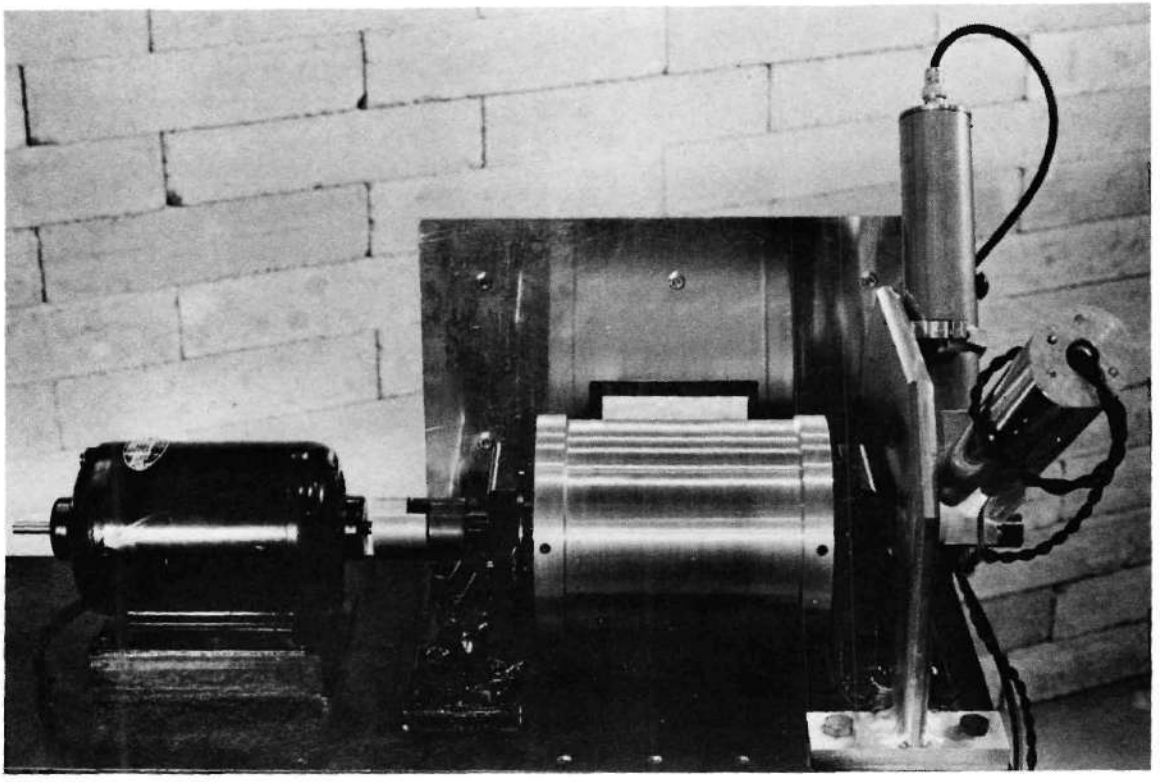

Figure 8. The Neutron Chopper. (The front cadmium collimator has been removed to reveal the drive motor, rotor assembly, and zero timing unit.)

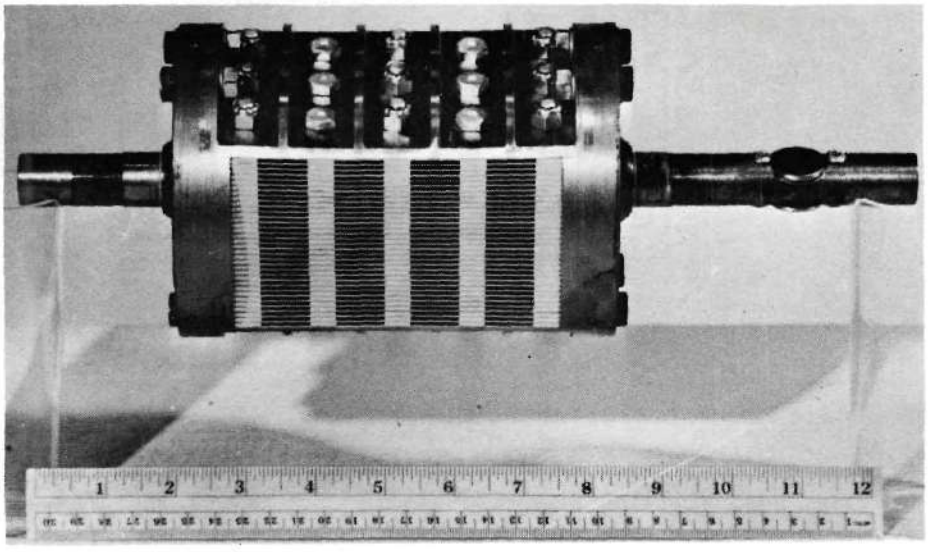

Figure 9. Details of the Chopper Rotor Assembly. (The aluminum housing has been removed to reveal the slit structure.)

induced bearing wear and the danger of high speed rotor disintegration.

In this particular rotor, the slits are filled primarily with air spaces rather than aluminum. Of the total area of the "open" chopper slits exposed to the incident neutron beam, 57 percent is air space, and, of the remaining 43 percent, 26 percent is blocked off by the cadmium plating on the through bolts inside the spacers, leaving only roughly 17 percent of the open area for neutron streaming filled by aluminum. Even though the aluminum cross section is quite low (of the order of 1.5 barns at 2200 m/sec), replacing most of the aluminum slit area with air space is believed to be significant since it reduced the necessary energy dependent corrections which must be applied to the transmitted beam for scattering and absorption losses, and it increased the overall transmission of the rotor slightly. One is especially concerned with the energy dependence of the rotor transmission, and removal of this much aluminum significantly reduced the effect of Bragg discontinuities in the aluminum cross section on the low energy portion of the beam spectrum.

It has been possible to replace the solid aluminum slit spacers in the original rotor design, which were necessary to support the soft cadmium blades under the forces of high rotation speeds, by the use of cadmium plated stainless steel blades which are much stronger and less subject to plastic deformation than the conventional solid cadmium blades.

The rotor was constructed such that the blade configuration could be changed from the present flat-plate Fermi design to one with a slight curvature, as was the case with the Brookhaven design, by replacing the upper and lower flat steel shaper plates with appropriately curved ones.

The advantage to slightly curved blades is that, since the slit profile conforms more closely to the slightly parabolic neutron path through the rotor, the low energy transmission can be improved. Furthermore, the resulting duty cycle can be reduced from two to one burst per revolution which can be advantageous in alleviating problems with burst overlap encountered with long flight paths. However, all the spectrum measurements reported herein were carried out with the flat-plate chopper configuration.

Chopper Drive Motor and Speed Control

The rotor was driven by a General Electric 1/3 horsepower, series-wound ac motor rated at 10,000 RPM at 117 vac. Intermediate rotation speeds were obtained by changing the ac rms voltage with a standard 0-140 volt Variac. The unit has been operated repeatedly in the range 2000-13,000 RPM without difficulty.

Constant rotation speed is an important factor in the neutron timing scheme. Long term speed stability was accomplished by simply allowing the unit to run and warm up over a one to two hour period, from which time the system operated completely open-ended, that is, without any sort of speed control feedback. The Variac was, however, powered from an ac regulated voltage source to eliminate speed changes as a result of line voltage fluctuations. Experience has shown that, operated in this open-ended mode, the motor speed stayed well within ±1 percent over long periods of time, of the order of hours. Short term speed fluctuations were damped out by the inertia of the 25 pound rotor, a fact which was verified by observation of the nominal rotor speed oscillation with a strobe light. This mode of operation is a significant simplification over the usual SCR,

current-load feedback controls, or the exotic and expensive digital or variable frequency, synchronous speed control systems. In the early speed control test program it was concluded that the smooth sinusoidal power fluctuations produced by the Variac were superior to the chopped waveform from a current-load SCR speed control since the sharp voltage changes from the SCR, at switching, tended to power pulse the motor at random points in its rotation period, and one could not guarantee that the angular rotation velocity was constant over a single revolution, even though it might have appeared stable on the average. In addition, it is doubtful whether this type of current-load feedback system could have been successful at stabilizing the rotor speed much better than the ±1 percent obtained with the open loop Variac system without considerable additional electronics design effort.

Zero Timing Unit

For purposes of accurate neutron timing a reference or "zero time" point is required to indicate the time when the neutron burst left the chopper. This zero time was obtained by detecting a reflected light beam from one of two small mirrors attached to the spinning rotor shaft. The light beam from an 18 watt light bulb passed along one arm of the zero timing unit, pictured in Figure 10, through a circular iris aperture and was focused on the chopper rotor shaft. At some point in its period of rotation, one of the mirrors attached to the rotor reflected the beam back up the second arm of the timing unit where it illuminated a small phototransistor. This phototransistor sent out an electrical signal which was proportional to the incident light intensity. The peak in the phototransistor electrical pulse then corresponded precisely to some particular

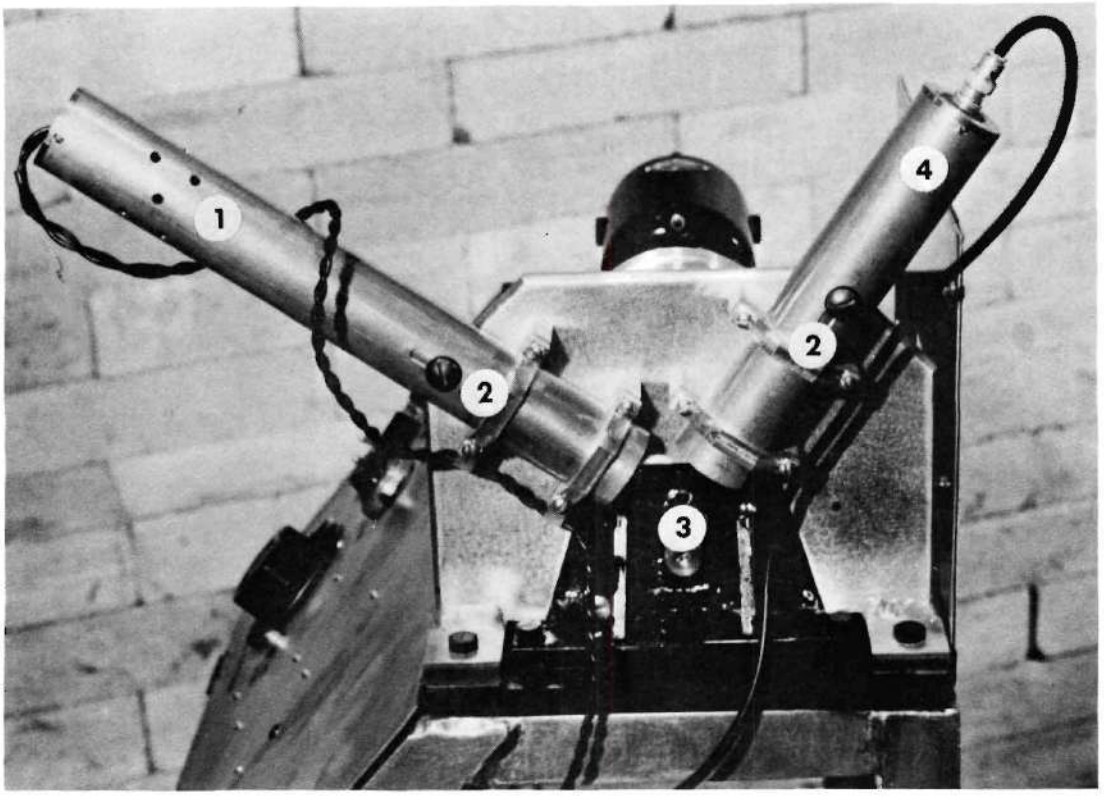

Figure 10. Details of the Zero Timing Unit. (1. light source and iris aperture, 2. focusing lenses, 3. chopper rotor shaft and attached mirrors, and 4. photodetector.)

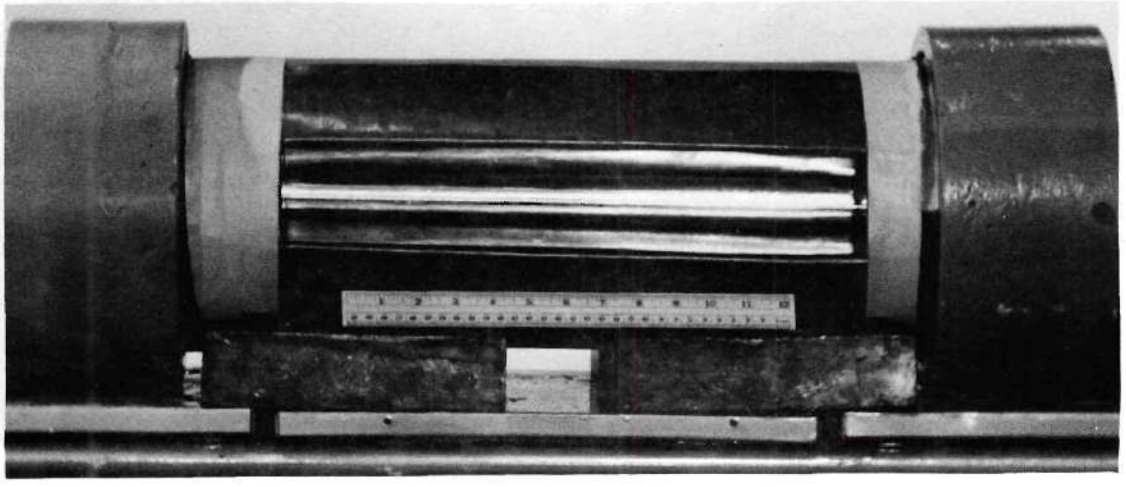

Figure 11. The BF_3 Neutron Detector Embedded in the Boric Acid Background Shield

rotor orientation with respect to the center of the neutron burst that occurred when the rotor slits were exactly parallel to the neutron beam.

To provide flexibility in gating the time-of-flight analyzer on such that it was ready to record the arrival times of the fastest neutrons, the zero timing unit was mechanically preset to deliver the timing pulse approximately 10 degrees of rotation before the chopper rotor actually emitted the neutron burst. This mechanical preset allowed the analyzer to record a few channels of background before the fastest neutrons from the burst began arriving at the detector. The timing pulse was then electronically delayed and shaped before it was sent on to the analyzer. This electronic delay was variable such that, for any given rotation speed, it could be adjusted to provide as many channels of background as deemed necessary. In general, 20-40 background channels were sufficient.

The circuit diagram and a detailed explanation of the operation of the zero timing unit electronics may be found in Appendix A.

Neutron Detection

BF_3 Detectors

Some important requirements for suitable neutron detectors in time-of-flight work are that the detectors must have reasonably high efficiency over the energy range of interest and that the behavior of this efficiency with energy must be well known. In addition, the detectors must be short in the direction of neutron flight to minimize uncertainties in the length of the flight path, and they must have a fairly short characteristic response time to minimize timing errors. The detector of choice, that best fulfills the above requirements in the thermal energy

range, has been the BF_3 proportional counter filled to high gas pressure for improved efficiency.

One of the detectors used in the beryllium spectrum measurements is pictured in Figure 11. It is a two inch diameter, aluminum cathode, BF_3-filled proportional counter, model RSN-44A, with an active length of 16 inches. The fill gas pressure has been increased to a practical maximum of 900 Torr of 96 percent enriched BF_3 to meet the requirement of high efficiency.

In order to reduce stray background counts from sources other than neutrons in the flight path, the entire detector was enclosed in a cadmium covered cylindrical shield made up of a homogeneous mixture of boric acid (B_2O_3) and Epoxy resin binder. The minimum shield thickness was three inches on each side of the detector except for a narrow open window facing down the flight path toward the chopper. The shield provided excellent thermal as well as epithermal neutron attenuation with an estimated one millimeter thermal neutron mean-free-path in the boric acid medium.

In situations where the beam intensity was such as to make the analyzer dead time correction greater than about 10 percent with the high efficiency detector, a smaller, one inch diameter, 400 Torr fill pressure, 12 inch long BF_3 detector (RSN-7A) was substituted. Due to the increased signal counting rate in this situation, only a simple cadmium-wrap background shield was necessary with this detector.

Detector Signal Pulse Processing Electronics

The low level signal pulses from the detector were processed and

separated from the dc high voltage bias in a nearby solid state preamplifier before they were sent down a long coaxial cable to the electronics rack located outside the flight path cave. Here the detector pulses were amplified and the leading and trailing edges sharpened in a double-delay-line linear amplifier. Electronic and low voltage gamma ray noise pulses were blocked-out in an integral discriminator prior to feeding the detector signal pulses into the time-of-flight analysis unit.

Beam Catcher

The unused portion of the neutron beam which streamed around the detector, as well as the associated gamma ray beam from the reactor core was stopped in a specially constructed three foot high by four foot wide by two foot thick mobile beam catcher located at the end of the three meter flight path cave. The 2400 pound bulk shielding beam catcher contains an eight inch thick layer of boric acid/paraffin mixture for thermal and fast neutron attenuation and capture, and a 12 inch thick layer of high density concrete for gamma ray attenuation.

Data Processing and Recording

Operation of the Time-of-Flight Analyzer

The function of the time-of-flight analyzer is to measure and record the arrival time of neutrons at the detector with respect to the chopper zero timing reference pulse.

The analyzer, operating in the multi-scaler mode, was started by the trigger pulse from the zero timing unit. After a short, 15 μsec, delay while the analyzer logic was set, the sequencing action began by gating open the first channel for a preselected period of time known as

the "analysis channel length," 17 μsec in this case. At the end of this period of time, that channel was closed and the next consecutively higher channel was gated open. The sequence continued until the detector recorded the arrival of a neutron, at which time the process was stopped for roughly 17 μsec, known as the "dead time," while the event was recorded in the memory of whatever channel happened to be gated open at the time. The analyzer then performed an automatic time-base correction to put the sequence back in the proper time relationship to the trigger pulse, before continuing. The sequence of successive channel stepping and recording counts in the "open" channels continued until the analyzer reached the end of the last channel. There, the system was reset and waited for the next trigger pulse from the zero timing unit before restarting the sequence. This whole process was repeated from one hundred thousand to two million times until adequate statistics (20 thousand counts in the peak channel as a rule of thumb) were accumulated. At the end of the sequence, the counts in the analyzer memory represented an inverse velocity distribution with the fastest neutrons appearing in the first few channels.

Data Collection System Electronics

Figure 12 is a block diagram of the data collection system showing the trigger and detector signal pulse processing sequences. Figure 13 is a photograph of the electronics rack containing most of the equipment in that same data collection system.

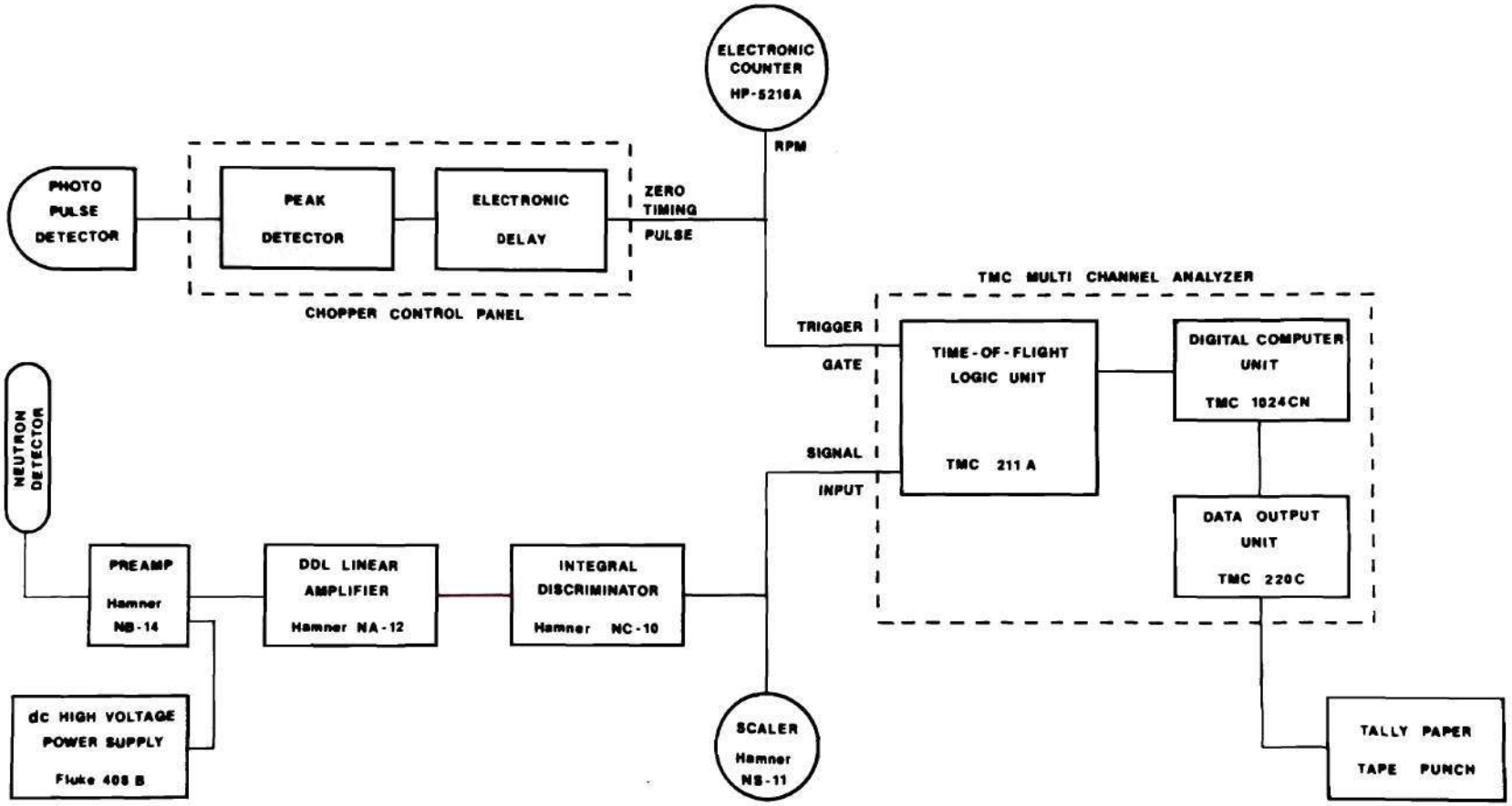

Figure 12. Block Diagram of the Time-of-Flight Data Acquisition System

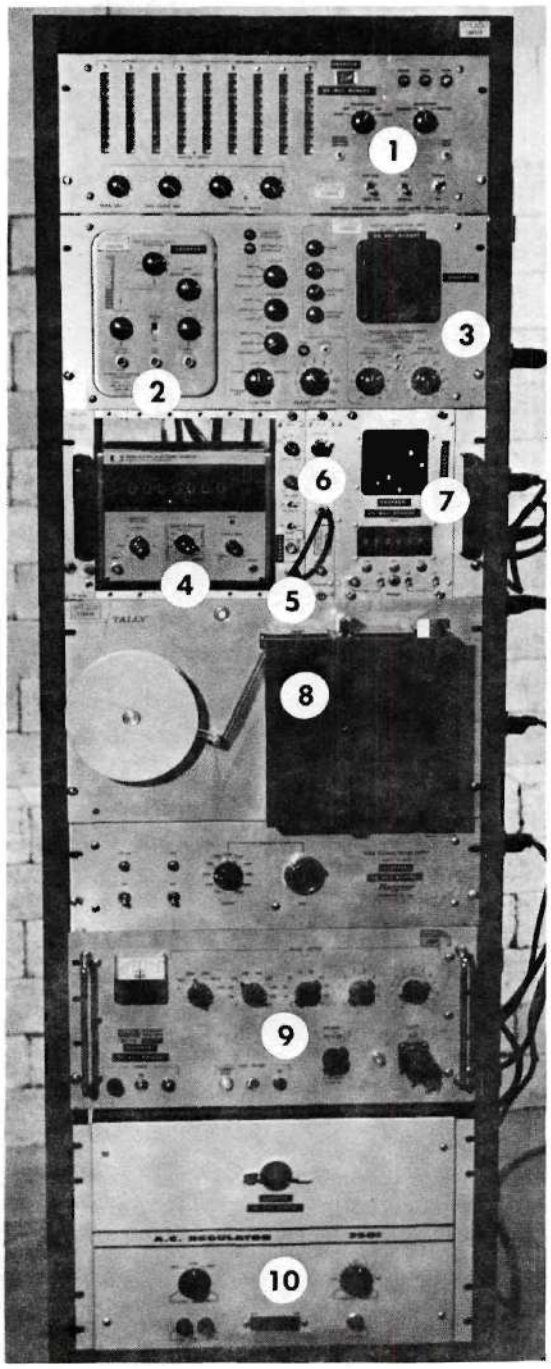

Figure 13. Experiment Control and Data Collection Electronics. (1. TMC data output unit, 2. TMC time-of-flight logic unit, 3. TMC multi channel analyzer digital computer unit, 4. RPM meter, 5. double-delay-line linear amplifier, 6. integral discriminator, 7. scaler, 8. tally paper tape punch, 9. dc high voltage power supply, and 10. ac line voltage regulator.)

CHAPTER III

BERYLLIUM SAFETY AND HANDLING

Beryllium and its compounds are known to be highly toxic. The symptoms of exposure to beryllium or its compounds, and the manifestations thereof, are discussed in some detail in Appendix B entitled Beryllium Toxicology wherein it is shown that inhalation of beryllium or beryllium oxide dust is clinically much more harmful than either prolonged skin contact or ingestion. As a result, the guidelines for industrial hygiene dealing with beryllium compounds are built around permissible airborne dust concentrations. The standards, recommended by the American Industrial Hygiene Association, and required of all facilities dealing with the Atomic Energy Commission, are as follows[58,59]:

A) A recommended maximum atmospheric concentration in an occupational environment of two $\mu g\ Be/m^3$ air. This is a time-weighted average concentration for an eight hour work day.

B) A short exposure tolerance, of 30 minutes or less duration, of 25 $\mu g\ Be/m^3$ air.

C) A maximum monthly average concentration of 0.01 $\mu g\ Be/m^3$ air in non-occupational or "community air" areas with no stated stipulation as to peak concentration limits.

To demonstrate the fact that these are very restrictive limits one need only note that the standards[60] analogous to A) above for mercury and lead, which are generally considered industrial "poisons," are 100 μg

Hg/m^3 air and 200 μg Pb/m^3 air.

The nuclear-grade beryllium used in the spectrum measurements consisted of a large number of rectangular parallelepiped shapes, mostly 5 × 5 × 10 cm blocks. Reactor grade beryllium contains a maximum oxide impurity concentration (as BeO) in the neighborhood of 0.9 weight percent,[52] including the tightly bound BeO surface film. Our block surfaces were all silvery-white metallic in appearance with no visible signs of loose beryllium dust, or white powdery beryllium oxide. Physical and surface integrity appeared to be very good.

The possibility of facing an acute exposure to a high concentration of beryllium, or beryllium oxide dust from these blocks therefore seemed remote, except in the event one of the brittle blocks were dropped and shattered. Rather, the concern in the day to day use of the material was restricted to 1) the chronic respiratory effects from inhalation of small quantities of the dust, especially in confined storage places, and 2) the skin irritant effects as a result of frequent handling of the blocks during stacking and unstacking of various sized assemblies.

In the early planning stages of the beryllium program Mr. Newell Bolton of the Industrial Hygiene Division at Oak Ridge National Laboratory was employed as a consultant to examine the condition of the beryllium, and, in light of his experiences, to make recommendations about setting up and operating an air monitoring program. After reviewing our safety procedures and discussing our proposed use of the beryllium for neutron spectrum measurements, it was his opinion that use of the beryllium would not result in exposure of any of our personnel to a hazardous concentration

of airborne dust.[61] Mr. Bolton also concurred that the skin contact hazard could be alleviated by the use of disposable plastic gloves in all instances where the beryllium blocks were to be handled.

Visual inspection of the blocks indicated that they should be cleaned, perhaps routinely, with a cloth dampened with isopropyl alcohol to remove any dirt, grease, or surface dust. Air samples were run with high volume (18-40 ft^3/min) air samplers during all cleaning operations since this was expected to generate more dust than the usual handling and stacking procedures. The cleaning cloths were discarded periodically in sealed plastic bags to preclude creation of a localized concentration of dust when the cloths dried. Until the exact quantity of dust being generated in the cleaning operation could be ascertained, a filter-type respirator was worn as an added safety precaution. Mr. Bolton was kind enough to volunteer his services to chemically analyze some of the early air filter samples at Oak Ridge so that the effectiveness of our safety precautions could be judged and adjustments made where necessary. The results were that, even at the table level close to where the blocks were being cleaned, the airborne beryllium dust concentration was at all times less than 0.8 μg Be/m^3 air, a factor of 30 lower than the maximum permissible 30 minute exposure concentration. The concentration at breathing level was another factor of two lower than that due to the action of the table-top air sampler which served to draw in and trap a substantial fraction of the dust on the filter paper directly from the cleaning area. Therefore, the breathing level concentration of beryllium dust, even during vigorous cleaning operations, was roughly a factor of five lower than the eight-hour-average limit, and cleaning operations never lasted longer

than two hours. These results have subsequently been independently confirmed by a quantitative spectrographic analysis performed by the National Spectrographic Laboratories, Inc. in Cleveland, Ohio.

It was concluded that the low concentration of dust generated even in the vigorous cleaning operations eliminated the need for constant air monitoring and certainly negated the necessity for the respirator. However, it was considered prudent to continue the use of plastic gloves and to continue running spot-check air samples at times when the beryllium was being handled. In addition, the two high volume air samplers were operated whenever cleaning and/or rough handling of the blocks was involved. One sampler was located on the cleaning table itself where it served as a "vacuum" to draw air and airborne dust away from personnel in the area and to trap the dust on the Whatman-41 filter paper. The other sampler was located at breathing level to measure the actual beryllium dust concentration likely to be inhaled. Subsequent analysis of a number of the air sample filters by the National Spectrographic Laboratories revealed that the airborne beryllium dust concentration during vigorous cleaning operations averaged approximately 0.6 μg Be/m^3 air at the table level, and 0.3 μg Be/m^3 air at the breathing level. During normal handling and stacking of the beryllium blocks the dust concentration averaged in the neighborhood of 0.03 to 0.2 μg Be/m^3 air. All these values are well below the recommended average safety limit of two μg Be/m^3 air.

When the beryllium was not in use it was kept sealed and locked in one of two shipping crates or in a storage cabinet on the reactor floor. Each storage location was clearly marked with a warning about the potential dust hazard.

CHAPTER IV

EXPERIMENTAL PROCEDURES

The following description serves to illustrate the procedures in a more or less typical experimental data run.

Stacking or rearrangement of the beryllium assembly configuration was nearly always performed on the afternoon just prior to the experimental run. This allowed sufficient time after any previous neutron exposure for the short lived radioactivity from the beryllium impurities and from the BORAL box support structure to decay away to acceptable working levels. Typical dose rate levels at this time around the assembly (15-20 hours after the assembly had been removed from the neutron flux) were of the order of 40-100 millirems per hour to the hands at the hotter source end of the assembly primarily from activation in the steel bolts and screws holding the system together. The average body dose one to two feet from the assembly was in the neighborhood of 10 millirems per hour. As long as the box was wiped down occasionally to keep it reasonably free of dust, dirt, and grime (especially sodium-laden perspiration from handling the assembly), the smearable radioactivity was minimal and presented no particular contamination hazard.

The equipment for the day's experiment was set-up in the early morning before reactor start-up. At this time the radiation level in the flight path cave with the biological shielding removed was generally acceptably low. A small Towmotor fork lift was used to remove the thermal

column shielding. The beryllium assembly was placed on the loading platform in front of the thermal column. The loading platform, a portion of which can be seen in Figures 5 and 6, is a specially constructed wooden table equipped with a set of dry graphite lubricated, cold-rolled steel slides which match up with a similar set of slides attached to the bottom of the BORAL box. These slides extended out on a tongue-like protrusion over the steps in the biological shielding and in toward the thermal column. When the large thermal column shutter doors were opened, allowing direct access to the 16 x 16 x 24 inch deep reentrant cavity in the graphite, health physics personnel surveyed the area and set the working dose rates. These rates generally ranged in the neighborhood of 50 to 200 millirems per hour to the body, depending on the day of the week and the previous operating history of the reactor, and upwards of 600 millirems per hour to the hands up inside the thermal column cavity. This dose rate was not considered excessive due to the small amount of time required to slide the beryllium assembly out over the loading platform tongue and into the thermal column cavity. A wedge-shaped tool was forced back and forth along the side of the box, squaring the assembly inside the thermal column and aligning it with the cavity walls. The shutter doors were closed and the shielding plug was replaced in the reactor face with the fork lift. An Epoxy collimator, containing a homogeneous mixture of roughly 50 percent by weight boron carbide grit, was placed in the 4 x 4 inch beam extraction hole in the center of the shielding plug to restrict the size of the neutron beam to roughly 2-1/4 x 3-1/2 inches (5.7 x 8.9 cm).

The chopper was then positioned squarely in front of the face of

the thermal column, aligned with the center of the beam collimator, and leveled. The detector was set up and centered horizontally across the end of the flight path and the flight path was measured from the center of the chopper rotor to the detector center axis.

If the experiment was designed to measure a leakage spectrum, the existing BORAL collimation on the beryllium assembly face and the cadmium collimators at the front and rear of the chopper were sufficient to define the 2-1/4 X 3-1/2 inch (5.7 X 8.9 cm) wide neutron beam. In this case, the full 16 inch horizontal active length of the detector was left exposed to the beam to improve counting statistics. However, for interior spectra, measured with a 5 X 5 cm reentrant channel in the front face of the beryllium block, it was necessary to restrict the size of the neutron beam with a series of 3.8 X 3.8 cm cadmium blade-type collimators attached to the front of the beryllium assembly and to the front of the chopper. A tightly collimated beam was necessary to insure that the experiment was "seeing" only neutrons from the base of the reentrant channel and not those from other nearby sources such as the channel sides. For interior spectrum measurements, two cadmium covered, boric acid/paraffin blocks were placed in front of the exposed extremities of the detector, tightening the beam collimation to eight inches at the end of the flight path and shielding out background neutrons from the active extremities of the detector which were not exposed directly to the tightly collimated neutron beam itself. The open end of the shielded flight path cave was blocked-off with the large mobile concrete beam catcher.

Figure 14 is a schematic of the arrangement of equipment for a

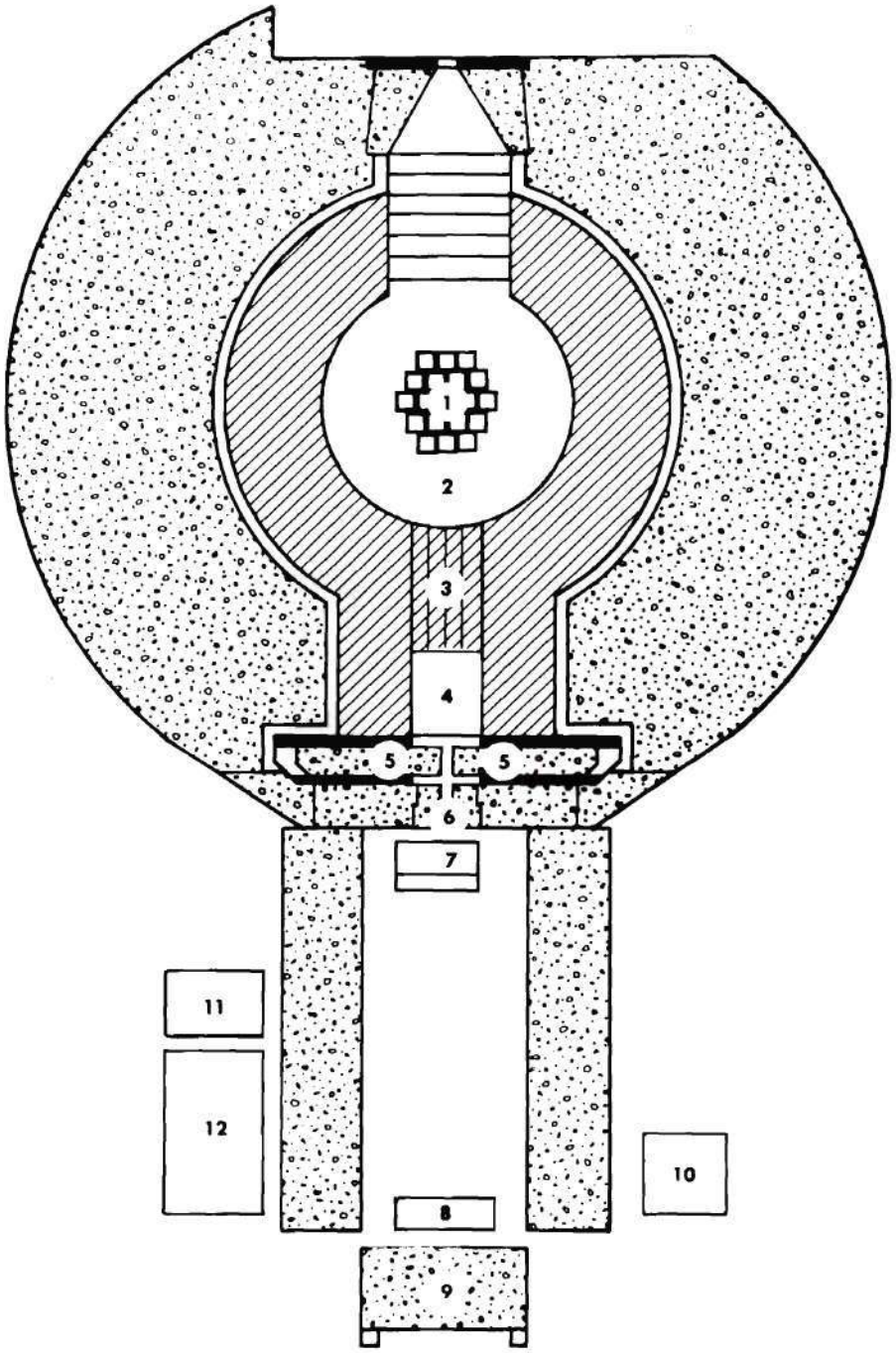

Figure 14. Horizontal Section Through the GTRR Showing the Placement of the Time-of-Flight Equipment at the Thermal Column. (1. reactor core, 2. D_2O, 3. graphite thermal column, 4. beryllium assembly, 5. thermal column shutter doors, 6. B_4C collimator, 7. chopper, 8. detector, 9. beam catcher, 10. data collection and storage electronics, 11. beryllium storage cabinet, and 12. beryllium cleaning and work area.)

typical experiment. Figure 15 is a photograph of this same arrangement showing the location of the experiment on the reactor floor.

The chopper rotor speed was variable from 2000 to nearly 13,000 RPM. An intermediate speed in the neighborhood of 3900 RPM was selected for the measurements which provided a reasonable compromise between narrow energy resolution (which improves with increasing rotor speed) in the high energy range and acceptable neutron transmission (which increases with decreasing rotor speed) in the low energy end of the spectrum. At this speed, the neutron burst width was narrow enough to result in fair energy resolution (nine percent full width at half maximum) at 0.1 eV, and yet the relative neutron transmission through the rotor was as high as 50 percent in the important low energy range around the beryllium Bragg peak at 0.005 eV and it never fell below 30 percent at the extreme low energy tail of the spectrum.

The chopper was brought up to speed and allowed to warm up over a period of from three to five hours before the measurements commenced. This was determined to be sufficient time for the bearings, electric motor windings, etc. to reach an equilibrium temperature. Once this equilibrium was attained the rotor speed would level out and remain steady over long periods of time of the order of hours. Running with power from the line voltage regulator, the only speed variations detected after the warm up period were long term statistical oscillations contained well within a one percent statistical envelope and a very slight tendency for the speed to continue drifting upwards which was of no consequence in data runs lasting less than a few hours.

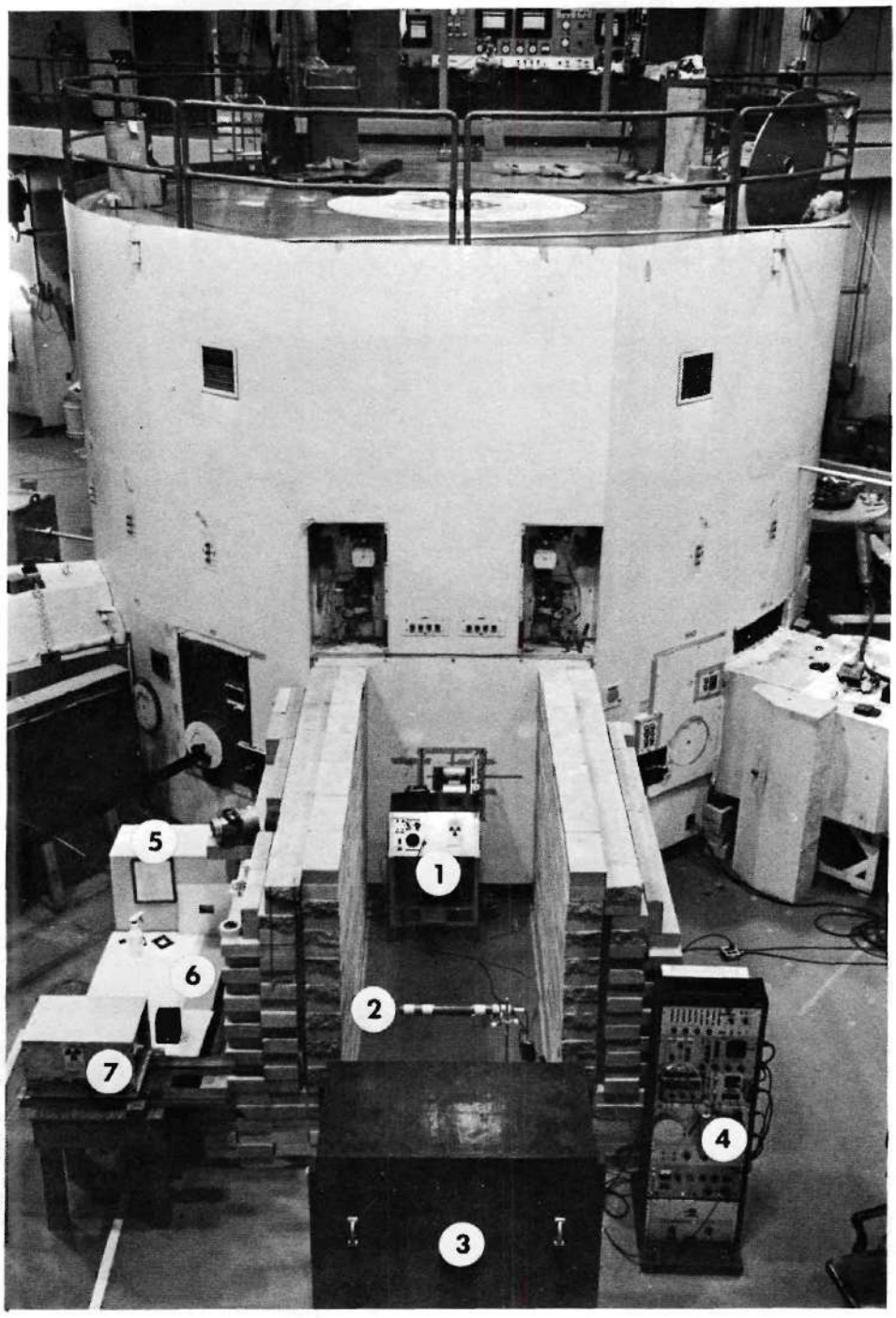

Figure 15. Location of the Time-of-Flight Experiments at the GTRR Thermal Column. (1. chopper, 2. cadmium-wrapped detector, 3. beam catcher, 4. data collection and storage electronics rack, 5. beryllium storage cabinet, 6. beryllium cleaning and work area, and 7. beryllium assembly situated on the loading platform.)

After the chopper warm up period, and with the reactor operating at full power (1000 kilowatts), the small 4 X 4 inch thermal column shutter doors were opened allowing a neutron beam from the beryllium assembly to pass out through the biological shielding. Health physics personnel surveyed the area to ascertain that the radiation level was within predicted limits and to set the dose rates in the working area. This dose rate was generally constant in the neighborhood of 170 millirems per hour at the end of the flight path cave in front of the beam catcher, and was comprised mostly of gamma rays from the reactor core, the neutron beam itself being fairly tightly confined to the detector area. The heavy concrete beam catcher was effective in stopping most of the stray gamma ray beam except for that small portion streaming around the edges and especially over the top of the shielding. In light of this streaming radiation hazard, the immediate area behind the beam catcher and around the end of the flight path was roped off and posted as a "High Radiation Area" during the course of the experiments. The dose rate to the side of the shielded cave in the actual working area around the data collection and control electronics was only of the order of three to five millirems per hour, which presented no particular hazard.

Just prior to the start of the data run the time integrated counting rate was measured on a scaler in order that some feel for the relative neutron intensity in the beam might be obtained. The time-of-flight analyzer memory was then zeroed, and the system started. Once under way, the analyzer collected data with repetitive neutron bursts triggered by the zero time pulse. The chopper speed (RPM) was measured by repeatedly counting the number of zero timing pulses in a fixed 10 second interval

with a digital frequency meter. The speed was monitored and recorded throughout the run in 15 minute intervals every 30 minutes to assure that the chopper speed variations were remaining within limits.

The repetitive data collection sequence was allowed to continue until there were at least 20,000 counts stored in the peak channel in the analyzer memory. This arbitrary stopping criterion guaranteed that there would be at least reasonable counting statistics throughout the spectrum. However, in situations where the beam intensity was high, substantially larger numbers of counts could be collected in the same period of time. The total time required for the data collection sequences ranged from one to six hours, depending on the beam intensity.

The data stored in the analyzer memory represented the differential neutron intensity at the end of the flight path as a function of time after the zero timing trigger pulse. This time "spectrum" was punched out on binary-coded paper tape for future analysis. Also recorded were the number of sweep cycles the analyzer had gone through, the average chopper speed, and the elapsed time after reactor start up, for purposes of calculating the beryllium temperature during the run.

At the completion of the experiment, the thermal column shutter doors were closed, the dose rate in the area was checked, and the roped-off area behind the beam catcher was reopened.

On alternate days, between experimental runs, the morning set-up procedure was reversed to remove the beryllium assembly from the thermal column for restacking. On rare occasions where modifications to the assembly were minor, the restacking was done on the loading platform in front of the thermal column and the assembly was replaced in the thermal column cavity on the same morning, eliminating the need for a full "out" day.

CHAPTER V

ANALYTICAL PROCEDURES

The information one seeks is the neutron spectrum at various locations within a beryllium assembly and what has been measured is the differential time distribution of neutrons in a pulsed beam extracted in some manner from the assembly. The measured time spectrum has been distorted by the actions of the experiment itself and thus there were a number of corrections which had to be applied to the data before the true form of the neutron energy spectrum could be deduced. The task was simplified somewhat by the fact that one is interested only in the energy dependent shape of the spectrum, and how this shape changes as a function of certain distorting factors, rather than in the magnitude of the flux itself. It is this fact which allowed us to ignore a number of touchy experimental and correctional problems such as the absolute source intensity, the beam size and quantitative effects of collimation, and the absolute neutron transmission probability through the chopper rotor. The concern in the following pages then will be exclusively with those energy dependent factors which distorted the shape, but not the overall magnitude, of the measured spectrum.

Figure 16 is a plot of a typical measured time spectrum and the associated (normalized) background spectrum. The first 40 channels of the time spectrum contain only background information since the zero timing pulse has triggered the analyzer sequence before the neutron burst

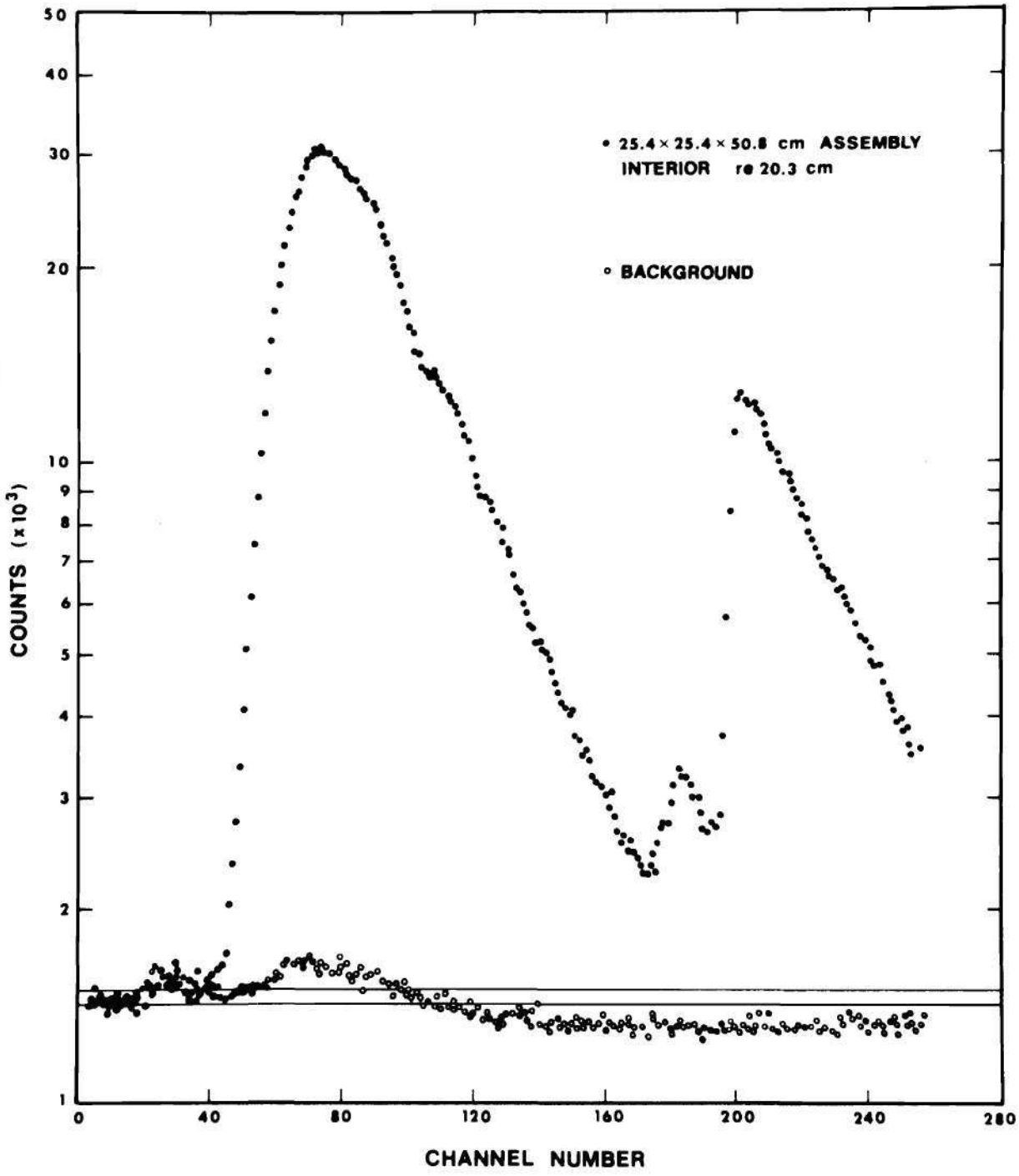

Figure 16. Typical Measured Neutron Time Distribution and the Associated Background Spectrum. (The upper and lower solid lines represent constant background estimates calculated from the number of counts in the first 40 and 20 channels of the spectrum, respectively.)

emerged from the chopper rotor. The time spectrum represents the distribution of neutron arrival times at the detector, with respect to some arbitrary zero time pulse. As such, it is an inverse velocity spectrum, the fastest neutrons appearing in the earliest channels. The large peak between channels 50 and 160 contains what shall be referred to as the "thermal" spectrum of neutrons, those lying roughly in the energy range between 0.1 and 0.007 eV. The smaller peak, above channel 200, contains the sub-Bragg or "cold" beryllium neutrons below 0.005 eV.

Detector-Analyzer Live Time

The sequence in which the time distribution data was collected was one in which an analyzer gate sequentially swept across a field of memory channels at a constant rate until a detector signal pulse appeared, indicating that a neutron had arrived at the detector. The analyzer then stopped for a period of time to process and store the "count" in whatever memory channel was gated open at the time. The time required for the processing operation has been determined, by a dual pulsing technique, to be of the order of 17 μsec, about one channel length. Subsequently, the time base was advanced one channel, to account for the pause, and the sweep sequence resumed. During the period of time when the analyzer was stopped and involved in processing the pulse, the system was effectively dead; that is to say, if another detector signal pulse were to have appeared during the 17 μsec processing period, it would have, of necessity, been ignored. The number of counts which missed being recorded in a particular channel in the differential time spectrum, due to this system dead time, depends on the probability that two or more random detector

signal pulses would have appeared at the analyzer input within the dead time interval. This probability, in turn, depends on the count rate in the channel, and on the fixed length of the pulse processing time during which the input was dead. The higher the count rate in a channel, the higher the probability that more than one detector signal pulse would have appeared at the analyzer input within the dead time interval, and thus the larger the fraction of counts that missed being recorded in that channel.

To a somewhat lesser extent, the detector itself was also dead for a short time after each pulse was formed due to the finite amount of time necessary to sweep the ions formed by a neutron interaction out of the chamber volume under the influence of the applied electric field. If another neutron were to have interacted in the chamber while significant ionization from the previous interaction was still present, the resulting electrical pulse might not have been "clean" enough to be sensed as a distinct and separate signal. The dead time interval for a gas filled proportional counter is, however, only of the order of a few μsec,[62] which is a small fraction of the total detector-analyzer system dead time. At any rate, the analyzer dead time, being larger than the detector dead time, masked the effect of the detector dead time interval.

One was confronted in this situation with a system dead time which varied as a function of count rate from channel to channel. The net effect of this dead time loss was to depress the peaks, or areas of higher count rate, over other regions in the measured time spectrum.

The following experiment was performed to determine the magnitude of the (detector plus analyzer) system dead time losses as a function of measured count rate, and to aid to the development of an empirical

correction factor to account for these losses. With the reactor shut down, the two inch diameter BF_3 detector was situated a short distance away from the open beam port in the thermal column (chopper not in place). The reactor was then brought up to critical and the power leveled out at one kilowatt. The detector count rate, number of counts per channel per analyzer sweep, was measured with the time-of-flight analyzer by repeatedly triggering the analyzer with an electronic pulser. The "time spectrum" in this case was of course a time independent straight line since the neutron beam was continuous rather than pulsed. When sufficient statistics were accumulated, the sequence was stopped and the reactor power level was raised by a factor of two, at which time the count rate determination was repeated. This process continued until the maximum reactor power level of 1000 kilowatts was reached.

Since the neutron flux incident on the detector was directly proportional to the reactor power level, one expected to observe a simple linear relationship between the measured count rate, recorded in the analyzer, and the reactor power level. Figure 17 is a plot of the count rate, expressed as the average number of counts recorded in the memory channels per 100 analyzer sweeps, versus reactor power level (incident flux). At lower count rates, the aforementioned linear relationship does in fact hold. As the incident flux was increased, however, the observed count rate dropped below the simple proportional behavior as a consequence of successively more counts being missed during the system dead time.

As an aside, it is informative to point up the following very graphic example of the effects of system dead time on the measured time spectrum. At the highest reactor power level, the count rate was so high

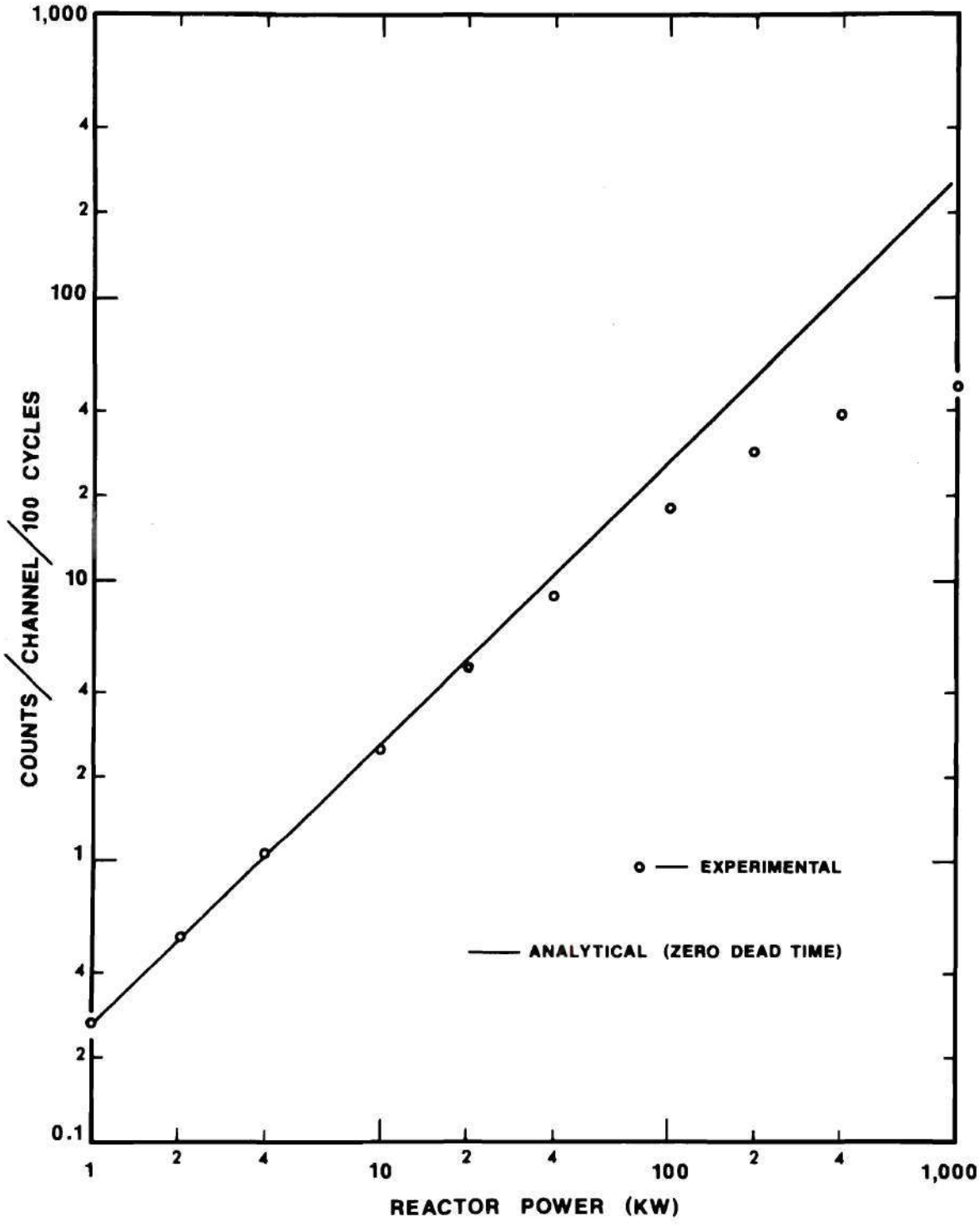

Figure 17. Neutron Count Rate as a Function of Reactor Power Level Demonstrating the Effect of System Dead Time

that the time spectrum appeared as a high and low envelope of points converging toward a single straight line near the end of the sweep. Figure 18 is a sketch of the analyzer scope display of the "time spectrum" from this continuous, high intensity neutron beam.

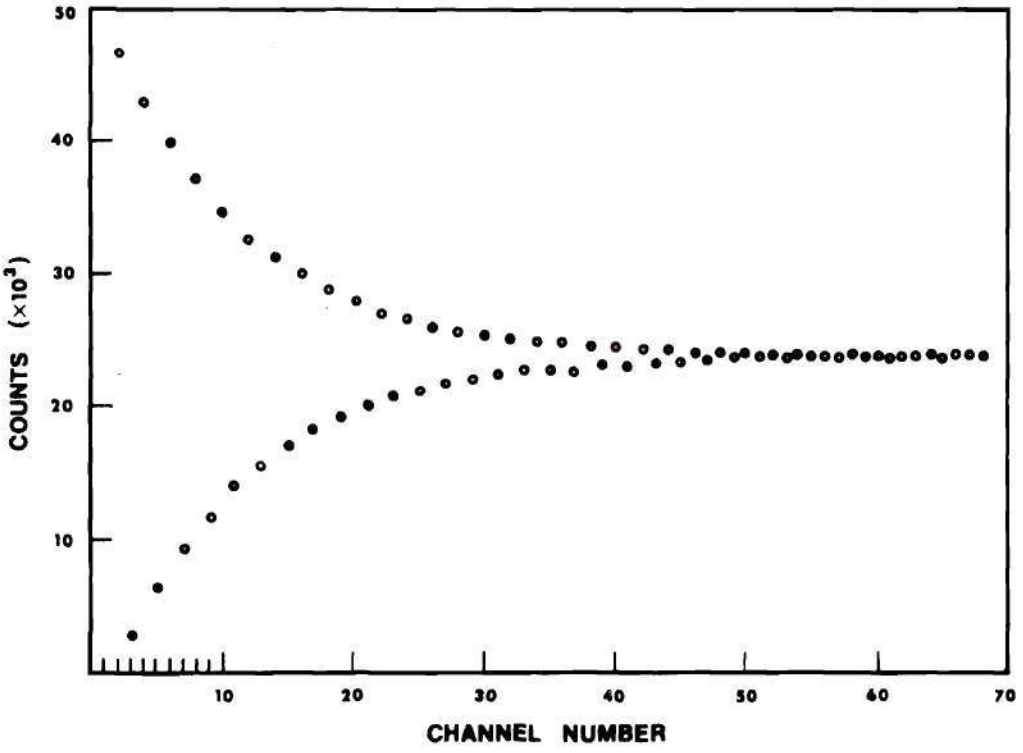

Figure 18. Measured Time "Spectrum" Envelope at a Very High Count Rate Illustrating an Extreme Limit of Analyzer Dead Time

The envelope of points was a result of the following unusual chain of events. As soon as the analyzer sweep sequence was triggered to start, there was nearly always a detector count at the signal input within the first "open" channel, due to the high count rate. Thus, there was nearly always a count stored in the first channel, and consequently the system was nearly always dead through the second channel while the analyzer was involved in processing the first count, resulting in the second channel

coming up nearly empty. Then, after the first channel count was stored, the time base corrected, and the system reenabled to accept the next count, there was nearly always a detector signal appearing in the next available "open" channel ready to be processed and stored. The sequence continued with alternate channels containing either a very high count rate or being shielded by the system dead time so that they contained very few counts. The envelope eventually converged to the usual straight line as the alternating pattern drifted out of synchronization in the later channels as a result of the statistical nature of the arrival time of counts in the "open" channels.

The ratio of the measured count rate at any particular power level to some arbitrary reference count rate at low power, where the dead time is assumed to be zero, is a direct measure of the system dead time at that power level. If the percent live time is defined as

$$\%\ \text{live time} \equiv 1 - [\%\ \text{dead time}] , \tag{24}$$

then one can write

$$\%\ \text{live time} = \frac{[\text{measured count rate at power X}]}{[\text{measured count rate at "zero" power}]} \cdot 100 , \tag{25}$$

where the normalized count rate is defined as the average number of counts per channel per analyzer sweep per kilowatt.

The percent system live time is plotted as a function of measured count rate in Figure 19. The points were fitted with a linear least squares technique[63] to an equation of the form

$$Y = MX + B \ , \tag{26}$$

where

Y is the % live time,

X is the measured count rate,

M is the slope,

and B is the intercept.

The results of the fit were that

$M = -1.665 \pm 0.031$ %/unit count rate,

and $B = 99.6 \pm 0.7$ % at zero count rate,

so that

$$\%\ \text{live time} = [(-1.665) \cdot \text{measured count rate}] + 99.6 \equiv \text{LIVETIM} \ . \tag{27}$$

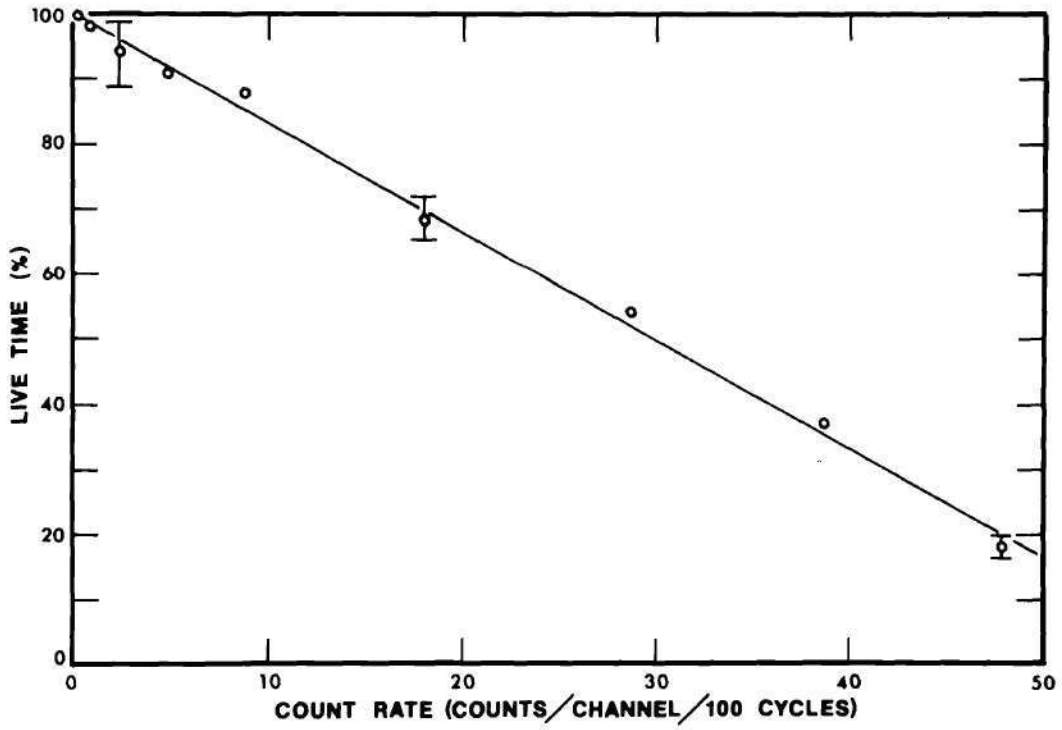

Figure 19. Linear Least Squares Fit to a Plot of the Percent System Live Time versus Measured Neutron Count Rate, from Which the Spectrum Dead Time Correction Factor is Calculated

The intercept in Figure 19 at 99.6 ± 0.7 is a good check on the least squares fit inasmuch as the physics of the situation demands that the zero count rate live time should have been 100 percent (i.e., zero dead time for zero count rate). To eliminate the effects of system dead time on the measured time spectrum, one calculated the percent system live time, LIVETIM, from the measured count rate in a channel and equation 27, and corrected the count rate according to

$$\text{actual count rate} = \frac{\text{measured count rate}}{\text{LIVETIM}} \tag{28}$$

at each point in the spectrum.

The beam intensities encountered in the beryllium spectrum measurements were typically such as to result in live times in the peak counting channels of the order of 90 to 100 percent, so that the correction factor never got much larger than about 10 percent. However, to test the accuracy of the live time correction, the very intense graphite source spectrum was measured with two different flight paths, and thus two very different measured peak counting rates, all other factors remaining the same. The resulting energy spectra, with peak-channel dead time corrections of 40 and 23 percent, respectively, at 0.033 eV, were divided, point by point, and the ratio plotted in Figure 20 as a function of energy. This technique of plotting the ratio of spectra was employed here and subsequently when one was not particularly interested in the details of the spectra themselves, but rather in the differences between the two. This ratio is sensitive to differences between the spectra of the order of a few percent, whereas the spectra themselves may have undergone shape

changes in excess of 100 percent over the energy range of interest. That there is no apparent systematic difference between the two spectral shapes, that is to say, the ratio of the two in Figure 20 hovers statistically around 1.0, leads one to conclude from this relatively severe test that there was no significant error in the live time correction.

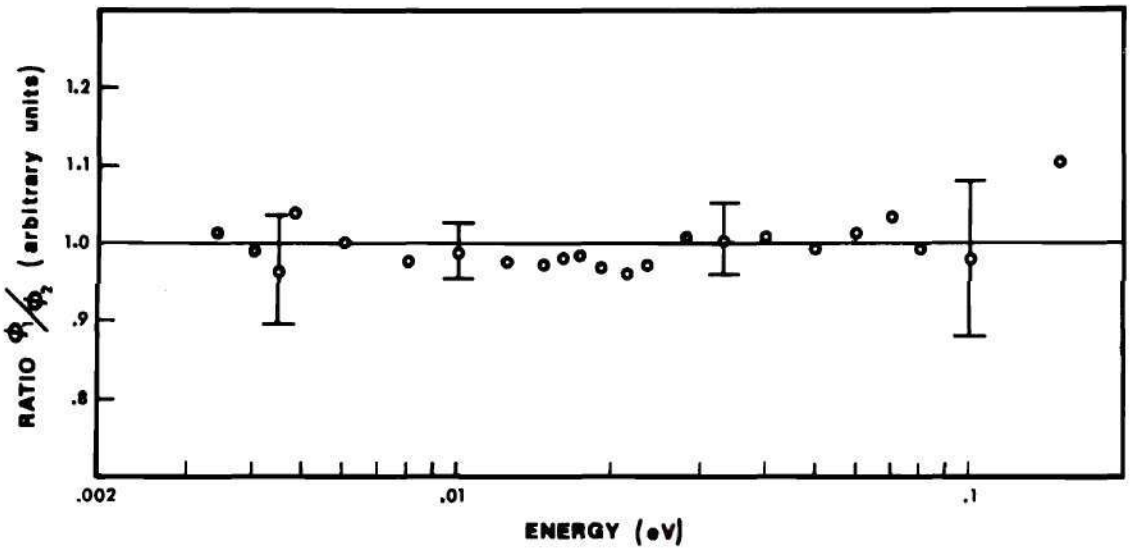

Figure 20. Ratio of Identical Measured Source Spectra with Relative Peak Dead Time Corrections of 40 and 23 Percent

Neutron Background

The neutron background was made up of a time dependent and a time independent part. Of these, the time independent part was of the least concern, so long as it was not a significant fraction of the total counts, since it could be subtracted as a constant from each channel of the measured time spectrum. The time independent background, by virtue of its continuous nature, arose from sources which were not pulsed by the chopper, like the scattered neutrons which came around, rather than through, the chopper, the epithermal and fast neutrons in the beam which were not pulsed

by the cadmium blades in the chopper rotor, and the ubiquitous neutron field which prevailed around the reactor from neutrons escaping through the biological shielding or from other beam ports open on the reactor floor, to mention only a few. A large portion of the time independent background, which was not directly in the flight path, was stopped by the thick boric acid/Epoxy detector shield.

The time dependent background, on the other hand, originated from sources which passed through the chopper rotor and were pulsed. The structure in the time dependent background can obscure details in the measured time spectrum. The time dependent background in the pulsed beam arose from sources like neutron scattering from the steel chopper support structure which periodically directed neutrons into the beam at certain rotor angles, epicadmium neutrons which were only slightly chopped by the stainless steel rotor blades, and neutrons from the intense thermal column source which streamed along the air gap outside the beryllium assembly and then scattered off the heavy lead shutter doors in such a manner as to be directed through the chopper and towards the detector. This door scattering effect was enhanced by the V-block shaped structure of the thermal column shutter doors above and below, and directly in front of, the point where the neutron beam was extracted from the beryllium assembly. Also included in the strict definition of "background" were neutrons which entered the beryllium assembly from points other than through the plexiglass source plate, such as by leaking through the BORAL surrounding the structure, fast neutrons which thermalized in the assembly, and photoneutrons produced by the interaction of hard gamma rays with the beryllium atoms and which eventually emerged in the beam. These background neutrons

could have had a very different angular spectrum than those which originated at the source plane. However, these sources of neutrons were all expected to be small. In particular, the transmission factor for an isotropic thermal spectrum of neutrons incident on a BORAL plate containing 50 percent B_4C has been calculated[64] to be of the order of 2.0×10^{-5}.

The background spectrum in Figure 16 was determined by repeating the time spectrum measurement for that particular beryllium assembly under identical experimental conditions except that the plexiglass source plate was replaced with a neutron absorbing BORAL one. It is felt that this measurement technique reasonably included all the sources of background neutrons discussed above. The background spectrum itself appears to be made up primarily of a time independent, flat distribution with a small amount of superimposed time dependent structure in the thermal energy range between 0.03 and 0.1 eV. There are also some smaller peaks in the very early channels, between 25 and 40, which may have been a result of the fact that the stainless steel core in the chopper rotor blades had a very slight tendency to pulse or scatter epicadmium and higher energy neutrons.

It was deemed unnecessary to measure the background distribution for each set of experimental conditions since the time dependent component especially was minimized by judicious shielding such that it had a negligible effect on most of the measured time spectra. In this light, it was convenient to estimate the entire background distribution for each experimental spectrum from the information contained in the first few channels before the neutron burst left the chopper. Averaging the total counts in channels 1-40, which included the epicadmium structure, and then assuming

constant background throughout the spectrum, yielded the upper solid line in Figure 16. The estimate was not too bad in the high-thermal energy range, but beyond channel 100 or so the actual measured background dropped significantly below the linear estimate. However, if the average was calculated only from the counts in the first 20 channels, which specifically excluded the small epicadmium peaks, one got the lower solid line in Figure 16 which appears to be a more evenly balanced estimate of the background over the entire range of channels. This estimate was better especially in the area around the small shoulder peak between channels 160 and 200 where the spectrum signal to background ratio was smallest, since a seemingly small error in the background estimate there could have resulted in a significant error in the net (that is, signal minus background) count rate and thus in the resulting shoulder peak height. The fact that the constant background estimate was not especially good in the thermal peak region was generally of little consequence in light of the relatively high spectrum peak counting rates. That is, whereas a few percent error in the estimated background in the area of the small shoulder peak might have been significant in some spectra, one could generally tolerate as much as a 10 percent error in the background around the larger thermal or Bragg peaks without adversely affecting the accuracy of the resultant spectra in these regions.

The constant background estimate, calculated from the average number of counts in the first 20 channels of a measured spectrum, appears to be a reasonable estimate of the background for most spectra. Confidence limits of from 5-10 percent in the high energy range, above 0.02 eV, and from 2-3 percent in the low energy range, below 0.02 eV, are included to

account for time dependent background structure.

The one notable case where the constant background estimate failed was in the 25.4 x 25.4 x 50.8 cm leakage spectrum measurement. This failure can be attributed to a combination of factors. With the narrow 25.4 x 25.4 cm assembly in the thermal column cavity, there was nearly a 10 cm air gap remaining on all sides of the assembly through which source neutrons were free to stream directly onto the lead thermal column shutter doors. The close proximity of the beryllium leakage surface to the shutter doors served to scatter relatively more than the usual number of these source-background neutrons out into the beam. Thus, the intensity of this time dependent thermal component of the background was increased greatly over that in previous (interior spectrum) measurements. The increased thermal neutron background was coupled with the fact that the measured leakage spectrum itself in this small assembly was strongly distorted and severely depleted of neutrons in the thermal energy range where most of the background structure was observed. The combination of these effects resulted in the background intensity completely swamping the structure in the beryllium spectrum by something like 5:1 in the thermal energy range.

The high background problem was alleviated by attaching a set of BORAL, neutron absorbing skirts around the periphery of the assembly near the front face. The purpose of the skirts was to reduce the intensity of source neutrons impinging on the thermal column shutter doors. Also, a cadmium collar-like contrivance was attached to the front face of the assembly, completely enclosing the beam extraction point, to absorb those remaining door scattered neutrons which were trying to enter the beam by scattering from the exposed beryllium or any of the nearby assembly

structural materials. Reference to Figure 6 shows the placement of the BORAL skirts and cadmium collar on the 25.4 x 25.4 cm assembly.

Figure 21 is a plot of the measured beryllium time spectrum in the 25.4 x 25.4 x 50.8 cm leakage assembly and the corresponding background distribution, both measured with the BORAL skirts and cadmium collar shielding in place. The background distribution was measured, as in previous cases, by replacing the plexiglass source plate with a neutron absorbing BORAL one, all other parameters being identical to the beryllium spectrum measurement. The addition of the shielding skirts and cadmium collar has reduced the background level to something less than 50 percent of the measured time spectrum intensity in the thermal energy range. This level, though greatly improved over that without the additional shielding, was still too high to justify using the constant background estimate. Therefore, for this one spectrum, the normalized background distribution was subtracted, point by point, from each channel of the beryllium spectrum.

As a precaution, the BORAL skirts and cadmium collar were used on all the spectrum measurements in the 25.4 x 25.4 cm assemblies to restrict the intensity of the door scattered source neutron background. That the additional shielding was successful in keeping the overall background structure within acceptable limits such that the constant background estimate was applicable in all cases except the 50.8 cm leakage spectrum, is illustrated by the fact that the "typical" background distribution in Figure 16 was measured in one such assembly. Check measurements in the 35.6 x 35.6 cm assembly revealed that this background source was considerably smaller in the larger assemblies, probably because of the reduc-

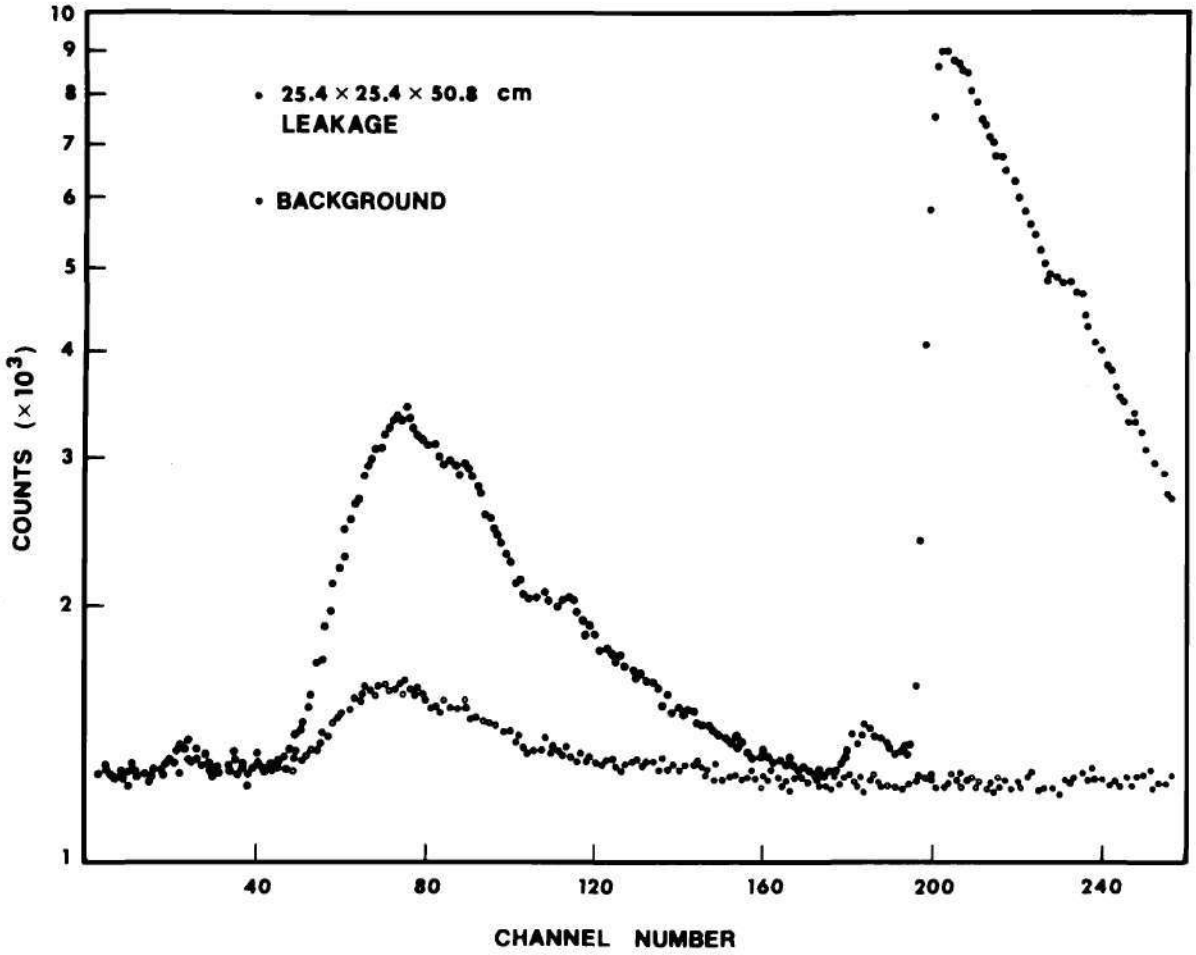

Figure 21. Measured Time Distribution and the Associated Measured Background Spectrum for Neutrons Leaking from the Center of the Front Face of the 25.4 x 25.4 x 50.8 cm Beryllium Assembly

tion in the door scattered intensity as a result of the smaller two cm air gap around the assembly. In addition, the beam extraction point at the center of the front face of the 35.6 x 35.6 cm assembly was further removed from this streaming source such that the door scattered neutrons had less of a chance of being scattered into the beam within a solid angle that would direct them toward the detector. Furthermore, the beryllium spectra in the 35.6 x 35.6 cm assemblies were characterized by a higher intensity in the thermal energy range than those in the 25.4 x 25.4 cm assemblies; thus the background distribution had a sufficiently smaller percentage effect on the structure of the spectra in the larger assemblies in this energy range such that no additional neutron shielding was deemed necessary.

Zero Time Calibration

The measured time spectrum, as it stood, was the time distribution of a burst of neutrons arriving at a detector with respect to some arbitrary reference time pulse. In order to calculate the actual neutron flight time, and subsequently the neutron velocity, one needed to know when the neutrons left the chopper, that is to say, one needed to know the "zero" time. This zero time was selected to coincide with the middle of the triangular chopper burst. The smear in the zero time caused by the finite width of the burst, among other things, was accounted for by a time resolution uncertainty to be discussed in Appendix E. The time difference between the middle of the chopper burst, the actual zero time, and the middle of the first analysis channel, the measured zero time, is called the flight time correction, FT. Application of the flight time

correction shifted the reference time base of the measured time spectrum allowing one to calculate the actual flight time for neutrons in any particular analyzer channel by simply multiplying the (channel number minus one) times the width of each channel (seconds).

The flight time correction is made up of:

1) The time difference between the middle of the chopper burst and the phototransistor pulse initiated by the reflected light beam from one of the mirrors attached to the rotor shaft, henceforth called the angular preset. This correction was negative since the light pulse appeared before the chopper neutron burst.

2) The electronic time delay between the peak in the phototransistor pulse and output zero timing pulse sent to the analyzer trigger gate.

3) The time delay after receipt of the trigger pulse before the time-of-flight sweep sequence was initiated by the analyzer.

4) The time from the initiation of the sweep to the middle of the first analysis channel.

In reverse order, the time to the middle of the first analysis channel was simply $\Delta/2$, where Δ is the analysis channel width of 16 μsec in this case.

The time-of-flight logic unit "fixed delay," which is the time after receipt of the timing trigger pulse before the analyzer sweep sequence can be set up and initiated, was determined experimentally using a dual pulsing technique. The first pulse was used to trigger the analyzer and the second pulse was successively applied to the analyzer signal input at increasing lag times after the trigger until the signal pulse

was just recorded in the first analysis channel. This smallest lag time, the analyzer "fixed delay," was found to be 15 μsec with 16 μsec channel widths.

The electronic time delay, between the peak in the phototransistor pulse and the output of the zero timing pulse, in the monostable multivibrator was determined by the variable RC decay constant settings on the chopper control panel, as described in Appendix A. A convenient combination which was stable, easily reproducible, and which triggered the analyzer early enough before the chopper burst such that there were roughly 20 channels of clean background before the time spectrum began to form, was selected. This time delay was measured with a calibrated-time-base oscilloscope and found to be 99 μsec at switch settings of coarse:1, fine:0 on the control panel. Due to the characteristics of the RC decay in the electronic delay unit, the exact duration of the delay was somewhat sensitive to the applied line voltage, so the circuit was powered from the same ac line voltage regulator used to control fluctuations in the chopper rotation speed.

The time difference, τ, between the middle of the chopper burst, where the rotor slits were by definition full open, and the phototransitor pulse from one of the mirrors attached to the rotor shaft is dependent on the angular preset of the light beam timing unit and the rotation speed of the chopper in the following way

$$\tau(\text{sec}) = \frac{\text{angular preset (degrees)}}{2\pi \cdot \omega(\text{sec}^{-1})} \qquad (29)$$

$$= \frac{\text{angular preset}}{6 \cdot \text{RPM}} .$$

In order to determine the exact angular preset, that is, the number of degrees of rotation between the chopper slit full-open position and the correct mirror alignment for the light beam to be reflected up to the phototransistor, the following calibration experiment was performed. A monoenergetic neutron beam, diffracted from a germanium single crystal, was pulsed by the chopper and the resultant time spectrum was measured for two very different flight paths (and thus very different total flight times) of 0.7 and 3.6 meters, respectively, all other experimental parameters being held constant. The flight time correction factor, and specifically that part having to do with the angular preset delay, was a different fraction of the recorded neutron arrival time in each case. By iteratively varying the assumed angular preset in the flight time correction factor, one could find some "effective" angular preset which resulted in the same calculated peak energy for each case. Figure 22 is a plot of the resulting energy spectra of the germanium beam using an angular preset of 9.4 degrees in the flight time correction factor. Within the accuracy limits that one could extrapolate the peak energies, they are the same in each case. The considerable width of the lower peak, measured with a very short, 0.7 meter, flight path, demonstrates the degradation of the energy resolution as a function of decreasing flight path.

Another similar experiment was conducted, this time in which the chopper rotation speed was varied between 7500 and 11,850 RPM, holding the flight path and other experimental parameters constant. Because of the RPM dependent nature of the angular preset delay time in equation 29, the flight time correction factor and thus the recorded neutron arrival times were different in each case. Again this difference allowed one to

extract that effective angular preset which resulted in the same peak energy for both measurements. The effective angular preset determined from this experiment was also 9.4 degrees.

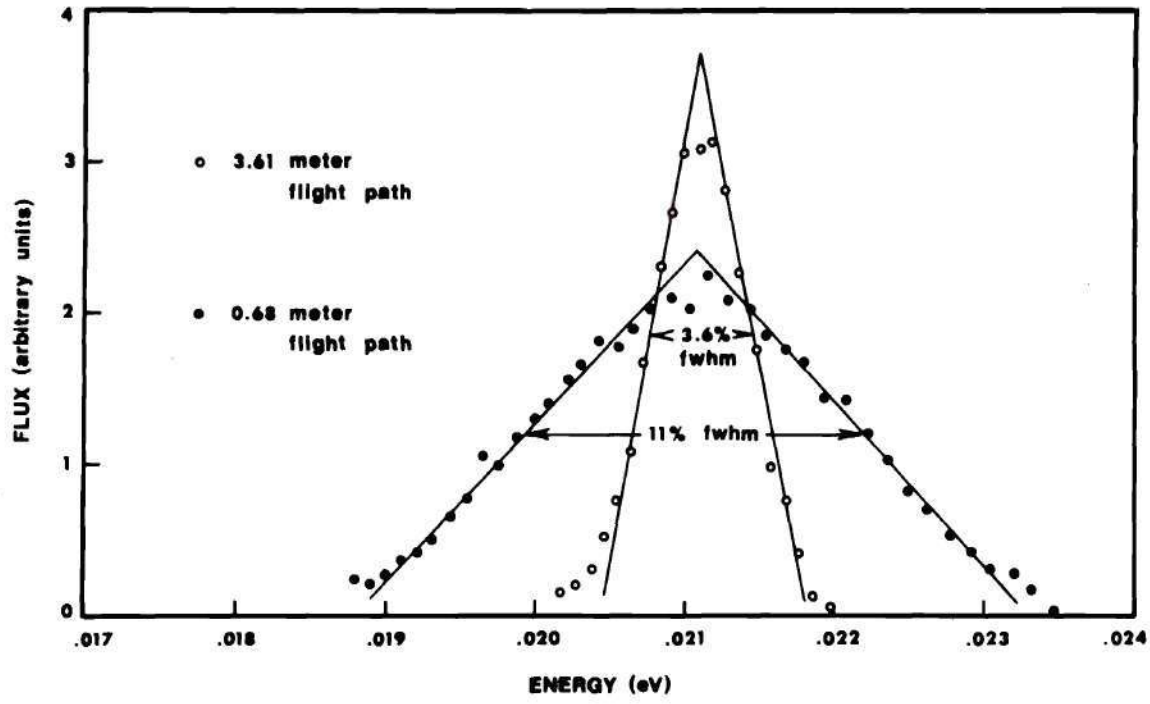

Figure 22. Measured Energy Spectra of a Monoenergetic Neutron Beam Diffracted from a Single Germanium Crystal. (The spectra have been corrected with a timing-pulse-to-chopper-burst angular preset of 9.4 degrees in the flight time correction factor. The resulting peak beam energy is 0.02105 eV. The width of the burst is a measure of the time-of-flight system resolution at high chopper RPM and for a particular flight path.)

An additional check on the time-of-flight analysis is that the peak beam energy determined from these measurements should have been the same as that determined from the beam diffraction angle and the characteristic crystal lattice spacing for germanium according to the Bragg

relation:

$$n\lambda = 2d \cdot \sin\theta \tag{30}$$

where

n is the order of reflection, here = 1,

λ is the neutron wavelength, proportional to energy according to the relation $E(eV) = 8.17/\lambda^2(\text{Å})$,

d is the crystal lattice spacing,

and θ is the Bragg diffraction angle.

The germanium peak beam energy derived from the time-of-flight measurements was 0.02105 ± 0.00005 eV which compares with 0.02106 eV from the crystal diffraction characteristics. This is excellent agreement indeed and leaves one relatively assured that the treatment of the timing parameters was correct.

An analogous experiment to determine the characteristic beam energy diffracted from a single copper crystal was equally rewarding. The peak beam energy derived from the time-of-flight spectrum was 0.06840 ± 0.00010 eV compared to 0.06855 eV from the crystal diffraction characteristics. The small difference in this case (about 1/4 percent) was hardly significant and could be attributed to difficulties in the determination of the exact diffraction angle rather than to a fault in the time-of-flight analysis.

The composite flight time correction factor, FT, with 16 μsec channel widths is

$$\begin{aligned} FT = &[\text{angular preset delay}] + [\text{chopper electronic delay}] \\ &+ [\text{time-of-flight analyzer "fixed" delay}] \\ &+ [\text{time to the middle of the first analysis channel}] . \end{aligned} \tag{31}$$

Therefore, substituting from the previous discussions,

$$FT = \frac{-9.4^{\circ}}{6 \cdot RPM} + 99\ \mu sec - 15\ \mu sec + 8\ \mu sec\ . \qquad (32)$$

Unfolding $\phi(t)$ into $\phi(E)$

The following simple relations hold for the flight time, velocity, and energy, respectively, for neutrons recorded in the N^{th} analysis channel in a time-of-flight measurement.

$$t(sec) = FT + (N-1)\Delta \qquad (33)$$

where

FT is the zero time correction factor,

N is the channel number,

and Δ is the analysis channel width;

$$v(m/sec) = fp(meters)/t(sec) \qquad (34)$$

where

fp is the neutron flight path measured from the chopper rotor axis to the center of the detector,

and t is the flight time calculated from equation 33;

and

$$E(eV) = 5.216 \times 10^{-9} \times v^2(m/sec)\ . \qquad (35)$$

The neutron energy spectrum, $\phi(E)$, is derived from the measured time distribution, $\phi(t)$, by application of the following relation

$$\phi(E)dE = \phi(t)dt \ . \tag{36}$$

E varies like v^2 and therefore like $1/t^2$, so that

$$dt/dE \approx 1/v^3 \approx t^3 \ . \tag{37}$$

Substituting in equation 36,

$$\phi(E) = \phi(t)dt/dE \approx \phi(t)\cdot t^3 \tag{38}$$

where extraneous constants that serve simply as scale factors and do not affect the spectrum shape have been dropped from the proportional relationship.

The energy spectrum, which resulted from point by point application of equation 38 to the measured time distribution of neutrons still included some of the distorting effects of the actions of the experiment on the neutron beam. To derive the true form of the spectrum within the beryllium assembly from the measured beam spectrum, one still had to apply a number of energy dependent corrections, most notably for the energy dependence of the chopper transmission, for neutron losses from the beam as a result of scattering or absorption in the air, aluminum, and other materials in the flight path, and for the energy dependence of the detector efficiency.

Chopper Transmission

For a perfectly collimated beam of infinite velocity neutrons, incident on a narrow rectangular slit located near the spin axis of a rotating shutter, the emerging neutron burst shape will be triangular, as can be deduced from consideration of the straight-through open area

projected by the slit as it rotates through the "open" position. The burst duration is given by

$$\tau = h/\omega R \ , \tag{39}$$

where

h is the slit width,

ω is the rotor angular velocity (radians/sec),

and R is the slit radius.

As the neutron velocity decreases, the burst shape shrinks from the perfect triangle, until a lower bound is reached where no neutrons are transmitted. This lower bound, called the "cut-off" velocity, corresponds to the case where the neutron velocity is sufficiently low such that the time required for the neutrons to traverse the rotor diameter is always greater than the total "open" time of the slit. In other words, neutrons with velocities below the cut-off, regardless of when they enter the slit, will always find that the slit has rotated into the "closed" position before they can emerge from the other side. If the neutron takes the time

$$t_n = 2R/v \tag{40}$$

to traverse the rotor diameter, 2R, and the "open" duration of the slit is

$$t_s = 2h/R\omega \ , \tag{41}$$

then all neutrons with flight times through the rotor $t_n < t_s$, or velocities,

$$v_c < \omega R^2/h \tag{42}$$

will be cut off. The cut-off velocity for the Georgia Tech Neutron Chopper, at a more or less typical rotation rate of 3900 RPM, is 465 m/sec (0.0011 eV).

This cut-off property is what prevented the slowest neutrons in a burst from overlapping the arrival time at the detector of the fastest neutrons in the next burst. The necessary condition to exclude burst overlap is that the flight time, t_f, of the slowest neutrons must be less than the duty cycle of the chopper, that is the time between bursts, t_d. The condition is then,

$$t_f \leqq t_d \ . \tag{43}$$

The flight time of the slowest neutrons in the burst, those just above the cut-off velocity, is

$$t_f = fp/v_c = fp/[\omega R^2/h] \ , \tag{44}$$

and the duty cycle is given by

$$t_d = \pi/\omega \ . \tag{45}$$

Substituting equations 44 and 45 into equation 43 yields

$$fp \leqq \pi R^2/h \tag{46}$$

as the condition for no burst overlap. The condition in equation 46 does not depend on the chopper rotation rate, but rather simply on the physical dimensions of the slit. The maximum allowable flight path which still avoids burst overlap with the Georgia Tech Neutron Chopper is

$$fp \leqq 3.6 \text{ meters} .$$

The burst shape in the velocity range $v_c \leqq v \leqq \infty$ has been calculated by Stone and Slovacek.[65] Figure 23 shows a typical calculated high and low velocity burst shape as compared to the infinite velocity triangle.

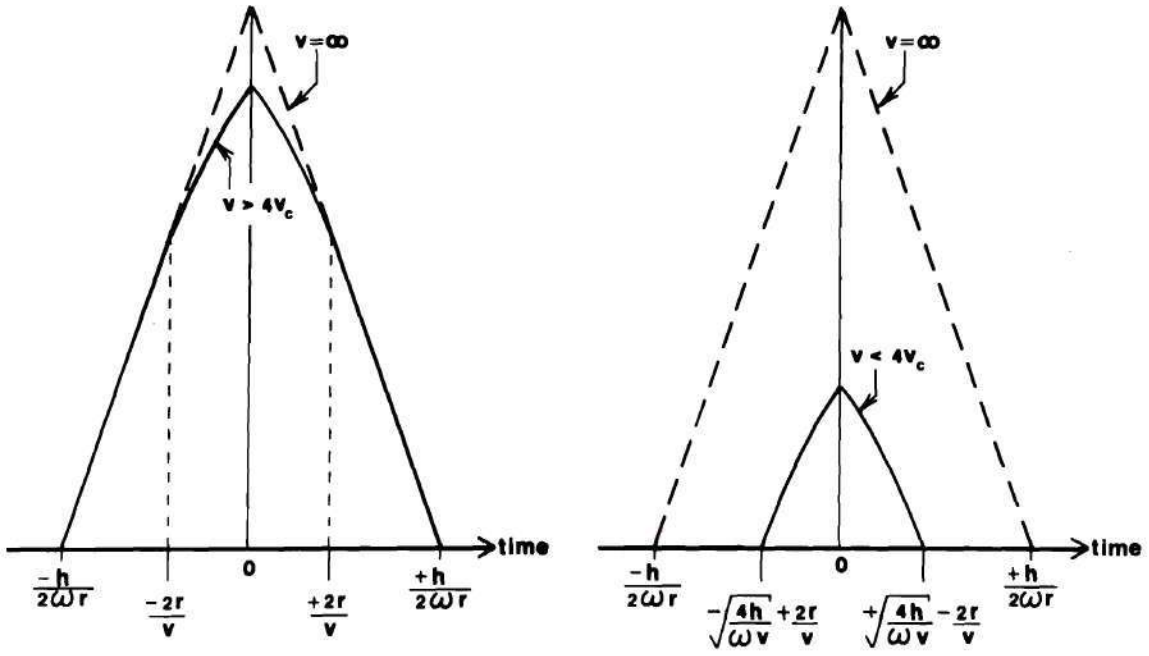

Figure 23. Calculated Chopper Burst Shapes Relative to the Infinite Velocity Triangle for High and Low Velocity Neutrons, Respectively. (Terms are as defined in the text.)

The integrated area under the burst shape curve, for some given velocity neutrons, represents the total number of neutrons of this velocity transmitted through the shutter. The ratio of this area to the area under the triangular burst for infinite velocity neutrons is a measure of the fractional transmission of the rotor for neutrons of a velocity v. From the above definition of "relative transmission" and from the equations for the burst shape as a function of neutron velocity, the following expres-

sions can be derived[66] for the relative rotor transmission function, TRANS

$$\text{TRANS} = \begin{cases} 1-(8/3)\cdot x^4 & \text{for } 0 \leqq x < 1/2 \ (E > 0.025 \text{ eV}) \\ (16/3)\cdot x\cdot(1-x)^2\cdot(1+x/2) & \text{for } 1/2 \leqq x \leqq 1 \ (E \leqq 0.025 \text{ eV}) \end{cases} \quad (47)$$

where

$$x = R\cdot\sqrt{\omega/hv} \ .$$

The fractional transmission can be calculated from equations 47 for any given chopper rotation rate and neutron velocity, and this transmission used to correct the measured spectrum for the energy dependent neutron losses resulting from traversing the chopper rotor. The energy dependent behavior of a typical transmission correction is shown in Figure 24 for the case of the Georgia Tech Neutron Chopper at a rotation rate of 3900 RPM.

Inasmuch as the transmission correction became quite large in the low energy range (200-300 percent), some care had to be exercised in determining the parameters in equations 47 to avoid the possibility of introducing a rather large error into the final spectrum shape. This was especially true of the slit width, h, which was fixed by the thickness of the 14 gauge aluminum spacers (nominally 0.064 inch). However, the actual slit width was influenced by things like the variation in gauge thickness in the as-rolled aluminum sheet from which the spacers were cut, the punching burrs around the bolt holes in the stainless steel rotor blades, and the thickness of cadmium buildup around these same bolt holes and around the edges of the blades due to preferentially heavy plating in the areas around sharp peaks in the electric field. This last effect was kept

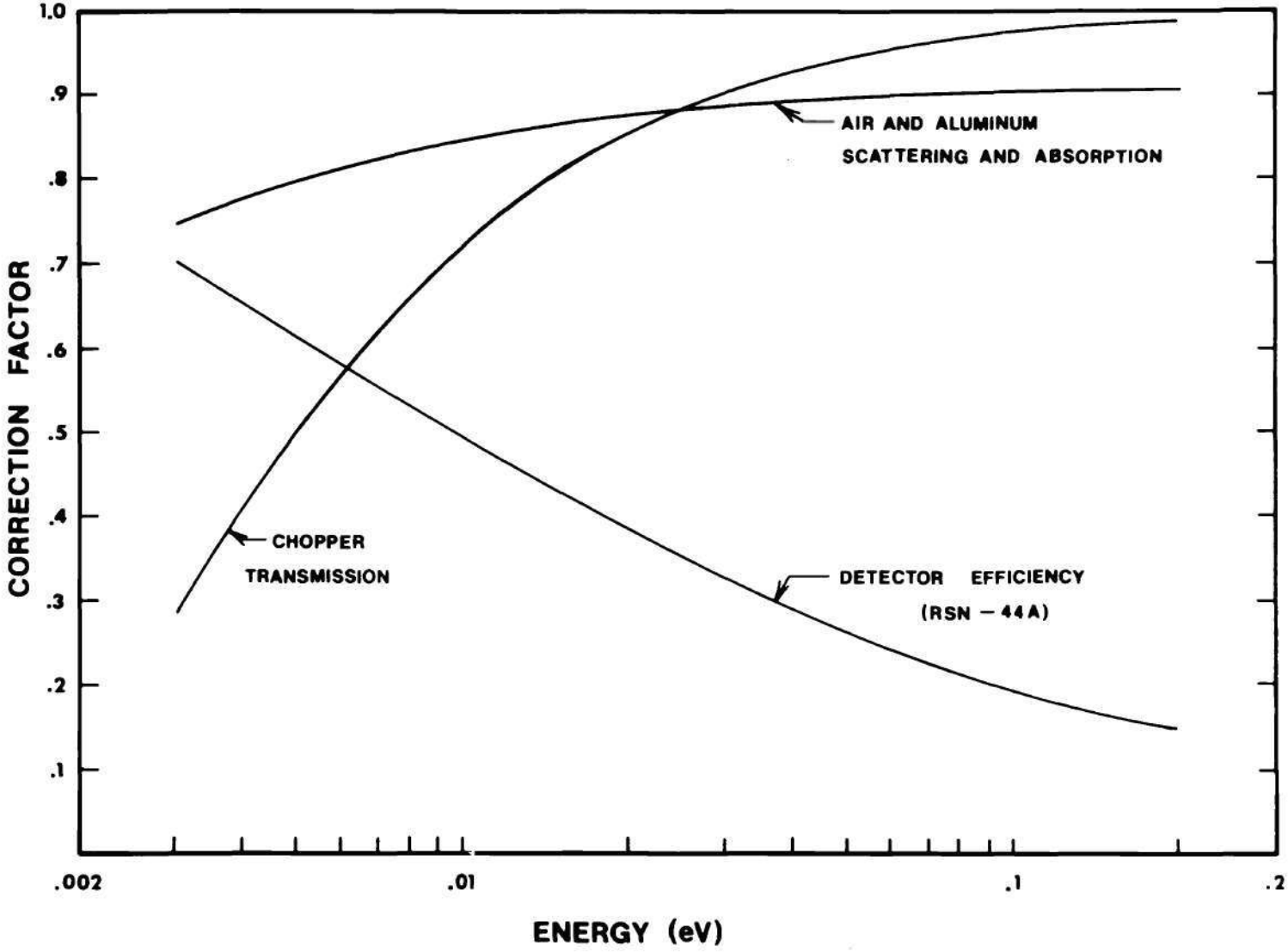

Figure 24. Energy Dependence of the Major Spectrum Correction Factors

to a practical minimum by smoothing the electric field around the edges of the plates with "fringing" wires during the cadmium plating operation. All things considered, then, the slit width was expected to be somewhat larger than the nominal gauge thickness of the aluminum spacers.

The following experiment was performed to determine the "actual effective" slit width. A typical beryllium energy spectrum was measured twice under identical experimental conditions except that the chopper rotation speed was changed from 3900 to 3000 RPM. According to equations 47, the fractional energy dependence of the chopper transmission was different in each case, especially in the low energy range. That value of the slit width which, when used in equations 47 to correct the spectra for transmission losses, resulted in the same spectrum shape for each RPM was then the "correct" effective slit width. The ratio of the two energy spectra corrected with a 0.069 inch slit width and arbitrarily normalized to 1.0 in the high energy range, is plotted in Figure 25.

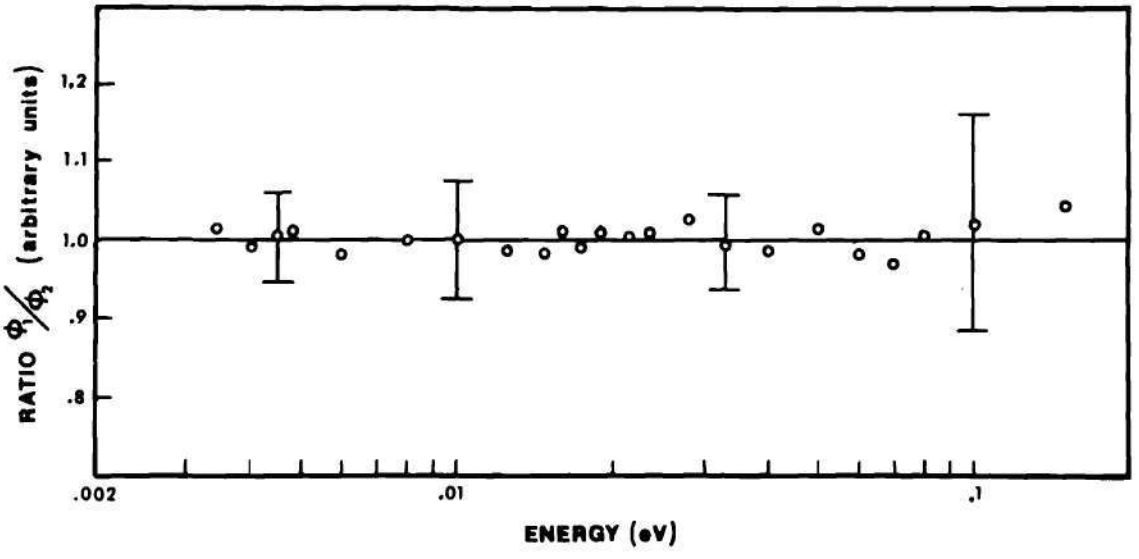

Figure 25. Ratio of Identical Beryllium Spectra Measured with Chopper Rotation Rates of 3900 and 3000 RPM

As mentioned earlier, this plotting technique, while it removes the details of the spectra themselves, tends to emphasize small differences. The points in Figure 25 hover around 1.0 over the entire energy range indicating that there was no evident systematic difference between the two corrected spectra and one concludes that 0.069 inch was the proper effective slit width. This experiment was repeated using 3700 and 5700 RPM; in the latter case the low energy neutron transmission was very small, of the order of 10 percent at 0.004 eV, so that the transmission correction was quite large and hence the shape of the final corrected spectrum was very sensitive to the parameters in equations 47. The result of this second experiment was essentially the same as the first, that is the correct effective slit width was 0.069 ± 0.0015 inch.

An important assumption[67] in the derivation of the equations for the burst shape, and hence equations 47 for the relative chopper transmission, was that all the chopper slits were located at a distance, H, from the rotor axis which was much less than R, the rotor radius. The implication here was that, to a first approximation, the slit spin axis and the rotor spin axis were one and the same so that the motion of any slit could be described in a straightforward manner as simple circular spinning about its own axis. If this was indeed the case, then the transmission of the shutter as a whole would have been simply proportional to that calculated from equations 47 for a central slit. However, the Georgia Tech Chopper, pictured in Figures 8 and 9, was constructed in such a manner that there are some slits located almost as far from the rotor axis as $H \approx R$, in clear violation of the above assumption, such that one must question the neglect of the horizontal and vertical motion of the centers

of rotation of off-axis slits during the time when these slits are "open." The question is, what is the relative influence of the motion of these peripheral slits when compared to the transmission calculated for a central slit?

Figure 26 is a simplified schematic of a cross section of the chopper rotor showing the relative behavior of typical upper and lower peripheral slits. The translational motion of these peripheral slit spin axes can conveniently be broken down into a horizontal and a vertical component.

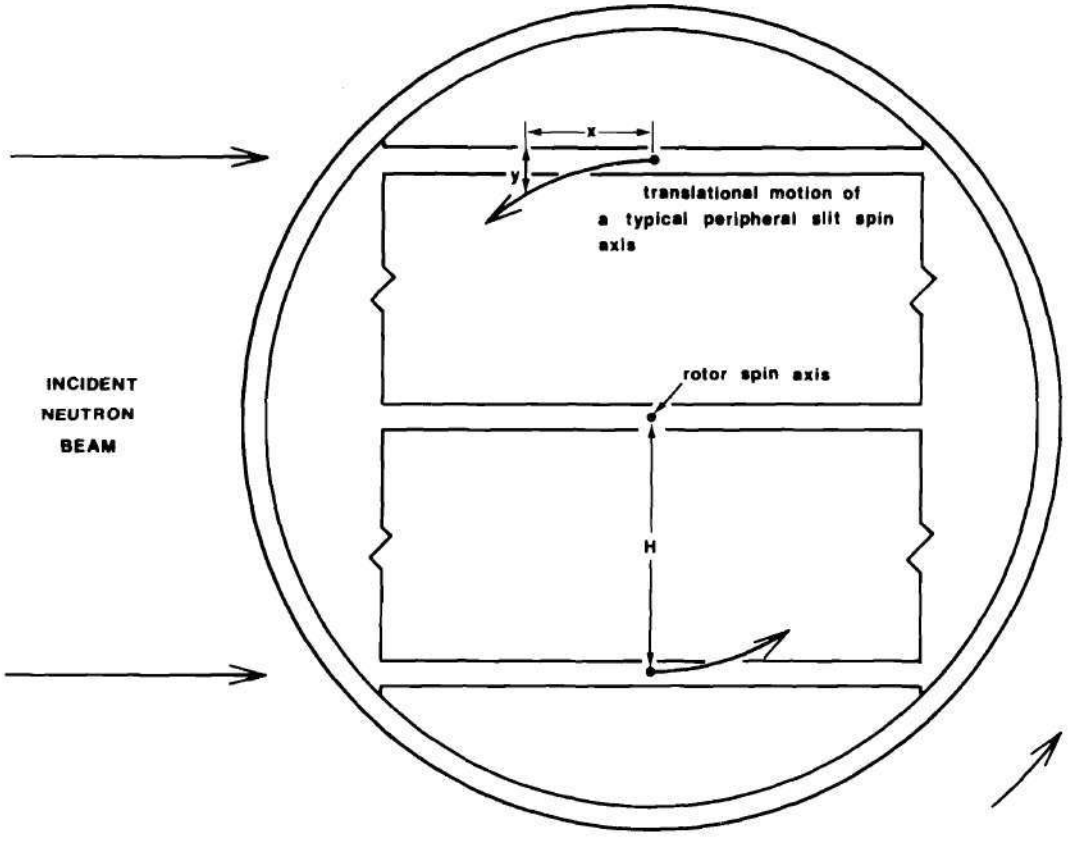

Figure 26. Vertical Section Schematic of the Chopper Rotor Illustrating the Translational Motion of Typical Upper and Lower Peripheral Slit Spin Axes for the Anomalous Transmission Effect

Consider first the horizontal component of motion. At the chopper orientation where the rotor blades were horizontal, and where the slit window was "open," the entire slit was moving parallel to the neutron beam, resulting in a Doppler-type velocity shift between the neutrons and the slit axis. Recall that the key to the neutron transmission probability for any slit is in the relationship between the neutron transit time through the slit and the time duration of the slit "open" window. To see the effect of the Doppler velocity shift on the neutron transmission probability for off axis slits, consider those neutrons in the beam which passed through the slits situated near the lower periphery of the rotor where the horizontal component of the slit motion was in the same direction as that of the neutrons (for the direction of rotation indicated). The Doppler velocity shift in this case was such as to make the neutrons seemingly spend a longer time, of the order of 10 percent longer at 4000 RPM, in traversing the slit diameter, and hence relatively fewer neutrons would have been transmitted through the slit than if it were located at the central rotor spin axis. The effect was most pronounced at lower energies where the fractional Doppler velocity shift was greatest. A similar argument for the slits near the upper periphery of the rotor where the Doppler velocity shift was in the opposite direction to that of the neutron flight reveals that relatively more neutrons would have been transmitted than through an identical slit located at the central rotor axis.

There was one further complication due to the vertical modulation of the off axis slits. Examination of the rotor schematic in Figure 26 reveals that, for the slits in the upper half of the rotor and for the direction of rotation indicated, the chopping action is controlled by the

upper blade during the first half of the burst (from the time when the slit is first open to the middle of the burst when the slit is exactly parallel to the neutron beam), whereas the action is controlled by the lower blade throughout the last half of the burst (from the middle of the burst to the time when the slit passage closes completely). The vertical modulation causes the upper blade to move up and out of the neutron beam path in the first half of the rotation period, and similarly the lower blade is caused to move down (relative to the behavior of a central slit) and out of the neutron beam path in the last half of the rotation period. Thus, some of those neutrons incident on the upper slits, which, based on the transmission probability for a central slit, one would have predicted to have been blocked by the slit sides, would pass on through the rotor as the slit sides moved out of their path. It is apparent then that the effect of the vertical slit modulation in the upper half of the rotor is to increase the relative transmission probability (over that for a central slit), the relative increase becoming more pronounced at lower neutron energies. Similar arguments for the slits in the lower half of the rotor reveal that the effect of the vertical slit modulation is to decrease the relative transmission probability over that for an identical central slit. The effect on the relative neutron transmission probability for slits above and below the chopper rotor spin axis, from vertical slit modulation, is then in the same direction as the effect from the horizontal Doppler velocity shift for these same slits. That is, the relative neutron transmission probability is higher than that calculated from equations 47 (for an identical slit located on the rotor spin axis) for lower energy neutrons incident on the slits in the upper half of the rotor and the relative

transmission probability is lower for lower energy neutrons incident on the slits in the lower half of the rotor. The magnitude of these effects can be seen to increase with distance from the rotor spin axis.

Since the calculated neutron transmission function in equations 47, which was used to correct the measured spectra, was based on the assumption that all the chopper slits were located "near" the rotor axis, how do the transmission anomalies in the upper and lower portions of the beam affect the outcome of the final transmitted-beam spectrum? If the neutron beam was exactly centered on the chopper axis such that, on the average, the same number of neutrons fell above and below the axis, then the complimentary nature of the increased low energy transmission above the rotor axis and the decreased low energy transmission below the rotor axis appear to cancel one another in such a manner as to make the appropriate average transmission function, for the rotor as a whole, equal to that for a central slit as calculated from equations 47. However, should the beam center lie above or below the rotor axis, such that statistically more or less neutrons passed through the upper or lower half, then the calculated transmission function based on a central slit would have been in error. Following our earlier arguments, one would expect to "see" a higher fraction of low energy neutrons if the beam were centered above the rotor axis and vice versa, one would expect to "see" a lower fraction of low energy neutrons if the beam were centered below the rotor axis.

In support of these contentions, the following experiment was performed wherein the neutron energy spectrum was measured from a typical beryllium assembly first with the lower half of the beam blocked off with cadmium absorbers so that the detector "saw" only those neutrons passing

through the upper half of the rotor. Then the cadmium absorbers were moved to block off the upper half of the beam so that the detector "saw" only those neutrons passing through the lower half of the rotor. The resulting spectra, corrected with the "central slit" transmission function, equations 47, are presented in Figure 27 along with the spectrum measured with the full beam exposed. The spectra have been arbitrarily normalized in the high energy range to emphasize the relative shapes. The results of the experiment certainly support our earlier contentions, that is, the low beam contained about 40 percent fewer low energy neutrons than the average, and the high beam contained roughly 30 percent more low energy neutrons than the average. The fact that the combination of the high and low beam spectra does not appear to exactly reproduce the full beam spectrum is not conclusive due to problems with precise high energy normalization, and since no real effort was made to block out exactly half the neutron beam in the experiment in each case. What is important is that the behavior of the spectra was in keeping with that predicted by the Doppler velocity shifts in the rotor, above and below the spin axis.

It may be concluded then that the measured beryllium spectra can reasonably be corrected for energy dependent chopper transmission losses using the transmission function in equations 47, which assumes an average behavior like a central slit, so long as the beam is vertically centered on the chopper axis. This contention is further supported by the comparative measurements in Figure 25 wherein identical spectra were measured at different chopper speeds. If the central slit transmission correction in equations 47 was influenced by some non-canceling behavior from the peripheral slits, then one would expect this behavior to be apparent in Figure

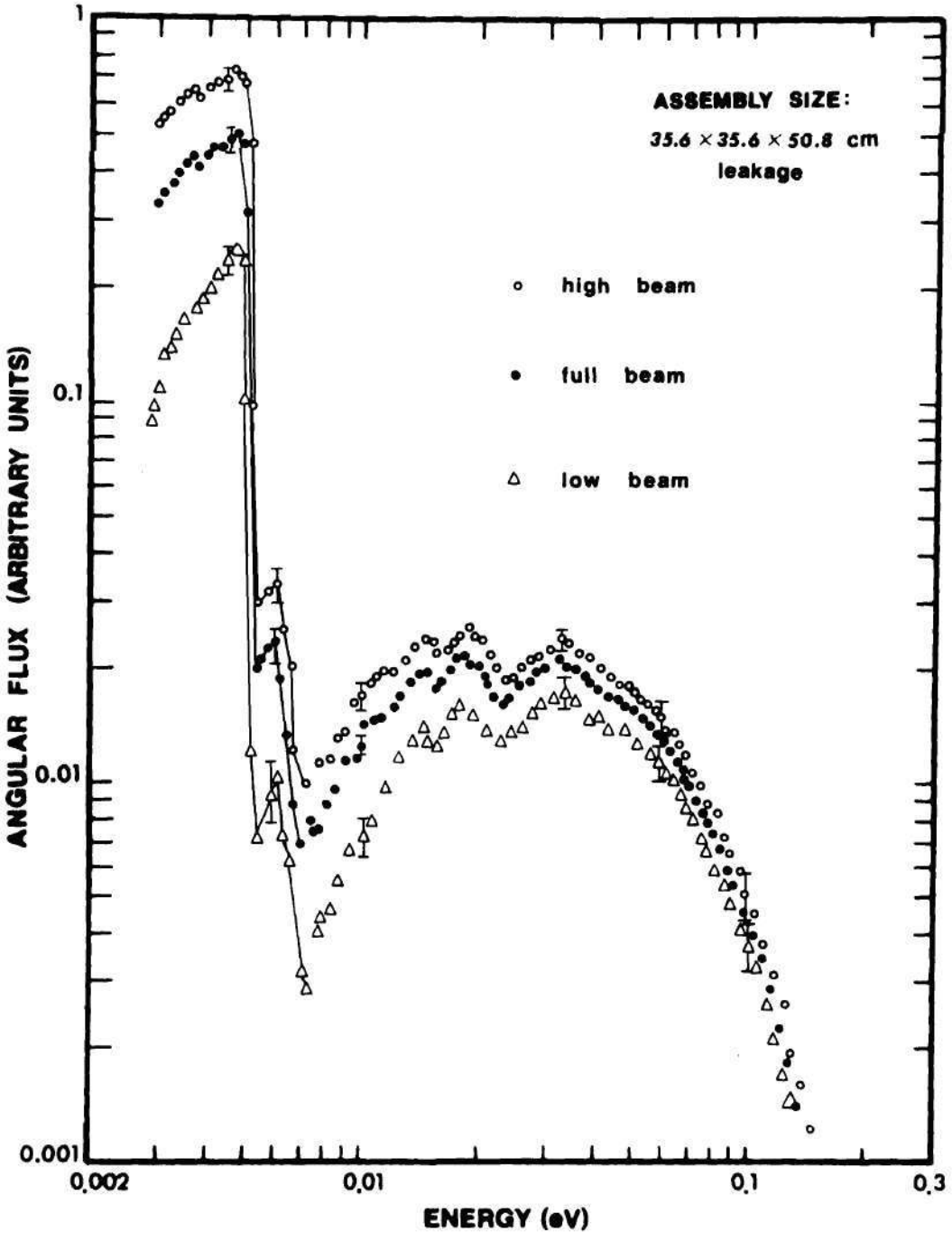

Figure 27. The Effects of Anomalous Chopper Transmission on the Shape of the Beryllium Energy Spectrum Measured with the Neutron Beam Passing Through the Upper Half Only, Full Area, and Lower Half Only of the Rotor. (The spectra have all been corrected with the central-slit approximation. Normalization is arbitrary in the high energy range.)

25 where the ratio of spectra with different neutron transmission corrections (from the different chopper speeds) was plotted. The fact that the ratio of the spectra in Figure 25 hovered statistically around 1.0, showing no apparent difference trend, is additional evidence that the average transmission correction for the chopper as a whole is indeed the central slit correction given by equations 47. However, one had to exercise some care to ensure that the apparatus was carefully aligned to preclude the possibility of biasing the measurements with a high or low anomalous transmission. The confidence limits attached to the final spectrum shape reflect the uncertainty in beam position with respect to the rotor axis to include just this effect.

Scattering and Absorption Losses in the Flight Path

The neutron energy spectrum measured at the detector was distorted to some extent from that emerging from the beryllium assembly by the effects of energy dependent scattering and absorption losses from the neutron beam as it traversed the flight path. The materials in the path of the beam included the aluminum in the chopper and detector housings and the air in the flight path.

The fractional neutron intensity transmitted through L cm of air is given by

$$I/I_o = e^{-\Sigma_T(v)\cdot L} \qquad (48)$$

where

$\Sigma_T(v)$ is the total, macroscopic, velocity dependent cross section for air (1/cm),

and L is the total air path traversed from the beryllium assembly to the neutron detector (cm).

The total macroscopic cross section for air includes both scattering and absorption losses, the latter being a small contribution, 80 millibarns in nitrogen and less than two millibarns in oxygen. If one considers only the two major constituents of dry air, 78.1 percent nitrogen and 21.0 percent oxygen, then

$$\Sigma_T(v) = [N \cdot \sigma_T(v)]_{\text{nitrogen}} + [N \cdot \sigma_T(v)]_{\text{oxygen}} , \qquad (49)$$

where

N is the atom density (number/cm^3),

and $\sigma_T(v)$ is the appropriate total microscopic cross section (cm^2).

The atom density for each element is given by

$$N = \% \cdot \rho \cdot N_o / A , \qquad (50)$$

where

% is the atom percent for a particular element,

ρ is the density of air at 20°C and 760 Torr (0.001205 g/ml),

N_o is Avogadro's number (6.023×10^{23}),

and A is the atomic weight,

which results in

$$N_{\text{nitrogen}} = 4.045 \times 10^{19} \text{ atoms/cm}^3$$

and

$$N_{\text{oxygen}} = 0.950 \times 10^{19} \text{ atoms/cm}^3 .$$

The total cross section, $\sigma_T(v)$, for each element was obtained by an iterative fitting procedure to the experimental data[14] from BNL-325 in the thermal energy range with an empirical equation of the form

$$\sigma = a + b/v + c/v^2 \tag{51}$$

where the coefficients, a, b, and c, were not intended to convey any particular physical significance, but rather to provide an approximate analytical expression to be used in the subsequent calculation of the air scattering correction factor. Figure 28 is a plot of the total cross sections of nitrogen and oxygen with their respective fits to equation 51, which yielded

$$\sigma_n(v) = 9.5 + 3.0(2200/v) + 0.5(2200/v)^2 \tag{52}$$

and

$$\sigma_o(v) = 3.5 + 0.5(2200/v) + 0.3(2200/v)^2 \ . \tag{53}$$

The fits appeared to be very good over the energy range of interest between 0.003 and 0.3 eV. Substituting into equation 48, and making use of the fact that

$$e^{x+y} = e^x \cdot e^y \tag{54}$$

to divide out the constant part of the nitrogen and oxygen cross sections (since one is only interested in the energy dependent spectrum shape) equation 48 becomes

$$(I/I_o)_{air} = \exp[-(0.2775/v + 111.7/v^2)\cdot L] \ , \tag{55}$$

where

v is the neutron velocity (m/sec),

and L(cm), the total air thickness, is given by

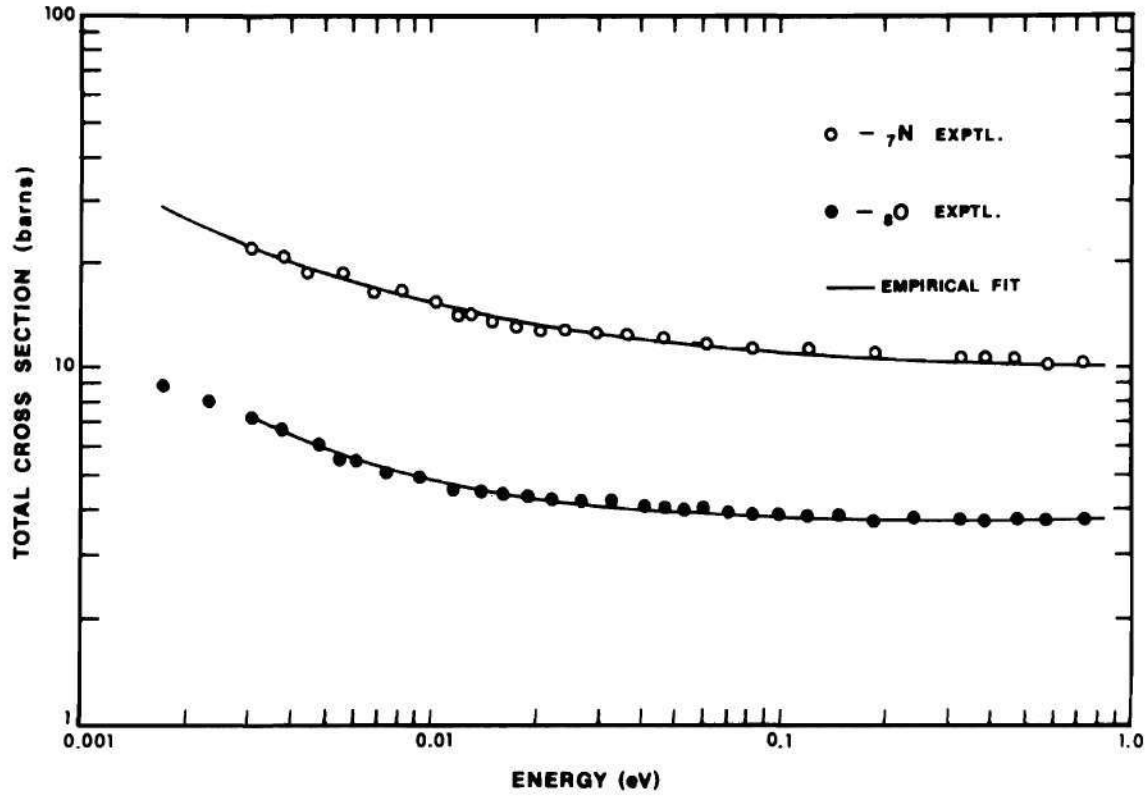

Figure 28. The Low Energy Cross Sections of Nitrogen and Oxygen from BNL-325 (reference 14) and the Associated Analytical Model Quadratic Fits

L = [reentrant channel depth (cm)] (56)

+ [air gap between the beryllium assembly front face and the thermal column inside shutter face, approximately five cm]

+ [thickness of the thermal column shutter doors and shield plug, approximately 66 cm]

+ [distance from the reactor face to the chopper rotor centerline, approximately 18-20 cm]

+ [flight path, distance from the chopper rotor centerline to the detector centerline]

- [1/2 detector diameter] .

The total air scattering correction factor, plotted in Figure 24, varied typically from 0.9 at high energy to roughly 0.8 at low energies (0.005 eV).

The ratio of two beryllium test spectra, measured with flight paths of 2.35 and 2.95 meters, respectively, and thus with different air scattering losses, is plotted in Figure 29 to emphasize any differences between the two. The normalized ratio scatters statistically around 1.0 indicating that the corrected spectra were essentially the same and suggesting that the air scattering correction in equation 55 accurately described the physical situation over the range of interest.

Similarly, the transmitted neutron intensity through d cm of aluminum is given by

$$I/I_o = e^{-\Sigma_T(v)\cdot d} = e^{-N_{al}\cdot\sigma_T(v)\cdot d} \qquad (57)$$

where

N_{al} is the atom density of aluminum (6.03×10^{22} atoms/cm^3) ,

$\sigma_T(v)$ is the total microscopic aluminum cross section (cm^2) ,

and d is the thickness of aluminum in the flight path (cm) .

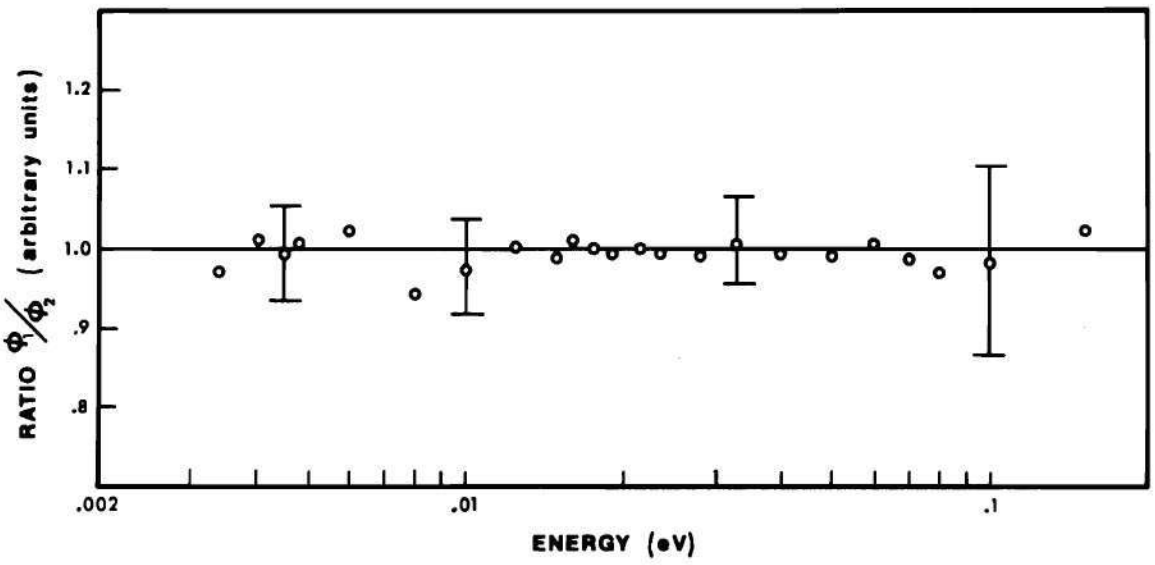

Figure 29. Ratio of Identical Beryllium Spectra Measured with Flight Paths of 2.35 and 2.95 Meters

The total cross section of aluminum is plotted in Figure 30 with data[14] from BNL-325. The cross section is relatively flat over the thermal energy range except for some low energy Bragg structure; specifically a sharp 50 percent drop at 0.0037 eV which showed up in the measurements as a small five percent peak superimposed on the low energy tail of the beryllium spectrum. Since there was very little aluminum directly in the flight path, and hence the scattering correction factor was small, there is very little error introduced into the final spectrum shape by assuming that the cross section was indeed flat down to 0.0037 eV where it dropped to a relative 1/v dependence. The neglect of the higher energy Bragg

structure, specifically those peaks just above 0.0037 eV, is corroborated by the narrowness of the peaks and thus their expected negligible effect on the overall spectrum shape. This assumed energy dependence is shown as the solid line in Figure 30.

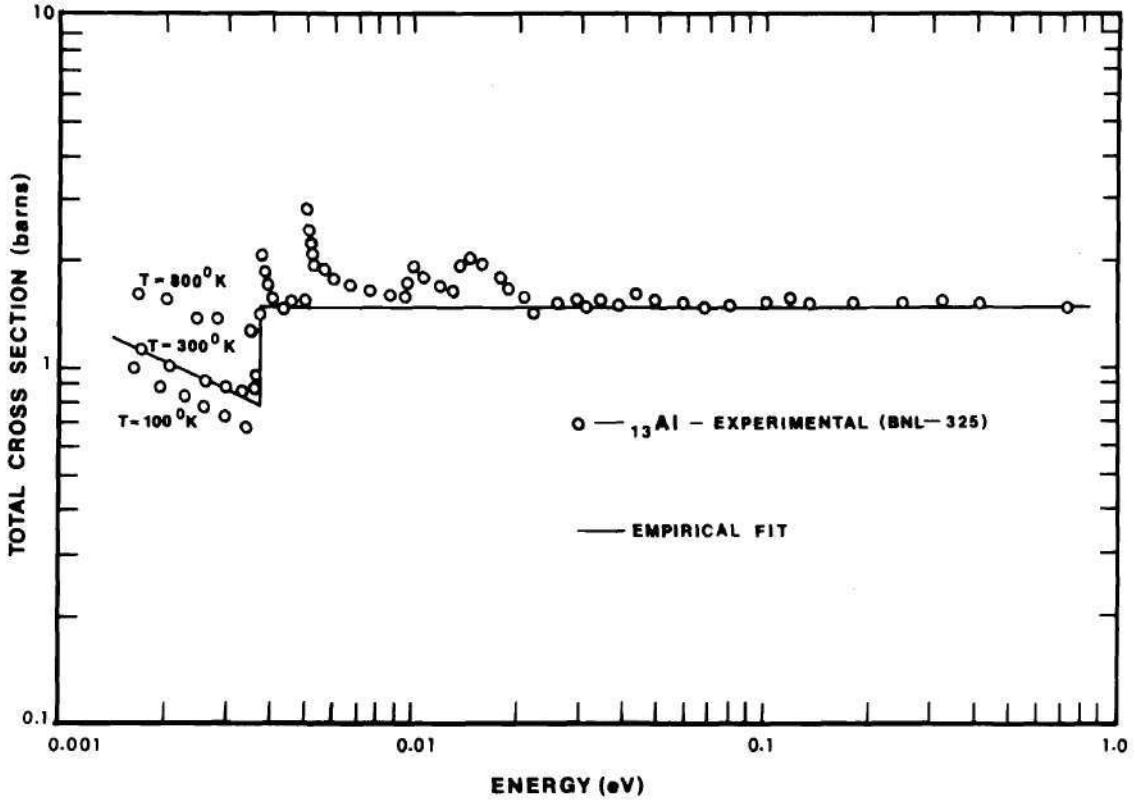

Figure 30. The Low Energy Cross Section of Aluminum from BNL-325 (reference 14) and the Associated Analytical Model Empirical Fit

The thickness of aluminum which the neutron beam passed through in the flight path consisted of:

1. both sides of the cylindrical chopper rotor housing (0.7 cm total), and

2. one side only of the BF_3 detector cathode (0.14 cm).

In the latter, it has been assumed that none of the neutrons which scattered in the detector cathode entered the active detector volume, an assumption which, though conservative, was probably not entirely valid due to the close geometric proximity between the two. Also neglected was the fraction of neutrons which scattered in that portion of the aluminum slit spacers not shielded by the cadmium plated bolts that hold the rotor assembly together. In retrospect, it appears that this last assumption may have been a bit overoptimistic. Even though those neutrons which passed through the unshielded portion of the aluminum slit spacers constituted a small fraction of the total neutrons, the thickness of aluminum traversed in this case was large, such that the net effect still showed up slightly in the measured spectra and was roughly of the same order of magnitude as the effect from the aluminum in the chopper housing and the detector cathode. It is well to remember, however, that the effect appears as a constant, small peak (< 5%) superimposed on the beryllium spectrum in the extreme low energy range (0.0037 eV) and that it in no way interferes with the interpretation of the spectrum behavior.

Substituting the appropriate cross section estimate and aluminum thickness into equation 57 results in

$$(I/I_o)_{\text{aluminum}} = 0.9268 \qquad \text{for } E \geq 0.0037 \text{ eV} \qquad (58)$$

$$= \exp[-33.4/v(\text{m/sec})] \quad \text{for } E < 0.0037 \text{ eV} .$$

The net effect on the final spectrum shape from application of the aluminum scattering correction, equation 58, was to drop the superimposed aluminum

Bragg peak, below 0.0037 eV, by roughly 3-4 percent.

The total flight path scattering and absorption correction, SCATT, is defined as

$$\text{SCATT} \equiv \left[(I/I_o)_{air} \times (I/I_o)_{aluminum} \right] . \tag{59}$$

Detector Efficiency

The task here is one of calculating the energy dependent detector efficiency given a parallel beam of polyenergetic neutrons incident on a cylindrical BF_3 detector located at the end of the flight path, perpendicular to the direction of neutron flight. The detector efficiency, DTEFF(E), is defined as the probability that a neutron of energy E will be detected as it passes through the active detector volume.

The probability of neutron absorption in a thickness 2x is given by

$$1 - e^{-2\Sigma(v)x} , \tag{60}$$

where

$\Sigma(v)$ is the macroscopic $B^{10}(n,\alpha)$ cross section

and 2x is the thickness of detector traversed (see Figure 31).

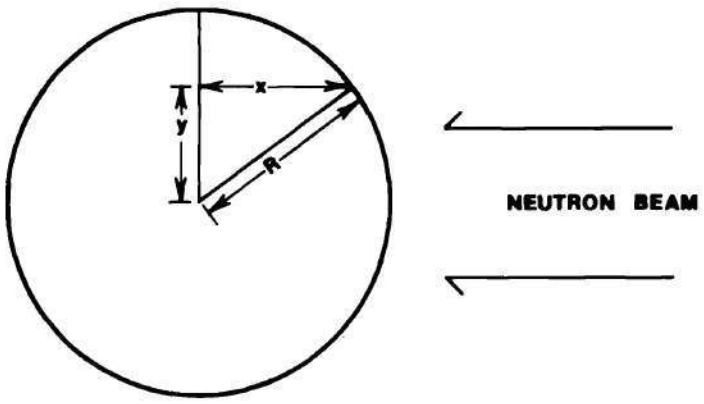

Figure 31. Vertical Section of a Cylindrical BF_3 Detector with Coordinates for the Calculation of the Detector Efficiency

Thus, the absorption probability for the detector as a whole is obtained from the volume integral

$$\text{DTEFF}(E) = \frac{1}{R} \cdot \int_o^R \left[1 - e^{-2\Sigma(v)x}\right] \cdot dy \ . \tag{61}$$

Substituting $x^2 + y^2 = R^2$ and $x = y$, equation 61 reduces to

$$\text{DTEFF}(E) = \frac{1}{R} \cdot \int_o^R \left[1 - e^{-2\Sigma(v)\cdot(R^2-x^2)^{\frac{1}{2}}}\right] \cdot dx \ . \tag{62}$$

The integration of equation 62 is carried out in detail in Appendix C resulting in

$$\text{DTEFF}(E) = 1 - \frac{\pi}{2}\left[L_{-1}(s) - I_{+1}(s)\right] , \tag{63}$$

where

$L_{-1}(s)$ is the modified Struve function[68] of order -1,

$I_{+1}(s)$ is the modified Bessel function[69] of the first kind,

and $s = 2\Sigma(v)R$.

The modified Struve and Bessel functions are calculated from the power series expansions[70]

$$L_\nu(s) = (s/2)^{\nu+1} \times \sum_{k=o}^{\infty} \frac{(s/2)^{2k}}{(k+\frac{1}{2})! \times (k+\nu+\frac{1}{2})!} \tag{64}$$

which, for $\nu = -1$ reduces to

$$L_{-1}(s) = \sum_{k=o}^{\infty} \frac{s^{2k}}{\pi[(2k-1)!]^2 \times (k+\frac{1}{2})} \ . \tag{65}$$

The first four terms of equation 65 are

$$L_{-1}(s) = 2/\pi + 2s^2/3\pi + 2s^4/45\pi + 2s^6/105\pi \ . \qquad (66)$$

Similarly, for the Bessel function,

$$I_\nu(s) = (s/2)^\nu \times \sum_{k=0}^{\infty} \frac{(s/2)^{2k}}{k! \times (k+\nu)!} \ , \qquad (67)$$

which, for $\nu = 1$ is

$$I_1(s) = \sum_{k=0}^{\infty} \frac{(s/2)^{2k+1}}{(k+1) \times (k!)^2} \ . \qquad (68)$$

The first four terms of equation 68 are

$$I_1(s) = s/2 + s^3/16 + s^5/128 + s^7/18{,}432 \ . \qquad (69)$$

The modified Struve and Bessel functions are plotted in Figure 32. Recall from equation 63 that the detector efficiency was determined by one minus the difference in the two functions, which becomes quite small for high values of s (low energies). The power series expansions for the modified Struve and Bessel functions, equations 65 and 68, have been found to converge in the sixth decimal place after only seven terms. However, 12 terms were carried in each expansion to assure adequate convergence in the difference.

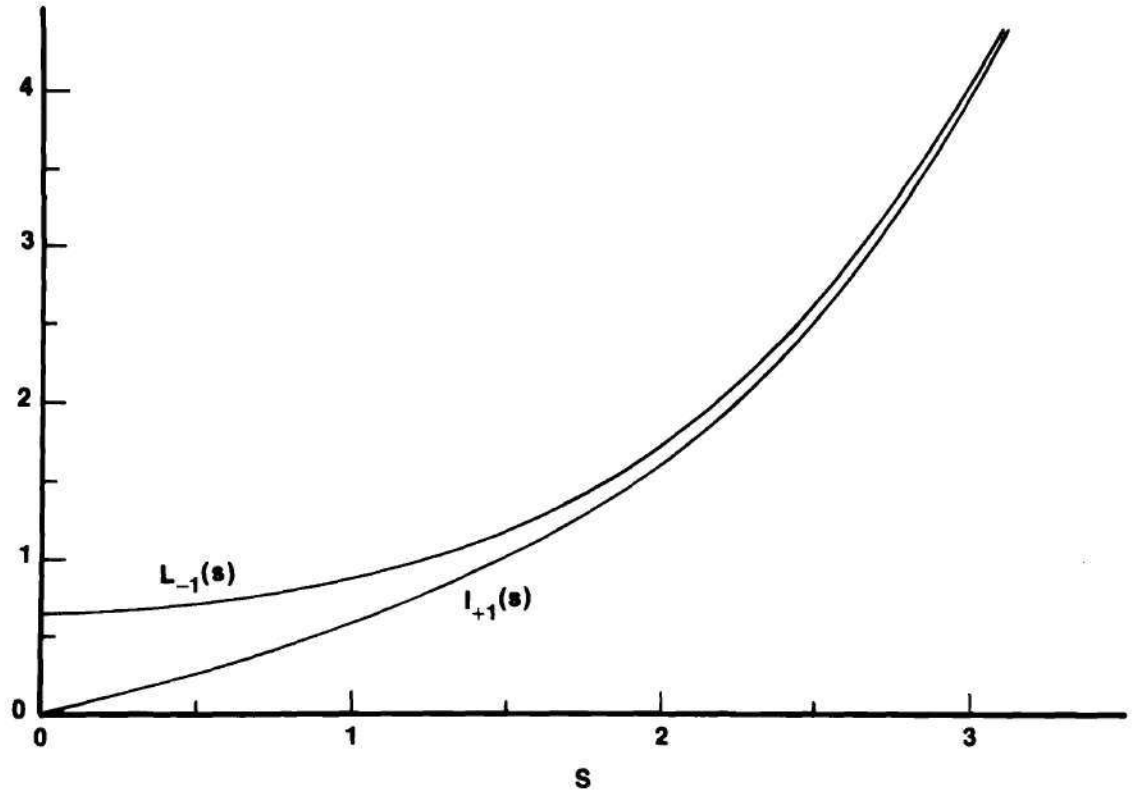

Figure 32. Modified Struve, L, and Bessel, I, Functions

From equation 63, s can be written as

$$s = 2 \cdot N_{B^{10}} \cdot \sigma(v) \cdot R \tag{70}$$

where

N is the B^{10} atom density (atoms/cm^3),

$\sigma(v)$ is the $B^{10}(n,\alpha)$ cross section (cm^2),

and R is the detector radius (cm).

Two different detectors were used in the spectrum measurements, dependent on the neutron beam intensity. The first was a two inch diameter, 24 inch long Reuter-Stokes RSN-44A filled to 900 Torr of enriched

(96 percent) $B^{10}F_3$. The high fill gas pressure in this detector necessitated that it be operated at the highest practical voltage to obtain good pulse response time. Figure 33 is a plot of the measured detector response versus applied high voltage. The curve exhibits the usual proportional counter plateau extending roughly from 3100 to 3300 volts. All the spectrum measurements with this detector were made at 3200 volts.

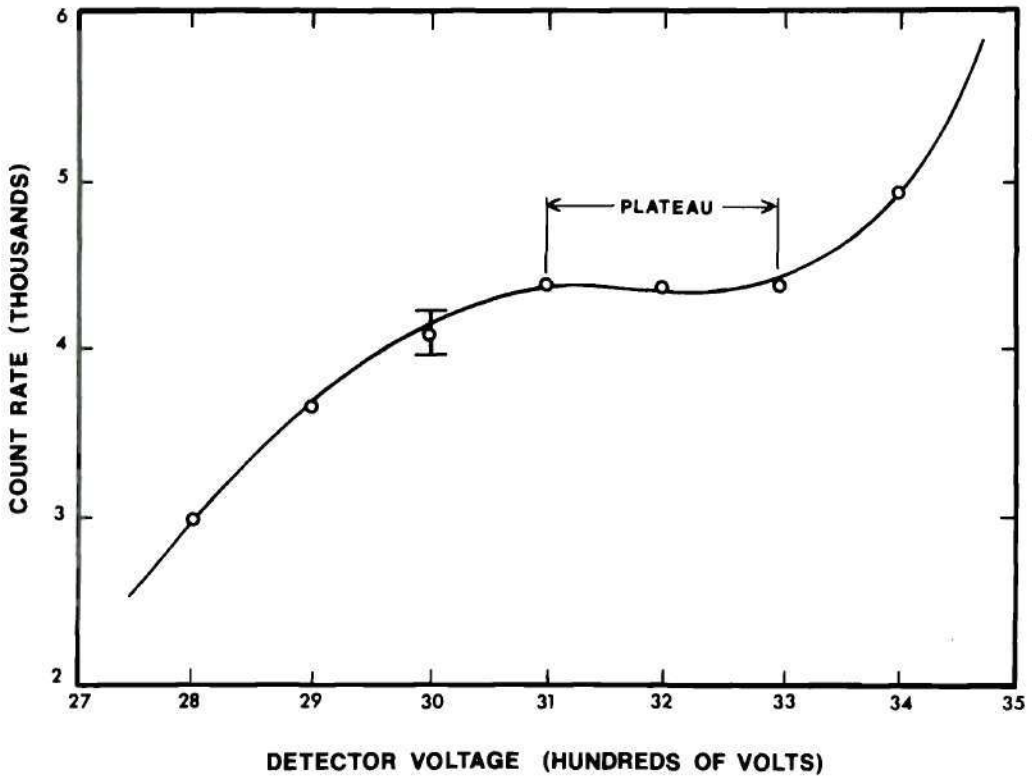

Figure 33. Measured Detector Response versus Applied Voltage Displaying the Typical Proportional Counter Plateau

With $N_{B^{10}}$ calculated for this detector of 3.0198×10^{19} B^{10} atoms/cm^3, the detector radius of R = 2.40 cm, and assuming the usual 1/v dependence in the $B^{10}(n,\alpha)$ cross section, equation 70 yields

$$s = 1218.1/v \qquad \text{with v in m/sec} \tag{71}$$

for the RSN-44A detector. S in Figure 32 varied from 0.278 at 0.1 eV to 2.78 at 0.001 eV for this detector.

The other detector was a one inch diameter, 12 inch long Reuter-Stokes RSN-7A filled to 400 Torr of enriched (96 percent) $B^{10}F_3$. Because of the lower fill gas pressure and the smaller diameter, this detector was operated at 1700 volts.

$N_{B^{10}}$ calculated for this fill pressure was 1.34×10^{19} B^{10} atoms/cm^3. With R = 1.13 cm and the 1/v behavior of the B^{10} cross section, substitution into equation 70 yields

$$s = 254.93/v \tag{72}$$

for the RSN-7A detector.

The energy dependent detector efficiency correction for the RSN-44A detector, calculated from equation 63, is pictured in Figure 24 along with its relation to the other major correction factors.

As a check on the behavior of the detector efficiency correction, the same beryllium spectrum was measured with each of the above detector systems, and the ratio of the resultant corrected spectra is plotted in Figure 34 to emphasize any differences between the two. The fact that the normalized ratio of the two spectra hovers statistically around 1.0, meaning that the corrected spectral shapes in each case were essentially the same, is evidence to the accuracy of the detector efficiency correction.

Resolution Correction

The resolution width in time-of-flight measurements originates from certain neutron timing uncertainties, most important among these

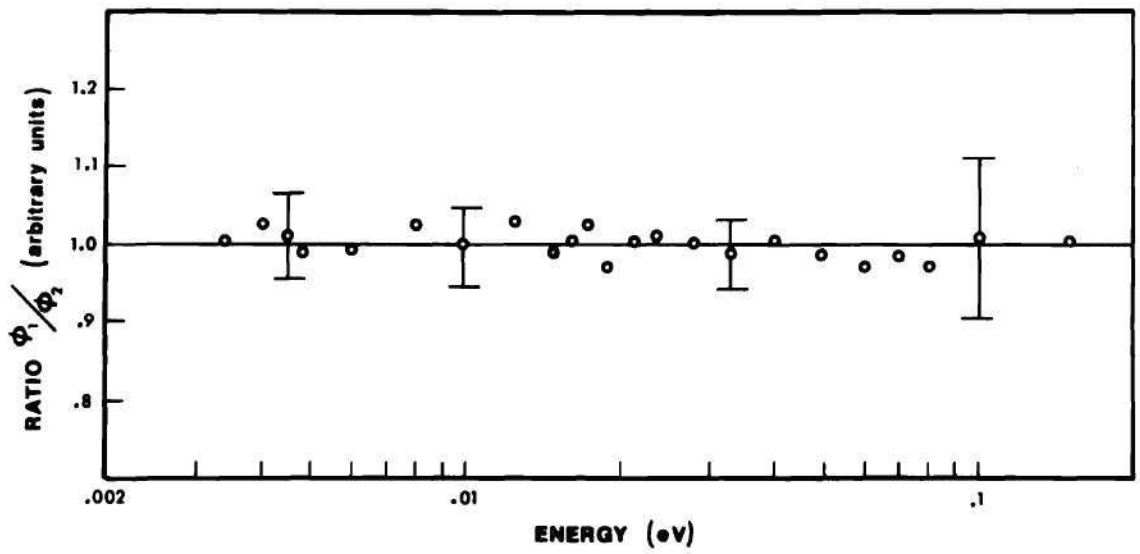

Figure 34. Ratio of Identical Beryllium Spectra Measured with the RSN-7A and RSN-44A Detectors

being the width of the chopper burst (zero time smear), the finite neutron path length in the detector, and the duration of the analyzer data recording channels. According to Beckurts and Wirtz,[1] the instrumental resolution uncertainty distorts the measured time spectrum like

$$\phi(t) = \phi_o(t) + \phi_o''(t) \cdot \frac{1}{2} \cdot \int_{-\infty}^{\infty} \lambda^2 \cdot R(\lambda) \cdot d\lambda \ , \tag{73}$$

where

$\phi(t)$ is the measured time distribution,

$\phi_o(t)$ is the "actual" time distribution if there were no resolution uncertainty,

$R(\lambda)$ is the normalized resolution function,

and $\phi_o''(t) = \partial^2 \phi_o(t) / \partial t^2$.

The resolution width, δ, is defined according to

$$\delta^2/2 \equiv \frac{1}{2} \cdot \int_{-\infty}^{\infty} \lambda^2 \cdot R(\lambda) \cdot d\lambda \ . \tag{74}$$

The resolution width is a superposition of the triangular chopper burst resolution,

$$\delta_{burst} = \delta t_{burst} / \sqrt{6} \ , \tag{75}$$

where δt_{burst} is the half-width of the chopper burst; the rectangular detector path length resolution,

$$\delta_{det} = \delta t_{det} / \sqrt{3} \ ; \tag{76}$$

and the rectangular analyzer channel resolution,

$$\delta_{chan} = \delta t_{chan} / \sqrt{3} \quad . \tag{77}$$

Combining, and substituting into equation 73, results in a resolution correction factor,

$$\frac{\phi(t)}{\phi_o(t)} = 1 + \left[\frac{\phi_o''(t)}{\phi_o(t)} \cdot \frac{1}{2} \cdot \left(\frac{\delta t_{burst}^2}{6} + \frac{\delta t_{det}^2}{3} + \frac{\delta t_{chan}^2}{3} \right) \right] . \tag{78}$$

The resolution error in the measured time spectrum was large, then, whenever $\phi_o''(t)$, the second time derivative, was large. This became especially important around sharp discontinuities in the spectrum where the tendency was to round-off peaks and valleys, and at the high energy end of the Maxwellian-type distributions where the spectrum was changing rapidly.

In order to apply the resolution correction factor in equation 78 to the measured time spectrum, one must be able to calculate $\phi_o''(t)$ and, therefore, an analytic form for $\phi_o(t)$ was necessary for differentiation. A similar relation to 73 can be developed for the resolution correction in terms of $\phi(t)$, the measured time spectrum (with the resolution error included), rather than in terms of $\phi_o(t)$, the analytical time spectrum (without the resolution error), although this option has been discounted here since the statistical and other fluctuations in the data would likely have introduced large errors in the necessary numerical differentiation to produce $\phi''(t)$. Due to the state of the theory, the only energy region where one could reasonably assume some analytic form for $\phi_o(t)$ was at high energies, above about 0.1 eV, where the leakage induced spectral dis-

tortions due to Bragg scattering effects were smallest, and where the spectrum was well approximated by a Maxwellian distribution.

The spectrum recorded in the time-of-flight analyzer was distorted by

1. the chopper transmission, TRANS,
2. the detector efficiency, DTEFF,

and 3. scattering and absorption losses in the flight path, SCATT, so that

$$\phi_o(E) = M(E) \cdot TRANS(E) \cdot DTEFF(E) \cdot SCATT(E) \qquad (79)$$

in the high energy range. Table 1 expresses the relative importance of each of these correction factors throughout the energy range from 0.08 to 0.35 eV.

Table 1. Relative Importance of the Chopper Transmission, Detector Efficiency, and Flight Path Scattering Correction Factors in the High Energy Range

E(eV)	TRANS	DTEFF	SCATT
0.08	0.965	0.050	0.901
0.10	0.972	0.045	0.904
0.20	0.986	0.032	0.911
0.29	0.990	0.027	0.914
0.35	0.992	0.024	0.915

It is obvious from Table 1 that only the detector efficiency varies significantly in this energy interval. Thus, equation 79 becomes

$$\phi_o(E) = M(E) \cdot DTEFF(E) \; . \qquad (80)$$

The Maxwellian flux distribution, M(E), is given by

$$\frac{M(E)}{M} = \frac{E}{E_o} \cdot e^{-E/E_o} \cdot \frac{dE}{E_o} \tag{81}$$

where the "o" subscript here refers to the peak energy in the Maxwellian distribution, $E_o = kT_o$.

To transfer equation 81 from energy to time space, one writes

$$M(t)dt = M(E)dE \tag{82}$$

and since

$$dE/dt \approx 1/t^3 , \tag{83}$$

where t is understood to indicate the flight time then, from equation 81,

$$M(t) \approx \frac{t_o^4}{t^5} e^{-t_o^2/t^2} . \tag{84}$$

The detector efficiency in a BF_3 proportional counter in this energy range goes like 1/v so that

$$DTEFF(t) \approx t . \tag{85}$$

Substituting equations 84 and 85 into equation 80,

$$\phi_o(t) = \frac{t_o^4}{t^4} \cdot e^{-t_o^2/t^2} . \tag{86}$$

Defining $\alpha \equiv t_o^2/t^2$, and differentiating equation 86 twice with respect to time,

$$\partial^2\phi_o/\partial t^2 = \frac{4}{t_o^2} \cdot e^{-\alpha} \cdot [5\alpha^3 - 5\tfrac{1}{2}\alpha^4 + \alpha^5] \tag{87}$$

and ϕ_o''/ϕ_o becomes

$$\frac{\phi_o''(t)}{\phi_o(t)} = \frac{4}{t_o^2} \cdot \left[5\left(\frac{t_o}{t}\right)^2 - \frac{11}{2}\left(\frac{t_o}{t}\right)^4 + \left(\frac{t_o}{t}\right)^6\right] . \tag{88}$$

The resolution correction factor from equation 78 is then

$$\frac{\phi(t)}{\phi_o(t)} = 1 + \left[\frac{2}{t_o^2} \cdot \left\{5\left(\frac{t_o}{t}\right)^2 - \frac{11}{2}\left(\frac{t_o}{t}\right)^4 + \left(\frac{t_o}{t}\right)^6\right\}\right. \tag{89}$$

$$\left. \cdot \left(\frac{\delta t_{burst}^2}{6} + \frac{\delta t_{det}^2}{3} + \frac{\delta t_{chan}^2}{3}\right)\right] \equiv 1/\text{RESOLTN}$$

where

$$\delta t_{burst} = s/2\omega R = 0.0197/\omega,$$

$$\delta t_{det} = \text{detector diameter}/v(\text{m/sec}),$$

and $$\delta t_{chan} = 16\ \mu\text{sec}.$$

The resolution correction factor, 1/RESOLTN, typically ranges from 1.00 (zero percent correction) at 0.1 eV to roughly 1.12 (12 percent correction) at 0.2 eV.

There is, of course, a resolution error in energy regions other than $E > 0.1$ eV which one cannot estimate quantitatively because of the lack of an analytic form for $\phi_o(E)$. However, this resolution error was only important within a few channels of sharp discontinuities in the measured spectrum, such as around the low energy beryllium Bragg peak, and, as such, the resultant spectrum shape within a few channels on either

side of the Bragg cut-off is suspect.

Miscellaneous Calibrations

In addition to those major instrumental spectrum distortions discussed in the previous sections of this chapter, which sometimes required elaborate correction schemes, there were also a number of other experimental forces at play which one had to either eliminate or otherwise convince one's self that they were of negligible importance to the measured spectrum shapes. The technique employed here was one of parametric calibration and testing for isolated effects.

In the following pages the principal experimental factors which might be expected to be troublesome, either because they might be difficult to remove by analytic corrections, or because they could cause the experimental situation to deviate unnecessarily from that which a theoretical treatment could easily model, will be discussed. The order in which the material is covered is entirely arbitrary and is not meant to convey any artificial sense of importance weighting.

Effect of Changes in the Source Neutron Characteristics

In the day-to-day operation of the GTRR there were a variety of dynamic changes taking place within the reactor core; among these were non-uniform fuel burnup and related reactor power peaking effects, fuel element and experiment shuffling in the core, and xenon poison peaking, which might conceivably have altered the source spectrum structure, and hence the background to a smaller extent, sufficiently to be detectable in the beryllium spectrum measurements. A maximum source change was simulated experimentally by tilting the neutron flux first away from and

then toward the thermal column by fully banking the reactor control blades in or out of one side of the core.

The normalized ratio of the beryllium spectra measured with the flux tilted away from and then toward the thermal column is plotted in Figure 35 to emphasize any differences between the two. A six percent overall change in the spectrum intensity was noted, but the behavior of the ratio of the spectra suggests that the important spectrum shape was not affected noticeably by these changes, as was expected.

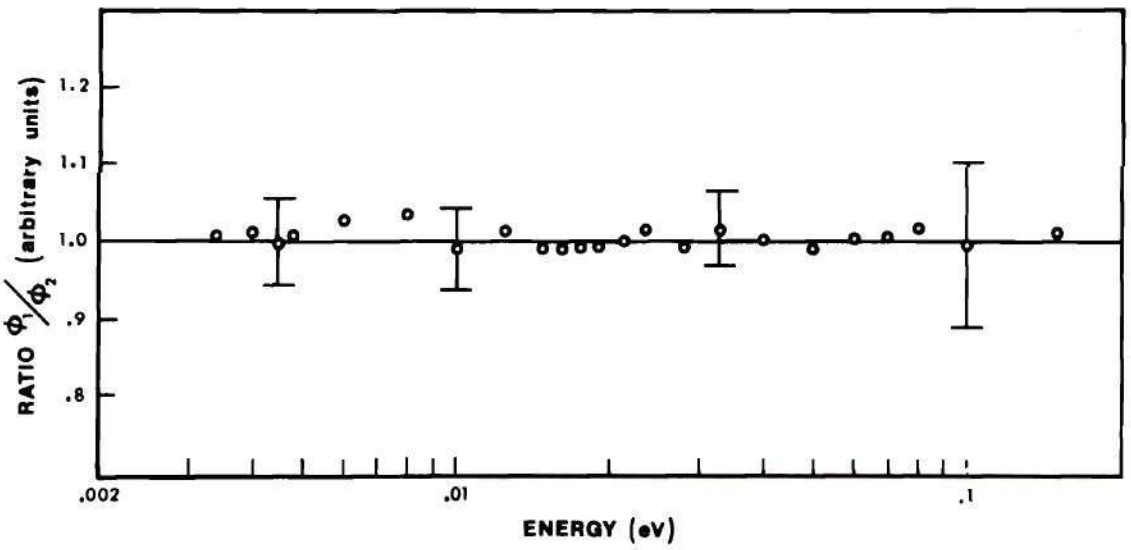

Figure 35. Ratio of Beryllium Spectra Measured in Identical Assemblies but with the Source Neutron Flux Tilted Successively Away from and then Toward the Thermal Column. (The ratio has been normalized to 1.0 to remove the effect of intensity changes in the spectra.)

Effects of the Surface Condition and Arrangement of the Constituents of the Beryllium Assembly

Each assembly was made up of a stack of small beryllium blocks, usually 5 x 5 x 10 cm, but including an assortment of sizes from 2 x 5 x 5

cm to 2.5 x 7.5 x 30 cm and 5 x 7.5 x 15 cm. The blocks ranged in surface condition from fairly clean for the 5 x 5 x 10 cm size to being coated with small amounts of a dye-like substance for some of the 5 x 7.5 x 15 cm size. All the blocks were thoroughly alcohol wiped prior to installation in the thermal column to remove any traces of loose dust and grease or oils from the surfaces.

An experiment was performed to determine the effect on the energy spectrum of the condition of the blocks from which the beryllium assembly was constructed. A representative energy spectrum was measured twice under identical experimental conditions except that the assembly was first loaded with all 5 x 5 x 10 cm "clean" blocks stacked with their long sides parallel to the neutron beam direction, and then the experiment was repeated with the assembly loaded with primarily 5 x 7.5 x 15 cm "dirty" blocks stacked with their long sides perpendicular to the neutron beam direction. In this manner a number of possible effects could be tested for. For example, one could see if the measured spectra were sensitive to the surface impurities on the blocks. Also, since each of the blocks was covered with a thin oxide layer, the assembly containing a large number of small blocks should have a larger atom fraction of beryllium oxide than the assembly containing only a few larger blocks. By stacking one assembly with the long direction of the blocks parallel to the beam direction, and the other assembly with the long direction of the blocks perpendicular to the beam direction, one could look for effects of preferential polycrystal orientation in the bulk material. This same physical arrangement allowed us to test the assumption that the measured spectra

were not sensitive to neutron streaming between the small beryllium blocks, whether it be preferentially out the sides of the assembly or directly from the source plane to the beam extraction point.

The normalized ratio of the spectra in these two assemblies is plotted in Figure 36 to emphasize any differences between the two.

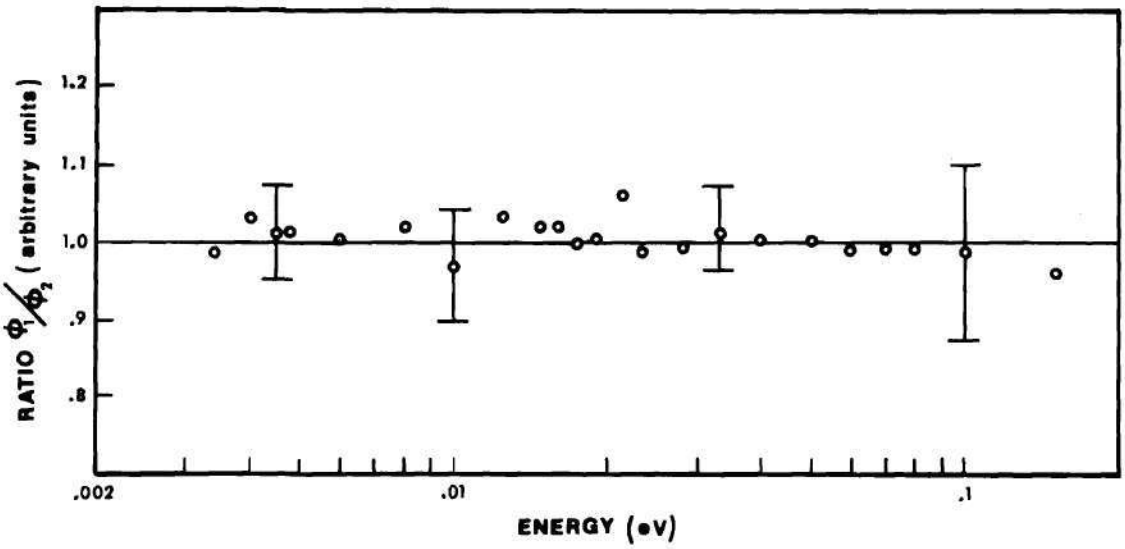

Figure 36. Ratio of Measured Beryllium Spectra in Assemblies Made Up of Small, Clean Blocks Stacked Longitudinal to the Assembly Axis, and Large, "Dirty" Blocks Stacked Perpendicular to the Assembly Axis

The points appear to scatter statistically around 1.0 indicating that the two spectra are the same. Discounting the unlikely possibility of exact cancellation of opposing spectrum distortions, one therefore seems justified in neglecting the effects of surface impurities on the blocks, "dissolved" oxide fraction, preferential polycrystalline orientation, and angle dependent streaming between blocks.

Effect of Beryllium Temperature

With reference to the beryllium cross section in Figure 2, it is apparent that the value of the inelastic scattering cross section below the Bragg cut-off at 0.005 eV depends strongly on temperature, varying something like 0.5 percent per °K. One might, therefore, reasonably expect the measured beryllium spectrum, particularly the relative height of the low energy Bragg peak, to be sensitive to temperature in a similar (qualitative) manner.

The ambient room temperature in the air conditioned reactor containment building remained relatively constant around 72°F, even with seasonal changes. The primary source of temperature changes in the beryllium assembly, from day-to-day or during some of the longer spectrum measurement runs, was heating from the reactor core itself. The temperature in the graphite thermal column increased in a roughly linear fashion during the course of the day as a function of elapsed full power operating time. Since the beryllium assembly was installed in the thermal column early in the morning, before reactor start-up, and the spectrum measurements were generally not begun until the chopper rotor speed had a chance to stabilize, perhaps three to four hours later, the assembly was warmed perceptibly over the room temperature when the spectrum measurements were made.

The following experiment was devised to measure the beryllium temperature at representative positions in a typical assembly as a function of elapsed time after reactor start-up. Five iron-constantan wire thermocouples were attached to beryllium blocks with a small patch of masking

tape in the relative positions indicated in the inset to Figure 37. Thermal contact between the wires and the beryllium blocks was assured with a small drop of Dow Corning Silicone vacuum grease. The thermocouple wires were brought out through the reactor biological shielding to where they were connected to a Thermo Electric brand portable pyrometer indicator. The sensitivity of the temperature measurement was $\pm$ 0.5°F. The temperature inside the beryllium assembly was monitored at one half to one hour intervals throughout the reactor operating day, and the results plotted as a function of elapsed time after reactor start-up in Figure 37. After an initial fast warmup, the temperature at any point in the assembly appeared to increase linearly with time, roughly 1°F per hour. The only obvious space temperature gradient was along the block in the longitudinal direction from the hotter source end. There were no apparent transverse gradients as indicated by the fact that positions two and five read nearly the same temperature at each point in time.

The important question, of course, is how this temperature change manifests itself in the measured neutron spectra. Another experiment was performed wherein the neutron leakage spectrum from the 35.6 x 35.6 x 50.8 cm beryllium assembly was measured, first in the "cold" block a few minutes after initial reactor startup. The same measurement was then repeated under identical experimental conditions at the end of the day when the assembly had heated roughly 10°F. The ratio of the "cold" and "hot" spectra is plotted in Figure 38 to emphasize any differences between the two. There is no clearly discernible trend in the ratio of the spectra which would suggest that the "cold" and "hot" spectra are any different.

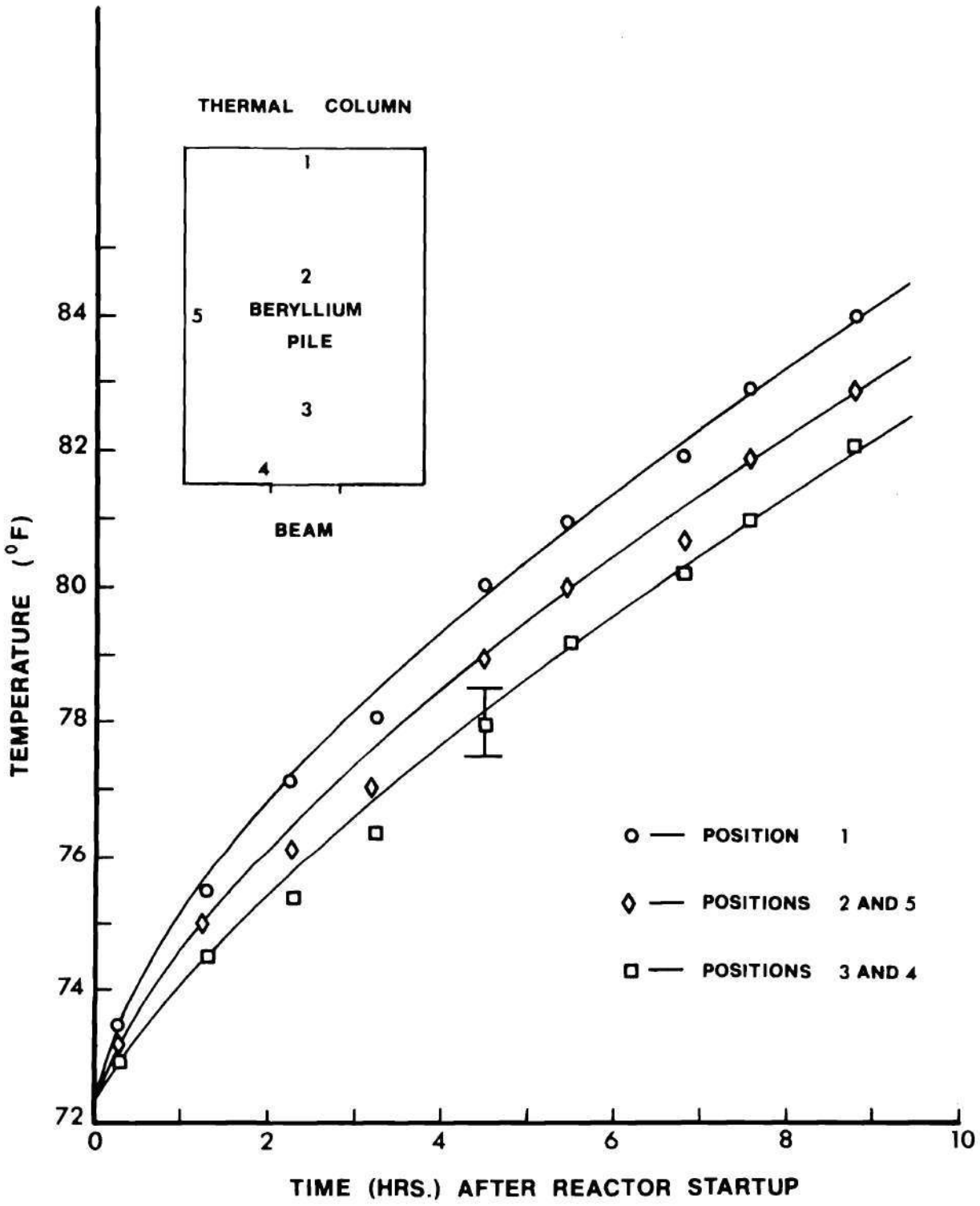

Figure 37. Measured Beryllium Temperature as a Function of Time After Reactor Start-up at Various Positions on the Midplane of the Assembly

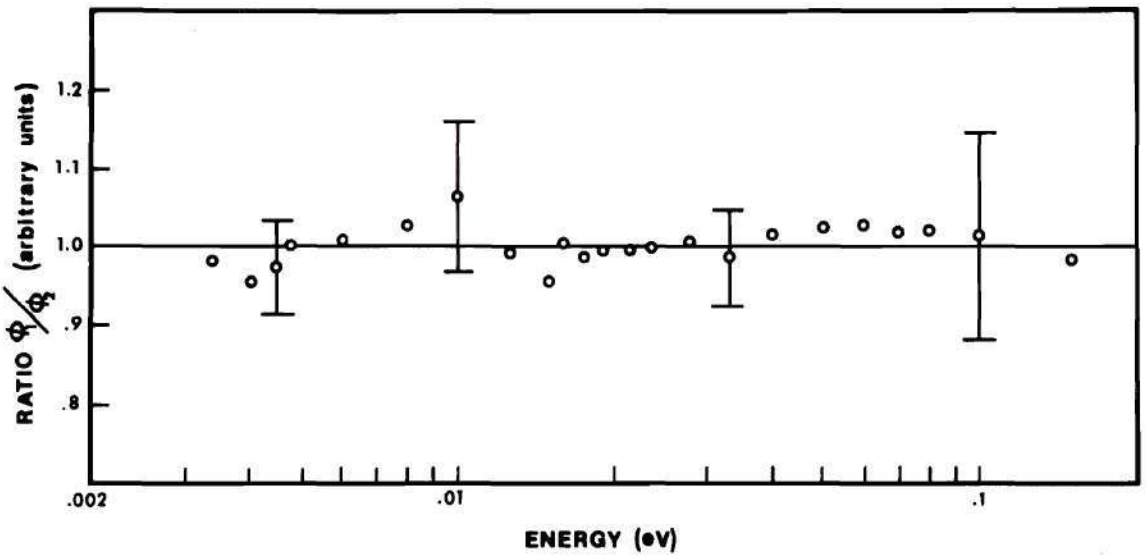

Figure 38. Ratio of Neutron Energy Spectra Measured in Identical Assemblies with Beryllium Temperatures of 72 and 82°F

Thus one is justified in neglecting spectrum changes as a result of temperature variations within a long spectrum measurement run or from day-to-day.

However, as a consequence of the overall temperature sensitivity of the low energy beryllium cross section and the coupling of this influence to the shape of the neutron energy spectrum, the beryllium temperature has been recorded for each spectrum measurement for future reference. The temperature was determined by noting the starting and finishing time for each measurement relative to the time when the reactor was started up, and then extrapolating the temperature from the appropriate curve in Figure 37. All the spectra were measured in beryllium assemblies ranging in temperature from 298 to 302°K.

Effect of the Size of the Reentrant Channel

Measurement of the neutron energy spectrum at an interior position in the beryllium assembly by the time-of-flight method required that a representative neutron beam be extracted from that position. The beam extraction was accomplished using a small reentrant channel which reached from the front face back into the assembly to the point of the measurement.

The presence of the reentrant channel can alter the neutron energy spectrum in the vicinity of the point of observation. Mechanisms having to do with things like the removal of moderator material to create the void, and energy and angular dependent streaming from one region to another down the voided channel have been variously proposed to explain the observed spectrum perturbations. However, in the limit of very small channels, a point should be reached where the neutrons no longer "notice" the presence of the channel and the spectrum should be unperturbed. As a rule of thumb, Beckurts and Wirtz[1] have assumed that the energy spectrum perturbation in the region around the voided channel is negligibly small as long as the dimensions of the channel are small compared to the mean free path of the neutrons in the spectrum. In some pulsed source experiments[71] in large graphite and water systems, the measured energy spectra were observed to change imperceptibly while the diameter of the beam extraction channel was increased to about five cm (two inches). The spectrum distortions from the effects of the size of the reentrant channel do, however, increase when flux gradients are present. There appear to be no similar experimental guidelines for small steady-state beryllium assemblies with a longitudinal flux gradient. However, based on the relative

mean-free-paths for neutrons in graphite and beryllium, one might expect that a five cm reentrant channel would be acceptable in beryllium as well.

The criteria which determine the acceptable dimensions of a reentrant channel are that they should be large enough so that the intensity of the extracted neutron beam will give an appropriate counting rate at the detector, and yet they should be small enough so that the perturbation caused by the void does not significantly affect the shape of the measured spectrum. The following experiment was designed to find the largest reentrant channel that did not alter the measured neutron spectrum perceptibly in a typical steady-state beryllium assembly with a longitudinal gradient. Since the spectrum perturbation in the pulsed case has been found[72] to be strongest for shallow reentrant holes in the region of strong surface leakage gradients, the test measurements were all performed on the shallowest channel depth that was expected to be encountered in the subsequent spectrum determinations, that depth being 10 cm, where the spatial decay as well as leakage gradients were important. Spectra were measured in the 35.6 x 35.6 x 50.8 cm assembly under identical experimental conditions with reentrant channel dimensions of 2.5 x 5 x 10 cm, 5 x 5 x 10 cm, and 5 x 7.5 x 10 cm, respectively. In Figures 39 and 40 are plotted the ratios of the spectra measured with the (2.5 x 5)/(5 x 5) and (5 x 7.5)/(5 x 5) cm channels. Examination of Figure 40 reveals that the spectrum perturbations had just begun to manifest themselves above the error limits in the measurement with the 5 x 7.5 x 10 cm reentrant channel. However, there was no such apparent difference, suggested by the ratio in Figure 39, between the spectrum measured with the 5 x 5 x 10 cm channel and that measured with the lower intensity 2.5 x 5 x 10 cm

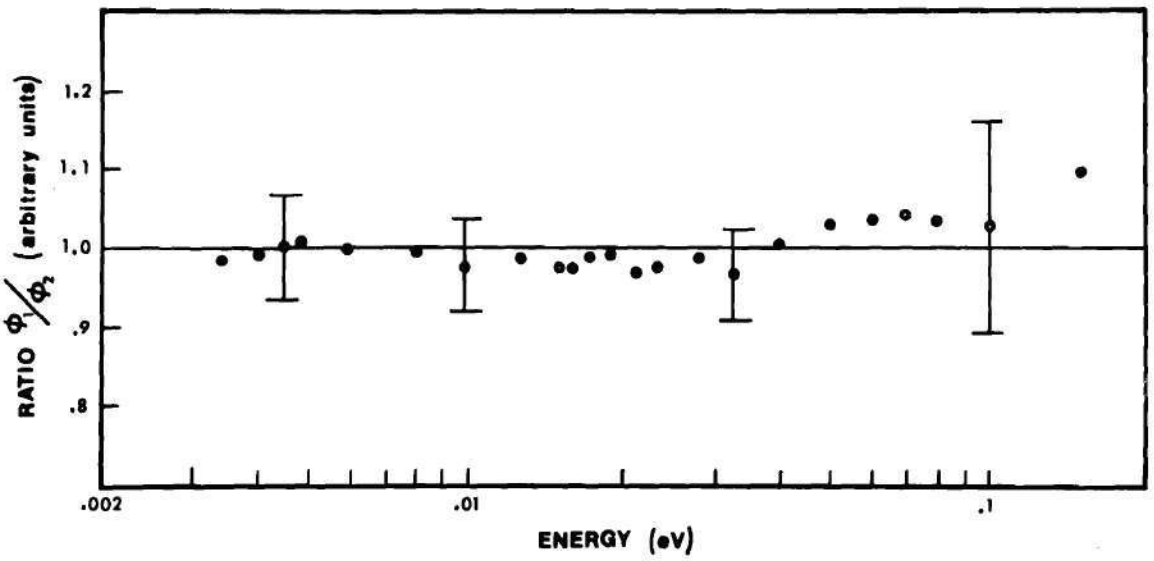

Figure 39. Ratio of Beryllium Interior Spectra Measured in Identical Assemblies with Reentrant Channel Dimensions of 2.5 X 5 X 10 and 5 X 5 X 10 cm

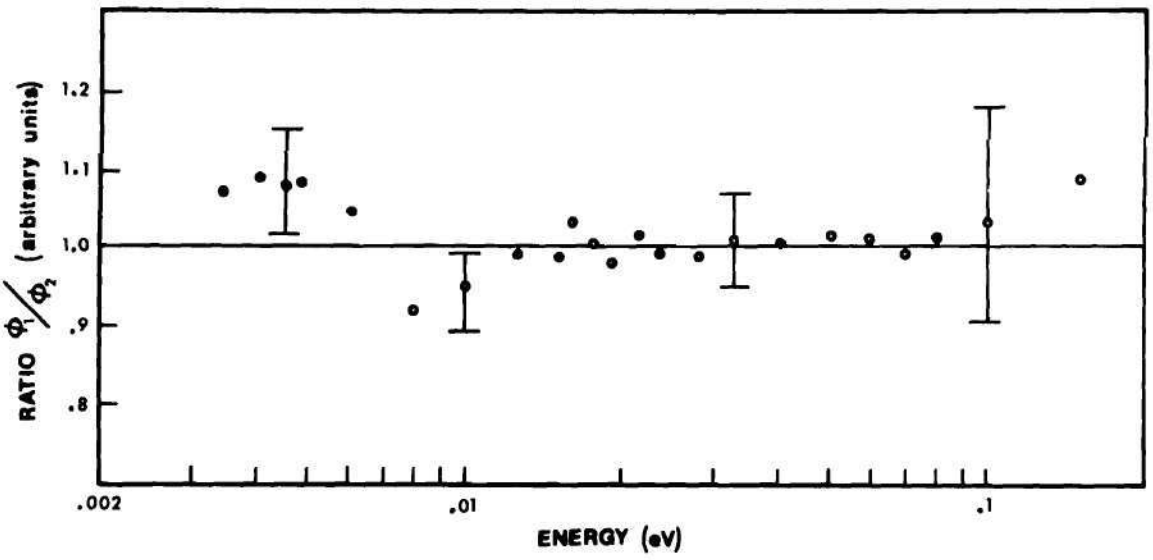

Figure 40. Ratio of Beryllium Interior Spectra Measured in Identical Assemblies with Reentrant Channel Dimensions of 5 X 7.5 X 10 and 5 X 5 X 10 cm

channel. The reentrant channel dimensions of choice then were the 5 x 5 cm ones.

Beam collimation in the reentrant channel spectrum measurements was more critical than in the leakage spectrum measurements since it was necessary to guarantee that only the neutrons originating at the base of the reentrant channel in the assembly reached the detector. It was especially important that neutrons from along the sides of the reentrant channel be shielded out of the beam due to the strong spatial dependence of the flux along the axis of the assembly. This shielding was accomplished by the addition of a 3.8 x 3.8 cm cadmium blade-type collimator attached directly to the front face of the assembly to cut off any neutrons from the channel sides or from the front leakage face of the assembly which might have emerged in a solid angle directed toward the detector. An additional 5 x 5 cm cadmium collimator was attached to the front side of the chopper and all but the center 20 cm of the detector was shielded with cadmium covered, B_2O_3/paraffin blocks to assure tight collimation on the neutron beam. The arrangement was examined visually with a precision surveyor's telescope from the end of the flight path and found to be very conservative, that is to say, there was no place within the collimation "cone" where one could get a line of sight at the reentrant channel sides. Additionally, a spectrum measurement was made with a cadmium square at the base of the deepest reentrant channel (30 cm) where the collimation was most critical, resulting in a "thermal background" distribution similar to that discussed in connection with the background spectrum in Figure 16. That there was no apparent spectrum structure in the low energy region

is evidence that the collimation was successful in shielding out the neutrons coming from the reentrant channel sides.

Effect of "Z" Direction Infinity

Some theoretical models of the diffusion length problem assume the moderator pile to be infinite in the longitudinal, "Z", direction. Since the spectrum measurements reported herein were made in assemblies which never exceeded 51 cm in length, the question arises as to whether the neutron spectrum at a point in the interior of the assembly had any "knowledge" of how much beryllium was further "downstream." That is, was the shape of the interior neutron energy spectrum affected by the finite length of the assembly?

Two spectra were measured at the same distance (20 cm) from the source plane in beryllium assemblies with the same transverse dimensions (35.6 x 35.6 cm), but different overall lengths (30.5 and 50.8 cm, respectively). Thus, the first assembly had only 10 cm of beryllium on the "downstream" side, whereas the second had 30 cm. If, in fact, the neutron energy spectrum was unaffected by the finite length of the assemblies, then these two measured spectra should be identical.

In Figure 41 the ratio of these measured spectra is plotted to emphasize any differences between the two. The spectra appear to be very nearly identical except for a small, roughly five percent, difference in the extreme low energy range below the Bragg cut-off. This difference can be attributed to the onset of surface leakage effects in the short assembly in the sub-Bragg energy range where the neutron mean-free-path is of the order of 17-18 cm. In terms of the behavior of the energy

spectrum then, the assumption of an infinitely long assembly appears to be reasonable except at small distances, somewhat less than 10 cm from the front face, where energy dependent surface leakage effects can become important. This five percent surface leakage distortion was expected to be present in all the spectra measured with the 10.2 cm deep reentrant channel.

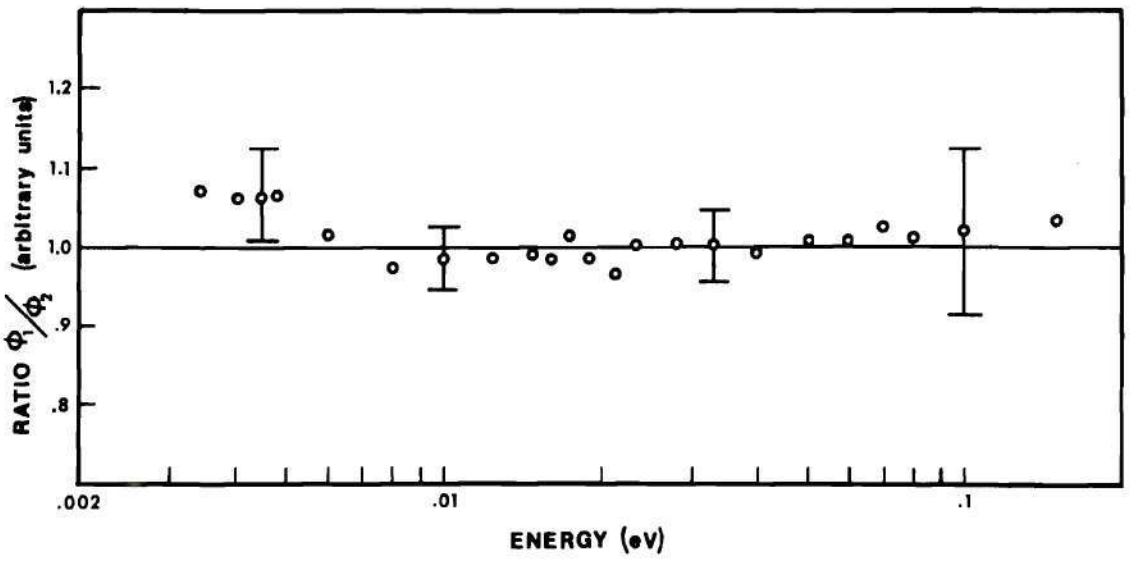

Figure 41. Ratio of Beryllium Interior Spectra Measured at 20.3 cm from the Neutron Source Plane in 35.6 x 35.6 cm Assemblies, 30.5 and 50.8 cm in Length

Effect of High Energy Gamma Rays

The low threshold energy, 1.66 MeV, for the photoneutron (γ,n) reaction in beryllium could create a problem with a ubiquitous fast neutron background in large assemblies exposed to a hard gamma ray source. It has been estimated[73] that the overall power yield per unit of fuel in a beryllium reflected reactor could be increased by as much as seven to ten percent as a result of this photoneutron flux. A primary source of

hard gamma rays in these experiments was the reactor core itself. However, our calculations have indicated that these gamma rays should have been sufficiently degraded by the time they reached the beryllium assembly, having traversed at least two feet of heavy water and three feet of graphite, such as to produce a photoneutron flux which was very much smaller than the neutron flux from other sources in the assembly. If the photoneutron flux were significant, it would have shown up as so in the background measurement in Figure 16, which it did not.

The sensitivity of beryllium to high energy gamma rays was the primary reason that BORAL was chosen as the neutron absorbing structural material for the assembly, rather than cadmium. Boron-10, of course, absorbs neutrons by the (n,α) reaction whereas cadmium absorbs thermal neutrons by the (n,γ) reaction with a substantial fraction of the emerging gamma rays lying in the 3-5 MeV range[62] and the highest gamma ray energy approaching nine MeV. Consequently, every effort was made to keep cadmium shielding away from areas of high neutron fluence to hold the hard gamma ray flux around the beryllium pile to a minimum. However, it became necessary to install a cadmium collar around the beam extraction point on the front face of the smaller beryllium assemblies to prevent the aforementioned door-scattered background neutrons from entering the beam. In order to determine if the presence of the large cadmium collar, even though it was located in a region of relatively low neutron fluence, had an effect on the shape of the measured beryllium spectrum (by way of photoneutron contamination), the neutron energy spectrum from a typical beryllium assembly was measured, first with the cadmium collar in place,

and then the measurement was repeated under identical experimental conditions except that the cadmium collar was replaced with a BORAL one. The BORAL collar still absorbed the door scattered background neutrons, but it did so without producing the hard gamma rays.

The results of this experiment are plotted in Figure 42 as the ratio of the spectra with and without the cadmium collar.

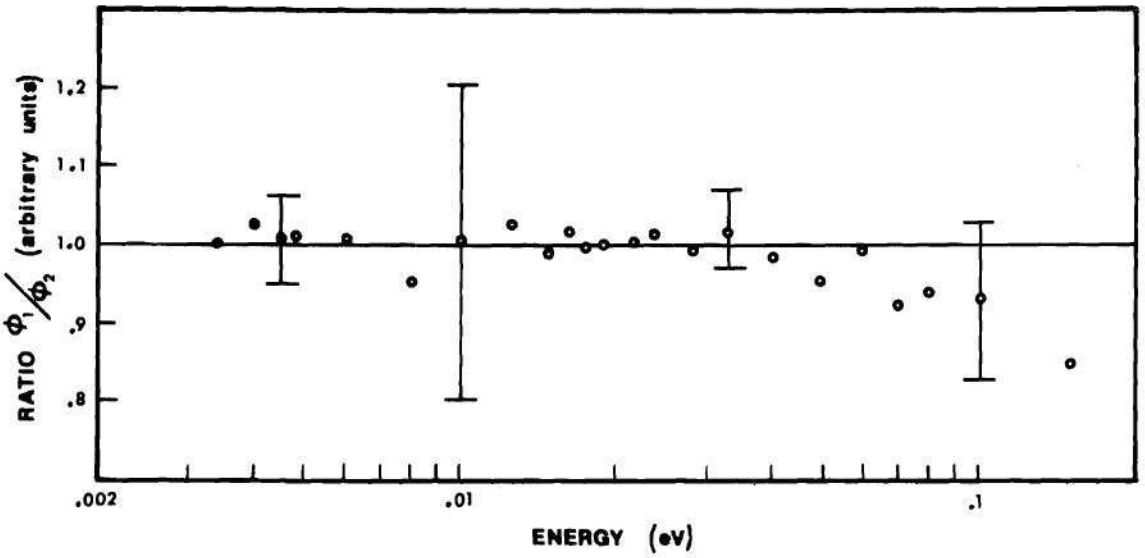

Figure 42. Ratio of Identical Beryllium Leakage Spectra Measured with Cadmium and BORAL Beam Shielding Collars, Respectively

The only apparent trend is for the ratio to fall off slightly at high energies and even this is not significant in light of the limits indicated. In addition, a fall-off in the ratio of spectra in the high energy range would be indicative of less high energy neutrons with the cadmium collar than with the BORAL one which is just the opposite effect to what one would expect to observe if there was a significant high energy photoneutron background. Thus one concludes that the addition of the cadmium collar to the front face of the assembly for background surpression does

not detectably alter the shape of the measured spectrum by contamination with beryllium photoneutrons.

Effect of Neutron Scattering from Materials Around the Beam

In the normal course of one of the spectrum test measurements, one of the 2 x 4 inch thermal column shutter doors became lodged in the closed position, blocking out roughly half of the neutron beam. The effect of the presence of this large lead door in the neutron beam was not only to reduce the neutron intensity, but in addition the remaining beam which passed through was enriched nearly 15 percent in low energy neutrons. This enrichment may have been the result of Bragg scattering effects in those neutrons transmitted through the steel-jacketed, lead doors. The discovery that this effect distorted the neutron energy spectrum shape raised the question of whether or not the beam collimation was tight enough at all times to prevent this scattering from taking place in the periphery of the beam, even though the shutter doors were ostensibly pulled back into their "full open" positions. To resolve this question, a typical beryllium leakage spectrum was measured first with the full beam, and then the measurement was repeated under identical experimental conditions except that the beam was collimated down to a narrow vertical slit to eliminate any neutrons which might have been scattered from materials around the outer edges of the beam. The resulting spectra in both cases were the same, indicating that neutron scattering from shielding and structural materials around the beam was not a problem when the shutter doors were fully opened.

Final Form of the Spectrum

The final form of the neutron energy spectrum, unfolded from the measured time distribution and corrected for the major instrumental distortions discussed in the preceding paragraphs, is given by

$$\phi(E) = \frac{\frac{\phi(t)}{\text{LIVETIM}} - \text{BKGND}}{v^3 \cdot \text{TRANS} \cdot \text{SCATT} \cdot \text{DTEFF} \cdot \text{RESOLTN}} \qquad (90)$$

where

$\phi(t)$ is the measured time distribution,

LIVETIM is the detector/analyzer dead time correction,

BKGND is the neutron background counting rate,

v is the neutron velocity,

TRANS is the chopper rotor relative transmission correction,

SCATT is the air and aluminum scattering and absorption loss correction,

DTEFF is the BF_3 detector efficiency correction,

and RESOLTN is the high energy instrumental resolution correction.

The correction factors were calculated for each of the roughly 250 points in a measured time spectrum on a PDP-8/I digital computer according to the schemes outlined earlier in this chapter. The resulting differential energy distribution from equation 90 represents the angular, energy dependent neutron flux in the energy range from 0.003 to 0.2 eV at some location in the beryllium assembly.

Whereas the differential time interval widths were the same over the range of channels, the differential energy intervals behaved like $E^{3/2}$. As a result of the higher density of energy intervals in the low

energy end of the spectrum, a significant improvement in statistical accuracy was realized by averaging two or more channels in the low energy range while still retaining more than ample spectrum detail. The final spectrum distributions, output from the analysis program, and listed in Appendix G, gave single-channel results down to 0.045 eV, double-channel averages from 0.045 to 0.015 eV, and triple-channel averages from 0.015 down to 0.003 eV. The averaging was performed on the final, corrected, energy dependent flux values so that this step would not deteriorate the low energy resolution by increasing the effective time channel widths.

Because of slight variations in flight paths and chopper speeds from measurement to measurement, the final spectrum data points emerged from the unfolding and averaging program at a rather arbitrary set of energy points, thus making it difficult to carry out certain quantitative spectrum comparisons for which it would have been convenient to have all the flux values in terms of the same energy grid. This was especially important in the calibrations discussed earlier where pairs of spectra were compared and examined for differences by taking the ratio of one spectrum divided by the other.

Consequently, a standard grid structure was devised, based on the statistically significant spectrum detail to be retained, at which points the flux values for each measured spectrum were extrapolated from the surrounding data to facilitate subsequent comparisons. This grid structure, shown in Figure 43 overlayed on a typical beryllium leakage spectrum, consisted of 23 energy points, 17 of which were located in smoothly varying regions of the spectrum and the six remaining points located at sharp peaks and valleys.

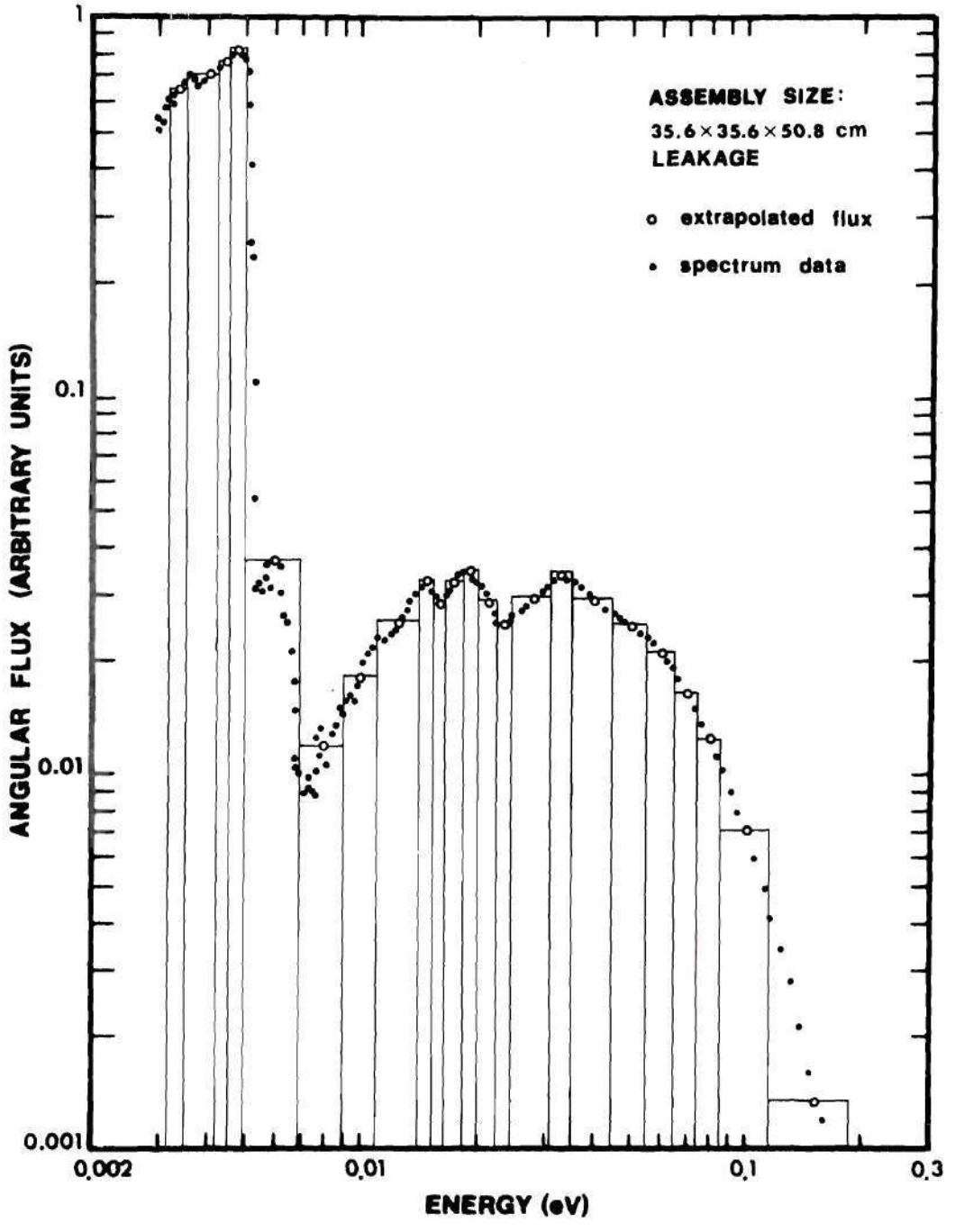

Figure 43. Typical Measured Beryllium Neutron Energy Spectrum Showing the Extrapolated Flux Values and the Associated Histogram Grid Structure

The flux values in the smoothly varying regions of the spectrum were obtained from the measured energy distribution by a simple linear extrapolation between the average of the first two data points on the high energy side and the average of the first three data points on the low energy side of the grid point (in order to maintain approximately equal energy intervals on each side). Figure 44 shows the details of the flux extrapolation at the 0.028 eV grid point on the same beryllium leakage spectrum pictured in Figure 43.

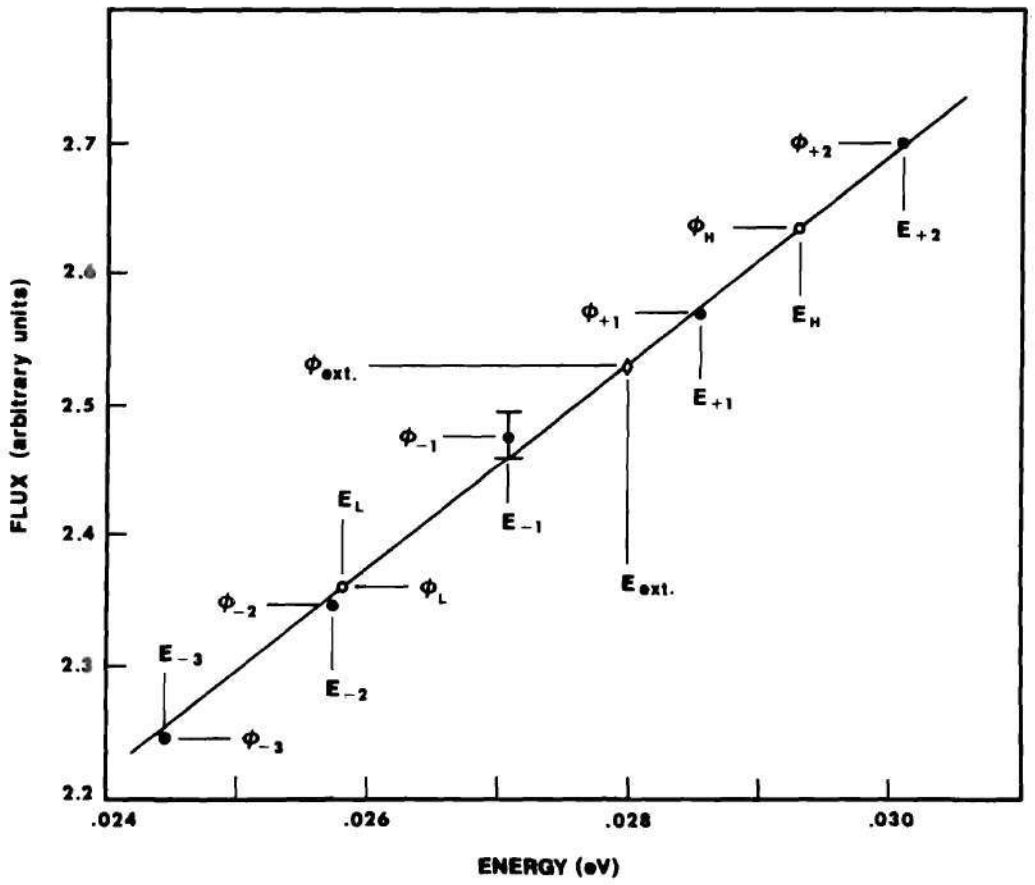

Figure 44. Details of a Typical Linear Flux Extrapolation

The extrapolated flux is given by

$$\phi_{ext} = \frac{\phi_L - \phi_H}{E_H - E_L} (E_H - E_{ext}) + \phi_H \ , \tag{91}$$

where the subscripts L and H refer to the averages on the low and high energy sides of the grid point, respectively. For example,

$$\phi_L = \frac{\phi_{-1} + \phi_{-2} + \phi_{-3}}{3} \ , \tag{92}$$

with similar equations for the extrapolated energies. Performing the extrapolation between averages, rather than just between the raw data points themselves, on either side of a grid point improved the accuracy of the resulting extrapolated flux values by lessening the effects of statistical and other fluctuations in the data. The simple linear extrapolation proved to be more than adequate since the energy intervals over which one had to extrapolate were generally quite narrow. The six peak and valley points were picked off of the raw spectrum by eye.

Calculation of the Average Energy

A single parameter which describes the shape behavior of the neutron energy spectrum is the flux-averaged energy, $\bar{E}_\phi$, given by

$$\bar{E}_\phi = \frac{\int_0^\infty E \cdot \phi(E) dE}{\int_0^\infty \phi(E) \cdot dE} \ . \tag{93}$$

For example, for a Maxwellian distribution, $\bar{E}_m$ is 2kT.

Employing a numerical (histogram) integration technique, equation 93 becomes

$$\bar{E}_{\phi} = \frac{\sum_{i=1}^{23} [E_i \phi_i(E)\ \Delta E_i]}{\sum_{i=1}^{23} [\phi_i(E)\ \Delta E_i]} \qquad (94)$$

where

E_i and ΔE_i constitute the aforementioned 23 group energy grid structure in Figure 43,

and $\phi_i(E)$ are the extrapolated flux values.

Equation 94 covered the measured spectra in the energy range from 0.0032 to 0.185 eV. In addition, one had to estimate the contribution of the energy ranges 0.185 eV to infinity and 0 to 0.0032 eV to the final value of $\bar{E}_{\phi}$.

Estimation of $\phi(E)$ in the Energy Range 0.185 eV to Infinity

Since the beryllium cross section in Figure 2 is essentially flat above 0.1 eV, the flux is expected to behave like a (slightly shifted) Maxwellian. Therefore, $\phi(E)$ above 0.185 eV was calculated from a Maxwellian distribution, normalized to the extrapolated flux value at the last grid point at 0.15 eV. As it turns out, very little of this energy range was important to the calculation of $\bar{E}_{\phi}$ since the flux fell off nearly four orders of magnitude between 0.2 and 0.5 eV. Inclusion of the entire energy range above 0.185 eV typically increased $\bar{E}_{\phi}$ less than two percent, and only 2.5 percent in the worst case.

Estimation of $\phi(E)$ in the Energy Range 0 to 0.0032 eV

In view of the fact that the beryllium cross section below the Bragg cut-off is relatively flat over a short energy interval and then begins to rise slowly at lower energies, one expects the neutron energy spectrum in this range to roughly resemble the low energy portion of a Maxwellian distribution, that is, a straight line, and then to fall off progressively faster at lower energies. Table 2 illustrates the relative rate of flux fall-off below the Bragg cut-off from E_{Bragg} to $(E_{Bragg})/2$ for:

1) a Maxwellian distribution,

2) a theoretical calculation by Williams[22] for the (asymptotic) angular flux spectrum in the positive "Z" direction with leakage induced distortions ($B^2 = 0.001$), from Figure 4, and

3) a diffusion theory calculation by Kothari et al.[24] for the total "asymptotic" flux spectrum in a 30 x 30 cm beryllium assembly.

Table 2. Relative Rate of Flux Fall-Off with Decreasing Energy Predicted by: 1) a Maxwellian Distribution, 2) a Williams[22] Transport Theory Calculation, and 3) a Kothari[24] Diffusion Theory Calculation

E	M(E)	$\phi(E)_{Williams}$	$\phi(E)_{Kothari}$
E_{Bragg}	6.0	4.5	23.0
$(E_{Bragg})/2$	3.3	1.5	5.5
% Drop	45%	70%	76%

Whereas both of the aforementioned theoretical treatments correctly predict a qualitative low energy flux fall-off which is faster than a Maxwellian, one must be cautious about using the numbers in Table 2 to predict

the quantitative effect in the measured spectra inasmuch as the magnitude of the fall-off is expected to be a function of the spectral distortion and none of the above treatments applies exactly to the physical situation in our measurements. In order to get an approximate idea of how fast the low energy flux actually fell off below the Bragg cut-off in the measured spectra, an experiment was carried out to measure the low energy leakage flux from a typical beryllium assembly, operating the chopper at slow speed (1800 RPM) where, although the high energy resolution was poor, the low energy transmission was greatly improved over that at 3900 RPM. The results of this experiment are presented in Figure 45 along with the room temperature Maxwellian behavior. The measured rate of flux fall-off in Figure 45 was not nearly so great as predicted by the Williams or Kothari numbers in Table 2. The flux dropped roughly 51 percent between E_{Bragg} and $(E_{Bragg})/2$ and lay only about 12 percent below the Maxwellian at $(E_{Bragg})/2$.

At lower energies, the deviation from the Maxwellian distribution in Figure 45 appears to be roughly linear so that the low energy flux was approximated by

$$\phi(E) = M(E) \cdot LDF \tag{95}$$

where

M(E) is the room temperature Maxwellian distribution, normalized to the extrapolated flux value at the 0.004 eV grid point,

and LDF is an arbitrary linear distortion factor which accounts for the fact that the measured flux falls off faster than the Maxwellian.

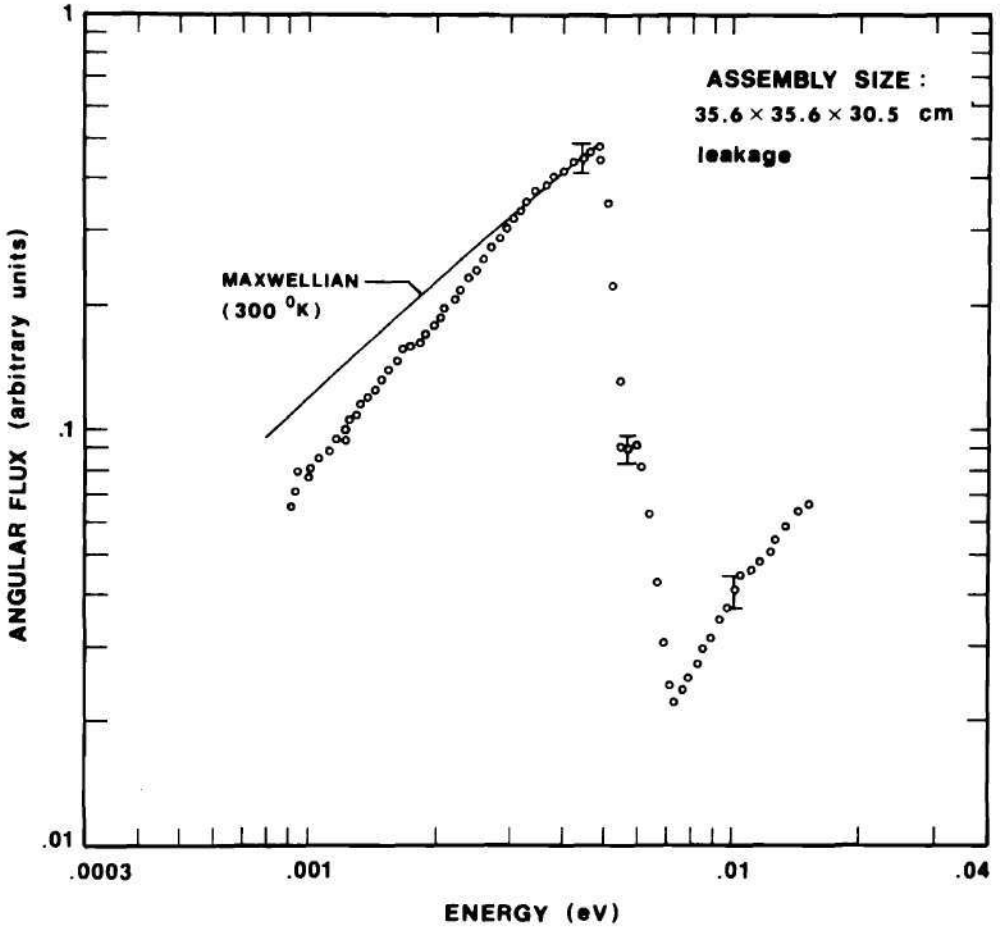

Figure 45. Measured[74] Low Energy Distorted Beryllium Spectrum Relative to the Shape Behavior of a Normalized Maxwellian Distribution

No particular physical significance is attached to the linear distortion factor at this time, but rather it is intended simply as an artificial fitting parameter which allows one to write an analytic expression, equation 95, for the low energy flux.

By fitting $\phi(E)$ in equation 95 to the flux data in Figure 45, one arrives at the following expression for the linear distortion factor.

$$LDF = 1 - 150(0.0032 - E) \ , \qquad (96)$$

so that equation 95 becomes

$$\phi(E) = M(E)\cdot[1 - 150(0.0032 - E)] \qquad (97)$$

in the extreme low energy range. Equation 97 describes only the behavior of the low energy angular flux spectrum in a particular (but relatively typical) assembly. In other assemblies where the spectral distortion was either greater or less than this, one expects the rate of low energy flux fall-off to also be, respectively, greater or less than that given by equation 97. However, equation 97 describes the best available approximation to the low energy flux behavior for all the measured spectra. The error limits, to be discussed in Appendix D, will be sufficient so as to account for individual variations from spectrum to spectrum.

Due to the strong flux peaking below the Bragg cut-off in the measured spectra, the inclusion of the extreme low energy range, below 0.0032 eV, typically lowered the calculated average energy nearly 15 percent, with a maximum effect of 25 percent in the most severely distorted spectrum. This was the primary reason that the average energy was calculated from the flux-weighted average, equation 93, rather than the neutron density-weighted average, $N(E) = \phi(E)/v$, which would have placed even more weight on the very low energy range where one was forced to estimate the spectrum shape. Thus, the average energy calculated with neutron density averaging would necessarily have contained even larger uncertainty limits as a result of this low energy shape estimation than was the case with flux averaging.

CHAPTER VI

RESULTS AND DISCUSSION

The Structure of the Beryllium Spectra

Figure 46 shows the shape of a typical spectrum of neutrons leaking from the front face of the 35.6 × 35.6 × 50.8 cm beryllium assembly in the (forward) positive "Z" direction. The dominant feature is the very pronounced peak below the Bragg cut-off energy at about 0.005 eV, which extends nearly two orders of magnitude above the relative level that one would expect if the distribution were equilibrium Maxwellian. The shoulder at 0.006 eV and the small peaks and valleys in the energy range between 0.01 and 0.1 eV conform to the higher order Bragg fluctuations in the beryllium cross section pictured in Figure 2. It is interesting to note that there is more detail apparent in the spectrum than is obvious in the cross section in this energy range.

The tendency for the spectrum to peak in regions where the cross section drops, and vice versa, can be explained as follows. The transverse neutron leakage rate in these small assemblies was high, due to the "close-in" proximity of the assembly boundaries. Inasmuch as the beryllium scattering cross section undergoes drastic fluctuations in the energy region around the Bragg cut-off, the transverse leakage losses and the consequent increase in the axial gradient lead to a proportionally larger increase in the net instreaming in the positive "Z" direction for neutrons below the Bragg cut-off, where the cross section is relatively much lower.

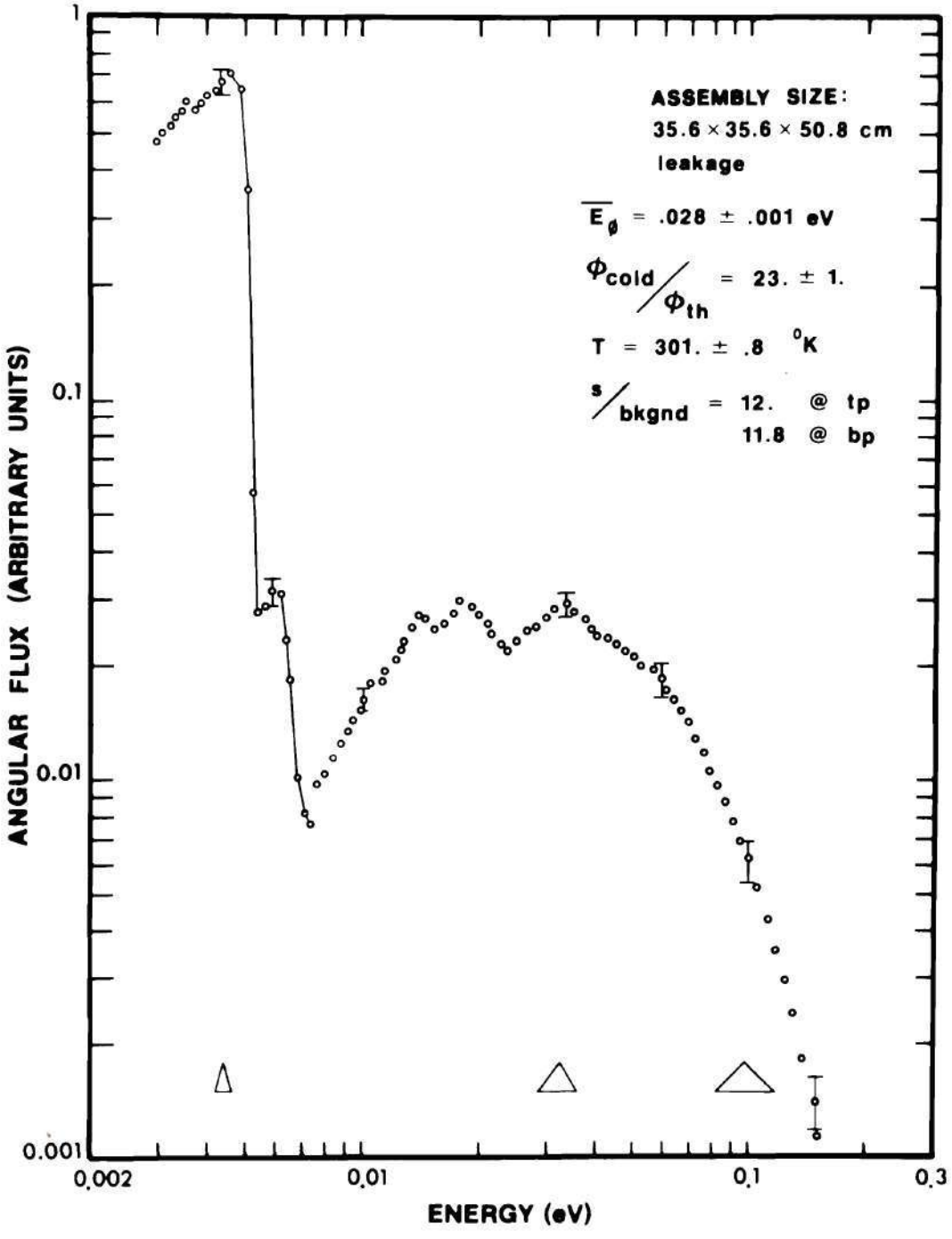

Figure 46. Typical Measured Energy Spectrum of Neutrons Leaking from the Center of the Front Face of a 35.6 X 35.6 X 50.8 cm Beryllium Assembly in the Positive "Z" Direction. (Normalization is arbitrary.)

Below the Bragg cut-off, this energy dependent instreaming overpowers the transverse leakage and absorption losses, causing a progressive buildup of low energy neutrons in the spectrum. In addition, in the positive "Z" direction, the spectrum one "sees" consists in part of neutrons streaming directly from the source plane, the distribution of which is depleted strongly of scattered neutrons in the higher energy range above the Bragg cut-off. Furthermore, one expects the angular flux in the direction of the spatial decay gradient to be enriched in neutrons with long mean-free-paths, independent of the origin of the gradient. The quantity of relative neutron depletion in the high energy range depends on two factors, the transverse leakage rate (determined by the assembly buckling) and the distance from the source plane.

The information in the upper right hand corner of Figure 46 identifies the spectrum in terms of the physical dimensions (transverse versus length) of the assembly in which it was measured and whether it was a leakage or interior spectrum. The interior spectra were measured with a 5 X 5 cm reentrant channel as described earlier, and are designated by

interior re X cm

where X is the reentrant channel depth measured from the front face of the assembly. The distance from the source plane to the point in the assembly where the interior spectrum measurement was made (that is, from which the beam was extracted), can be obtained by subtracting the reentrant channel depth, X, from the total block length. All the spectra

have been measured on the longitudinal axis of the assembly and represent the angular flux in the (forward) positive "Z" direction, except where otherwise noted. The remaining nomenclature represents:

$\bar{E}_{\phi}$ is the flux-weighted average energy calculated from the measured spectrum,

ϕ_{cold}/ϕ_{th} is the ratio of the flux intensity at 0.0045 eV, near the Bragg peak, to that at 0.033 eV, the peak in the "thermal" region of the spectrum,

T is the approximate beryllium temperature ($^{\circ}$K) at the point in the assembly where the neutron beam was extracted. The temperature was estimated from the mean-time after reactor start-up and from the temperature curves in Figure 37,

and s/bkgnd is the counting signal intensity to background ratio in the raw time spectrum data at the "thermal" and Bragg peaks respectively. The signal is defined as the spectrum minus background counts.

The error bars on the spectrum, at representative energies of

0.0045
0.0060
0.010
0.033
0.06
0.10
and 0.15 eV,

include the effects of uncertainties in the spectrum shape from, among other things, counting statistics, background determination, equipment alignment uncertainties and estimated errors in the energy resolution, timing parameters and spectrum correction factors. The complete details of the determination of the error limits are presented in Appendix D. It is sufficient to point out here that the error bars on each spectrum reflect a reasonable and well-founded estimate of the accuracy of the data. We have used the word accuracy here in contrast to precision or reproducibility since we have included systematic effects in the error estimate

which did not vary from measurement to measurement, like the system alignment, but which contributed to the absolute uncertainty in the spectrum shape determination. The error limits on the spectrum accuracy are larger, and thus even more conservative, than those on the spectrum reproducibility. This fact can be readily demonstrated by examining one of the figures in Chapter V where the ratio of two spectra is plotted, and where the indicated error limits appear to be larger than is seemingly dictated by the purely statistical scatter in the points.

The base width in the three resolution triangles at 0.0045, 0.033, and 0.1 eV represents the full-width-at-full-maximum in the calculated energy resolution, $\Delta E/E$. The energy resolution, which resulted from timing uncertainties in the chopper burst width, the neutron path length in the detector, and the width of the analysis channels, among other things, is calculated in detail for a typical spectrum in Appendix E.

The 15 basic angular neutron energy spectra which were the product of the experimental program are collected in Appendices F and G, in graphical and tabular form, respectively. The spectra display various degrees of distortion as a result of the combinations of spatial position and assembly transverse dimensions outlined in Table 3. As discussed earlier in connection with the "Z" direction infinity effects, all the re 10.2 cm interior spectra contain a roughly five percent (positive) influence in the Bragg peak height due to the proximity of the assembly front leakage face for sub-Bragg neutrons with long mean-free-paths.

An additional product of the experimental program was an unexpected result of the door-scattered neutron background problem discussed in

Table 3. Assembly Dimensions and Measurement Site for the 15 Measured Beryllium Spectra

Assembly Size width height length (cm)	Measurement Type, distance from source plane (cm)
35.6 × 35.6 × 30.5 cm	interior, 0 cm (re 30.5 cm, Source)
35.6 × 35.6 × 30.5 cm	interior, 10.2 cm (re 20.3 cm)
35.6 × 35.6 × 30.5 cm	interior, 20.3 cm (re 10.2 cm)
35.6 × 35.6 × 30.5 cm	leakage, 30.5 cm
35.6 × 35.6 × 40.6 cm	leakage, 40.6 cm
35.6 × 35.6 × 50.8 cm	interior, 20.3 cm (re 30.5 cm)
35.6 × 35.6 × 50.8 cm	interior, 30.5 cm (re 20.3 cm)
35.6 × 35.6 × 50.8 cm	interior, 40.6 cm (re 10.2 cm)
35.6 × 35.6 × 50.8 cm	leakage, 50.8 cm
25.4 × 25.4 × 30.5 cm	leakage, 30.5 cm
25.4 × 25.4 × 40.6 cm	leakage, 40.6 cm
25.4 × 25.4 × 50.8 cm	interior, 20.3 cm (re 30.5 cm)
25.4 × 25.4 × 50.8 cm	interior, 30.5 cm (re 20.3 cm)
25.4 × 25.4 × 50.8 cm	interior, 40.6 cm (re 10.2 cm)
25.4 × 25.4 × 50.8 cm	leakage, 50.8 cm

Chapter V. The origin of the intense thermal neutron background component in the leakage spectrum from the 25.4 X 25.4 X 50.8 cm assembly was deduced to be source neutrons from the thermal column which streamed alongside the assembly, scattered off of the wedge-shaped, lead thermal column shutter doors, and then scattered again in the beryllium leakage face to be directed out into the beam and towards the detector, thus acting as a false "source" in the (reverse) negative "Z" direction. Figure 47 shows the measured composite neutron energy spectrum with this background component included compared to the spectrum after the background intensity had been substantially reduced by the addition of the BORAL skirts and the cadmium beam shielding collar. The spectrum including the door scattered background, that is without the BORAL skirts and the cadmium collar, was relatively more intense in the energy range above the Bragg cut-off. Additionally, the structure in this spectrum in the energy range between 0.006 and 0.1 eV contained some distinct peaks where there were valleys in the spectrum from which the background had been removed. The following experiment was devised to measure the energy spectrum of just this "reflected" neutron background. The source plate on the 25.4 X 25.4 X 50.8 cm assembly was removed and replaced with a neutron absorbing BORAL one, and the BORAL skirts and cadmium beam shielding collar were removed from around the front face. The neutron source in this case consisted of only those neutrons which scattered from the thermal column shutter doors and entered the beryllium assembly through the beam extraction port on the front leakage face. The neutrons which scattered in the assembly and reemerged from the front leakage face, relative to what had been measured

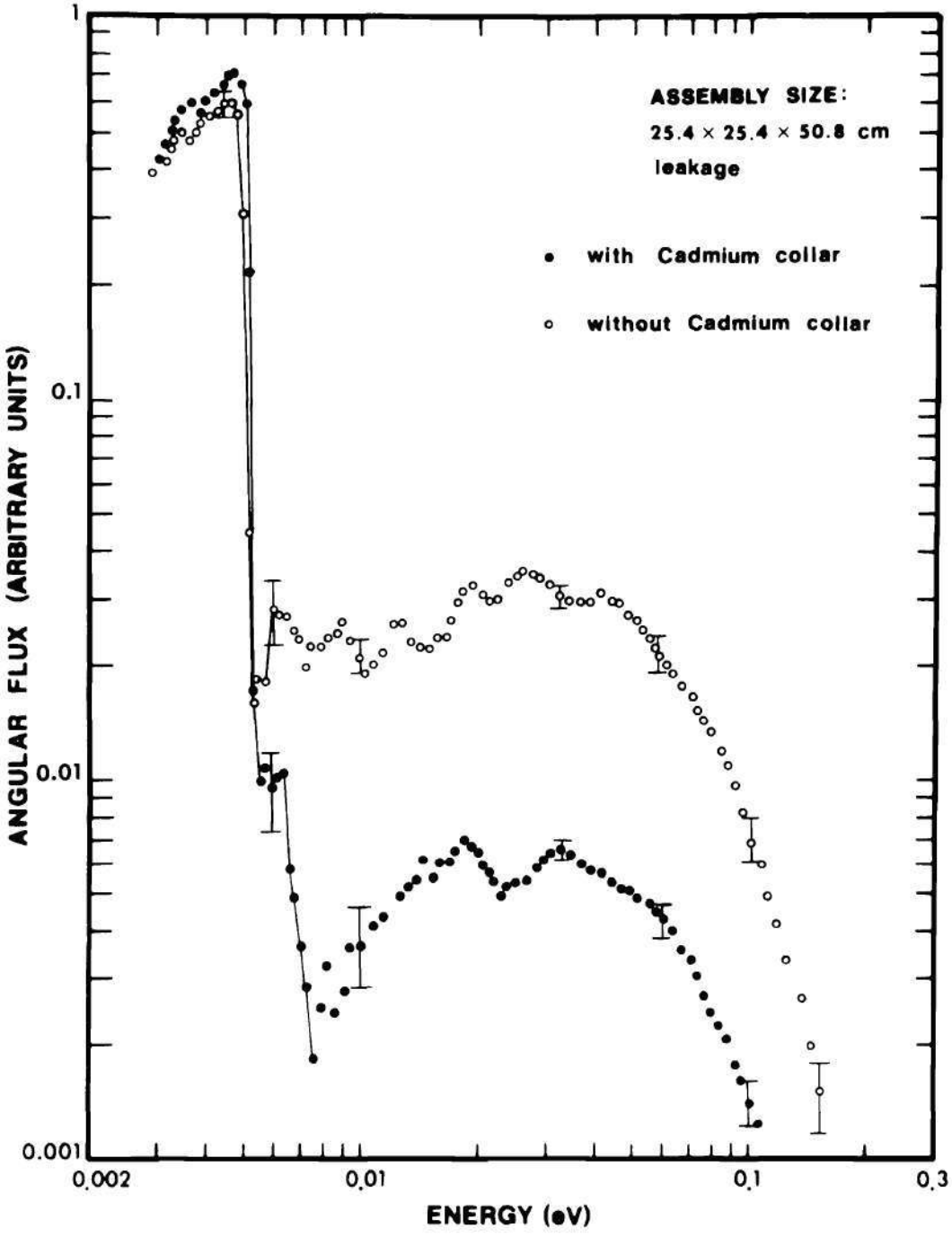

Figure 47. Neutron Leakage Spectra from the 25.4 X 25.4 X 50.8 cm Beryllium Assembly With and Without the BORAL Skirts and Cadmium Beam Shielding Collar Showing the Effect of Door-Scattered Background Neutrons on the Measured Spectrum Shape. (Normalization is arbitrary.)

with the plexiglass source plate, was in the negative "Z" direction.

The spectrum resulting from this measurement is pictured in Figure 48. Whereas no definite quantitative conclusions should be drawn about the spectrum, due to the unknown effects of the door scattering on the energy distribution and the fact that the "source" neutrons entered the assembly only through a relatively small opening in the center of the leakage face, still the qualitative behavior is unmistakable. The spectrum appears to follow the structure in the beryllium scattering cross section in that it peaked where the cross section peaked and vice versa, it dropped where the cross section dropped, especially below the Bragg cut-off. This is in contrast to the behavior of the spectrum in the positive "Z" direction, discussed in connection with Figure 46, which followed the mirror image of the scattering cross section. The shape of the spectrum in the negative "Z" direction can be justified by considering that, for a neutron to reemerge from the beryllium leakage face in this case, it must have been backscattered or perhaps multiple scattered in the assembly. Therefore, the spectrum one "sees" emerging from the leakage face consisted of only those neutrons which have been scattered in the assembly rather than those streaming directly from the source plane as was the case in the positive "Z" direction. In light of this fact it is not surprising that the negative "Z" direction angular spectrum behaved like the cross section; that is, the spectrum tended to peak in the energy regions where the scattering probability also peaked, and the spectrum was depleted in neutrons below the Bragg cut-off where the scattering cross section dropped drastically.

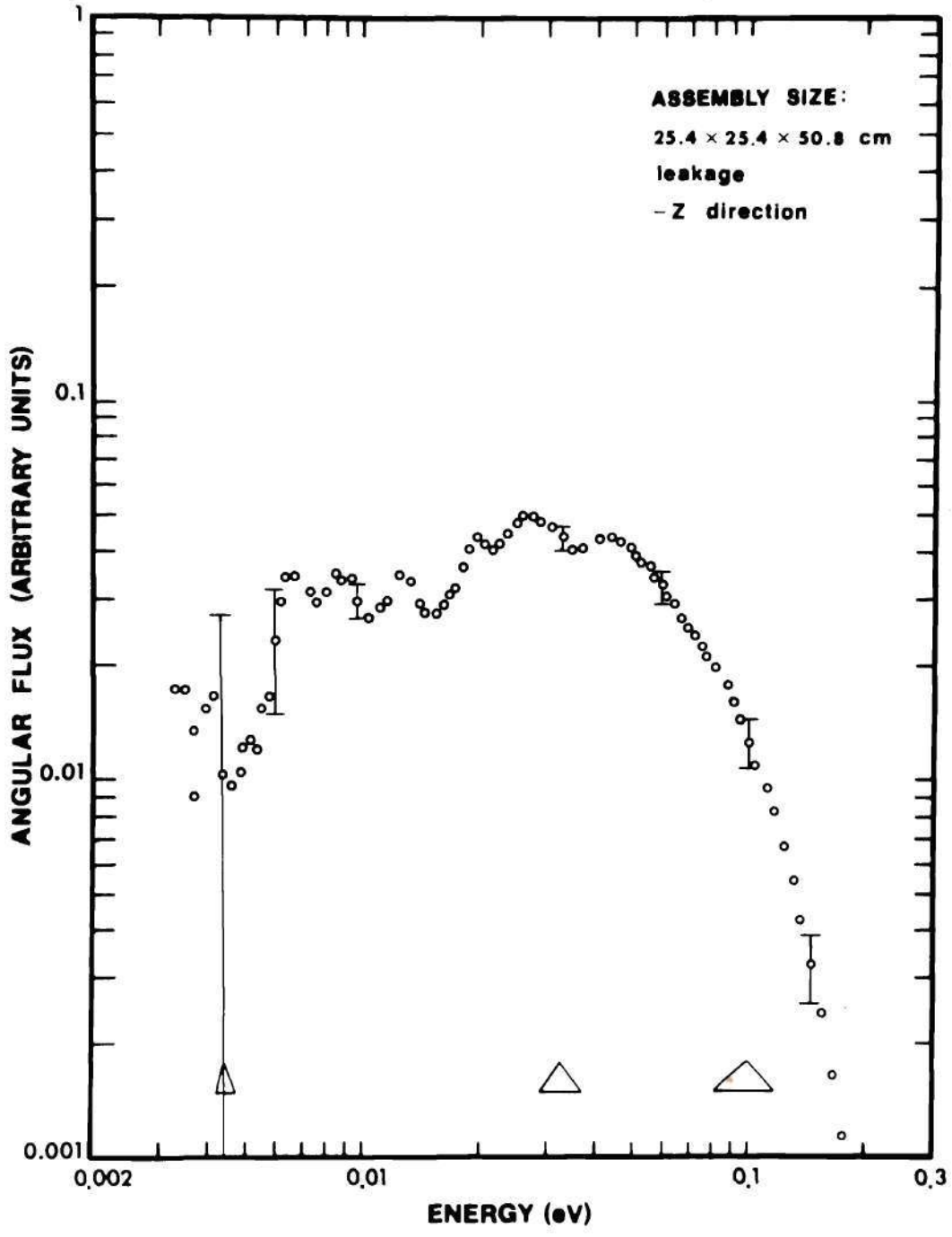

Figure 48. Neutron Leakage Spectrum from the 25.4 X 25.4 X 50.8 cm Beryllium Assembly with the Source in the Negative "Z" Direction. (The "source" consists of those door-scattered background neutrons which enter the assembly through the front leakage face.)

Space and Buckling Dependence of the Spectra

Figures 49 and 50 show the space dependence of the angular neutron energy spectra in the 35.6 X 35.6 cm and 25.4 X 25.4 cm assemblies, respectively. The spectra have been arbitrarily normalized in the low energy range, below the Bragg cut-off, such that successive spectra lay roughly ten percent apart. This normalization emphasizes the relative changes in the spectrum shape as one moves further away from the source plane in each assembly. The spectrum change along the longitudinal axes of the assemblies was quite dramatic; amounting to something of the order of 100-150 percent per 10 cm in the larger assembly and 300-400 percent per 10 cm in the smaller assembly. The leakage spectra in each case were distorted even further by the additional effects of Milne-problem surface leakage.

It is perhaps most important to note that in neither assembly is there any indication from Figure 49 or 50 that the spectrum was tending towards an equilibrium distribution out to distances in excess of 40 cm from the source plane.

Figures 51 and 52 show the longitudinal space dependence of the surface leakage spectra in the 35.6 X 35.6 cm and 25.4 X 25.4 cm assem blies respectively. The qualitative aspects of the space dependent behavior of the spectra are similar to those discussed previously in connection with the interior spectra. However, the quantitative distortion in the leakage spectrum shape, above and below the Bragg cut-off, at some distance from the source plane is larger than it was in the case of the interior spectra due to the additional distortion in each spectrum from surface leakage effects.

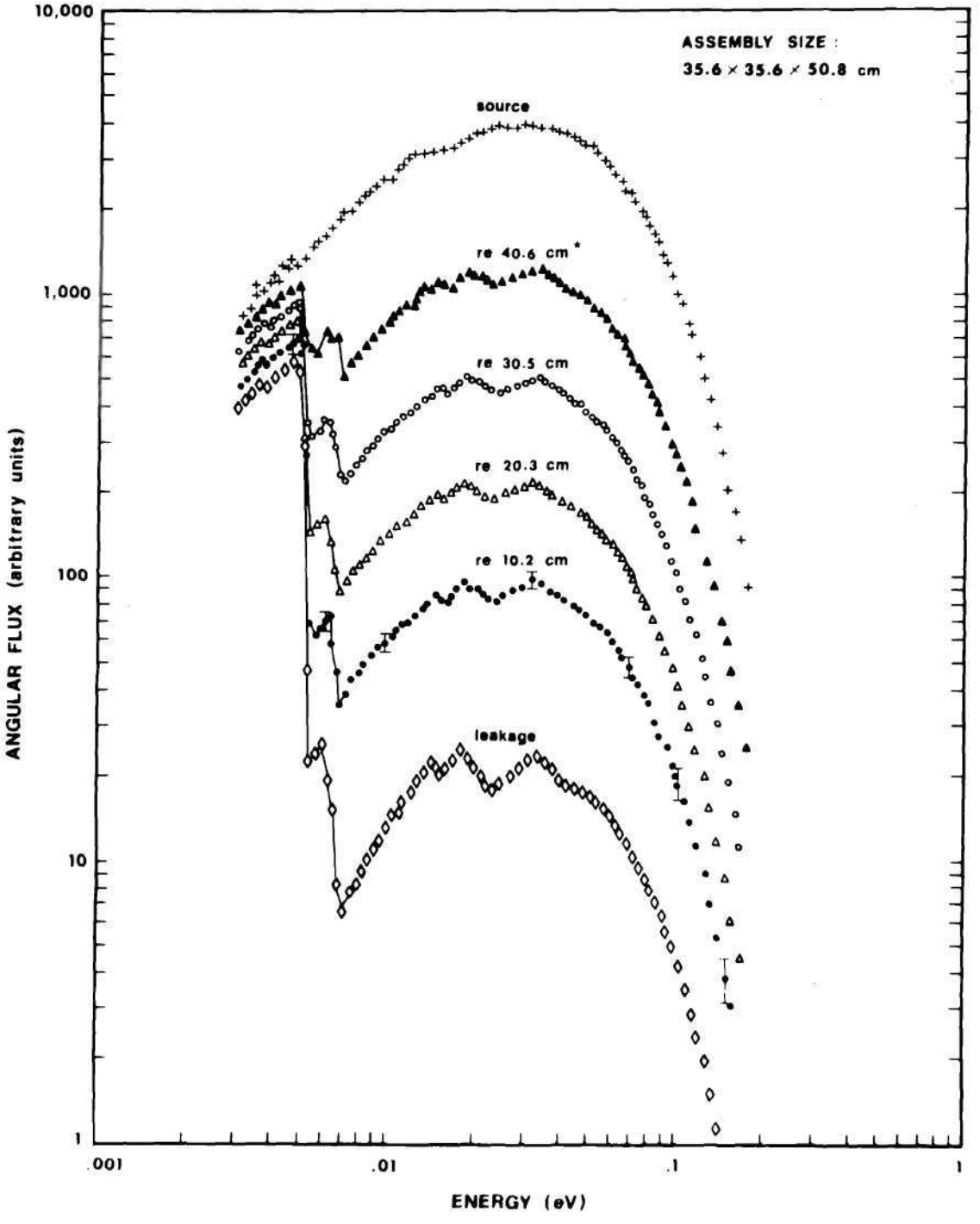

Figure 49. Space Dependence of the Measured Angular Neutron Energy Spectrum in the Positive "Z" Direction Along the Longitudinal Axis of the 35.6 X 35.6 X 50.8 cm Beryllium Assembly. (Normalization is arbitrary. *Equivalent spectrum measured in the 35.6 X 35.6 X 30.5 cm assembly, 10.2 cm from the source plane.)

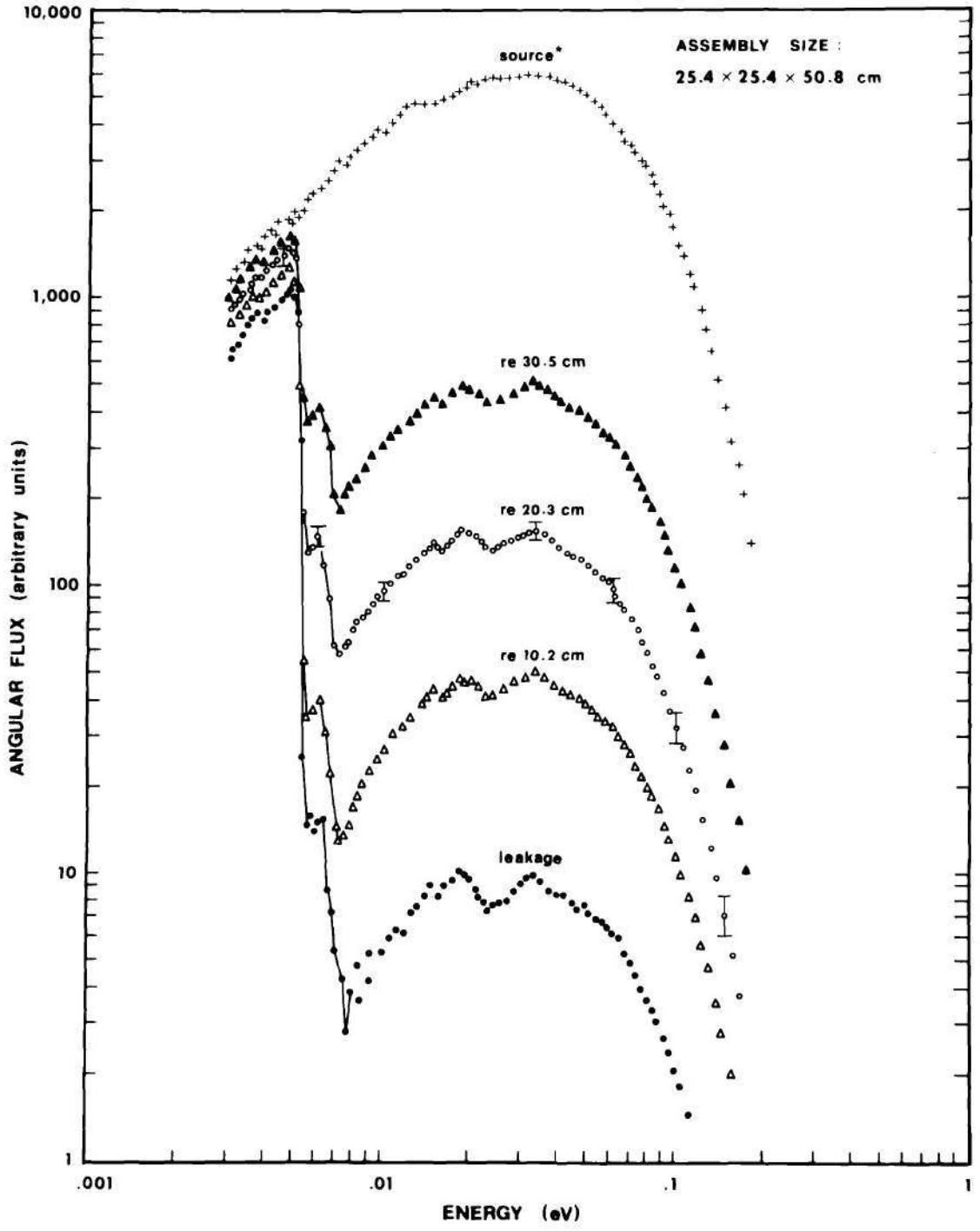

Figure 50. Space Dependence of the Measured Angular Neutron Energy Spectrum in the Positive "Z" Direction Along the Longitudinal Axis of the 25.4 X 25.4 X 50.8 cm Beryllium Assembly. (Normalization is arbitrary. *Equivalent source spectrum measured in the 35.6 X 35.6 X 30.5 cm assembly.)

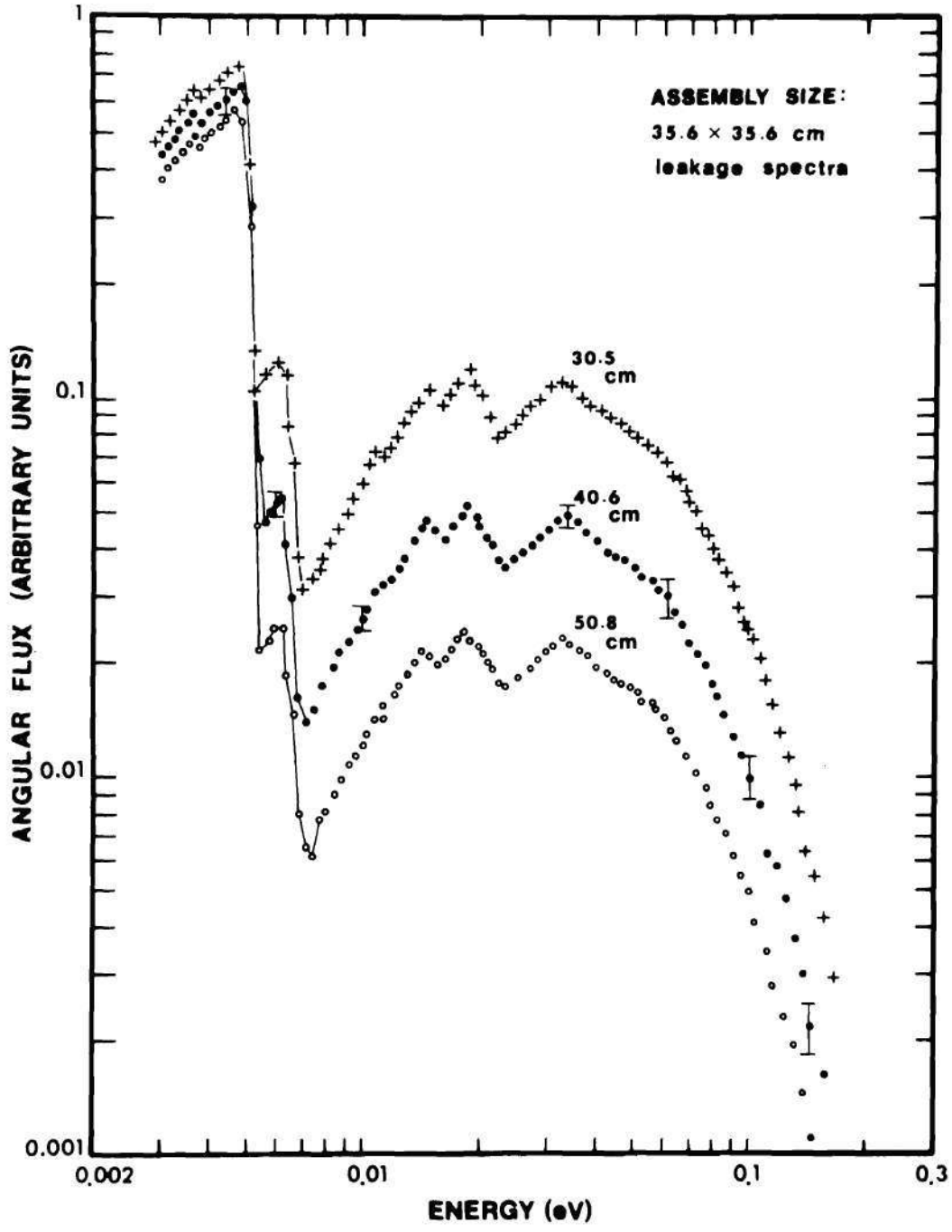

Figure 51. Space Dependence of the Measured Angular Neutron Energy Spectra Leaking from the Front Faces of the 35.6 X 35.6 X 30.5, 40.6, and 50.8 cm Beryllium Assemblies, Respectively. (Normalization is arbitrary.)

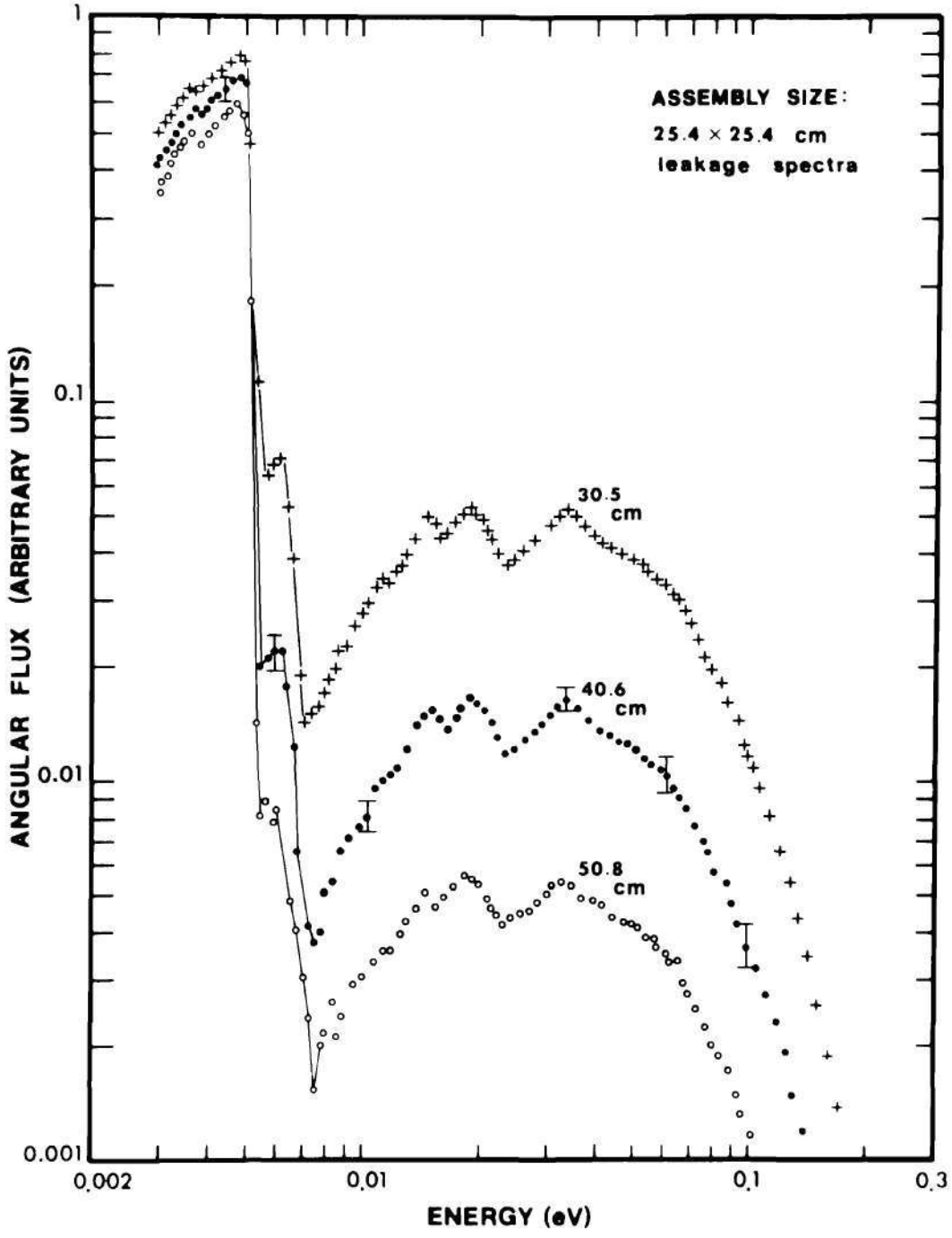

Figure 52. Space Dependence of the Measured Angular Neutron Energy Spectra Leaking from the Front Faces of the 25.4 X 25.4 X 30.5, 40.6, and 50.8 cm Beryllium Assemblies, Respectively. (Normalization is arbitrary.)

Figure 53 shows the space dependence, starting at the source plane, of the angular neutron energy spectrum in the 35.6 X 35.6 x 30.5 cm assembly.

Of interest is the buckling dependent behavior of the angular spectrum. Figure 54 shows the relative shapes of two typical spectra at the same distance from the source plane (space position), but in assemblies with transverse dimensions of 25.4 X 25.4 cm and 35.6 X 35.6 cm respectively. The spectra are arbitrarily normalized throughout the thermal energy range. Above the Bragg cut-off energy the two spectra were very nearly identical, but the spectrum in the smaller 25.4 X 25.4 cm assembly was peaked roughly 150 percent more strongly below the Bragg cut-off. The major effect of a change in transverse buckling in these small assemblies then appears to be to change the relative rates of decay between the sub-Bragg and thermal neutron energy groups such that the relative spectrum distortion increases with increasing transverse buckling (decreasing transverse dimensions). Had the spectra in Figure 54 been normalized below the Bragg cut-off, it would have been somewhat more apparent that the buckling dependent behavior of the spectral distortion is in keeping with the earlier qualitative reasoning about the dependence of the transverse leakage rate on the proximity of the assembly boundaries and on the energy dependent relative neutron scattering probability. That is, ignoring coupling between the groups, one would expect the thermal energy group, where the beryllium scattering cross section is highest, to have decayed away at an increasing rate, relative to the sub-Bragg group, with decreasing assembly dimensions due to the rise in the transverse leakage rate for scattered neutrons. The stronger overall spatial decay

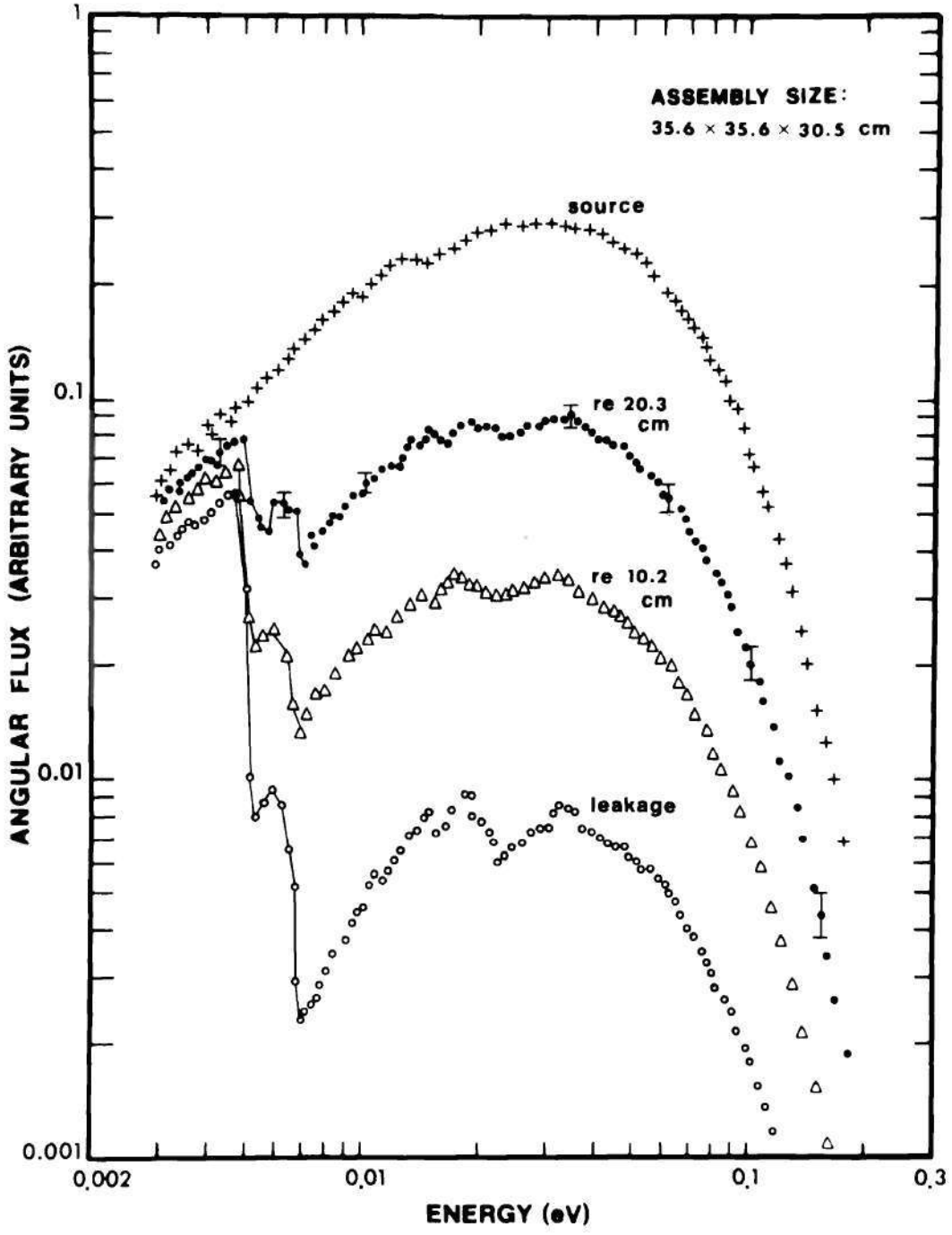

Figure 53. Space Dependence of the Measured Angular Neutron Energy Spectrum in the Positive "Z" Direction Along the Longitudinal Axis of the 35.6 X 35.6 X 30.5 cm Beryllium Assembly. (Normalization is arbitrary.)

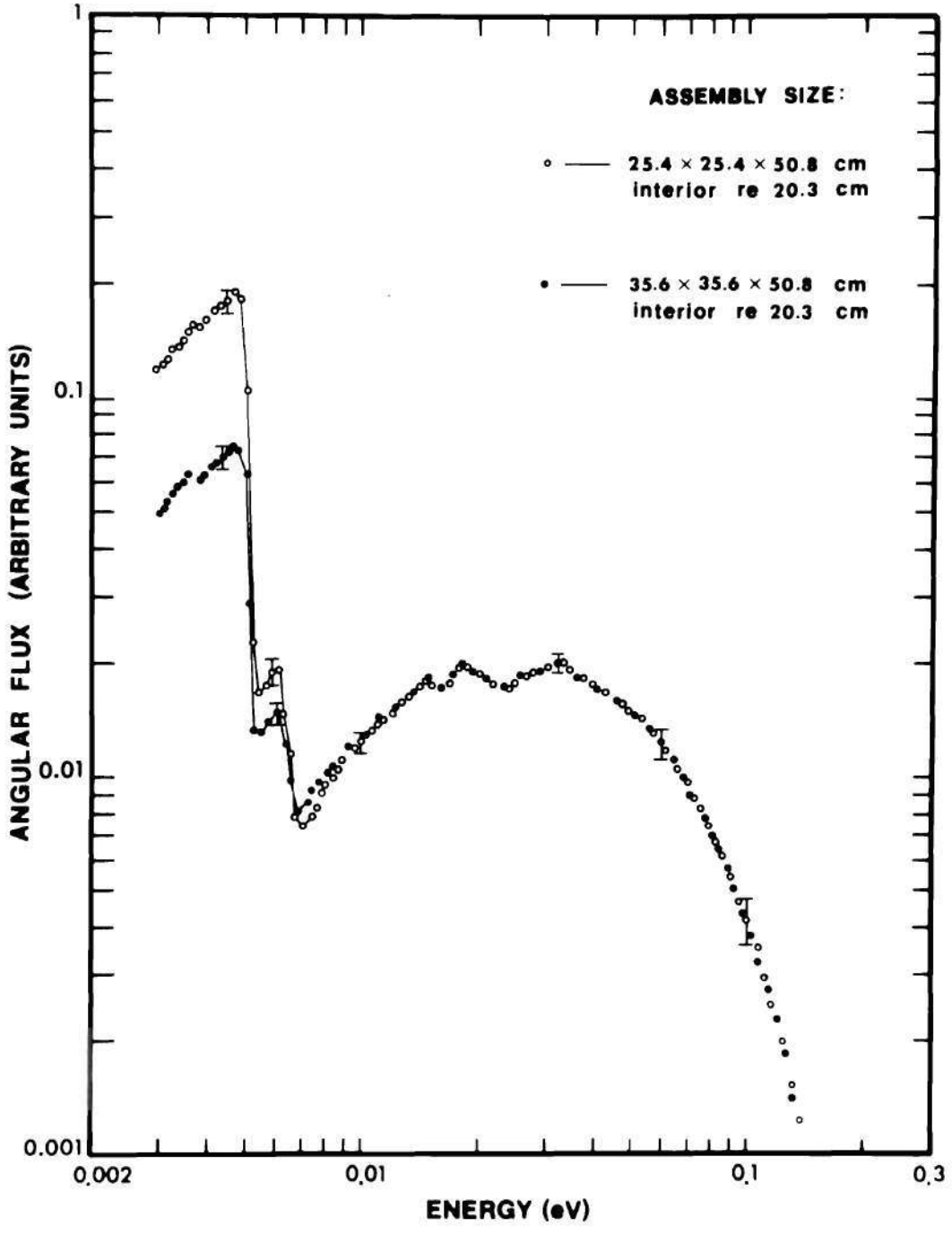

Figure 54. Effect of Transverse Dimensions on the Shape of the Measured Angular Neutron Energy Spectrum 30.5 cm from the Source Plane. (Normalization is arbitrary.)

gradient itself in the smaller assembly further increases the predominance of long mean-free-path neutrons (below the Bragg cut-off) in the spectrum. These contentions are borne out by the behavior of the spectra in Figure 54.

In Figures 55 and 56 are plotted the ratios of spectra at the same distance from the source plane in the two assemblies with different transverse bucklings for interior and leakage measurements, respectively. The technique of plotting the ratios of spectra is employed here to emphasize the relative transverse buckling dependent change in the spectrum shape above and below the Bragg cut-off as a function of distance from the source plane, without regards to the details in the spectra themselves. It is apparent from Figures 55 and 56 that the relative buckling dependent distortion increases with increasing distance from the source plane.

Figure 57 is a plot of the ratio ϕ_{cold}/ϕ_{th} where ϕ_{cold} and ϕ_{th} are the angular flux intensities at 0.0045 and 0.033 eV (roughly the Bragg and thermal peaks respectively), versus distance from the source plane. At distances beyond about 10 cm, the cold neutron flux intensity (in the positive "Z" direction) appears to increase (relatively) over the thermal flux intensity in a nearly linear fashion (on semi log paper) with increasing distance from the source. This linear behavior is indicative of a purely exponential relative growth of the cold neutron flux intensity over the thermal flux in the distorted spectra. It appears then that the spatial flux decay could be describable by the independent decay of the two energy groups where, to a first approximation, the groups are uncoupled (or at least very weakly coupled) by inelastic scattering mechanisms. From the exponential behavior in Figure 57, one could write

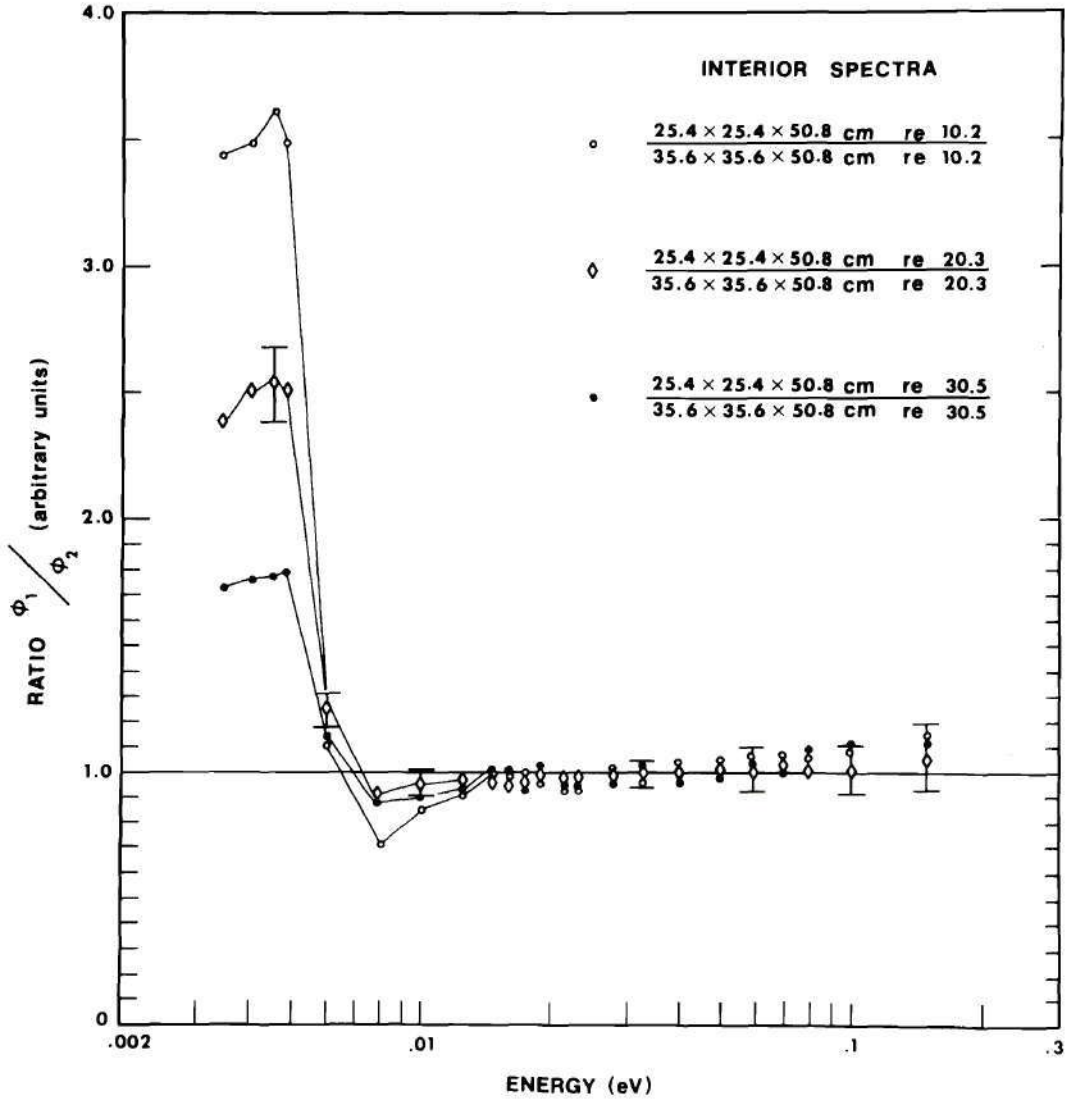

Figure 55. Ratios of Measured Neutron Energy Spectra in the Interior of Beryllium Assemblies with Transverse Dimensions of 25.4 x 25.4 and 35.6 x 35.6 cm at 40.6, 30.5, and 20.3 cm from the Source Plane. (The ratios emphasize the transverse buckling dependence of the relative spectrum shape above and below the Bragg cut-off as a function of distance from the source. Normalization is arbitrary.)

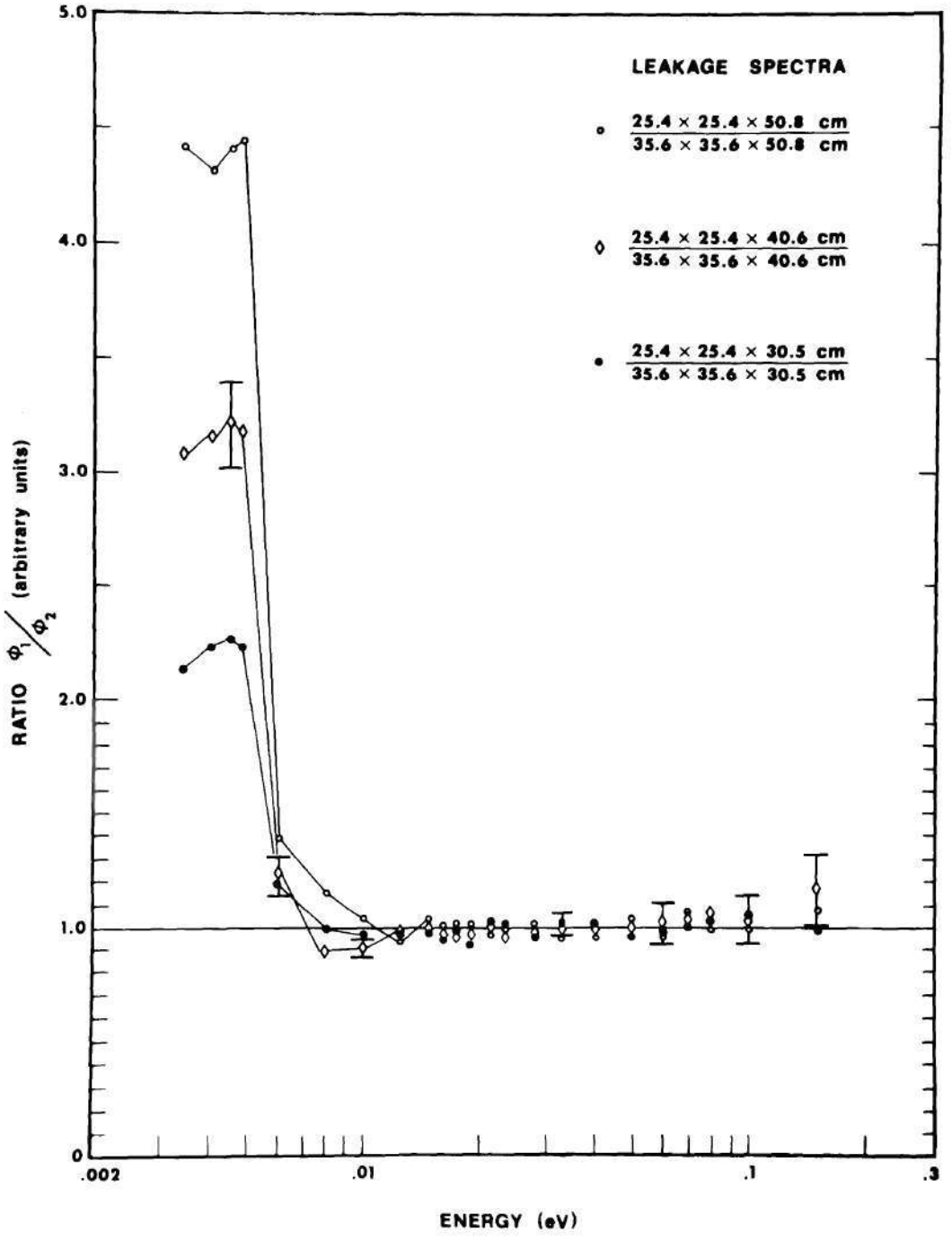

Figure 56. Ratios of Measured Neutron Energy Spectra for Neutrons Leaking from the Front Faces of Beryllium Assemblies with Transverse Dimensions of 25.4 x 25.4 and 35.6 x 35.6 cm at 50.8, 40.6, and 30.5 cm from the Source Plane. (The ratios emphasize the transverse buckling dependence of the relative spectrum shape above and below the Bragg cut-off as a function of distance from the source. Normalization is arbitrary.)

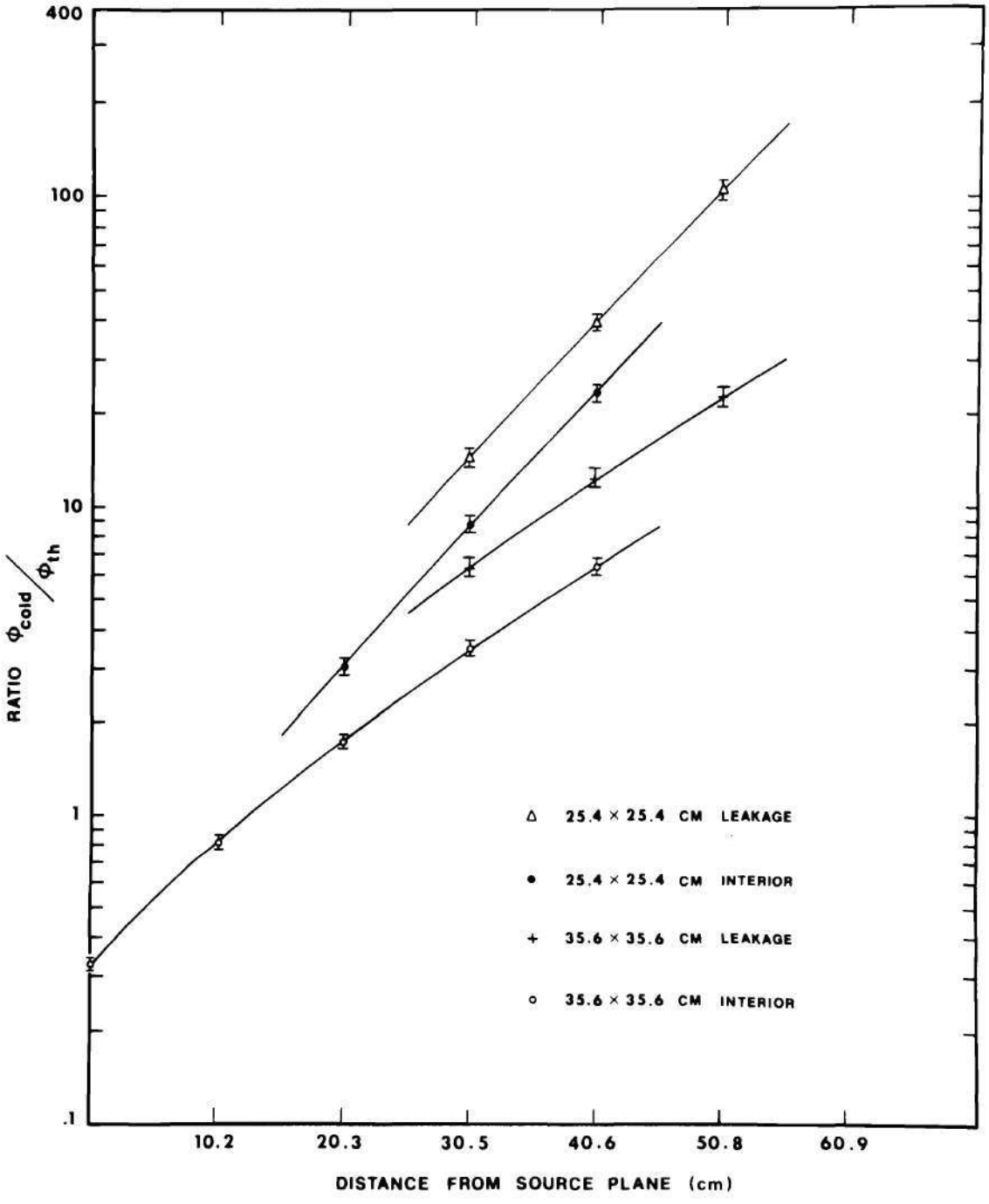

Figure 57. The Ratio of the Angular Flux Intensity at 0.0045 eV to that at 0.033 eV as a Function of Distance from the Source Plane. (The progressive buildup of cold neutrons is shown below the Bragg cut-off, for measured leakage and interior spectra in the 25.4 x 25.4 and 35.6 x 35.6 cm beryllium assemblies.)

$$\frac{\phi_{cold}}{\phi_{thermal}} = e^{-az} \tag{98}$$

where "a" is a constant characteristic of the relative rate of cold neutron buildup. It is interesting that this exponential relative growth of the cold neutron flux intensity over the thermal energy flux is consistent with (but not exclusively) the pure, uncoupled exponential decay of a thermal and a sub-Bragg group, characterized by discrete decay constants κ_{th} and κ_{cold}, respectively, in that this behavior reproduces Figure 57. That is, if $\phi_{th} = \phi_o e^{-\kappa_{th} z}$ and $\phi_{cold} = \phi_o e^{-\kappa_{cold} z}$, then

$$\frac{\phi_{cold}}{\phi_{th}} = \frac{e^{-\kappa_{cold} z}}{e^{-\kappa_{th} z}} = e^{-(\kappa_{cold} - \kappa_{th})z} = e^{-az} \tag{99}$$

where "a" is a constant, equal to $\kappa_{cold} - \kappa_{th}$. Since the thermal energy flux intensity decays away faster than the sub-Bragg flux, see for example Figures 49 or 50, the constant "a" is necessarily greater than 1.0. In addition, the transverse dimensions of the assembly affect the rate of cold neutron buildup in Figure 57, smaller assemblies being characterized by an increased distortion rate, so that "a" must be an increasing function of buckling in this range.

The fact that the ratio of flux intensities for the leakage spectra in each assembly display parallel slopes to their respective interior spectra in Figure 57 is evidence that the rate of cold neutron buildup is the same in each case and, therefore, the additional spectrum distortion as a result of Milne-problem surface leakage effects can be expressed simply as some constant fraction of the interior spectrum beneath the

leakage face (which serves as the "source" for the leakage spectrum). There is then some effective separation between the effects of Milne-problem surface leakage from the front face of the assembly and those of transverse leakage out the sides of the assembly in the space and buckling dependence of the leakage spectral shape.

Figure 58 is a plot of the flux-weighted average energy as a function of distance from the source plane for both interior and leakage spectra in the 35.6 X 35.6 and 25.4 X 25.4 cm assemblies. The fall-off in the average energy with increasing distance from the source plane in each case is the result of the relative buildup of sub-Bragg neutrons in the spectrum. The convex nature of the curves in Figure 58 is strong evidence that the spectrum is <u>not</u> tending toward an equilibrium distribution in either assembly out to distances in excess of 40 cm from the source plane.

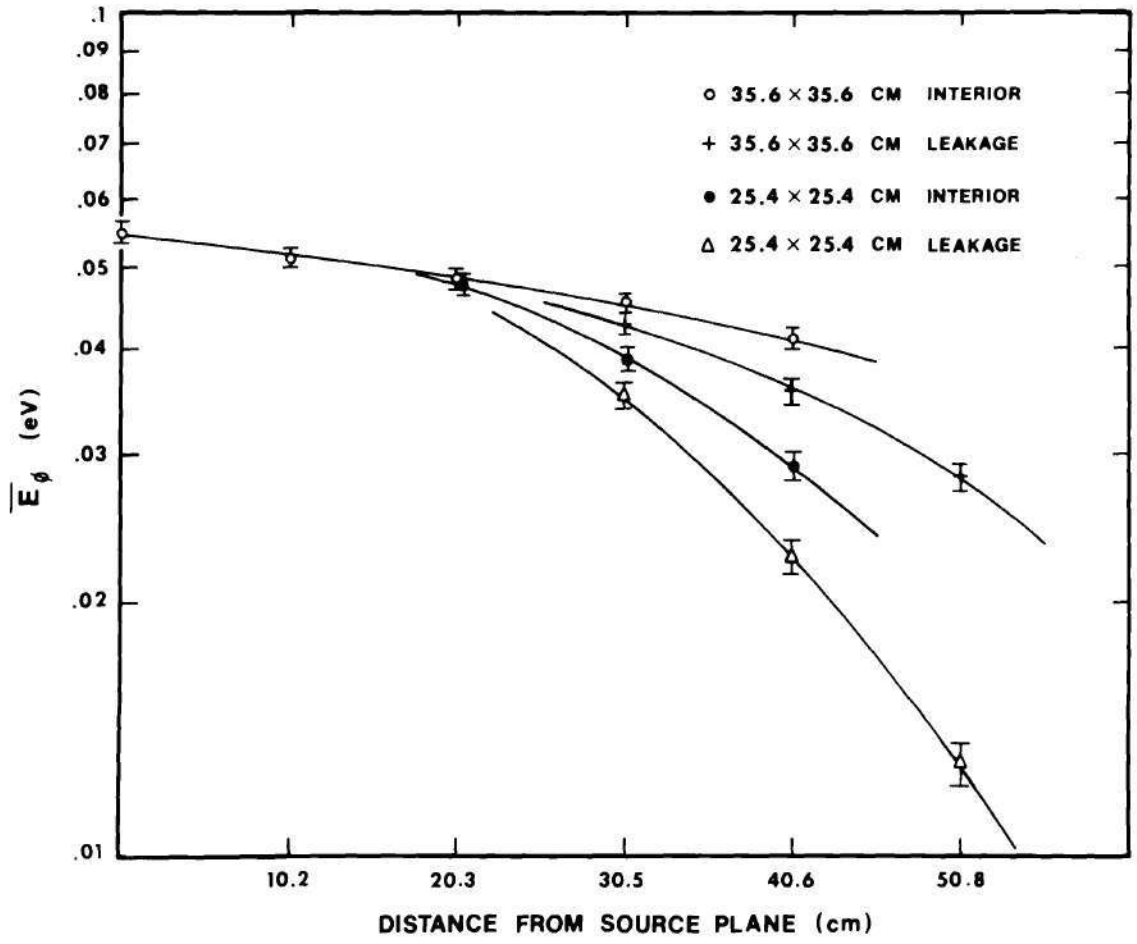

Figure 58. Behavior of the Flux Average Energy, $\overline{E}_\phi$, with Distance from the Source Plane for Angular Leakage and Interior Spectra in 25.4 × 25.4 and 35.6 × 35.6 cm Beryllium Assemblies

CHAPTER VII

CONCLUSIONS AND RECOMMENDATIONS

The most important conclusion to be drawn from the measured space dependence of the beryllium spectra in Figures 50 and 49 is that the angular spectrum in the positive "Z" direction does not appear to be tending toward an equilibrium distribution out to distances in excess of 40 cm from the source plane in either the 25.4 x 25.4 or the 35.6 X 35.6 cm beryllium assembly. One can deduce the non-asymptotic nature of the last interior spectrum at 40.6 cm from the source, and similarly the last leakage spectrum at 50.8 cm from the source, by taking note of the analogous rate-of-change behavior to those spectra just preceding. Similarly, assuming some form of smooth analytic continuation in the ratio $\phi_{cold}/\phi_{thermal}$ in Figure 57 beyond the last data points demonstrates the fact that the spectrum distortion in both assemblies is indeed a monotonically increasing function of distance from the source plane even at distances beyond the last data points.

The space dependence of the beryllium spectra is further demonstrated by the behavior of the spectrum-averaged energy, $\bar{E}_{\phi}$ in Figure 58, which is a decreasing function of distance from the source plane, reflecting the buildup of sub-Bragg neutrons in the spectrum. In the limit of very large distances from the source plane, the "thermal" portion of the angular spectrum (that above 0.007 eV) will have decayed away completely, and

the cold neutron flux will predominate at some point such that the average energy in the angular spectrum should eventually level out and approach some sub-Bragg distribution. However this leveling tendency cannot be deduced from Figure 58 for distances out to in excess of 40 cm from the source, which may be attributable to the flux-weighting which casts a somewhat heavier weight to the high energy end of the spectrum than, for example, does neutron density weighting. The reasons for choosing flux-weighting in this case have been discussed. As a result of the flux-weighting, the spectrum distortion below the Bragg cut-off may not be felt as strongly in the average energy in the early stages until the cold neutron buildup becomes significant.

The strong space dependence in the angular neutron energy spectrum means that the usual assumption of space-energy separability in the solution of the transport equation is clearly invalid in this buckling range. In addition, the complete lack of a tendency toward an equilibrium, asymptotic decay mode has serious ramifications to the extraction of the usual diffusion parameters from decay constant measurements in small beryllium assemblies. An integral parameter, like the decay eigenvalue κ, which describes the average integrated behavior of the flux in the assembly, in regions of strong spatial gradients, will clearly yield diffusion parameters which are functions of the spatial range over which κ was determined. This has in fact occurred in the equivalent pulsed source, time eigenvalue measurement at high buckling. Thus, a fit to the λ vs B^2 curve, like the one in Equation 8, which assumes a discrete fundamental mode decay, is incorrect in this buckling range in that the coefficients are not unique functions of the moderator diffusion parameters.

Our literature survey has shown that, to date, there exists no published comprehensive theoretical treatment of the exact experimental problem we have undertaken; that is, for the space dependent behavior of the steady-state angular neutron energy spectrum in small beryllium assemblies (above the "critical" buckling) with strong transverse leakage.

A promising theoretical treatment by Williams[21] involves an analytical solution of the integral transport equation, describing the diffusion length problem in a finite crystalline medium with transverse leakage, by way of a Weiner-Hopf technique. The details[75] of the solution are quite lengthy and will not be discussed here except to say that, for a simple separable scattering kernel, the final solution reduced to three physically distinct terms: the first representing the fundamental mode decay and the higher spatial harmonics, the second being a direct source transient which is unaffected by the size of the system, and the third representing the transient which arises directly from the finite dimensions of the system. The relative angular spectrum shapes in the forward, transverse, and reverse directions for the asymptotic (only) part of the solution are plotted in Figure 4 in Chapter I, and agree qualitatively with our measured spectra in the positive and negative "Z" directions in Figures 46 and 48, respectively, inasmuch as the spectrum in the positive "Z" direction is strongly peaked below the Bragg cut-off whereas the spectrum in the negative "Z" direction is depleted in sub-Bragg neutrons. In addition, the relative cold neutron buildup is shown, in the Williams theory, to increase with increasing transverse buckling (decreasing transverse dimensions) in agreement with our results in Figure 54. The physical

origins for the spectrum shape angular behavior have been discussed.

Williams does not present quantitative results for the specific case where the fundamental mode ceases to exist and the solution consists entirely of the source and leakage transient parts. However, he does state that the fundamental mode and leakage transient terms have the same total energy spectrum (but different spatial distributions), but this is not the case for the angular spectrum. Williams[76] has stated that he has been unable to obtain a closed-form analytical solution from this particular treatment for anything but the simple separable kernel which, although it correctly satisfies the requirement of detailed balance and yields the correct value of $\Sigma_s(E)$ upon integration over the final energy, E', is not expected to be capable of quantitatively accounting for Bragg effects in the elastic scattering cross section of crystalline systems.

In order to overcome this problem with the separable kernel, Williams[22] has undertaken an improved solution of the integral transport equation via a variational approach à la Kladnik and Kuscer.[77] Whereas this approach allows the incorporation of the separable-plus-elastic scattering kernel of Corngold,[39] which is a much improved kernel for crystalline moderators, the solution is specifically limited to the case where a discrete asymptotic decay mode still exists at some distance from the source plane. As such, it is not quantitatively capable of describing the strong spatial dependence of the angular flux spectrum, which is reminiscent of a progressive diffusion heating effect (that is, a buildup of neutrons with long mean-free-paths in the spectrum) in the direction of the spatial decay gradient, in these small beryllium assemblies above the critical buckling.

Williams[76] has expressed an interest in adapting one or the other of these theoretical treatments, perhaps by a direct numerical attack, to the specific problem of describing the behavior of the continuum spectrum where a great deal of information about the thermalizing characteristics of the scattering media are contained in the very distorted energy spectra, now that our concurrent experimental data are available for comparison.

The various aforementioned theoretical analyses of Corngold et al.[12,13,39] are all done in the time domain for the pulsed source problem, although Corngold and Durgun[39] do state that the extension of their diffusion theory analysis to the stationary source, diffusion length problem "should be straightforward." However, in light of the fact that the more recent Conn and Corngold[12,13] transport theory analysis of the same problem tends to refute some of the earlier diffusion theory results, it no longer appears to be worthwhile to make this extension in diffusion theory. The Conn and Corngold transport theory work is mathematically very sophisticated and it does not appear to embody such a "straightforward" extension to our experimental situation. Furthermore, these analyses deal primarily with the behavior of the discrete and continuum eigenvalues (decay constants), whereas we have measured spectra (eigenfunctions). Therefore, for the stated reasons of mathematical complexity and shifted emphasis between the available theory and our experimental situation, it does not appear feasible to quantitatively relate our results to the Corngold theories.

A number of the available theoretical treatments of the pulsed

source and diffusion length problems are based on some modified diffusion theory calculations.[18,30,37,39,44] In particular, in a recent paper, Ahmed, Kothari, and Kumar[24] have presented the results of diffusion theory calculations of the dependence of the diffusion length and average energy on the transverse dimensions of infinitely long blocks of polycrystalline beryllium. Using an energy dependent transverse buckling approximation, they find that a true discrete spatial decay mode exists for assemblies with transverse dimensions as low as 30 X 30 cm. This is substantially lower than the "critical" transverse dimensions, of the order of 127 X 127 cm, proposed by Williams.[22] They also find that pseudo-equilibrium conditions, governed by the independent decay rate of the cold neutron group, are established reasonably fast (of the order of 30 cm or less from the source plane) in assemblies with transverse dimensions smaller than 20 X 20 cm. In assemblies of intermediate size, that is, between 20 X 20 and 30 X 30 cm, equilibrium conditions are not predicted out to a distance of 100 cm from the source plane. Williams[25] has attacked these results on the basis of the questionable justification for the use of diffusion theory for this problem.

These diffusion theory results then predict that a true discrete asymptotic decay mode should exist in our 35 X 35 cm assembly, and that no equilibrium conditions should exist in our 25 X 25 cm assembly. Our measured angular spectra in both the 25 X 25 and 35 X 35 cm beryllium assemblies are strongly space dependent out to distances in excess of 40 cm from the source plane as is evident from Figures 49 and 50. In addition, the behavior of the ratio of cold to thermal neutrons and the

average energy in the measured angular spectra in Figures 57 and 58 show no tendency toward equilibrium conditions in either assembly. In short, we find no evidence of the establishment of discrete, asymptotic decay conditions in either the 25 X 25 or 35 X 35 cm beryllium assembly, in contradiction to the diffusion theory predictions of Ahmed, Kothari, and Kumar for assemblies larger than 30 X 30 cm, but in at least qualitative agreement with the transport theory predictions of Williams.[21,22]

We feel that the discrepancy lies in Ahmed, Kothari, and Kumar's use of diffusion theory for this problem. Some of the arguments for the justification of the applicability of diffusion theory, based on comparative studies of the behavior of the decay constant in the equivalent pulsed source problem, do not appear to apply to the steady-state problem. In the pulsed source problem, the spectrum is depressed below the Bragg cut-off which results in very little weight in the integral decay constant being attributable to the sub-Bragg energy group where the spectrum distortion manifests itself. However, in the steady-state, diffusion length problem, the spectrum is strongly peaked below the Bragg cut-off and this cold neutron group carries progressively more weight as the spectrum distortion increases as a result of decreasing transverse dimensions of the system. Therefore, it does not appear to be valid in the diffusion length problem to neglect the fact that the neutrons in this low energy range do not[78] fulfill the conditions demanded by the diffusion approximation (due to their long mean-free-paths) based on their relative weight in the spectrum.

In a comparative study of the behavior of the diffusion length in a poisoned beryllium system, where the sub-Bragg spectrum is peaked as

it is in our case, under the assumption of isotropic scattering, Grover, Kothari, and Ghatak[79] found reasonable agreement between a diffusion approximation and a more exact transport theory description of the problem for moderate spectral distortions. However, it appears that Ahmed, Kothari, and Kumar[24] have overextended the use of the diffusion theory in the equivalent leakage problem into the range of spectral distortions where Grover, Kothari, and Ghatak[79] found distinct discrepancies between the diffusion approximation and transport theory calculations; specifically, where they found that the diffusion theory analysis can severely underestimate the flux peaking below the Bragg cut-off (that is, underestimate the spectral distortion) and subsequently lead to considerable errors in the calculated decay constant. It is our contention then that this misrepresentation of the sub-Bragg flux peaking in appreciably distorted spectra is an indication of the inapplicability of diffusion theory to the diffusion length problem with strong transverse leakage, and offers an explanation for the discrepancy between the diffusion theory estimation of the "critical" transverse dimensions for the existence of a discrete decay mode and our experimental results.

The transport theory angular spectrum appears to be a superior experimental test for the existence of an equilibrium, asymptotic decay mode than is the diffusion theory, angle integrated, total flux spectrum due to the very strong anisotropic behavior of the elastic scattering contribution just above the Bragg cut-off energy, and subsequently of the angular spectrum. In addition, in one treatment,[21] the predicted strong space dependence in the angular spectrum canceled (neglecting source terms)

such that the total spectrum was not space dependent. Thus the non-equilibrium, non-asymptotic nature of the decay could not be deduced from the total spectrum in this case. However, it is felt that this sort of exact cancellation of the strong space dependence of the angular spectrum in one direction by an equal but opposite effect in all other directions is a non-physical effect most likely resulting from the approximate (separable) scattering kernel used in the analysis. In order to clarify this point, it would be of considerable interest to have subsequent measurements of the space dependence of the angular spectrum in both the negative "Z" and transverse directions to compliment our measurements in the positive "Z" direction, from which one could draw some conclusions about the behavior of the total spectrum in the continuum range. The preferred data is still, of course, the angular spectrum since it contains the most detailed information about the thermalizing characteristics of the moderator.

An independent approach to a theoretical treatment of the diffusion length problem in finite media with strong transverse leakage, which is free of some of the usual assumptions necessary to extract an analytical soltuion, is the Monte Carlo calculational program undertaken by Mr. B. I. Shamasundar here at Georgia Tech. A distinct advantage of this particular approach is in its inherent capability for testing the effects of any number of scattering kernels in various degrees of sophistication. The apparent limitation on the eventual success of the Monte Carlo technique with this particular theoretical problem seems to lie in the computer time necessary to follow a sufficient number of source particles to obtain a statistically significant spectrum shape due to the strong probability of

transverse neutron leakage out the sides of the small assemblies.

A further conclusion which can be deduced from the shape of the measured beryllium spectrum, for example Figure 46, is that the fine structure in the energy range roughly between the Bragg peak at 0.005 eV and the high-thermal region around 0.03 eV suggests that there may in fact be more detail in the beryllium cross section in this energy range than is indicated by the data[14] in BNL-325. This structure indicates that an independent measurement of the beryllium cross section in this range is appropriate. In addition, a further determination of the magnitude of the drop in the beryllium cross section below the Bragg cut-off at 0.007 eV is in order since the rate of cold neutron buildup (i.e. the distortion) in our spectra is clearly a strong function[45] of the minimum value of $\Sigma_T(E)$ below the Bragg cut-off. The minimum value of $\Sigma_T(E)$ can be sensitive to impurities in, and the physical condition of, the beryllium samples used in the measurements and this minimum value will eventually need independent confirmation in that it is an important parameter in all crystalline scattering kernels.

The behavior of the continuum spectrum in small crystalline systems is rich in the physics of neutron scattering and it provides a sensitive and demanding test situation for theoretical scattering kernels[32,45] and approximate methods of solution of the transport equation.[10] It is our expectation that publication of our measured space dependent, continuum angular spectra in small beryllium assemblies will stimulate theoretical comparisons for which there had previously been no benchmark, as was the case after publication of the complementary pulsed source, time dependent spectra by Gaerttner et al.[43]

APPENDICES

APPENDIX A

OPERATION OF THE ZERO TIMING UNIT CIRCUIT

Figure 59 is a diagram of the Zero Timing Unit electronic circuit.

The reflected light beam from one of the spinning mirrors attached to the chopper rotor shaft illuminates phototransistor PT1 and drives it into conduction causing a positive, 22 volt, electrical pulse to form across resistor R1. Transistor T1 shapes the pulse and matches it to the 100 ohm impedance of the coaxial cable so that it may be sent along to the remainder of the timing circuit located behind the chopper control panel.

At low chopper RPM's one finds that the photo pulse is spread out considerably by the fact that the light beam sweeps slowly across the face of the phototransistor. Therefore, it is necessary that the peak of the photo-timing pulse be processed rather than the more conventional leading edge to avoid a significant RPM-dependent timing error. The positive-going timing pulse drives transistor T2 into conduction, causing the voltage at point "A" to fall. Transistor T2 remains in conduction, continually charging capacitor C2, as long as the timing pulse is rising. As soon as the photopulse peaks and then begins to fall, the voltage at the emitter of T2 (from the charge stored in capacitor C2) will be higher than the voltage at the base of T2 (from the timing pulse) and T2 will switch off causing the voltage at point "A" to rise sharply. This sharp rise, which is coincident with the peak in the phototransistor timing pulse, is differentiated in capacitor C3, and the resulting positive pulse is used to

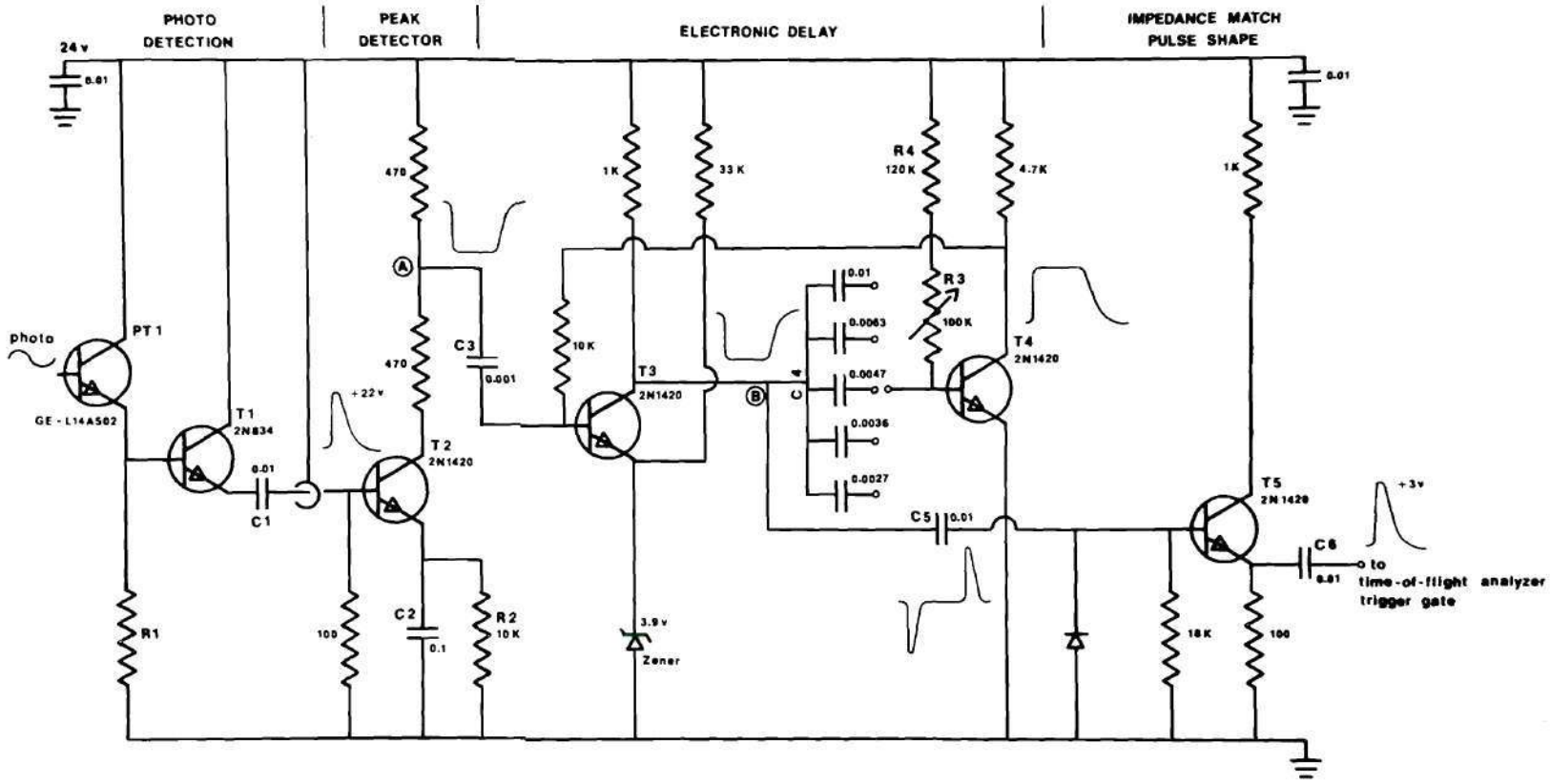

Figure 59. Diagram of the Zero Timing Unit Circuits

trigger a monostable multivibrator into an astable state. The multivibrator remains in this astable state for a time which is determined by the variable RC decay constant of resistors R3 plus R4 and one of the capacitors, C4, at which time it switches back to its stable state. The switch-back transition is picked up at point "B" and differentiated in capacitor C5. This new zero timing pulse, which is now delayed by the amount (R3 + R4) $\times$ C4, is shaped and tailored to the input requirements of the time-of-flight analyzer, impedance matched to the 100 ohm coaxial cable by transistor T5 and sent on to the analyzer trigger gate.

In summary then, the peak of the phototransistor timing pulse is delayed in the monostable multivibrator for a time which is characterized by the RC time constant of resistors R3 plus R4 and capacitor C4 before being shaped and sent on to start the time-of-flight analyzer counting sequence. The time difference between the beginning of the analyzer counting sequence and the middle of the chopper burst can then be calibrated out of the total neutron flight time.

APPENDIX B

BERYLLIUM TOXOCOLOGY

Contact with, or inhalation of, beryllium or its compounds can result in two types of disease, acute and chronic, depending on the duration and severity of exposure.

The acute disease results from a relatively brief exposure to a high concentration of beryllium, conditions that one might expect to encounter in a beryllium accident situation. The symptoms[60,80] following inhalation exposure, are: a dry nagging cough with occasional blood streaked sputum, burning and pain in the chest, some loss of appetite and increasing fatigue, and within a few days after exposure, a progressive shortness of breath which may be accompanied by a low grade temperature and a bluish discoloration of the skin due to an insufficient oxygen supply in the blood. In most cases of acute inhalation of beryllium or beryllium oxide, complete recovery will take place, with rest and removal from further exposure, in one to three weeks, however, in some cases the outcome has been fatal, although there have been no reported[81] fatalities from acute exposure since 1949.

Skin contact with a variety of beryllium compounds may result in acute dermatitis, ulceration, or subcutaneous granulomas, the exact occurrance depending largely upon the particular beryllium compound contacted and the nature of its contact with the skin. Acute contact dermatitis

usually arises in the manufacturing process during extraction of the beryllium by the fluoride and sulfate processes, but not from contact with beryllium metal itself or with beryllium oxide powder. Ulcerations are associated with penetration of the skin by any number of soluble beryllium salts. The ulcer is likely to remain on the skin indefinitely unless the beryllium material and surrounding tissue are removed surgically. Granulomas result chiefly from penetration through an open wound into the deeper subcutaneous layers of the skin by insoluble beryllium metal fragments or beryllium oxide powder. The granuloma behaves in a manner very similar to that of a benign tumor and is eventually surrounded by an area of heavily granulated scar tissue. The human body is generally able to isolate and surround the beryllium effectively, but it can never dissolve or remove it, so that, before complete healing can take place, the entire granuloma must be removed by extensive surgical excision.

The chronic form of the disease, commonly referred to as Berylliosis, may result from varying lengths of inhalation exposure to a wide range of beryllium concentrations, including very low concentrations. Berylliosis is insidious in that it mimics other lung diseases like pneumonia, chronic tuberculosis, and silicosis. The symptoms[60,80] are similar to the acute disease: shortness of breath on exertion and a dry, unproductive cough which gradually becomes more severe, are accompanied by dull pains in the chest area, rapid loss of weight, low blood pressure, fatigue and general malaise. In some cases there is a prompt onset of symptoms while in others there may be a delay of many months or even years between the last exposure and the onset of symptoms. The evolution of the disease also varies in individuals; a very few undergo spontaneous

recovery, but the prognosis is not good and the mortality rate is high.[82] As a rule, the course of the disease is that of progressive pulmonary involvement with eventual death from cardiac or respiratory failure. The chronic disease has been associated,[58,81] although not exclusively, with the more slowly soluble compounds such as the oxide or beryllium metal itself.

No harmful clinical effects have been reported from ingestion of beryllium containing materials.

APPENDIX C

DERIVATION OF THE DETECTOR EFFICIENCY EQUATION

To prove that

$$1 - \frac{\pi}{2}\left[L_{-1}(s) - I_1(s)\right], \tag{63}$$

as suggested by Beckurts,[83] is a solution of the detector efficiency equation

$$DTEFF(v) = \frac{1}{R}\int_o^R \left[1 - e^{-2\Sigma(v)(R^2-X^2)^{\frac{1}{2}}}\right] dX . \tag{62}$$

Substituting $s = 2\Sigma(v)R$ in equation 62 yields

$$DTEFF(v) = 1 - \frac{1}{R}\int_o^R e^{-\frac{s}{R}\left(R^2-X^2\right)^{\frac{1}{2}}} dX . \tag{100}$$

Let $X = R\cdot\sin\theta$ so that $dX = R\cdot\cos\theta\cdot d\theta$ and the integration limits $X = 0$ to R become $\theta = 0$ to $\pi/2$. Substituting in equation 100,

$$DTEFF(v) = 1 - \frac{1}{R}\int_o^{\pi/2} e^{-\frac{s}{R}\left(R^2-R^2\sin^2\theta\right)^{\frac{1}{2}}} R\cdot\cos\theta\cdot d\theta . \tag{101}$$

Replacing the identity $(1 - \sin^2\theta)^{\frac{1}{2}} = \cos\theta$ in the exponent of equation 101 and canceling terms,

$$\text{DTEFF}(v) = 1 - \int_o^{\pi/2} e^{-s\cdot\cos\theta}\ \cos\theta\cdot d\theta\ . \tag{102}$$

The problem is then reduced to one of proving that

$$\frac{\pi}{2}\left[L_{-1}(s) - I_1(s)\right] = \int_o^{\pi/2} e^{-s\cdot\cos\theta}\ \cos\theta\cdot d\theta\ . \tag{103}$$

If one expands the exponent in equation 103 in a power series according to

$$e^{-Z} = 1 - Z + Z^2/2! - Z^3/3! + \ldots\ , \tag{104}$$

then the right hand side, (RHS), of equation 103 becomes

$$\text{RHS} = \int_o^{\pi/2} \cos\theta\left[1 - s\cdot\cos\theta + \frac{s^2\cos^2\theta}{2!} - \frac{s^3\cos^3\theta}{3!} + \ldots\right] d\theta\ , \tag{105}$$

or

$$= \int_o^{\pi/2} \left[\cos\theta - s\cdot\cos^2\theta + s^2\,\frac{\cos^3\theta}{2!} - s^3\,\frac{\cos^4\theta}{3!} + \ldots\right] d\theta\ . \tag{106}$$

From the identity

$$\int_o^{\pi/2} \cos^n\theta\cdot d\theta = \frac{\sqrt{\pi}}{2}\cdot\frac{\Gamma\left(\frac{n+1}{2}\right)}{\Gamma\left(\frac{n+2}{2}\right)} \tag{107}$$

for $n > -1$, where Γ is the Gamma Factorial function, equation 106 reduces to

$$\text{RHS} = \sum_{n=1}^{\infty} \frac{\sqrt{\pi}}{2}\cdot(-s)^{n-1}\cdot\frac{\Gamma\left(\frac{n+1}{2}\right)}{\Gamma\left(\frac{n+2}{2}\right)}\cdot\frac{1}{(n-1)!}\ . \tag{108}$$

If the power series expansions for $L_{-1}(s)$ and $I_1(s)$, equations 65 and 68, are substituted into the left hand side, (LHS), of equation 103, then

$$\frac{\pi}{2}\left[\sum_{k=0}^{\infty}\frac{\left(\frac{s}{2}\right)^{2k}}{\Gamma\left(k+\frac{3}{2}\right)\cdot\Gamma\left(k+\frac{1}{2}\right)}-\sum_{k=0}^{\infty}\frac{\left(\frac{s}{2}\right)^{2k+1}}{k!\cdot\Gamma(k+2)}\right] \tag{109}$$

$$=\sum_{n=0}^{\infty}\frac{\sqrt{\pi}}{2}\cdot(-1)^{n-1}\cdot(s)^{n-1}\cdot\frac{\Gamma\left(\frac{n+1}{2}\right)}{\Gamma\left(\frac{n+2}{2}\right)}\cdot\frac{1}{(n-1)!}\cdot$$

Reversing the order of the left and right hand sides and performing some cancellation, the general term reduces to

$$\sqrt{\frac{\pi}{2}}\cdot\frac{1}{(n-1)!}\cdot\frac{\Gamma\left(\frac{n+1}{2}\right)}{\Gamma\left(\frac{n+2}{2}\right)}=\begin{cases}\dfrac{\frac{\pi}{2}\left(\frac{1}{2}\right)^{2k}}{\Gamma\left(k+\frac{3}{2}\right)\cdot\Gamma\left(k+\frac{1}{2}\right)} & \text{for } n=2k+1\\[2ex] \dfrac{\frac{\pi}{2}\left(\frac{1}{2}\right)^{2k+1}}{k!\cdot\Gamma(k+2)} & \text{for } n=2k+2\end{cases} \tag{110}$$

When we have proven the equality in equation 110, then we have also proven that

$$1-\frac{\pi}{2}\left[L_{-1}(s)-I_1(s)\right]$$

is a solution of the detector efficiency equation, equation 62.

Consider, in turn, each of the two terms on the right hand side

of equation 110. First, substituting n = 2k+1 into equation 110 yields

$$\frac{1}{(2k)!} \cdot \frac{\sqrt{\pi}}{2} \cdot \frac{\Gamma(k+1)}{\Gamma\left(k + \frac{3}{2}\right)} = \frac{\frac{\pi}{2} \cdot \left(\frac{1}{2}\right)^{2k}}{\Gamma\left(k + \frac{3}{2}\right) \cdot \Gamma\left(k + \frac{1}{2}\right)} \cdot \tag{111}$$

If we utilize the relations

$$\Gamma(k+1) = k\Gamma(k) \ , \tag{112}$$

$$\Gamma\left(\frac{1}{2}\right) = \sqrt{\pi} \ , \tag{113}$$

and

$$\Gamma(k) = (k-1)! \tag{114}$$

in equation 111, then

$$\frac{\sqrt{\pi}}{2} \cdot \frac{k!}{(2k)!} = \frac{\frac{\pi}{2}\left(\frac{1}{2}\right)^{2k}}{\Gamma\left(k + \frac{1}{2}\right)} \cdot \tag{115}$$

Writing out the $\Gamma\left(k + \frac{1}{2}\right)$ term,

$$\frac{k!}{(2k)!} = \frac{\sqrt{\pi} \cdot \left(\frac{1}{2}\right)^{2k}}{\left[\frac{1 \cdot 3 \cdot 5 \ . \ . \ . (2k-1)}{2^k} \cdot \Gamma\left(\frac{1}{2}\right)\right]} \tag{116}$$

$$= \frac{\frac{2^k}{2^{2k}}}{1 \cdot 3 \cdot 5 \ . \ . \ . (2k-1)} \tag{117}$$

$$= \frac{\frac{1}{2}}{1 \cdot 3 \cdot 5 \ . \ . \ . (2k-1)} \cdot \left[\frac{2 \cdot 4 \cdot 6 \ . \ . \ . (2k)}{2 \cdot 4 \cdot 6 \ . \ . \ . (2k)}\right] \tag{118}$$

$$= \frac{1\cdot 2\cdot 3 \ . \ . \ .k}{1\cdot 2\cdot 3\cdot 4\cdot 5\cdot 6 \ . \ . \ .(2k-1)\cdot(2k)} \tag{119}$$

$$\frac{k!}{(2k)!} = \frac{k!}{(2k)!} \ . \tag{120}$$

QED for the n = 2k+1 term.

Next, substituting n = 2k+2 into equation 110 yields

$$\frac{\sqrt{\pi}}{2} \cdot \frac{1}{(2k+1)!} \cdot \frac{\Gamma\left(k+\frac{3}{2}\right)}{\Gamma(k+2)} = \frac{\frac{\pi}{2}\left(\frac{1}{2}\right)^{2k+1}}{k!\ \Gamma(k+2)} \ . \tag{121}$$

Reversing the order of the left and right hand sides of equation 121, and canceling terms,

$$\frac{\sqrt{\pi}\cdot\left(\frac{1}{2}\right)^{2k+1}}{k!} = \frac{\Gamma\left(k+\frac{3}{2}\right)}{(2k+1)!} \ . \tag{122}$$

If the gamma function is expanded, the right hand side of equation 122 becomes

$$\text{RHS} = \frac{\left(k+\frac{1}{2}\right)}{(2k+1)!} \cdot \left[\frac{1\cdot 3\cdot 5 \ . \ . \ .(2k-1)}{2^k}\right] \cdot \Gamma\left(\frac{1}{2}\right) \cdot \left[\frac{2\cdot 4\cdot 6 \ . \ . \ .(2k)}{2\cdot 4\cdot 6 \ . \ . \ .(2k)}\right] \tag{123}$$

$$= \frac{\sqrt{\pi}\left(k+\frac{1}{2}\right)}{(2k+1)!} \cdot \frac{[1\cdot 2\cdot 3\cdot 4\cdot 5\cdot 6 \ . \ . \ .(2k-1)\cdot(2k)]}{2^k[2\cdot 4\cdot 6 \ . \ . \ .(2k)]} \tag{124}$$

$$= \frac{\sqrt{\pi}\left(k+\frac{1}{2}\right)}{(2k+1)\cdot(2k)!} \cdot \frac{(2k)!}{2^k[2\cdot 4\cdot 6 \ . \ . \ .(2k)]} \ . \tag{125}$$

Factoring out 2^k from the brackets in the denominator of equation 125,

$$RHS = \frac{\sqrt{\pi}\left(k + \frac{1}{2}\right)}{2\left(k + \frac{1}{2}\right) \cdot 2^{2k}[1 \cdot 2 \cdot 3 \ . \ . \ . (k)]} \tag{126}$$

$$= \frac{\sqrt{\pi}}{2^{2k+1} \cdot k!} \tag{127}$$

which is the same as the left hand side of equation 122, thus proving the equality for the n = 2k+2 term, and completing the proof of equation 110.

APPENDIX D

ERROR ANALYSIS

The basis and methods for the error analysis employed throughout this section are in accord with those outlined by Bevington[63] for the physical sciences. Wherever possible, comprehensive estimates have been made of the uncertainties in those factors in the measurements which were felt to have an effect on the outcome of the shape of the neutron energy spectrum. Included are estimates of both random and systematic uncertainties such that the resulting confidence limits are a measure of the overall accuracy of the experimental values rather than just the precision or reproducibility of the measurements. We use the terms accuracy to mean a measure of the relationship of the experimental value to the "true" value which is dependent to some extent on how well one is able to control or compensate for systematic errors; and precision to refer to the reproducibility or resolution of a value which is dependent on how well one can overcome or analyze random (perhaps statistical) errors.

The stated confidence limits, in all cases, are in terms of the standard deviation, σ, in an assumed Gaussian distribution of values, where the standard deviation corresponds roughly to the 67 percent probable error limits.

In general, the estimated uncertainty in a measured value is composed of any number of contributing parameters. If these parameters are independent, then a property of the Gaussian distribution is that the

standard deviation of the composite is equal to the square root of the sum of the squares of the standard deviations of the individual components. In mathematical terms, if x is influenced by uncertainties in y, z, etc., then

$$\sigma_x = \left(\sigma_y^2 + \sigma_z^2 + \ldots\right)^{\frac{1}{2}} . \tag{128}$$

Independent confidence limits propagate through a succession of mathematical manipulations to an uncertainty in the final value, x, where x is a function of variables, u, v, etc., according to[63]

$$\sigma_x^2 = \sigma_u^2 \cdot \left(\frac{\partial x}{\partial u}\right)^2 + \sigma_v^2 \cdot \left(\frac{\partial x}{\partial v}\right)^2 + 2\sigma_{uv}^2 \cdot \left(\frac{\partial x}{\partial u}\right) \cdot \left(\frac{\partial x}{\partial v}\right) . \tag{129}$$

The first two terms above are squares of individual deviations weighted according to the rates of change in their functional dependence within x. The third term is the average of cross terms involving simultaneous correlated deviations in u and v. If one makes the assumption that the fluctuations in u and v are uncorrelated, that is, u is not a function of v, then one would expect this simultaneous contribution to vanish by statistical cancellation in the limit of large random selections of observations such that equation 129 reduces to

$$\sigma_x^2 = \sigma_u^2 \cdot \left(\frac{\partial x}{\partial u}\right)^2 + \sigma_v^2 \cdot \left(\frac{\partial x}{\partial v}\right)^2 , \tag{130}$$

with additional similar terms corresponding to additional variables.

The following simple relations hold for the usual functional

dependencies encountered.

Addition or Subtraction: $x = au \pm bv$,

$$\sigma_x^2 = a^2 \cdot \sigma_u^2 + b^2 \cdot \sigma_v^2 \qquad (130\text{-a})$$

Multiplication or Division: $x = \pm auv$ or $x = \pm au/v$,

$$\frac{\sigma_x^2}{x^2} = \frac{\sigma_u^2}{u^2} + \frac{\sigma_v^2}{v^2} \qquad (130\text{-b})$$

Powers: $x = au^{\pm b}$,

$$\frac{\sigma_x}{x} = b \cdot \frac{\sigma_u}{u} \qquad (130\text{-c})$$

Exponentiation: $x = ae^{\pm bu}$,

$$\frac{\sigma_x}{x} = b \cdot \sigma_u \ . \qquad (130\text{-d})$$

The final form of the neutron energy spectrum, from equation 90, is given by

$$\phi(E) = \frac{[\phi(t)/\text{LIVETIM}] - \text{BKGND}}{v^3 \cdot \text{TRANS} \cdot \text{SCATT} \cdot \text{DTEFF} \cdot \text{RESOLTN}} \qquad (90)$$

where the symbols have the meanings defined earlier. The contributions of each of the terms in equation 90 to the overall uncertainty in $\phi(E)$ will be discussed in turn in the following pages.

Uncertainty in the Measured Time Spectrum, $\phi(t)$

Statistics

The uncertainty in the measured time spectrum, $\phi(t)$, due to counting statistics is expressed as

$$\sigma_N = \sqrt{N} \tag{131}$$

where N is the number of counts recorded in a particular channel of the spectrum. The fractional error is then

$$\frac{\sigma_N}{N} = 1/\sqrt{N} \quad . \tag{132}$$

Beryllium Temperature

The shape of the measured neutron energy spectrum, especially the distortion below the Bragg cut-off, bears an obvious relationship to the behavior of the low energy beryllium scattering cross section. The minimum value of the beryllium inelastic scattering cross section, below the Bragg cut-off, has been estimated, based on the cross section values at 300, and 440°K in Figure 2, to depend on temperature roughly like 0.5 percent per °K. The average temperature variation within a single spectrum measurement, or from one measurement to another, is estimated to be of the order of ± 2°K, which results in a total uncertainty in the minimum value of the cross section below the Bragg cut-off, from the temperature dependence of the inelastic scattering component, of roughly ± 1 percent. However, in Chapter V, it was determined that a temperature change of 5.5°K did not noticeably change the spectrum shape within the stated error limits (see Figure 38) such that one seems justified in

neglecting spectrum shape distortions as a result of small beryllium temperature fluctuations of the magnitude encountered within a single spectrum measurement or from one measurement to another.

Equipment Alignment

Included are the effects of vertical and horizontal alignment of the beryllium assembly, the chopper, and the detector.

Vertical Assembly Alignment. Figure 60 shows the ratios of pairs of interior and leakage spectra measured under identical experimental conditions except that, in one set, the beryllium assembly was situated approximately one fourth inch lower in the thermal column cavity. The behavior of these ratios indicates that the spectra measured in the lower assemblies were progressively depleted in lower energy neutrons. The origin of this behavior is related to the anomalous transmission effect, discussed in detail in Chapter V, and can be explained as follows. With the beryllium assembly situated one fourth inch low in the thermal column cavity, the extracted neutron beam passing through the chopper contained statistically more neutrons emerging from the lower rotor slits. The neutron spectrum was then depleted in lower energy neutrons as a result of the Doppler velocity shift between the neutrons and the peripheral slit spin axes and the vertical displacement of the slit sides.

The actual uncertainty in the assembly height in the thermal column cavity is estimated to be of the order of one sixteenth inch, resulting in an uncertainty in the shape of the measured neutron energy spectrum, deduced from Figure 60, which ranges from zero at high energies to nearly four percent at lower energies, below the Bragg cut-off.

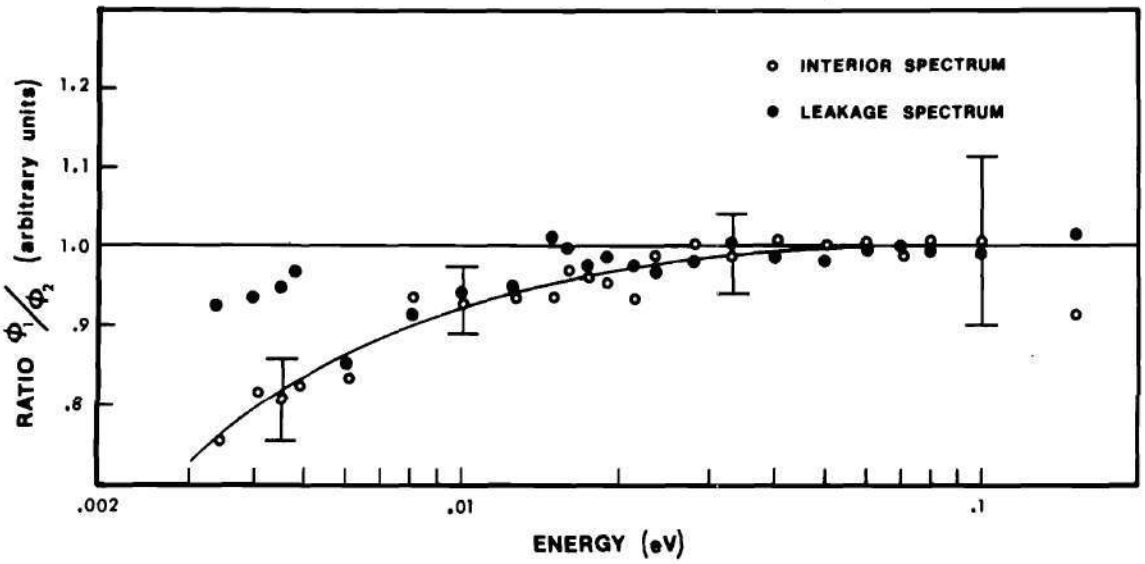

Figure 60. Ratio of Pairs of Angular Interior and Leakage Spectra Measured Under Identical Circumstances Except That, In One Set, the Beryllium Assembly Was Situated 1/4 Inch Below Center in the Thermal Column Cavity

Vertical Chopper Alignment. The sensitivity of the shape of the measured spectrum to changes in the chopper vertical alignment with respect to the center of the neutron beam is reflected in the high and low beam spectrum behavior in Figure 27. The origin of this spectral distortion again lay in the aforementioned anomalous transmission effect for neutrons traversing the rotor through the upper or lower peripheral slits. On a quantitative basis, it is not a straightforward matter to relate the distortions in Figure 27 to those for small changes in vertical alignment due to the complex nature of the combined effect of a slight addition of high beam coupled with a slight reduction in low beam, or vice versa. However, the quantitative Doppler velocity shift does go like H^2 where H is the radial distance from the rotor axis, so that the spectral distortion is expected to be small if the uncertainty in the chopper vertical

alignment is confined to a narrow range around the beam axis. Therefore, the uncertainty in the shape of the measured spectrum, as a result of the estimated uncertainty in the chopper height of roughly one sixteenth to one eighth inch, is assumed to be of the same order of magnitude as that from the aforementioned uncertainty in the assembly height in the thermal column.

Detector Vertical Alignment. The distortion in the measured spectrum shape resulting from raising or lowering the neutron detector approximately 1.4 inches is illustrated in Figure 61. Here again, the major neutron intensity distortions observed can be attributed to the anomalous transmission effect, vis-a-vis the detector in the high position "saw" statistically more neutrons in the beam which had passed through the upper slits in the chopper rotor, and the measured spectrum was thus enriched in low energy neutrons by the Doppler velocity shift and vertical slit motion; and vice versa for the low detector position. In addition, a very slight shift in peak energies, up for the low detector and down for the high detector, was noted in Figure 61. This energy shift resulted from changes in the angular preset delay, of the order of one degree of rotation, when the neutron beam passed through the "open" rotor slits at a slight angle from the horizontal, directed upwards or downwards toward the off-axis detector. The energy shift had the effect of applying inappropriate correction factors to the measured spectrum and resulted in a shape distortion which was roughly 10-20 percent as large as, and in the opposite direction to, that from the anomalous transmission effect. The net combined uncertainty, then, in the measured spectrum shape from the estimated one fourth inch uncertainty in the detector height, deduced from

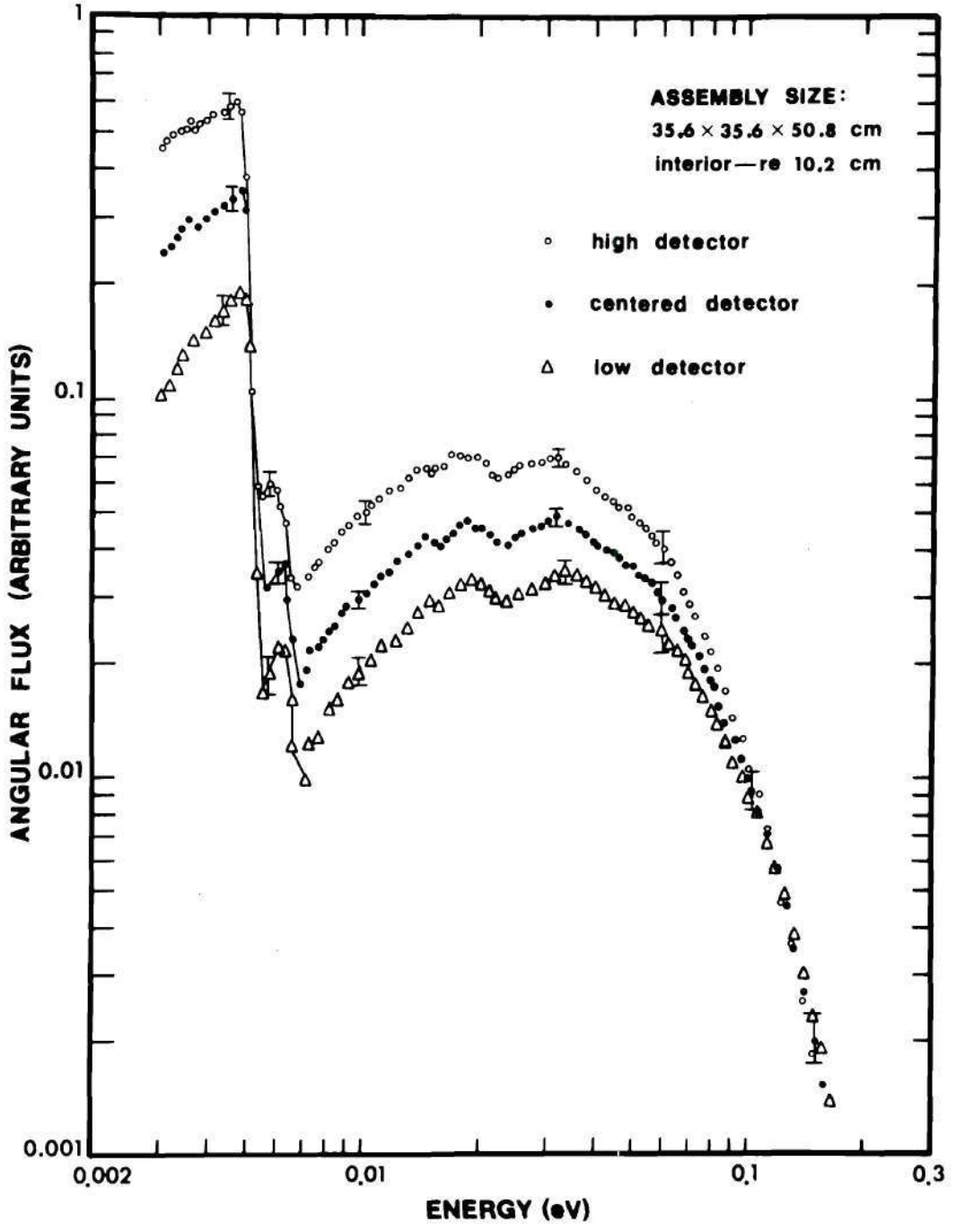

Figure 61. Identical Beryllium Spectra Measured with the Detector Situated, Respectively, 1.4 Inches High, in the Center of the Neutron Beam, and 1.4 Inches Low. (Normalization is arbitrary.)

Figure 61, ranges from zero at high energies to roughly four percent at very low energies.

Horizontal Alignment. Figure 62 shows the ratio of identical beryllium spectra measured with the detector located on the axis of, and subsequently shifted in a horizontal plane five inches off-of, the centerline of the flight path.

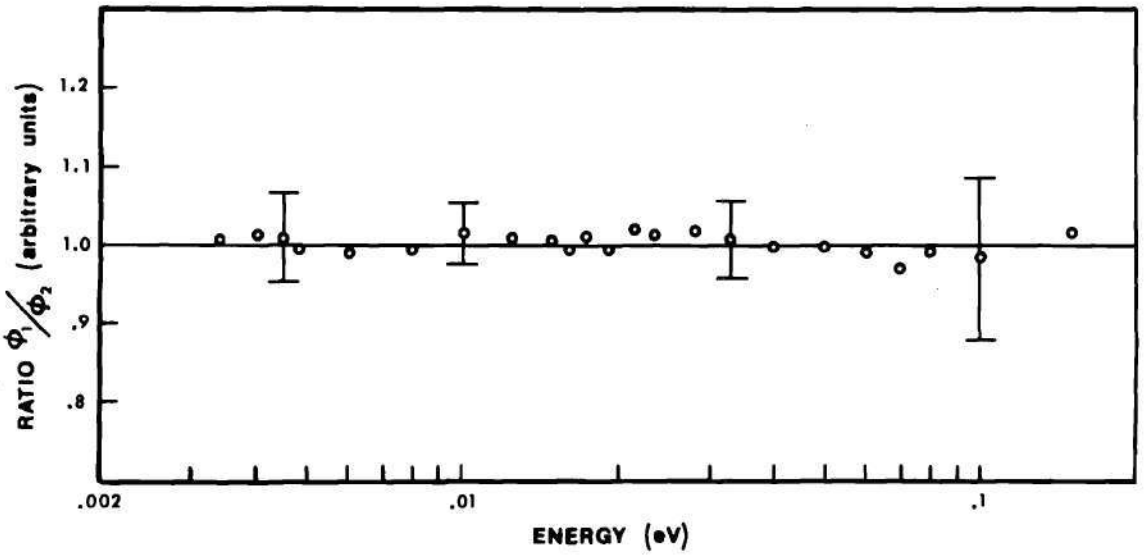

Figure 62. Ratio of Identical Beryllium Spectra Measured with the Detector Situated On, and Subsequently Shifted Off-Of, the Flight Path Center Axis

There was no spectrum shape distortion apparent in Figure 62, leading one to conclude that a negligible error existed from horizontal alignment uncertainties, which include the effects of small shifts in the horizontal positions of either the detector or the chopper, and additionally the uncertainty in centering or cocking of the beryllium assembly in the thermal column cavity (exclusive of extraction channel alignment effects which were treated separately).

Compilation of Alignment Uncertainties. If one assumes that the aforementioned effects of system alignment are statistically independent, then the net resultant uncertainty in the measured spectrum shape, from equation 128, can be calculated from the square root of the sum of the squares of the individual effects. The net uncertainty in the measured spectrum shape as a result of vertical system alignment is compiled in Table 4.

Table 4. Fractional Uncertainties (%) in the Measured Spectrum Shape Resulting from Uncertainties in Vertical Assembly, Chopper, or Detector Alignment

Uncertainty (%)	Energy (eV)
0.0	0.15
0.0	0.10
0.0	0.06
0.6	0.033
3.0	0.010
4.8	0.006
6.2	0.0045

It is important to point out that these confidence limits reflect a more or less absolute uncertainty in the assembly-chopper-detector system alignment, but, since this (especially vertical) alignment was the same from measurement to measurement, one does not expect to see these uncertainties manifest themselves in scatter in the measured data. Thus, these particular confidence limits express the overall accuracy in the system alignment rather than just the precision or reproducibility.

Uncertainty in Space Position Within the Assembly

Inasmuch as the measured energy spectra were strong functions of

space position along the longitudinal axis of the beryllium assemblies, an error in the location from which the neutron beam was extracted, the reentrant channel depth, could have resulted in a significant shift in the measured spectrum shape. The uncertainty in the reentrant channel depth is estimated to be of the order of 0.1 cm. From the roughly 150 percent per 10 cm and 250 percent per 10 cm changes in the spectrum shape above and below the Bragg cut-off in the 35.6 x 35.6 and 25.4 x 25.4 cm assemblies, respectively (see Figures 49 and 50), the uncertainty in the measured spectrum shape resulting from the estimated 0.1 cm uncertainty in the reentrant channel depth is 1.5 percent and 2.5 percent, respectively.

Other Errors

Supported by the calibration experiments discussed in Chapter V, it appears reasonable to neglect distortions in the measured spectrum shape from uncertainties in, or effects of, the following:

1. changes in the source neutron characteristics,

2. the assembly constituents, which includes block size and cleanliness, preferential polycrystal orientation direction, and angle dependent streaming between blocks,

3. the size of the reentrant channel,

4. the overall assembly length and "Z" direction infinity (except for the aforementioned five percent Bragg peak height influence in the re 10.2 cm spectra),

5. photoneutrons produced in the beryllium assembly by the interactions of high energy gamma rays from nearby cadmium shielding and significant numbers of photoneutrons from the interactions of fission gamma

rays, and

6. preferential scattering of low energy neutrons from materials around the beam.

The quantitative effect on the measured spectrum shape of characteristics like dissolved impurities, grain size, and void fraction in the polycrystalline beryllium blocks is difficult to estimate at this time without an absolute determination of the minimum value of $\Sigma_T(E)$ below the Bragg cut-off for these samples. However, the calibration measurement wherein spectra were measured in identical beryllium assemblies, composed of blocks with completely different histories, purchased years apart, is a check on these effects. The fact that the measured spectra were the same in each case (see Figure 36) is evidence that these effects were not too important in our beryllium samples.

The net combined confidence limits on the measured time spectrum, $\phi(t)$, from independent uncertainties in counting statistics, equipment alignment, and longitudinal space position, for a typical time spectrum, are shown in Table 5.

Table 5. Fractional Uncertainties (%) in a Typical Measured Spectrum Shape from the Combined Effects of Counting Statistics, Vertical Equipment Alignment, and Longitudinal Measurement Position

Energy (eV)	$\phi(t)$	$\sigma_{\phi(t)}/\phi(t)$ (%)
0.15	7200	1.18
0.10	15500	0.80
0.06	24500	0.64
0.033	19200	0.94
0.010	3670	3.42
0.006	3450	5.10
0.0045	20000	6.32

Uncertainty in the Analyzer Dead Time Correction Factor, LIVETIM

From equation 27, the analyzer dead time correction factor is given by

$$\text{LIVETIM} = (-\ 1.665 \cdot \text{N/SWEPS}) + 0.996 \qquad (27)$$

where

N is the count rate at a particular channel in the measured time spectrum,

SWEPS is the number of analyzer sweep cycles,

and - 1.665 and 0.996 are the slope and intercept, respectively, from the linear least squares fit to the data in Figure 19.

The standard deviations of the slope and intercept, determined from the least squares fitting procedure,[63] are, respectively, 0.031 and 0.007. Assuming insignificant error in the roughly 100,000 analyzer sweeps, and recalling that $\sigma_N = \sqrt{N}$, one finds that

$$\sigma^2_{\text{LIVETIM}} = \frac{1}{(\text{SWEPS})^2} \cdot (1.665 \cdot \text{N})^2 \cdot \left[\frac{(0.031)^2}{(1.665)^2} + \frac{1}{\text{N}}\right] + (0.007)^2 \ , \qquad (133)$$

which, for a more or less typical case of 10,000 counts recorded in a channel after 100,000 analyzer sweeps yields a roughly one percent confidence limit on the dead time correction factor for that channel.

Uncertainty in the Neutron Background Estimate, BKGND

From the measured background time distribution plotted in Figure 16, it is apparent that the primary source of error in the constant background estimate was a result of the superimposed structure from the

aforementioned background sources in the neutron beam which passed through and were pulsed by the chopper. The constant background estimate, calculated from the average number of counts in the first 20 channels of a measured spectrum, has been arranged to minimize the error in the region around the small Bragg shoulder peak between channels 160 and 200 where the net counting rate is low and thus where an error in the background estimate would be strongly felt in the resultant spectrum.

The estimated error in the constant background, from the structure in Figure 16, is outlined in Table 6.

Table 6. Fractional Uncertainties in the Constant Background Estimate from Superimposed Background Structure in Different Energy Regions of a Typical Spectrum

$\sigma_{BKGND}/BKGND$ (%)	E
10.0	above 0.03 eV
5.0	0.017 - 0.03 eV
2.0	below 0.017 eV

The 10 percent error in the background estimate around the "thermal bump" above 0.03 eV (below channel 100) was acceptable since the high spectrum counting rate in this same region reduced the net error in the final spectrum shape to only one to two percent.

In the special case of the 25.4 x 25.4 x 50.8 cm leakage spectrum, where the background intensity was such as to require that the background be subtracted channel by channel from the measured beryllium spectrum, the standard deviation was estimated from the square root of the number of counts in each channel of the measured background distribution.

Uncertainty in the Chopper Transmission Correction, TRANS

The energy dependent chopper neutron transmission function from equation 47 is

$$\begin{aligned} \text{TRANS} &= 1-(8/3)\cdot x^4 && \text{for } 0 \leqq x < 1/2 \quad (E > 0.025 \text{ eV}) \\ &= (16/3)\cdot x\cdot (1-x)^2\cdot (1+x/2) && \text{for } 1/2 \leqq x \leqq 1 \quad (E \leqq 0.025 \text{ eV}) \end{aligned} \tag{47}$$

where

$$x = R \cdot \sqrt{\omega/hv} \ .$$

Employing the techniques outlined in equations 130 to calculate the functional dependence of the standard deviation of the transmission correction on the uncertainty in the parameter x, one finds that,

$$\text{for} \quad E > 0.025 \text{ eV}, \quad \frac{\sigma^2_{\text{TRANS}}}{(\text{TRANS})^2} = \frac{113.8\ x^8}{(\text{TRANS})^2} \cdot \frac{\sigma_x^2}{x^2} \ , \tag{134-a}$$

and for $E < 0.025$ eV;

$$\frac{\sigma^2_{\text{TRANS}}}{(\text{TRANS})^2} = \frac{\sigma_x^2}{x^2} + \frac{4\sigma_x^2}{(1-x)^2} + \frac{0.25\ \sigma_x^2}{(1\ +\ 0.5x)^2} \ , \tag{134-b}$$

where

$$\frac{\sigma_x^2}{x^2} = \frac{\sigma_R^2}{R^2} + \frac{\sigma_\omega^2}{4\omega^2} + \frac{\sigma_h^2}{4h^2} + \frac{\sigma_v^2}{4v^2} \ . \tag{134-c}$$

The chopper slit radius, R, is 1.75 inches with an estimated uncertainty of 0.010 inch, so that

$$\frac{\sigma_R}{R} \cong 0.6\% \ .$$

The uncertainty in the measured chopper rotation rate, ω, has been estimated to be

$$\frac{\sigma_\omega}{\omega} \cong 1.0\% \ .$$

The uncertainty in the 0.069 inch chopper slit width, from the aforementioned gauge thickness in the slit spacers, punching burrs, and cadmium electroplate buildup on the chopper blades, is estimated to be of the order of 0.0015 inch, so that

$$\frac{\sigma_h}{h} \cong 2.2\% \ .$$

The uncertainty in the measured neutron velocity, v, is estimated from the chopper resolution function, calculated in detail in Appendix E and is outlined for a typical case in Table 7.

Table 7. Typical Fractional Resolution Uncertainties (%) in Measured Neutron Velocities

E (eV)	σ_v/v (%)
0.1	3.9
0.03	2.2
0.0045	1.1

Combining the uncertainties in equations 134 above, results in the following typical uncertainties in the chopper transmission function

$$\frac{\sigma_{TRANS}}{(TRANS)} \cong \begin{matrix} 0.8\% & @\ 0.03\ eV \\ 6.9\% & @\ 0.0045\ eV \ . \end{matrix} \qquad (135)$$

This uncertainty was a significant contributing factor to the overall error limits on the shape of the measured neutron spectrum, especially in the very low energy range where the relative chopper transmission fell below 50 percent, and hence where the correction factor became large.

The uncertainty in the shape of the measured energy spectrum resulting from the effects of anomalous neutron transmission above and below the chopper rotor spin axis has been included in the overall error estimate in the uncertainty in the assembly-chopper-detector vertical alignment limits.

Uncertainty in the Energy Dependent Scattering and Absorption Losses in the Air and Aluminum in the Neutron Flight Path, SCATT

The fractional neutron intensity transmitted through d cm of material is given by

$$I/I_o = e^{-\Sigma_T(v)\cdot d} \quad . \tag{48}$$

From equations 130, the uncertainty in the transmitted intensity is

$$\frac{\sigma_{(I/I_o)}}{(I/I_o)} = \sigma_{(\Sigma_T(v)\cdot d)} \quad . \tag{136}$$

For the case of the air in the neutron flight path between the beryllium assembly and the detector, the uncertainty in $\Sigma_T(v)\cdot d$ may have been as large as five percent from the effects of an estimated three to five percent uncertainty in the nitrogen and oxygen cross section fitting procedures in Figure 28, two to three percent fluctuations in the atmos-

pheric air pressure, and an estimated one to two percent uncertainty in the measured air flight path, d. Since the air scattering correction itself varied only from 10-20 percent over the energy range from 0.1 to 0.004 eV, then the resulting uncertainty in the measured spectrum shape from the aforementioned five percent uncertainty in the air scattering correction varied only from 0.5 to 1.0 percent, respectively, over this same energy range.

For the case of the aluminum in the neutron flight path, which was contained primarily in the chopper rotor and the detector cathode, the cross section shown in Figure 30 was assumed constant, dropping to a relative $1/v$ behavior below 0.0037 eV. The uncertainty in this fit is estimated to be of the order of 15 percent on the average above 0.0037 eV, due to neglect of the narrow superimposed higher order aluminum Bragg peaks in the cross section, and three percent below 0.0037 eV. The uncertainty in the thickness of aluminum in the flight path, primarily from neglect of the neutron streaming area through the exposed portions of the aluminum slit spacers in the chopper rotor, is estimated to be of the order of 20 percent. (Note that this particular error has been removed from the tabular data in Appendix G.) The total aluminum scattering correction factor was everywhere small, of the order of three to five percent, so that the resulting uncertainty in the shape of the measured spectrum from the aforementioned uncertainties in the aluminum scattering correction is only of the order of 1.9 percent above 0.0037 eV, and 0.8 percent below 0.0037 eV.

Uncertainty in the Detector Efficiency, DTEFF

The energy dependent detector efficiency has been shown to be given by

$$DTEFF = 1 - \frac{\pi}{2} \cdot \left[L_{-1}(s) - I_1(s) \right], \tag{63}$$

where

$L_{-1}(s)$ is the modified Struve function defined by the power series expansion in equation 65,

$I_1(s)$ is the modified Bessel function defined by the power series expansion in equation 68,

and $s = 2\Sigma(v)R$.

The uncertainty in the parameter "s" consisted of an estimated 0.5 percent uncertainty in the 96 percent B^{10} enrichment, 1.5 percent uncertainty in the 900 Torr detector fill gas pressure, 0.5 percent uncertainty in the $B^{10}(n,\alpha)$ cross section, and an estimated 1.0 percent uncertainty in the detector radius, R, from the additional path length for neutrons which traversed the detector at some angle other than perpendicular to the longitudinal axis. The uncertainty in the neutron velocity, which ranged from one to four percent from low to high energy, respectively, is given by the resolution function calculated in Appendix E, and outlined in Table 7. Table 8 follows from the combination of these independent effects according to the criterion in equation 128.

Table 8. Fractional Uncertainties (%) in the Parameter "s" in the Detector Efficiency Correction

σ_s/s (%)	E(eV)
4.3	0.1
3.0	0.03
2.2	0.0045

The uncertainty in the Struve and Bessel function expansions, equations 65 and 68, respectively, can be shown to be

$$\sigma^2_{L_{-1}}(s) = \sum_{k=1}^{\infty} \frac{4 \cdot k^2 \cdot s^{4k} \cdot \sigma_s^2 / s^2}{\pi^2 \cdot [((2k-1)!)^2 \cdot (k+1/2)]^2} , \tag{137}$$

and

$$\sigma^2_{I_1}(s) = \sum_{k=1}^{\infty} \frac{(s/2)^{4k+2} \cdot (2k+1)^2 \cdot \sigma_s^2 / s^2}{(k+1)^2 \cdot (k!)^2} , \tag{138}$$

and the resulting uncertainty in the detector efficiency is given by

$$\frac{\sigma^2_{DTEFF}}{(DTEFF)^2} = \frac{\pi^2}{4} \cdot \frac{\left[\sigma^2_{L_{-1}}(s) + \sigma^2_{I_1}(s)\right]}{(DTEFF)^2} . \tag{139}$$

Typical values of the energy dependent detector efficiency and associated uncertainty are shown in Table 9.

Table 9. Relative Detector Efficiency and Associated Fractional Uncertainty (%) in the Energy Range from 0.1 to 0.0045 eV

E(eV)	DTEFF (%)	σ_{DTEFF}/DTEFF (%)
0.1	19.5	4.99
0.03	32.5	4.06
0.0045	62.6	6.03

The high energy uncertainty was governed by the large resolution uncertainty, whereas at low energies (high values of s) the uncertainty was large due to the small difference between the Struve and Bessel functions in equation 63 (see Figure 32).

Uncertainty in the Resolution Correction Factor, RESOLTN

The resolution width correction factor applied to the measured neutron energy spectrum above 0.1 eV, from equation 78 is

$$\text{RESOLTN} = 1 + \left[\frac{\phi_o''(t)}{\phi_o(t)} \cdot \frac{1}{2} \cdot \left(\frac{\delta t^2_{burst}}{6} + \frac{\delta t^2_{det}}{3} + \frac{\delta t^2_{channel}}{3}\right)\right] \qquad (78)$$

where

$\phi_o(t)$ is the assumed high energy Maxwellian time distribution if there were no resolution distortion.

The uncertainty in the term in square brackets above was perhaps as large as 25 percent, primarily as a result of the sensitivity of the second time derivative

$$\phi_o''(t) = \frac{\partial^2 \phi_o(t)}{\partial t^2} \qquad (140)$$

to the assumed high energy Maxwellian behavior. The fractional error in the resolution correction factor from this uncertainty in the Maxwellian fit is then

$$\frac{\sigma_{RESOLTN}}{RESOLTN} = \frac{(RESOLTN - 1)}{RESOLTN} \cdot 0.25 \, . \qquad (141)$$

The resolution correction factor itself was only of the order of 1.03 at 0.15 eV and 1.08 at 0.20 eV so that the resulting uncertainty in the high energy spectrum shape from application of this correction was only one to two percent, respectively, in the high energy range.

There was, of course, a resolution error in other regions of the

spectrum besides E > 0.1 eV. However, due to the lack of an analytic form for $\phi_o(t)$ in these regions, one is unable to calculate a resolution correction, nor can one quantitatively estimate the error involved except to say that it was important only within a few channels of sharp discontinuities in the spectrum, such as around the low energy Bragg cut-off, where the effect was to round-off peaks and valleys. The resolution width $\Delta E/E$, from Appendix E is an indicator of the "importance width" of this resolution error in various areas of the measured neutron energy spectrum.

Compilation of Errors for the Uncertainty in the Final Spectrum Shape

Let

$$\phi_{net}(t) = \frac{\phi(t)}{\text{LIVETIM}} - \text{BKGND} \tag{142}$$

in equation 90 so that

$$\phi(E) = \frac{\phi_{net}(t)}{v^3 \cdot \text{TRANS} \cdot \text{SCATT} \cdot \text{DTEFF} \cdot \text{RESOLTN}} \; . \tag{143}$$

In addition, in the low energy range

$$\phi_{ave}(E) = \frac{1}{N} \sum_{N} \phi_N(E) \; . \tag{144}$$

The uncertainty in the final spectrum shape, $\phi(E)$, can be derived from the criteria in equations 130, and shown to be given by

$$\frac{\sigma^2_{\phi(E)}}{(\phi(E))^2} = \frac{\sigma^2_{\phi_{net}(t)}}{(\phi_{net}(t))^2} + 9\,\frac{\sigma^2_v}{v^2} + \frac{\sigma^2_{TRANS}}{(TRANS)^2} + \frac{\sigma^2_{SCATT}}{(SCATT)^2} \tag{145}$$

$$+ \frac{\sigma^2_{DTEFF}}{(DTEFF)^2} + \frac{\sigma^2_{RESOLTN}}{(RESOLTN)^2} ,$$

where

$$\frac{\sigma^2_{\phi_{net}(t)}}{(\phi_{net}(t))^2} = \frac{\left(\frac{\sigma^2_{\phi(t)}}{\phi(t)^2} + \frac{\sigma^2_{LIVETIM}}{(LIVETIM)^2}\right) \cdot \frac{\phi^2(t)}{(LIVETIM)^2} + \sigma^2_{BKGND}}{\left(\frac{\phi(t)}{LIVETIM} - BKGND\right)^2} . \tag{146}$$

In addition,

$$\sigma^2_{\phi_{ave}(E)} = \frac{1}{N^2}\sum_N \sigma^2_{\phi_N(E)} = \frac{1}{N}\,\sigma^2_{\phi_N(E)} . \tag{147}$$

The linear extrapolation between averaged flux values, to yield $\phi_{ext}(E)$ in equation 91, has been found to reduce the associated uncertainty limits by roughly $1/\sqrt{3}$. The extrapolation procedure was, however, somewhat unreliable at very high energies (above 0.1 eV) due to the large resolution uncertainty, such that "eyeball fitting" was found to be more reliable in the two highest energy extrapolated fluxes.

The uncertainty in the ratio of two spectra, from equations 130 is

$$\frac{\sigma^2_{[\phi_1/\phi_2]}}{(\phi_1/\phi_2)^2} = \frac{\sigma^2_{\phi_1}}{\phi_1^2} + \frac{\sigma^2_{\phi_2}}{\phi_2^2} , \tag{148}$$

where $(\sigma^2_{\phi_1})/\phi^2_1$ and $(\sigma^2_{\phi_2})/\phi^2_2$ are the uncertainties in the individual spectra as calculated from equations 145 and 146.

Table 10 is a breakdown of a typical compilation of fractional uncertainties resulting from application of equation 145 to the statistics and experimental conditions of a representative measured neutron energy spectrum (that from the 35.6 x 35.6 x 50.8 cm leakage assembly), and reflects the relative importance of the various components and correction factors to the overall error limits on the final spectrum shape over the energy range of interest from roughly 0.003 to 0.15 eV.

Table 10. Breakdown of Representative Fractional Uncertainties in the Parameters in a Typical Measured Neutron Energy Spectrum

E (eV)	ϕ(t)	LIVETIM	RESOLTN	BKGND	ϕ_{net}(t)	V	TRANS	DTEFF	SCATT	ϕ(E)	ϕ_{ave}(E)	ϕ_{ext}(E)
0.15	1.18	0.71	0.65	10.00	4.19	4.70	0.22	5.69	2.10	15.85	15.85	9.15
0.10	0.80	0.72	0.00	10.00	1.83	3.87	0.29	4.99	2.10	12.85	12.85	7.42
0.06	0.64	0.73	0.00	10.00	1.32	3.03	0.42	4.37	2.10	10.31	10.31	5.95
0.033	0.94	0.72	0.00	10.00	1.69	2.31	0.70	3.98	2.10	8.34	5.90	3.41
0.010	3.42	0.71	0.00	2.00	7.46	1.41	4.44	4.36	2.10	10.71	6.18	3.57
0.006	5.10	0.71	0.00	2.00	11.54	1.16	5.79	5.20	2.10	14.44	8.34	4.81
0.0045	6.32	0.72	0.00	2.00	7.01	1.06	7.07	6.03	2.10	12.16	7.02	4.05

APPENDIX E

ENERGY RESOLUTION

The resolution width in the time-of-flight analysis, which manifested itself in a statistical uncertainty in the measured neutron energy, was composed primarily of the time uncertainties in the chopper burst width and the detector and analysis channel widths as well as uncertainties in the determination of the timing parameters.

Chopper Burst Width

The chopper burst shape for a parallel neutron beam incident on a narrow rectangular spinning slit is nearly triangular at all neutron velocities above the cut-off, with a base width, $2\tau_{BW}$ from Figure 23 of

$$2\tau_{BW} = \begin{cases} h/\omega R & \text{for } v > 4v_{co} \\ 4(h/\omega v)^{1/2} - 4R/v & \text{for } v < 4v_{co} \end{cases} \qquad (149)$$

where

h is the slit width,

R is the slit radius,

and ω is the angular velocity of the spinning rotor.

The base width of the chopper burst from equation 149 at representative energies throughout the spectrum is shown in Table 11.

Table 11. Base Width of the Triangular Chopper Burst at Representative Energies in the Neutron Spectrum

E(eV)	$2\tau_{BW}$(μsec)
0.1	96.6
0.03	96.6
0.0045	80.0

Neutron Path Length in the Detector

The neutron path length in the detector reflects a statistical uncertainty in the neutron penetration distance into the detector volume before an interaction takes place to produce a signal pulse. The time uncertainty distribution is assumed rectangular with a base width, τ_{DW}, given by

$$\tau_{DW} = D/v \tag{150}$$

where

D is the detector diameter,

and v is the neutron velocity.

The detector path length uncertainty at representative energies throughout the spectrum is shown in Table 12 for the five cm diameter RSN-44A detector. The values in Table 12 are, in general, an overestimation of the detector path length uncertainty since the thickest detector was chosen for analysis, and, in addition, the "effective" diameter was expected to be considerably less than the "actual" diameter for low energy neutrons with short mean-free-paths in the detector.

Table 12. Detector Path Length Uncertainty at Representative Energies in the Spectrum for the Five cm Diameter RSN-44A Detector

E(eV)	v(m/sec)	τ_{DW}(μsec)
0.1	4374	12
0.03	2396	21
0.0045	928	55

Analysis Channel Length

The analysis channel length is also rectangular with a base width, τ_{CW}, of 16 μsec.

Resolution Function

The basic resolution function was a superposition of the above time uncertainty distributions which, according to the central limit theorem of probability theory, is approximately a Gaussian distribution[63] characterized by a dispersion, σ^2, which is the sum of the squared deviations of all the partial functions. That is,

$$\sigma^2 = \sigma_{BW}^2 + \sigma_{DW}^2 + \sigma_{CW}^2 \qquad (151)$$

where

$\sigma_{BW}^2 = (2\tau_{BW})^2/6$ for the triangular chopper burst width resolution,

$\sigma_{DW}^2 = \tau_{DW}^2/12$ for the rectangular detector path length resolution,

and $\sigma_{CW}^2 = \tau_{CW}^2/12$ for the rectangular channel width resolution.

If the Gaussian distribution is characterized by the full width at half maximum, Δt, where

$$\Delta t = 2.354 \cdot \sigma \ , \tag{152}$$

then, the usual measure of the resolution of time-of-flight experiments, $\Delta t/L$, the "micro second per meter" resolution, and the energy resolution, $\Delta E/E$, are related by[67]

$$\frac{\Delta E}{E} = 0.028 \ \frac{\Delta t}{L} \ . \tag{153}$$

In terms of the standard deviation, σ_E,

$$\frac{\sigma_E}{E} = \frac{\Delta E}{2.354 \cdot E} \ . \tag{154}$$

Table 13 summarizes a typical set of time and energy resolution values at representative energies throughout the neutron spectrum.

Table 13. Time and Energy Resolution Parameters for Typical Experimental Conditions at Representative Energies Throughout the Neutron Spectrum

E (eV)	$\Delta t/L$ (μsec/meter)	$\frac{\Delta E}{E}$ (%)	$\frac{\sigma_E}{E}$ (%)
0.1	16.9	15.0	6.42
0.03	18.6	9.0	3.86
0.0045	22.1	4.15	1.78

In addition to the aforementioned resolution widths in the recorded neutron energy, one must include the effects of uncertainties in the determination of the neutron timing parameters. Since

$$E \approx v^2 \tag{155}$$

and

$$v \approx (fp)/(ft) \tag{156}$$

where fp is the neutron flight path

and ft is the neutron flight time,

then $$E \approx [(fp)^2/(ft)^2] \, . \tag{157}$$

Therefore, the uncertainty in the neutron energy from uncertainties in the determination of the neutron flight path and measured flight time is

$$\frac{\sigma_E^2}{E^2} = 4 \frac{\sigma_{fp}^2}{(fp)^2} + 4 \frac{\sigma_{ft}^2}{(ft)^2} \, . \tag{158}$$

Flight Path Uncertainty

Consider first the sources of error in the determination of the neutron flight path. The uncertainty in the measurement of the flight path from the center of the chopper rotor to the center axis of the detector is estimated, conservatively, to be 3/8 inch. Small amounts of angular cocking of the neutron detector at the end of the flight path, such that it would no longer have been perpendicular to the neutron beam direction, are estimated to contribute a 1/2 inch uncertainty to the flight path. There was an additional increase in the neutron flight path near the extremities of the detector, related to the angular divergence of the beam, which was calculated to be of the order of 1/4 inch for a typical flight path resulting in an uncertainty of ± 1/8 inch. These last two effects, that for the detector cocking and the angular divergence

of the beam, were most important in the measurement of leakage spectra where the entire 16 inch active length of the detector was exposed to the beam.

Combining these effects according to the square root of the sum of the squares yields

$$\sigma_{fp} = 0.64 \text{ inch } (1.6 \text{ cm}) \ , \tag{159}$$

or, for a typical 2.8 meter flight path,

$$\frac{\sigma_{fp}}{fp} = 0.6\% \ . \tag{160}$$

Figure 63 is a plot of a parametric study of the effect of a 10 percent uncertainty in the neutron flight path on the shape of a typical measured neutron energy spectrum. The obvious energy shift was coupled with a slight change in the relative spectrum shape as a result of the application of inappropriate energy dependent correction factors to the distorted spectra.

Flight Time Uncertainty

The measured neutron flight time, from equation 33, is given by

$$ft = FT + (N-1)\ \Delta \tag{33}$$

where

FT is the zero time correction factor,

N is the channel number

and Δ is the analysis channel length.

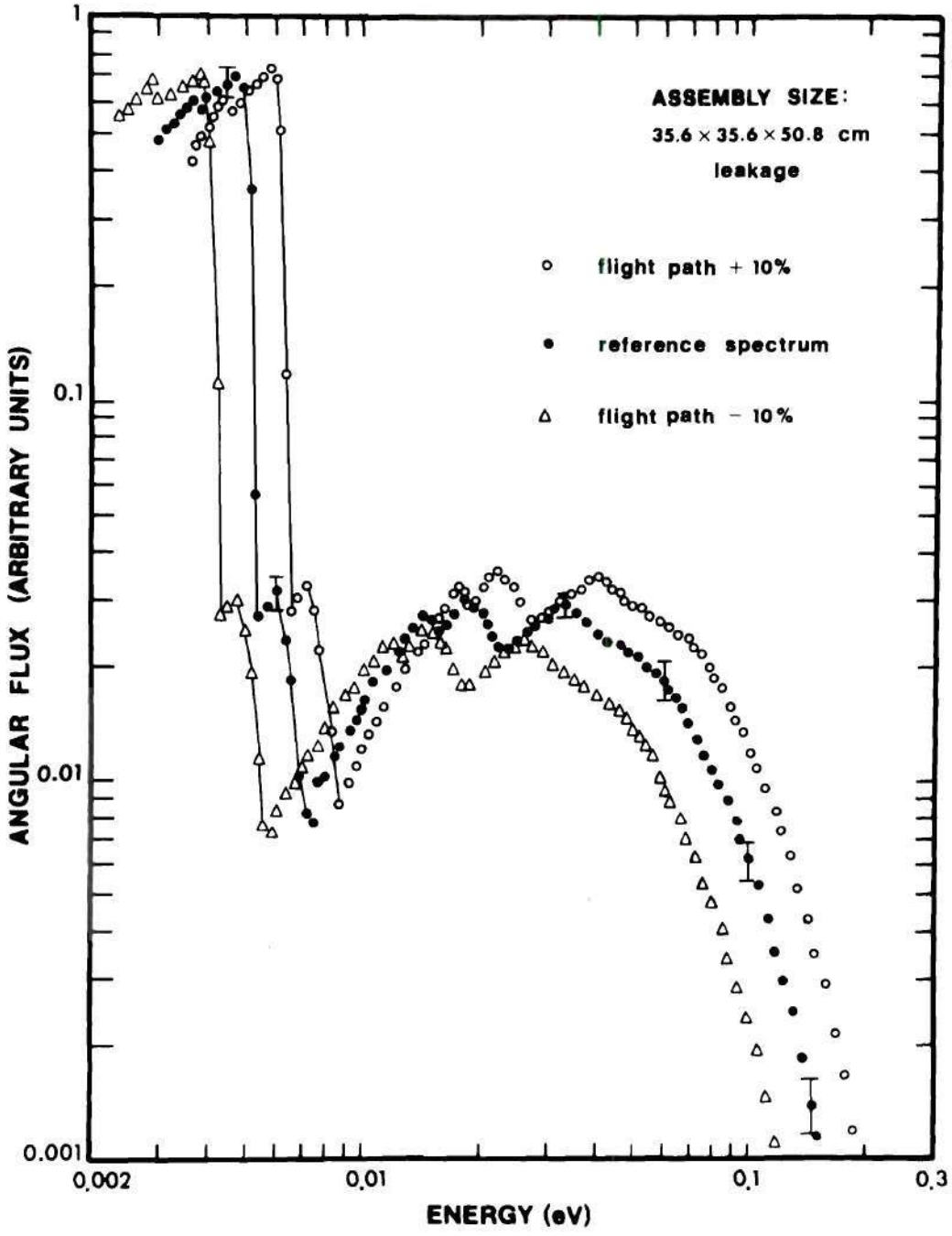

Figure 63. Parametric Study of the Effect of a ± 10% Error in the Neutron Flight Path on the Shape of a Typical Measured Beryllium Spectrum. (Normalization is arbitrary.)

The zero time correction factor, FT, has been shown in equation 31 to be composed of the following:

i) the chopper angular preset delay, $\frac{-9.4^{\circ}}{6 \cdot RPM}$,

ii) the 99 μsec chopper electronic delay,

iii) the 15 μsec time-of-flight analyzer fixed delay

and iv) the time from the initiation of the analyzer sweep to the middle of the first analysis channel, $\Delta/2$.

The sources of error in the neutron flight time in equation 33 then are:

1) the uncertainty in the 9.4° angular preset delay between the peak in the zero timing photo pulse and the peak in the chopper neutron burst,

2) the uncertainty in the chopper RPM,

3) the uncertainty in the chopper electronic delay,

4) the uncertainty in the time-of-flight analyzer fixed delay,

and 5) the uncertainty in or between the 16 μsec analysis channel widths.

Uncertainty in the Angular Preset Delay

The 9.4° angular preset delay was determined from the monoenergetic neutron beam calibration experiment, discussed in Chapter V, to an accuracy of no better than 0.1°. In addition, the assembly or detector vertical alignment affected the relative angular preset delay, as discussed in connection with Figure 61, when the neutron beam passed through the rotor slits at some angle other than horizontal, directed toward the detector. The actual uncertainty in the angular preset delay from the estimated 1/16 inch uncertainty in the assembly height and the 1/4 inch

uncertainty in the detector height is 0.19° and 0.18°, respectively. There was, in addition, a relative timing difference from one pulse to the next, due to slight mirror misalignments, which is estimated to be of the order of 1.0 percent (0.1°) from observation of the timing pulse electronic jitter. The total uncertainty, then, in the 9.4° angular preset delay from the combination of the aforementioned independent effects is of the order of 0.3° (3.0 percent).

Uncertainty in the Chopper RPM

The uncertainty in the measured chopper rotation rate, RPM, has been estimated to be of the order of 1.0 percent.

Uncertainty in the Chopper Electronic Delay

The uncertainty in the 99 μsec chopper electronic delay was composed of the following. The uncertainty in the initial oscilloscope calibration is estimated to be of the order of 1-2 μsec (1-2 percent). The duration of the delay has been found to be somewhat line voltage dependent, of the order of 2.0 percent per volt, due to the voltage sensitivity of the multivibrator flip-flop trigger points. Operating with power from the ac line voltage regulator, this sensitivity was expected to affect the delay uncertainty of the order of 1.0 percent. The small systematic error in the peak detector firing point with respect to the actual peak in the photo-timing pulse, that is, the fact that the peak detector fired consistently 0.7 volt early due to the inherent reverse bias voltage in the germanium transistor used in the unit, has been calibrated out of the delay in the monoenergetic neutron beam experiment. The statistical uncertainty in the peak detector firing point due to photo peak spreading

at low chopper RPM's has been observed to be negligibly small. Therefore, the net uncertainty in the 99 μsec chopper electronic delay, from the initial calibration and from the effects of small line voltage fluctuations is of the order of two μsec (two percent).

Uncertainty in the Time-of-Flight Analyzer Fixed Delay

The uncertainty in the 15 μsec time-of-flight analyzer fixed delay, between receipt of the timing trigger pulse and initiation of the data recording sequence, has been determined, from the aforementioned dual pulse calibration experiment, to be much less than one μsec and is thus considered to have a negligible effect on the total measured flight time.

Uncertainty in the Analysis Channel Width

The effect of a small error in the analysis channel width, or of a small switching time uncertainty between successive channels could be to compound a substantial time error in the later channels of a measured spectrum. Consequently, an experiment was performed wherein two pulses, one "trigger" and the other "signal," were put into the time-of-flight analyzer at an accurately known time interval. With very short (four μsec) channel widths, to compound small errors of the type discussed above at large N, the channel number into which the signal pulse fell was recorded. The experiment revealed that the stated channel widths were very accurate in that there was no detectable cumulative error inasmuch as there was no noticeable deviation from $N \cdot \Delta$. In addition, the time delay between channels was either very short or was included within the stated channel widths since, here again, there was no detectable cumulative error.

Superposition of Flight Time Uncertainties

The superposition of all of the aforementioned uncertainties in the measured neutron flight time, according to the criteria in equations 130 in Appendix D, results in a 13.6 μsec uncertainty, which is approximately equivalent to one 16 μsec analysis channel width. For a typical neutron flight path of 2.85 meters, the measured flight time, ft, and fractional flight time uncertainty, σ_{ft}/ft, are shown in Table 14 at representative energies throughout the spectrum.

Table 14. Measured Flight Time and Fractional Flight Time Uncertainty at Representative Energies in a Neutron Spectrum Measured with a 2.85 Meter Flight Path

E(eV)	ft(μsec)	σ_{ft}/ft(%)
0.1	652	2.1
0.03	1189	1.1
0.0045	3079	0.4

Figure 64 is a plot of a parametric study of the effect of a 100 μsec error in the measured neutron flight time on the shape of a typical spectrum. The energy shift was most pronounced at high energies where the fractional error in the neutron flight time was the greatest. There was also evidence of a slight shift in relative spectrum shape as a result of the application of inappropriate energy dependent correction factors to the distorted spectra.

Energy Uncertainty from the Combined Effects of Flight Path and Flight Time Uncertainties

The fractional uncertainty in the measured neutron energy in equation

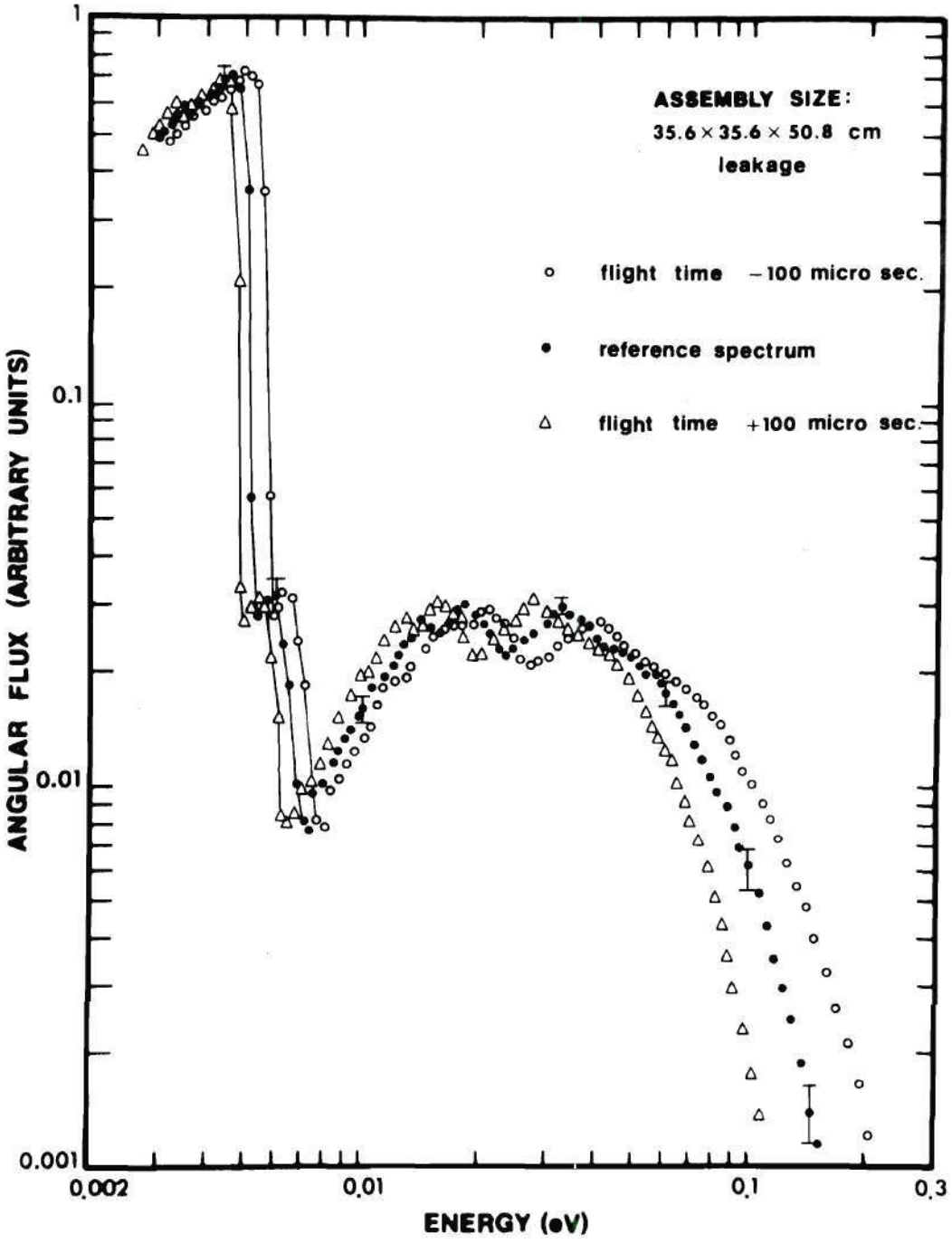

Figure 64. Parametric Study of the Effect of a ± 100 μsec Error in the Neutron Flight Time on the Shape of a Typical Measured Beryllium Spectrum. (Normalization is arbitrary.)

157 resulting from a combination of the effects of the 0.6 percent uncertainty in the determination of the neutron flight path with the uncertainty in the determination of the neutron flight time given by Table 14, from equation 158 can be shown to be

$$\frac{\sigma_E}{E} = 2\sqrt{\frac{\sigma_{fp}^2}{(fp)^2} + \frac{\sigma_{ft}^2}{(ft)^2}} \quad . \tag{161}$$

Table 15 lists this fractional uncertainty in the measured neutron energy from uncertainties in the determination of the neutron flight path and the measured flight time for a typical set of experimental conditions at representative energies throughout the spectrum.

Table 15. Fractional Uncertainty in the Measured Neutron Energy from Uncertainties in the Determination of the Neutron Flight Path and the Measured Flight Time for a Typical Set of Experimental Conditions at Representative Energies in the Spectrum

E(eV)	σ_E/E(%)
0.1	4.3
0.03	2.5
0.0045	1.4

Total Energy Resolution

Table 16 shows the total energy resolution width resulting from a combination of the effects of the chopper burst width, the detector path length, and the analysis channel width from Table 13 with the uncertainties in the determinations of the neutron flight path and the measured flight time from Table 15.

Table 16. Total Energy Resolution Width at Representative Energies in the Neutron Spectrum

E(eV)	σ_E/E(%)	$\Delta E/E$(%)
0.1	7.64	18.05
0.03	4.54	10.76
0.0045	2.24	5.29

APPENDIX F

MEASURED NEUTRON ENERGY SPECTRA (GRAPHICAL)

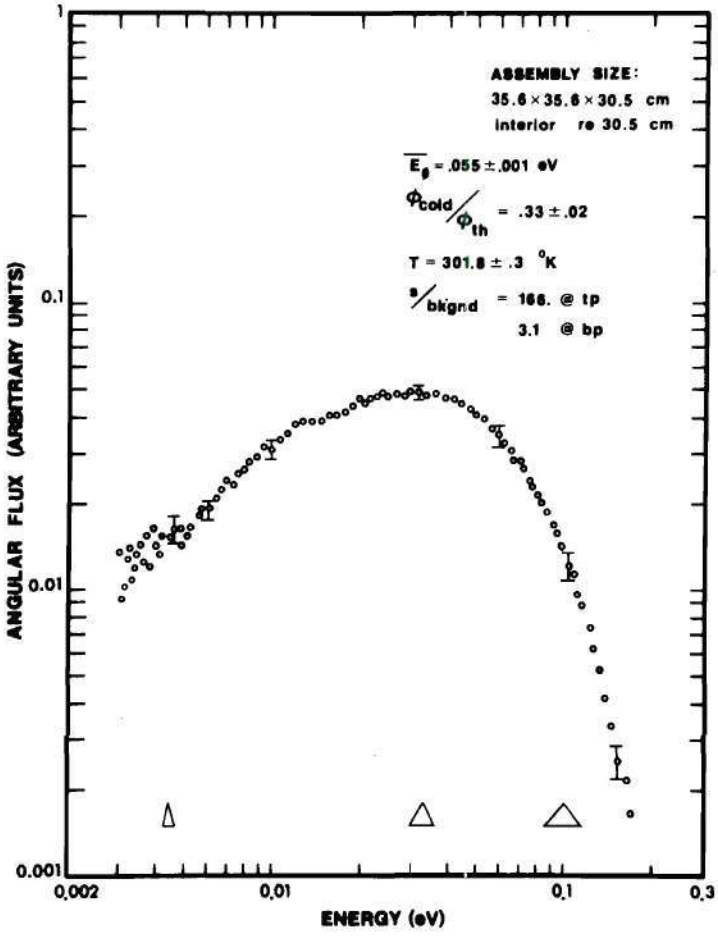

Figure 65. Measured Angular Neutron Energy Spectrum in the Positive "Z" Direction in the Interior of a 35.6 X 35.6 X 30.5 cm Beryllium Assembly, 0 cm from the Source Plane (re 30.5 cm)

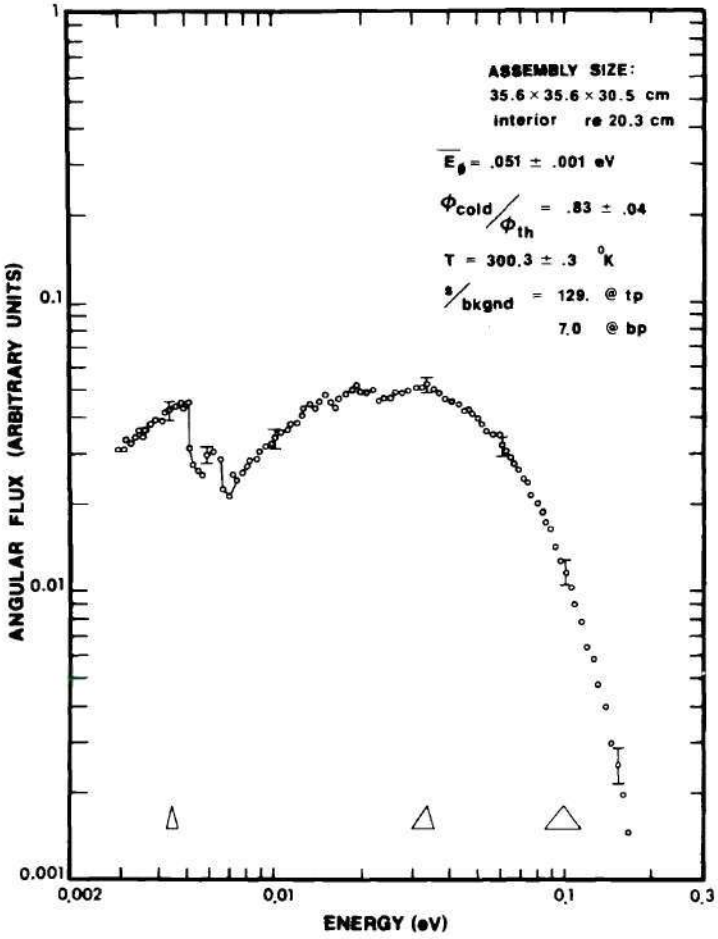

Figure 66. Measured Angular Neutron Energy Spectrum in the Positive "Z" Direction in the Interior of a 35.6 x 35.6 x 30.5 cm Beryllium Assembly, 10.2 cm from the Source Plane (re 20.3 cm)

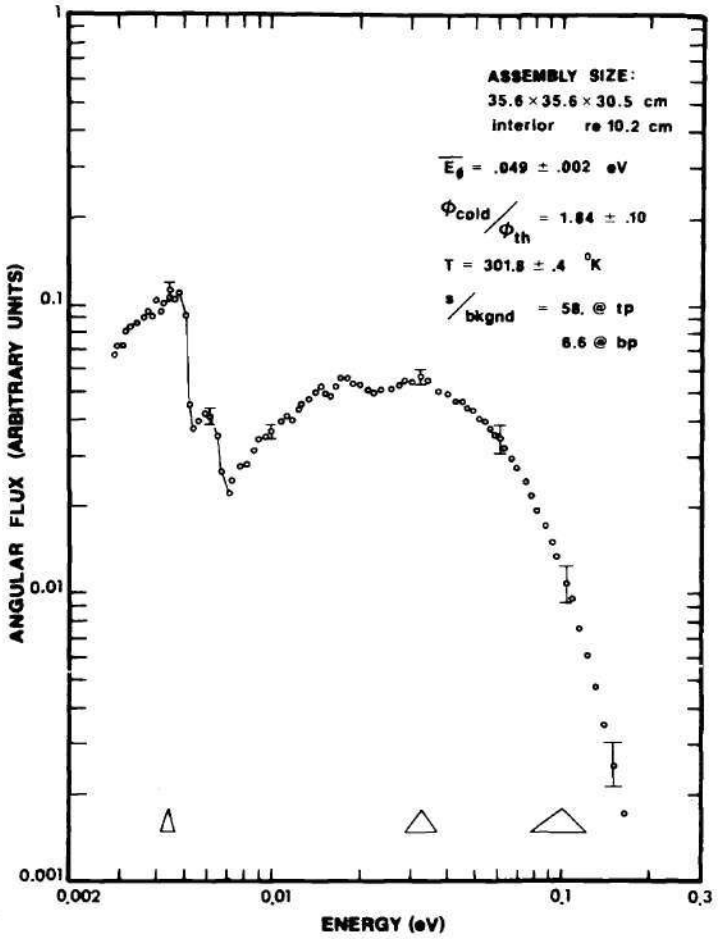

Figure 67. Measured Angular Neutron Energy Spectrum in the Positive "Z" Direction in the Interior of a 35.6 x 35.6 x 30.5 cm Beryllium Assembly, 20.3 cm from the Source Plane (re 10.2 cm)

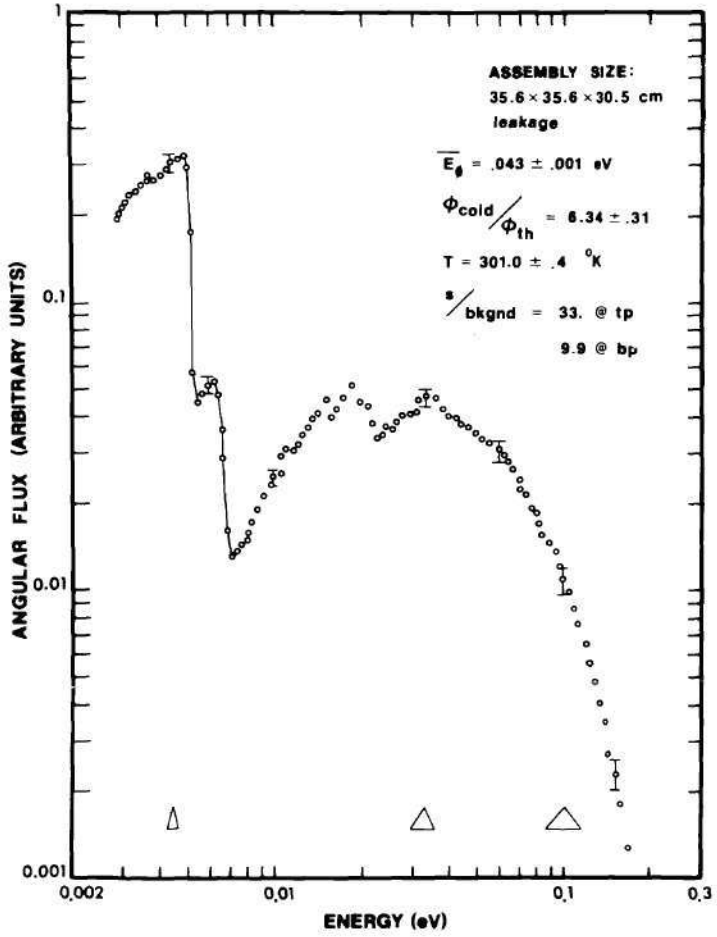

Figure 68. Measured Energy Spectrum of Neutrons Leaking from the Center of the Front Face of a 35.6 x 35.6 x 30.5 cm Beryllium Assembly in the Positive "Z" Direction

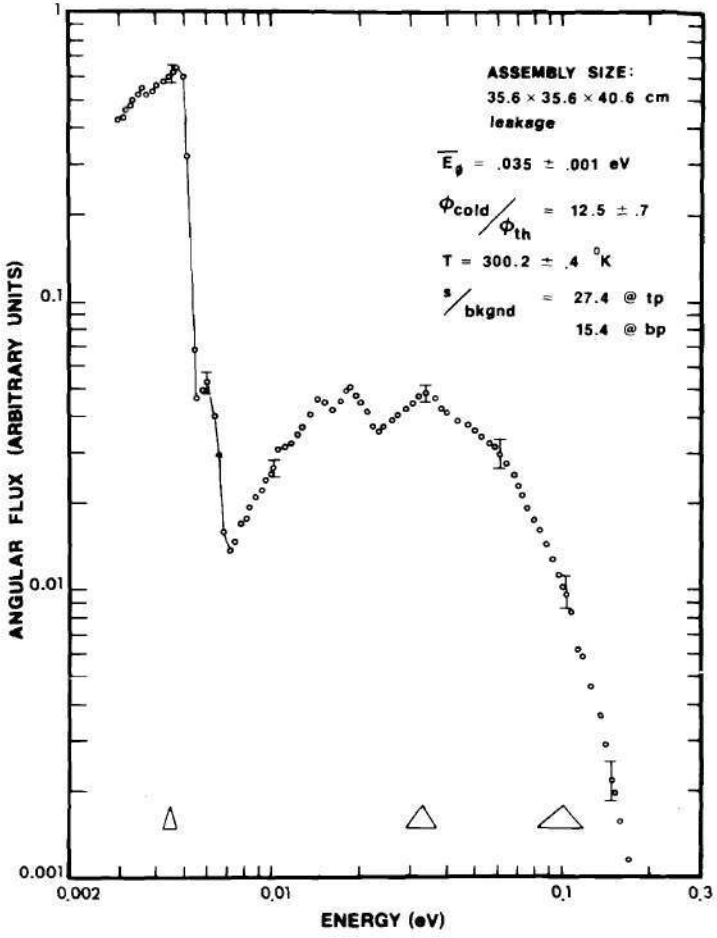

Figure 69. Measured Energy Spectrum of Neutrons Leaking from the Center of the Front Face of a 35.6 x 35.6 x 40.6 cm Beryllium Assembly in the Positive "Z" Direction

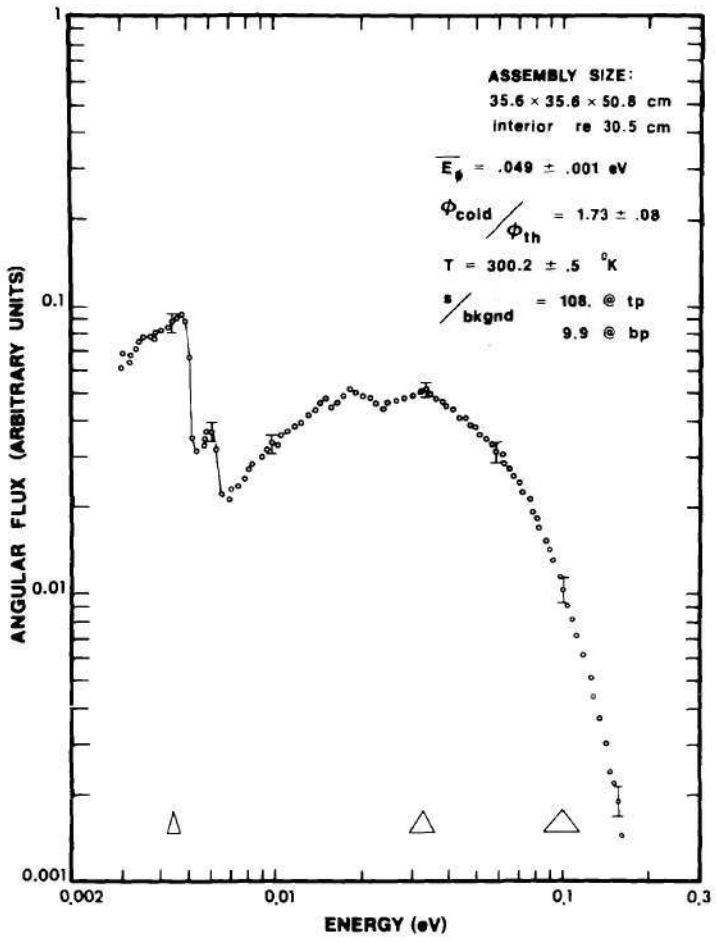

Figure 70. Measured Angular Neutron Energy Spectrum in the Positive "Z" Direction in the Interior of a 35.6 x 35.6 x 50.8 cm Beryllium Assembly, 20.3 cm from the Source Plane (re 30.5 cm)

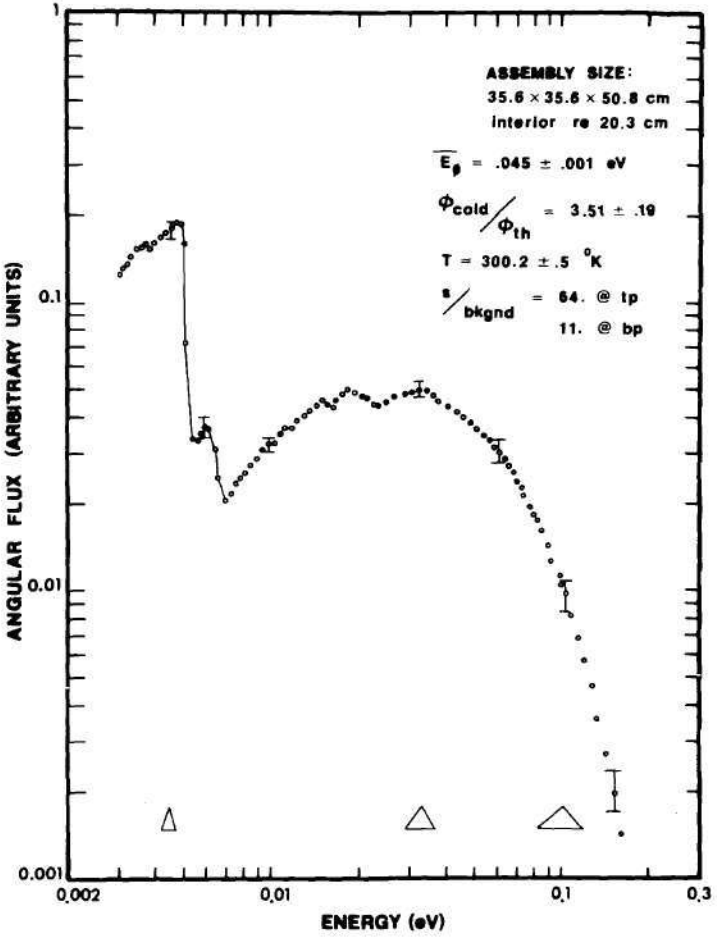

Figure 71. Measured Angular Neutron Energy Spectrum in the Positive "Z" Direction in the Interior of a 35.6 x 35.6 x 50.8 cm Beryllium Assembly, 30.5 cm from the Source Plane (re 20.3 cm)

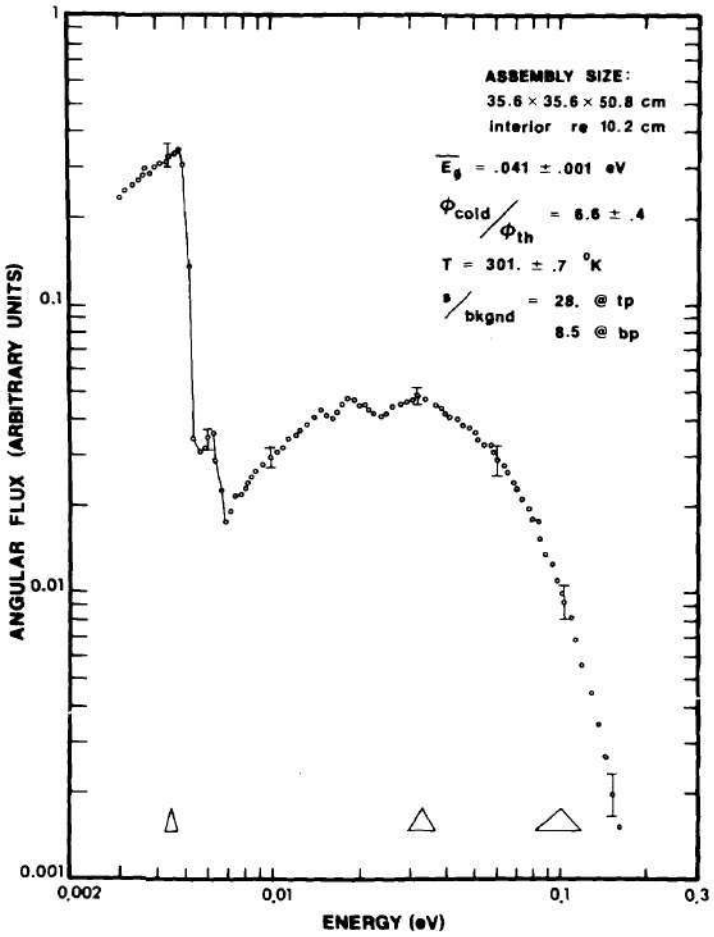

Figure 72. Measured Angular Neutron Energy Spectrum in the Positive "Z" Direction in the Interior of a 35.6 × 35.6 × 50.8 cm Beryllium Assembly, 40.6 cm from the Source Plane (re 10.2 cm)

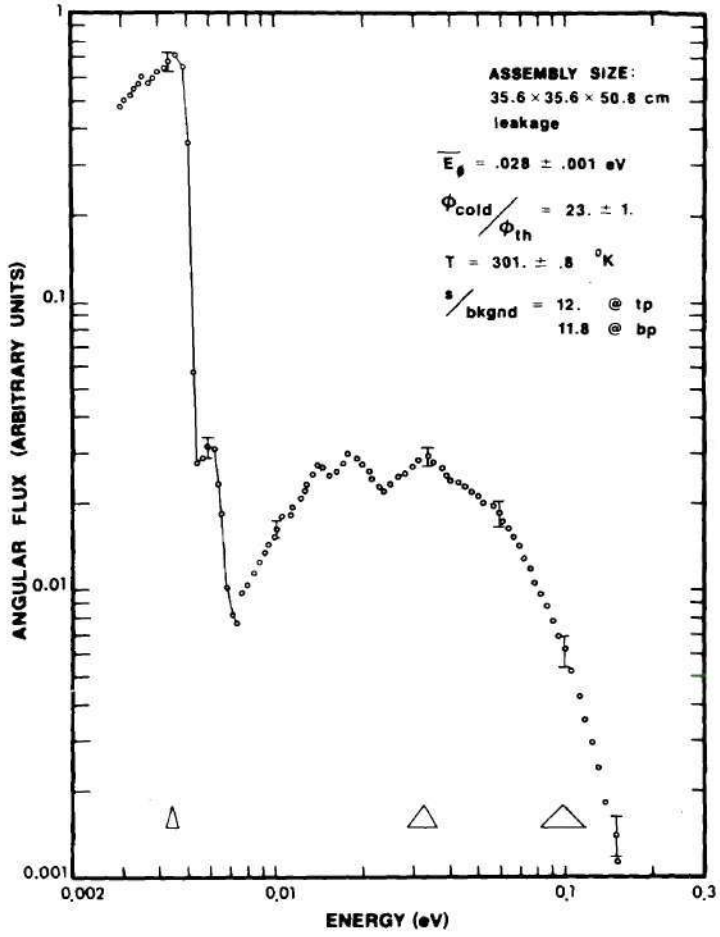

Figure 73. Measured Energy Spectrum of Neutrons Leaking from the Center of the Front Face of a 35.6 × 35.6 × 50.8 cm Beryllium Assembly in the Positive "Z" Direction

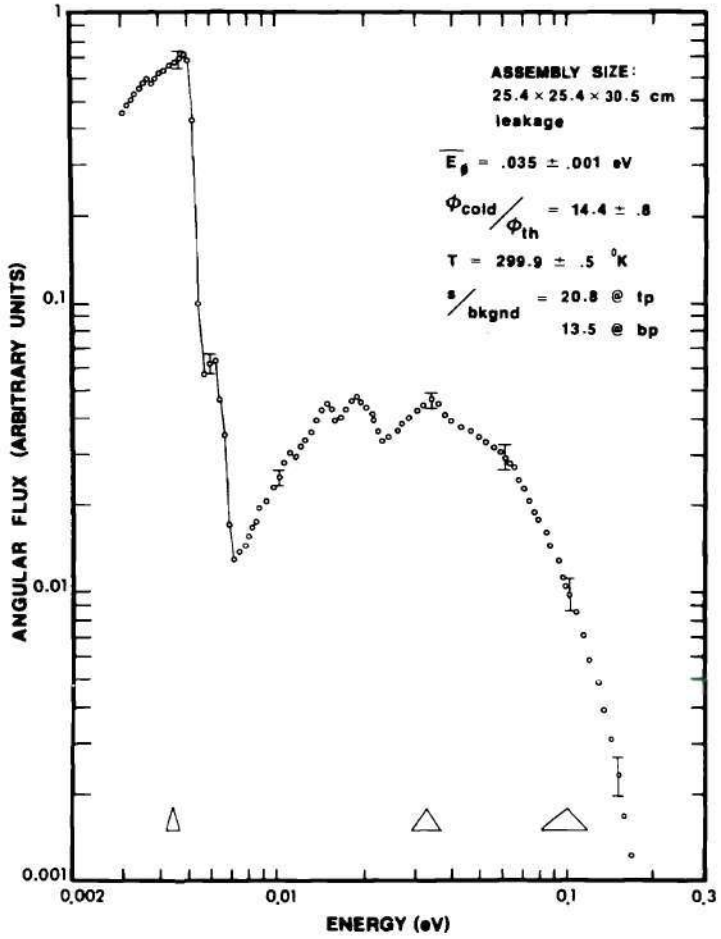

Figure 74. Measured Energy Spectrum of Neutrons Leaking from the Center of the Front Face of a 25.4 x 25.4 x 30.5 cm Beryllium Assembly in the Positive "Z" Direction

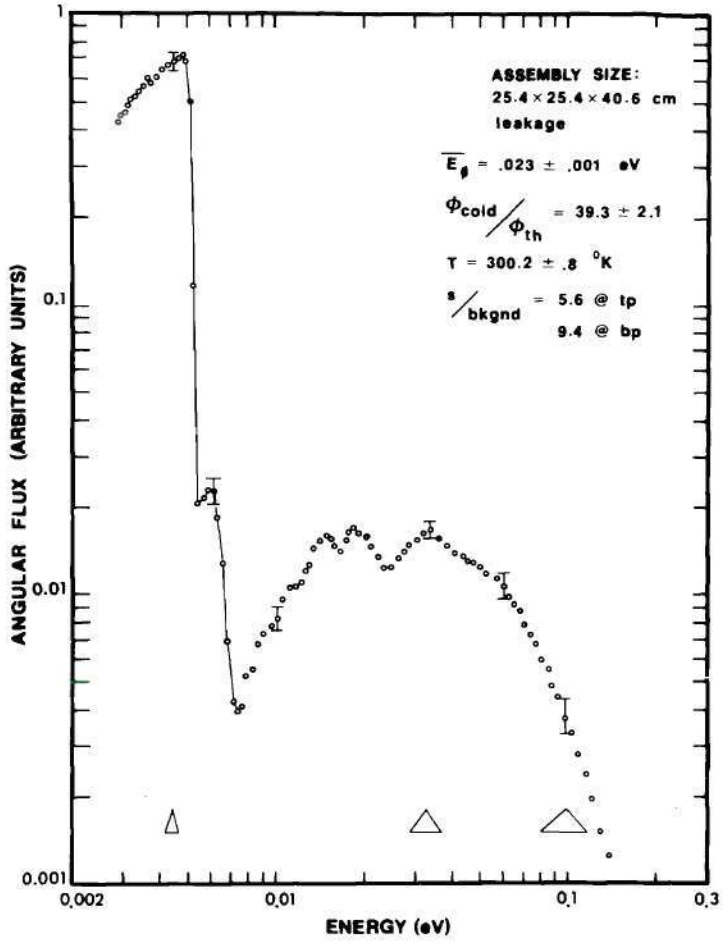

Figure 75. Measured Energy Spectrum of Neutrons Leaking from the Center of the Front Face of a 25.4 x 25.4 x 40.6 cm Beryllium Assembly in the Positive "Z" Direction

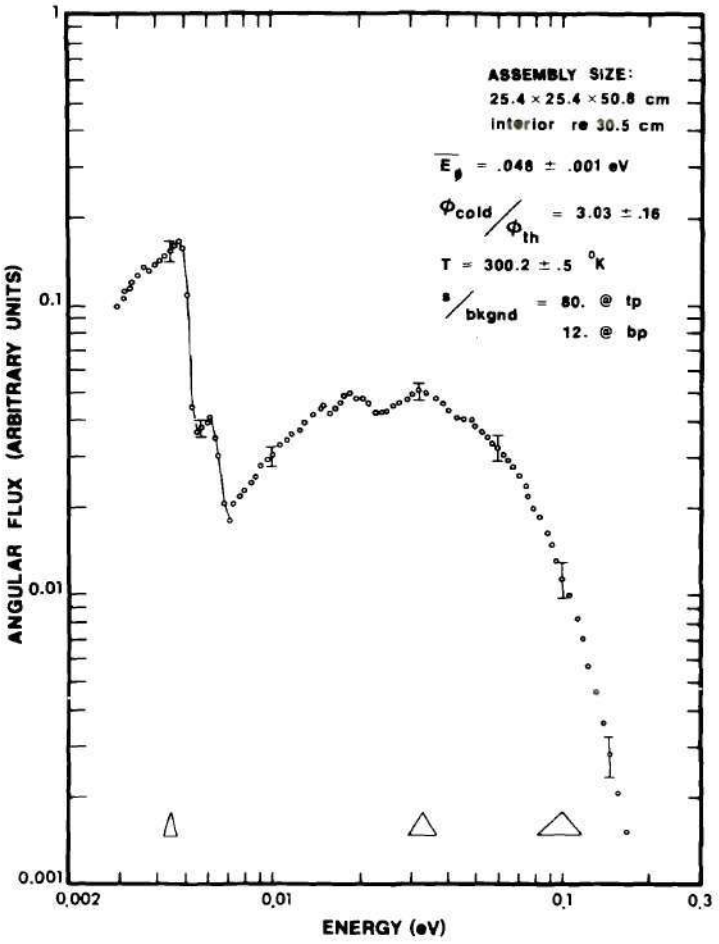

Figure 76. Measured Angular Neutron Energy Spectrum in the Positive "Z" Direction in the Interior of a 25.4 × 25.4 × 50.8 cm Beryllium Assembly, 20.3 cm from the Source Plane (re 30.5 cm)

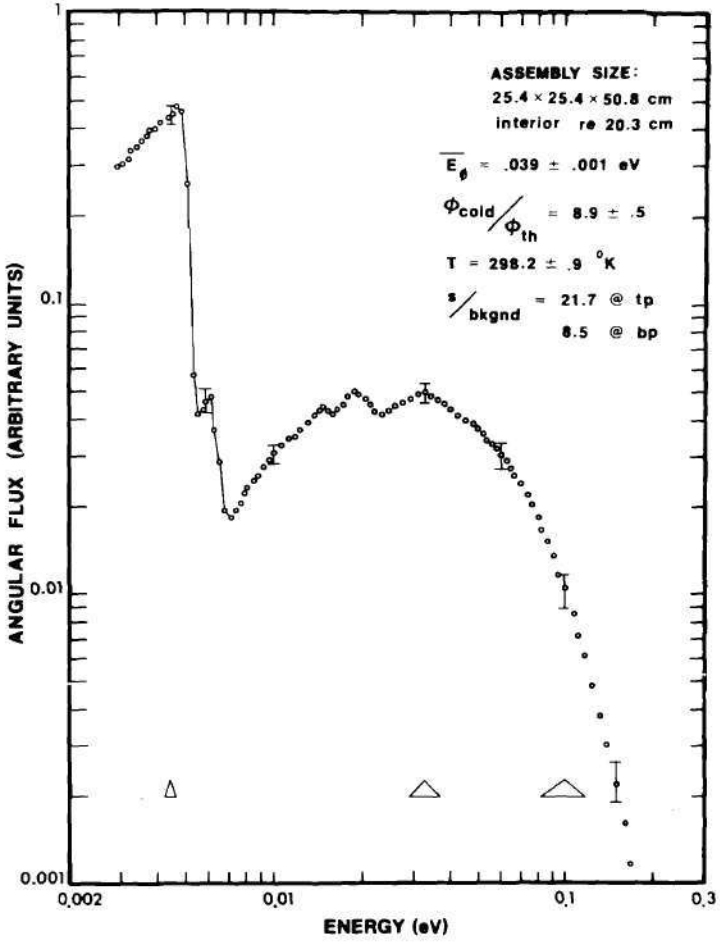

Figure 77. Measured Angular Neutron Energy Spectrum in the Positive "Z" Direction in the Interior of a 25.4 × 25.4 × 50.8 cm Beryllium Assembly, 30.5 cm from the Source Plane (re 20.3 cm)

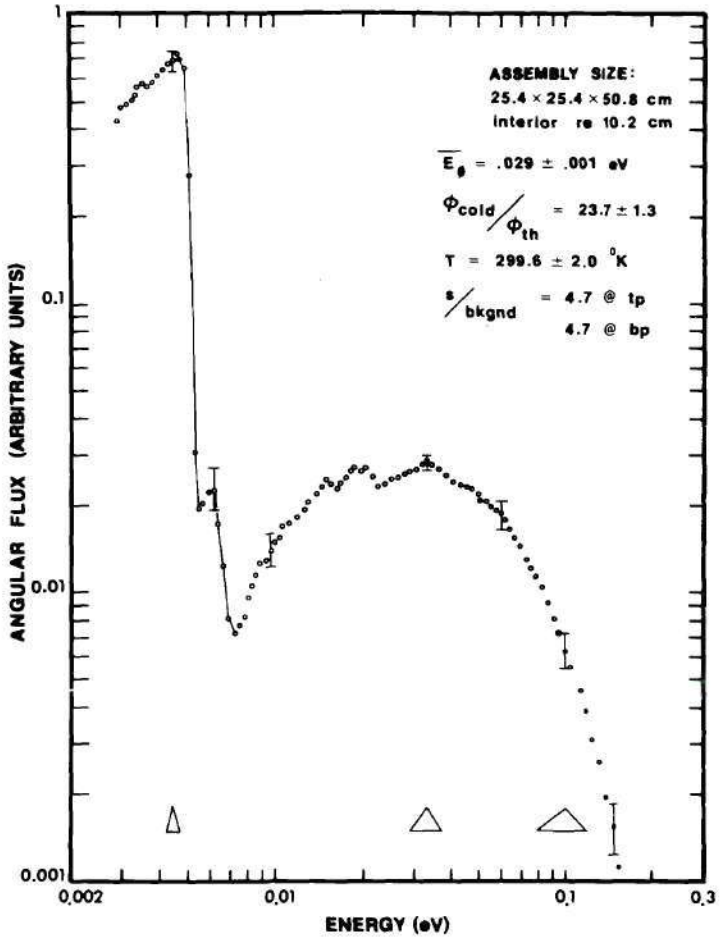

Figure 78. Measured Angular Neutron Energy Spectrum in the Positive "Z" Direction in the Interior of a 25.4 × 25.4 × 50.8 cm Beryllium Assembly, 40.6 cm from the Source Plane (re 10.2 cm)

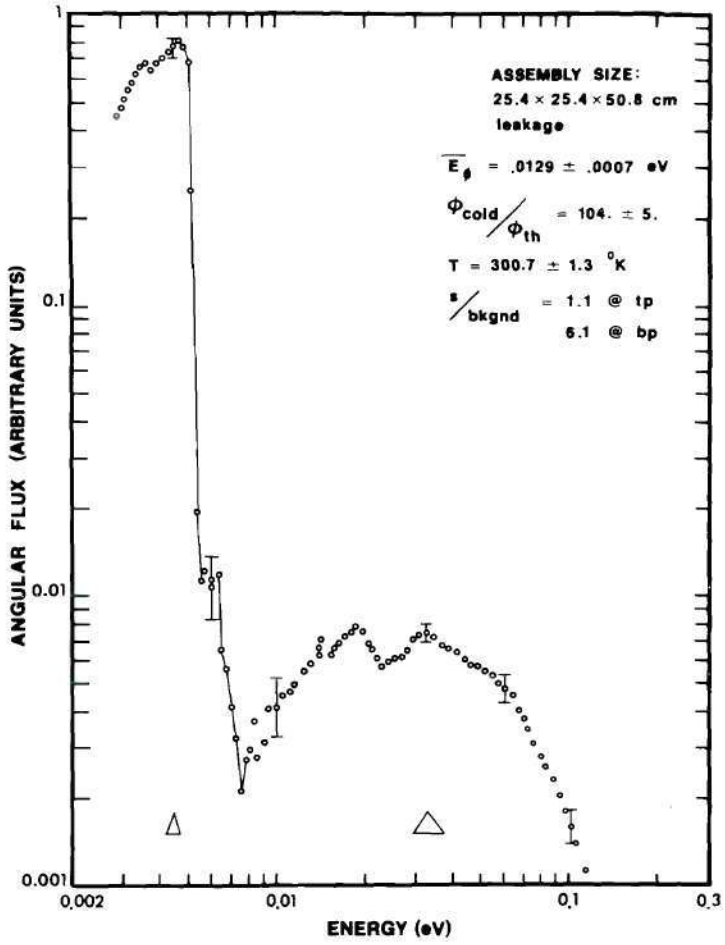

Figure 79. Measured Energy Spectrum of Neutrons Leaking from the Center of the Front Face of a 25.4 × 25.4 × 50.8 cm Beryllium Assembly in the Positive "Z" Direction

APPENDIX G

MEASURED NEUTRON ENERGY SPECTRA (TABULAR)

Table 17. Measured Angular Neutron Energy Spectrum in the Positive "Z" Direction in the Interior of a 35.6 x 35.6 x 30.5 cm Beryllium Assembly, 0 cm from the Source Plane (re 30.5 cm)

E(eV)	Ø(E)	E(eV)	Ø(E)	E(eV)	Ø(E)
0.20121	0.000583	0.03547	0.047772	0.00663	0.022960
0.19000	0.000825	0.03380	0.048104	0.00643	0.021048
0.17970	0.001132	0.03225	0.048904	0.00623	0.019772
0.17021	0.001704	0.03079	0.049291	0.00604	0.018769
0.16145	0.002110	0.02944	0.049669	0.00586	0.019482
0.15336	0.002545	0.02817	0.048663	0.00569	0.019218
0.14585	0.003396	0.02698	0.048034	0.00553	0.018205
0.13889	0.004236	0.02587	0.048897	0.00537	0.018956
0.13241	0.005266	0.02482	0.047868	0.00522	0.016597
0.12638	0.006222	0.02384	0.048611	0.00508	0.015454
0.12074	0.007339	0.02291	0.047528	0.00494	0.014242
0.11548	0.008936	0.02204	0.046833	0.00481	0.016476
0.11055	0.009742	0.02121	0.046643	0.00468	0.015324
0.10594	0.011535	0.02043	0.045794	0.00456	0.016379
0.10160	0.012281	0.01970	0.046418	0.00444	0.015223
0.09753	0.014392	0.01900	0.044215	0.00433	0.015880
0.09369	0.015819	0.01834	0.043630	0.00422	0.015680
0.09008	0.016923	0.01771	0.042716	0.00412	0.013396
0.08668	0.018976	0.01711	0.041570	0.00402	0.014934
0.08346	0.020302	0.01655	0.041230	0.00392	0.016360
0.08042	0.022028	0.01601	0.040251	0.00382	0.012063
0.07754	0.023262	0.01550	0.041068	0.00373	0.015744
0.07481	0.024492	0.01489	0.038898	0.00365	0.011769
0.07223	0.026489	0.01421	0.039426	0.00356	0.013664
0.06977	0.028107	0.01357	0.039439	0.00348	0.012657
0.06744	0.028766	0.01298	0.039684	0.00340	0.012496
0.06523	0.030656	0.01242	0.039594	0.00333	0.010418
0.06312	0.032620	0.01190	0.038086	0.00325	0.013424
0.06111	0.032686	0.01141	0.035813	0.00318	0.012132
0.05920	0.034716	0.01095	0.034705	0.00311	0.009817
0.05737	0.035617	0.01052	0.033462	0.00305	0.008972
0.05563	0.036920	0.01011	0.031288		
0.05397	0.038937	0.00972	0.031213		
0.05238	0.039317	0.00936	0.031767		
0.05086	0.040968	0.00902	0.029747		
0.04940	0.041490	0.00870	0.029125		
0.04801	0.041709	0.00839	0.027873		
0.04667	0.042564	0.00810	0.027543		
0.04539	0.044036	0.00782	0.026411		
0.04357	0.044623	0.00756	0.025793		
0.04131	0.046000	0.00731	0.023507		
0.03921	0.047130	0.00707	0.024240		
0.03727	0.048447	0.00685	0.024357		

Table 18. Measured Angular Neutron Energy Spectrum in the Positive "Z" Direction in the Interior of a 35.6 X 35.6 X 30.5 cm Beryllium Assembly, 10.2 cm from the Source Plane (re 20.3 cm)

E(eV)	Ø(E)	E(eV)	Ø(E)	E(eV)	Ø(E)
0.20806	0.000365	0.03744	0.048263	0.00704	0.021493
0.19642	0.000554	0.03565	0.050107	0.00682	0.022536
0.18574	0.000760	0.03399	0.051147	0.00660	0.028997
0.17590	0.001070	0.03244	0.050406	0.00640	0.029659
0.16682	0.001481	0.03099	0.050285	0.00621	0.030272
0.15843	0.001936	0.02964	0.050049	0.00603	0.029632
0.15065	0.002512	0.02837	0.048480	0.00585	0.030431
0.14344	0.003004	0.02719	0.048144	0.00568	0.025559
0.13673	0.003995	0.02608	0.048609	0.00552	0.025982
0.13048	0.004735	0.02503	0.047065	0.00537	0.027233
0.12465	0.005809	0.02405	0.046512	0.00522	0.030860
0.11920	0.006463	0.02312	0.045642	0.00508	0.044869
0.11410	0.007848	0.02225	0.046063	0.00494	0.043057
0.10932	0.009051	0.02142	0.049737	0.00481	0.043861
0.10484	0.010190	0.02064	0.049084	0.00469	0.044355
0.10062	0.011637	0.01990	0.049202	0.00457	0.043818
0.09666	0.012766	0.01920	0.050034	0.00445	0.042372
0.09292	0.014077	0.01854	0.049812	0.00434	0.042553
0.08940	0.016177	0.01791	0.049354	0.00423	0.042259
0.08607	0.017040	0.01731	0.046857	0.00413	0.037173
0.08293	0.018755	0.01674	0.046510	0.00403	0.038885
0.07996	0.020138	0.01620	0.044202	0.00393	0.039334
0.07714	0.021628	0.01568	0.044560	0.00384	0.039327
0.07447	0.023540	0.01519	0.047181	0.00375	0.038093
0.07193	0.024103	0.01461	0.045911	0.00366	0.035151
0.06952	0.026298	0.01396	0.043738	0.00358	0.032386
0.06724	0.027931	0.01334	0.044773	0.00350	0.032861
0.06506	0.029793	0.01277	0.040973	0.00342	0.033897
0.06299	0.030187	0.01224	0.037840	0.00334	0.030725
0.06101	0.031546	0.01173	0.038169	0.00327	0.031546
0.05912	0.034354	0.01126	0.038250	0.00320	0.030469
0.05733	0.034568	0.01081	0.035716	0.00313	0.031743
0.05561	0.034891	0.01039	0.035039	0.00306	0.029824
0.05397	0.036003	0.01000	0.034078	0.00300	0.029666
0.05240	0.037665	0.00963	0.031980		
0.05090	0.037772	0.00927	0.032103		
0.04946	0.040273	0.00894	0.030091		
0.04808	0.040318	0.00862	0.028011		
0.04676	0.042309	0.00832	0.028617		
0.04549	0.042048	0.00804	0.025464		
0.04369	0.043649	0.00777	0.025751		
0.04144	0.044256	0.00751	0.023753		
0.03936	0.046134	0.00727	0.025068		

Table 19. Measured Angular Neutron Energy Spectrum in the Positive "Z" Direction in the Interior of a 35.6 x 35.6 x 30.5 cm Beryllium Assembly, 20.3 cm from the Source Plane (re 10.2 cm)

E(eV)	Ø(E)	E(eV)	Ø(E)	E(eV)	Ø(E)
0.20288	0.000406	0.04301	0.047151	0.00857	0.032090
0.18716	0.000673	0.03993	0.049271	0.00815	0.028209
0.17321	0.001058	0.03716	0.051410	0.00776	0.027838
0.16076	0.001757	0.03468	0.055430	0.00740	0.025269
0.14960	0.002586	0.03243	0.056598	0.00706	0.022087
0.13957	0.003579	0.03040	0.054685	0.00675	0.026354
0.13051	0.004760	0.02855	0.054617	0.00646	0.035001
0.12231	0.006120	0.02687	0.052778	0.00618	0.040960
0.11486	0.007551	0.02533	0.052374	0.00592	0.041520
0.10806	0.009699	0.02392	0.050519	0.00568	0.040006
0.10186	0.011026	0.02262	0.049815	0.00545	0.037736
0.09617	0.013781	0.02143	0.051416	0.00524	0.045108
0.09095	0.015192	0.02033	0.053557	0.00504	0.091251
0.08614	0.017383	0.01931	0.053274	0.00485	0.108112
0.08170	0.019869	0.01837	0.055530	0.00467	0.104061
0.07759	0.022328	0.01749	0.056697	0.00450	0.111248
0.07379	0.025061	0.01667	0.052305	0.00434	0.102068
0.07026	0.028089	0.01591	0.048878	0.00418	0.093383
0.06698	0.030025	0.01521	0.050079	0.00404	0.102317
0.06392	0.033114	0.01439	0.050244	0.00390	0.090864
0.06107	0.034866	0.01349	0.048581	0.00377	0.092817
0.05841	0.035825	0.01267	0.045303	0.00365	0.086426
0.05591	0.037466	0.01192	0.040043	0.00353	0.084152
0.05357	0.040101	0.01124	0.040690	0.00342	0.081563
0.05138	0.040489	0.01061	0.039694	0.00331	0.079421
0.04932	0.043336	0.01004	0.036465	0.00321	0.078365
0.04737	0.043766	0.00951	0.035511	0.00311	0.068506
0.04555	0.046546	0.00902	0.034368	0.00302	0.067744

Table 20. Measured Energy Spectrum of Neutrons Leaking from the Center of the Front Face of a 35.6 × 35.6 × 30.5 cm Beryllium Assembly in the Positive "Z" Direction

E(eV)	Ø(E)	E(eV)	Ø(E)	E(eV)	Ø(E)
0.20530	0.000368	0.04146	0.039700	0.00806	0.015260
0.19444	0.000524	0.03948	0.040859	0.00780	0.015022
0.18443	0.000725	0.03764	0.043083	0.00755	0.014855
0.17516	0.000991	0.03592	0.046534	0.00732	0.013747
0.16658	0.001330	0.03432	0.047279	0.00710	0.013491
0.15861	0.001837	0.03283	0.046910	0.00688	0.016351
0.15121	0.002310	0.03143	0.046146	0.00668	0.029191
0.14430	0.002751	0.03012	0.042315	0.00649	0.035734
0.13786	0.003480	0.02889	0.040945	0.00630	0.048429
0.13185	0.004171	0.02773	0.040756	0.00612	0.053854
0.12621	0.004867	0.02664	0.039254	0.00595	0.052500
0.12094	0.005772	0.02561	0.037146	0.00579	0.048992
0.11598	0.006598	0.02464	0.037412	0.00563	0.049548
0.11132	0.007780	0.02373	0.035647	0.00548	0.044600
0.10694	0.008866	0.02287	0.034439	0.00533	0.057745
0.10282	0.010060	0.02205	0.038112	0.00519	0.175028
0.09892	0.011050	0.02127	0.044141	0.00506	0.299700
0.09525	0.012228	0.02054	0.043572	0.00493	0.307422
0.09177	0.013753	0.01984	0.044833	0.00481	0.312572
0.08848	0.014755	0.01918	0.051153	0.00469	0.308258
0.08537	0.015850	0.01855	0.051149	0.00457	0.307283
0.08242	0.017290	0.01795	0.047838	0.00446	0.301050
0.07961	0.018421	0.01738	0.046096	0.00436	0.301530
0.07695	0.019319	0.01684	0.042333	0.00425	0.286094
0.07442	0.021707	0.01632	0.040673	0.00415	0.278456
0.07201	0.022834	0.01582	0.041010	0.00406	0.274324
0.06972	0.024688	0.01535	0.045597	0.00397	0.269566
0.06753	0.026740	0.01479	0.044670	0.00388	0.266384
0.06545	0.026909	0.01415	0.041523	0.00379	0.263190
0.06346	0.028125	0.01356	0.040713	0.00371	0.269664
0.06156	0.029951	0.01300	0.036541	0.00363	0.252909
0.05975	0.030700	0.01248	0.034630	0.00355	0.239247
0.05801	0.030844	0.01198	0.032518	0.00347	0.231777
0.05635	0.032639	0.01152	0.030421	0.00340	0.230736
0.05476	0.032652	0.01108	0.031438	0.00333	0.221278
0.05323	0.032859	0.01067	0.029590	0.00326	0.224625
0.05177	0.034139	0.01028	0.025489	0.00319	0.211153
0.05037	0.035384	0.00991	0.025138	0.00313	0.211640
0.04902	0.035558	0.00956	0.023547	0.00306	0.200407
0.04773	0.037390	0.00923	0.021444	0.00300	0.192389
0.04649	0.037047	0.00891	0.019758		
0.04529	0.037580	0.00861	0.019613		
0.04359	0.038364	0.00833	0.017743		

Table 21. Measured Energy Spectrum of Neutrons Leaking from the Center of the Front Face of a 35.6 X 35.5 x 40.6 cm Beryllium Assembly in the Positive "Z" Direction

E(eV)	Ø(E)	E(eV)	Ø(E)	E(eV)	Ø(E)
0.20483	0.000300	0.02461	0.037007	0.00415	0.566017
0.19112	0.000501	0.02345	0.035800	0.00403	0.549300
0.17875	0.000776	0.02237	0.037165	0.00391	0.523274
0.16754	0.001182	0.02136	0.041967	0.00380	0.516283
0.15735	0.001611	0.02042	0.045533	0.00369	0.519956
0.14806	0.002205	0.01954	0.047073	0.00359	0.504608
0.13957	0.002925	0.01872	0.050299	0.00349	0.483598
0.13179	0.003788	0.01794	0.049358	0.00340	0.467973
0.12464	0.004642	0.01722	0.045616	0.00331	0.448698
0.11806	0.005883	0.01654	0.042575	0.00322	0.435498
0.11199	0.007204	0.01589	0.042327	0.00314	0.417972
0.10637	0.008428	0.01529	0.045112	0.00306	0.404646
0.10117	0.009974	0.01458	0.045860		
0.09634	0.011411	0.01379	0.041781		
0.09185	0.012968	0.01306	0.037653		
0.08766	0.014769	0.01239	0.035058		
0.08375	0.016055	0.01177	0.032299		
0.08010	0.017733	0.01120	0.032020		
0.07668	0.019710	0.01066	0.030176		
0.07348	0.021207	0.01017	0.026805		
0.07047	0.023062	0.00970	0.024699		
0.06765	0.025580	0.00927	0.022551		
0.06499	0.027045	0.00887	0.021356		
0.06248	0.029041	0.00849	0.018998		
0.06012	0.030518	0.00814	0.017384		
0.05789	0.031534	0.00781	0.017063		
0.05578	0.032305	0.00749	0.014786		
0.05378	0.033632	0.00720	0.013825		
0.05189	0.034838	0.00692	0.016039		
0.05010	0.035594	0.00666	0.029262		
0.04840	0.036675	0.00641	0.041210		
0.04678	0.037061	0.00618	0.053569		
0.04524	0.037881	0.00596	0.052154		
0.04309	0.039186	0.00575	0.049062		
0.04043	0.040800	0.00555	0.046577		
0.03801	0.042881	0.00536	0.069594		
0.03580	0.046188	0.00518	0.314893		
0.03378	0.047947	0.00501	0.581771		
0.03193	0.047349	0.00485	0.621852		
0.03022	0.044792	0.00470	0.628540		
0.02865	0.042776	0.00455	0.603350		
0.02720	0.040904	0.00441	0.590387		
0.02585	0.038978	0.00428	0.574177		

Table 22. Measured Angular Neutron Energy Spectrum in the Positive "Z" Direction in the Interior of a 35.6 x 35.6 x 50.8 cm Beryllium Assembly, 20.3 cm from the Source Plane (re 30.5 cm)

E(eV)	Ø(E)	E(eV)	Ø(E)	E(eV)	Ø(E)
0.20813	0.000284	0.04203	0.043393	0.00826	0.027623
0.19712	0.000407	0.04002	0.044578	0.00799	0.026089
0.18696	0.000598	0.03816	0.046397	0.00774	0.024797
0.17757	0.000835	0.03642	0.048089	0.00750	0.023720
0.16887	0.001134	0.03480	0.050069	0.00727	0.023698
0.16080	0.001482	0.03328	0.050474	0.00705	0.021871
0.15329	0.001940	0.03186	0.050142	0.00684	0.023030
0.14629	0.002414	0.03053	0.049617	0.00664	0.030039
0.13976	0.003068	0.02928	0.049018	0.00645	0.032049
0.13366	0.003706	0.02811	0.048301	0.00627	0.036032
0.12795	0.004518	0.02701	0.047525	0.00609	0.037420
0.12260	0.005265	0.02597	0.047129	0.00592	0.034801
0.11758	0.006238	0.02498	0.046789	0.00576	0.033271
0.11286	0.007149	0.02406	0.045761	0.00560	0.033111
0.10842	0.008282	0.02318	0.046104	0.00546	0.032208
0.10423	0.009400	0.02235	0.045916	0.00531	0.035081
0.10028	0.010596	0.02157	0.048760	0.00517	0.066713
0.09656	0.011655	0.02082	0.049310	0.00504	0.089084
0.09303	0.013167	0.02011	0.048619	0.00492	0.089910
0.08970	0.014418	0.01944	0.049637	0.00479	0.093032
0.08654	0.015728	0.01880	0.051559	0.00468	0.091066
0.08355	0.017040	0.01820	0.050723	0.00456	0.090376
0.08071	0.018610	0.01762	0.049182	0.00445	0.088107
0.07801	0.019570	0.01707	0.047040	0.00435	0.084652
0.07544	0.021379	0.01654	0.046091	0.00424	0.082892
0.07300	0.022581	0.01604	0.045211	0.00415	0.084386
0.07068	0.024298	0.01556	0.045233	0.00405	0.082067
0.06846	0.025975	0.01510	0.047269	0.00396	0.078413
0.06635	0.027405	0.01456	0.046559	0.00387	0.076449
0.06434	0.028459	0.01394	0.043849	0.00378	0.078453
0.06241	0.030210	0.01336	0.043208	0.00370	0.075886
0.06057	0.031172	0.01282	0.041012	0.00362	0.074028
0.05881	0.032407	0.01231	0.039182	0.00354	0.071862
0.05712	0.033743	0.01183	0.038042	0.00347	0.068092
0.05551	0.034502	0.01138	0.037547	0.00340	0.067198
0.05397	0.034591	0.01095	0.036843	0.00333	0.066301
0.05248	0.035854	0.01055	0.035546	0.00326	0.066569
0.05106	0.037202	0.01017	0.033181	0.00319	0.061102
0.04970	0.038036	0.00981	0.032807	0.00313	0.066666
0.04839	0.039648	0.00946	0.031856	0.00306	0.060662
0.04713	0.039495	0.00914	0.030173	0.00300	0.059016
0.04591	0.041090	0.00883	0.029302		
0.04419	0.041573	0.00854	0.028402		

Table 23. Measured Angular Neutron Energy Spectrum in the Positive "Z" Direction in the Interior of a 35.6 x 35.6 x 50.8 cm Beryllium Assembly, 30.5 cm from the Source Plane (re 20.3 cm)

E(eV)	Ø(E)	E(eV)	Ø(E)	E(eV)	Ø(E)
0.02487	0.045677	0.20762	0.000270	0.00419	0.165190
0.02370	0.044567	0.19370	0.000455	0.00407	0.164030
0.02260	0.044856	0.18113	0.000700	0.00395	0.157787
0.02159	0.046495	0.16975	0.001057	0.00384	0.152699
0.02064	0.047865	0.15940	0.001445	0.00373	0.153625
0.01975	0.048617	0.14998	0.002063	0.00362	0.145466
0.01891	0.049586	0.14136	0.002769	0.00353	0.145152
0.01813	0.048897	0.13347	0.003617	0.00343	0.135684
0.01740	0.047555	0.12622	0.004613	0.00334	0.132689
0.01671	0.045878	0.11954	0.005692	0.00325	0.127169
0.01606	0.044357	0.11338	0.006895	0.00317	0.125646
0.01545	0.045116	0.10769	0.008218	0.00308	0.120905
0.01473	0.045086	0.10241	0.009707		
0.01393	0.043233	0.09752	0.011189		
0.01320	0.041325	0.09296	0.012793		
0.01252	0.038991	0.08872	0.014425		
0.01189	0.036198	0.08476	0.016222		
0.01131	0.036163	0.08106	0.017884		
0.01077	0.035267	0.07760	0.019696		
0.01027	0.032757	0.07435	0.021364		
0.00980	0.031737	0.07130	0.023267		
0.00937	0.030800	0.06844	0.025372		
0.00896	0.028669	0.06575	0.027248		
0.00858	0.027153	0.06321	0.028988		
0.00822	0.025890	0.06082	0.030482		
0.00788	0.024661	0.05856	0.032113		
0.00757	0.023789	0.05642	0.033533		
0.00727	0.021827	0.05440	0.034380		
0.00699	0.020744	0.05248	0.035838		
0.00673	0.024993	0.05067	0.036979		
0.00648	0.030548	0.04895	0.038308		
0.00624	0.036147	0.04731	0.039197		
0.00602	0.037639	0.04575	0.039952		
0.00581	0.035620	0.04357	0.041705		
0.00561	0.033488	0.04088	0.043229		
0.00542	0.033806	0.03843	0.045226		
0.00524	0.071587	0.03620	0.047388		
0.00506	0.160669	0.03415	0.049193		
0.00490	0.183331	0.03228	0.049861		
0.00474	0.179986	0.03055	0.049194		
0.00460	0.181131	0.02896	0.048229		
0.00445	0.174108	0.02749	0.047328		
0.00432	0.170979	0.02613	0.046682		

Table 24. Measured Angular Neutron Energy Spectrum in the Positive "Z" Direction in the Interior of a 35.6 x 35.6 x 50.8 cm Beryllium Assembly, 40.6 cm from the Source Plane (re 10.2 cm)

E(eV)	Ø(E)	E(eV)	Ø(E)	E(eV)	Ø(E)
0.20757	0.000281	0.02472	0.042858	0.00416	0.309975
0.19359	0.000449	0.02355	0.041439	0.00404	0.303444
0.18098	0.000689	0.02246	0.042054	0.00392	0.290917
0.16956	0.000975	0.02145	0.044503	0.00381	0.281709
0.15918	0.001538	0.02051	0.045936	0.00370	0.271161
0.14974	0.002082	0.01962	0.045717	0.00360	0.277580
0.14110	0.002711	0.01879	0.047081	0.00350	0.270228
0.13320	0.003533	0.01801	0.047051	0.00340	0.252145
0.12594	0.004591	0.01728	0.045776	0.00331	0.237827
0.11926	0.005675	0.01660	0.042732	0.00322	0.237256
0.11309	0.006956	0.01595	0.040914	0.00314	0.231653
0.10739	0.008218	0.01534	0.041423	0.00306	0.222069
0.10212	0.009535	0.01463	0.043237		
0.09722	0.011067	0.01384	0.040613		
0.09266	0.012841	0.01311	0.039192		
0.08842	0.014028	0.01243	0.037278		
0.08447	0.015875	0.01181	0.034975		
0.08077	0.017826	0.01123	0.034519		
0.07731	0.019358	0.01070	0.032314		
0.07407	0.021141	0.01020	0.030716		
0.07102	0.022750	0.00973	0.029536		
0.06817	0.024427	0.00930	0.028638		
0.06548	0.026734	0.00889	0.026838		
0.06294	0.028167	0.00851	0.025012		
0.06055	0.029951	0.00816	0.024122		
0.05830	0.031313	0.00783	0.022325		
0.05617	0.032894	0.00751	0.022046		
0.05415	0.033528	0.00722	0.019333		
0.05224	0.034338	0.00694	0.017848		
0.05043	0.036358	0.00668	0.023521		
0.04871	0.036629	0.00643	0.029431		
0.04708	0.038156	0.00619	0.035663		
0.04553	0.038668	0.00597	0.034687		
0.04335	0.040326	0.00576	0.032539		
0.04067	0.041415	0.00556	0.031687		
0.03823	0.043499	0.00537	0.034805		
0.03600	0.045285	0.00520	0.134707		
0.03397	0.047740	0.00502	0.309262		
0.03210	0.048976	0.00486	0.342573		
0.03038	0.047071	0.00471	0.332514		
0.02879	0.045959	0.00456	0.332805		
0.02733	0.045687	0.00442	0.321574		
0.02598	0.044248	0.00429	0.312608		

Table 25. Measured Energy Spectrum of Neutrons Leaking from the Center of the Front Face of a 35.6 × 35.6 × 50.8 cm Beryllium Assembly in the Positive "Z" Direction

E(eV)	Ø(E)	E(eV)	Ø(E)	E(eV)	Ø(E)
0.20215	0.000193	0.02449	0.022442	0.00414	0.631233
0.18871	0.000321	0.02334	0.021765	0.00402	0.610722
0.17656	0.000511	0.02227	0.022517	0.00390	0.579715
0.16555	0.000745	0.02127	0.025679	0.00379	0.569624
0.15554	0.001061	0.02033	0.027675	0.00369	0.575437
0.14641	0.001415	0.01946	0.028342	0.00358	0.565214
0.13806	0.001846	0.01864	0.029863	0.00349	0.541327
0.13040	0.002434	0.01787	0.029406	0.00339	0.516560
0.12337	0.002965	0.01715	0.027305	0.00330	0.491474
0.11689	0.003591	0.01647	0.025611	0.00321	0.481833
0.11090	0.004295	0.01583	0.025177	0.00313	0.467264
0.10537	0.005196	0.01523	0.026720	0.00305	0.443326
0.10024	0.006125	0.01453	0.027189		
0.09547	0.006902	0.01374	0.025367		
0.09104	0.007860	0.01302	0.023295		
0.08691	0.008897	0.01235	0.020843		
0.08305	0.009832	0.01173	0.019172		
0.07944	0.010890	0.01116	0.019577		
0.07607	0.011915	0.01063	0.018367		
0.07290	0.012922	0.01014	0.016346		
0.06993	0.014163	0.00968	0.014262		
0.06714	0.015475	0.00925	0.013537		
0.06451	0.016520	0.00885	0.012421		
0.06203	0.017543	0.00847	0.011304		
0.05969	0.018437	0.00812	0.010400		
0.05749	0.019365	0.00779	0.009823		
0.05540	0.019817	0.00747	0.007789		
0.05342	0.020342	0.00718	0.008142		
0.05155	0.021139	0.00690	0.010133		
0.04977	0.021562	0.00664	0.018389		
0.04809	0.021827	0.00640	0.023684		
0.04649	0.022445	0.00617	0.030923		
0.04496	0.022946	0.00595	0.031498		
0.04283	0.023728	0.00574	0.028686		
0.04019	0.024511	0.00554	0.027549		
0.03780	0.026349	0.00535	0.055987		
0.03561	0.028059	0.00517	0.346874		
0.03360	0.028790	0.00500	0.648782		
0.03176	0.028574	0.00484	0.687857		
0.03007	0.026956	0.00469	0.696595		
0.02851	0.025778	0.00454	0.673618		
0.02707	0.024772	0.00440	0.648212		
0.02573	0.023464	0.00427	0.637615		

Table 26. Measured Energy Spectrum of Neutrons Leaking from the Center of the Front Face of a 25.4 x 25.4 x 30.5 cm Beryllium Assembly in the Positive "Z" Direction

E(eV)	Ø(E)	E(eV)	Ø(E)	E(eV)	Ø(E)
0.20738	0.000358	0.02477	0.034691	0.00417	0.627724
0.19344	0.000566	0.02360	0.033887	0.00405	0.606642
0.18086	0.000828	0.02251	0.035936	0.00393	0.585578
0.16947	0.001254	0.02150	0.041136	0.00382	0.576717
0.15913	0.001728	0.02055	0.043348	0.00371	0.577374
0.14970	0.002353	0.01966	0.045417	0.00361	0.545292
0.14108	0.003130	0.01883	0.047085	0.00351	0.518651
0.13319	0.003886	0.01805	0.046115	0.00341	0.500997
0.12595	0.004893	0.01732	0.042938	0.00332	0.483132
0.11927	0.005876	0.01664	0.040108	0.00323	0.467830
0.11312	0.007233	0.01599	0.039624	0.00315	0.453831
0.10743	0.008530	0.01538	0.043481	0.00307	0.429405
0.10216	0.009940	0.01466	0.043997		
0.09726	0.011584	0.01387	0.039097		
0.09271	0.013042	0.01314	0.035919		
0.08848	0.014467	0.01246	0.032408		
0.08452	0.016096	0.01184	0.030005		
0.08083	0.017547	0.01126	0.030146		
0.07737	0.019179	0.01072	0.028865		
0.07413	0.021032	0.01022	0.025369		
0.07109	0.023115	0.00976	0.023320		
0.06823	0.024834	0.00932	0.020441		
0.06554	0.027077	0.00892	0.019645		
0.06301	0.028112	0.00854	0.017597		
0.06062	0.029678	0.00818	0.016536		
0.05837	0.030467	0.00785	0.014574		
0.05623	0.031644	0.00753	0.013902		
0.05422	0.032353	0.00724	0.013065		
0.05231	0.033737	0.00696	0.017243		
0.05050	0.034359	0.00669	0.034506		
0.04878	0.035280	0.00645	0.047695		
0.04714	0.035864	0.00621	0.063265		
0.04559	0.036634	0.00599	0.061622		
0.04341	0.037856	0.00578	0.057094		
0.04073	0.039035	0.00558	0.056324		
0.03829	0.041802	0.00539	0.099720		
0.03606	0.044941	0.00521	0.420983		
0.03402	0.046484	0.00504	0.670689		
0.03215	0.044932	0.00488	0.699968		
0.03043	0.042183	0.00472	0.698308		
0.02885	0.040592	0.00457	0.680702		
0.02738	0.038189	0.00443	0.661197		
0.02603	0.036242	0.00430	0.645046		

Table 27. Measured Energy Spectrum of Neutrons Leaking from the Center of the Front Face of a 25.4 X 25.4 X 40.6 cm Beryllium Assembly in the Positive "Z" Direction

E(eV)	Ø(E)	E(eV)	Ø(E)	E(eV)	Ø(E)
0.20037	0.000149	0.02356	0.012270	0.00399	0.589372
0.18698	0.000243	0.02246	0.013209	0.00388	0.564850
0.17490	0.000360	0.02144	0.015034	0.00377	0.584513
0.16395	0.000533	0.02049	0.015619	0.00366	0.554324
0.15400	0.000682	0.01960	0.016510	0.00356	0.539490
0.14492	0.000951	0.01876	0.016997	0.00346	0.508167
0.13663	0.001245	0.01798	0.016166	0.00337	0.483455
0.12903	0.001538	0.01725	0.015246	0.00328	0.472505
0.12204	0.001936	0.01656	0.013999	0.00319	0.454718
0.11561	0.002388	0.01591	0.014693	0.00311	0.428055
0.10967	0.002806	0.01529	0.015652	0.00303	0.419814
0.10418	0.003288	0.01458	0.015346		
0.09909	0.003776	0.01378	0.014543		
0.09437	0.004356	0.01305	0.012473		
0.08997	0.004916	0.01238	0.011057		
0.08588	0.005494	0.01175	0.010900		
0.08206	0.005896	0.01117	0.010660		
0.07848	0.006630	0.01064	0.009879		
0.07514	0.007113	0.01014	0.008338		
0.07201	0.007890	0.00967	0.007803		
0.06906	0.008610	0.00924	0.007324		
0.06630	0.009313	0.00884	0.006823		
0.06369	0.009992	0.00846	0.005540		
0.06124	0.010618	0.00810	0.005487		
0.05893	0.010935	0.00777	0.004045		
0.05674	0.011364	0.00746	0.003962		
0.05468	0.011419	0.00716	0.004297		
0.05272	0.011772	0.00688	0.006838		
0.05087	0.012275	0.00662	0.012655		
0.04912	0.012606	0.00638	0.018668		
0.04745	0.012993	0.00614	0.022602		
0.04587	0.013085	0.00592	0.022694		
0.04364	0.013619	0.00571	0.021246		
0.04091	0.013807	0.00551	0.020533		
0.03843	0.014657	0.00533	0.114492		
0.03617	0.015645	0.00515	0.499659		
0.03410	0.016660	0.00498	0.677410		
0.03221	0.016148	0.00482	0.697523		
0.03046	0.015429	0.00466	0.692638		
0.02886	0.014730	0.00452	0.666264		
0.02738	0.013870	0.00438	0.650408		
0.02601	0.013245	0.00424	0.640453		
0.02474	0.012274	0.00412	0.617095		

Table 28. Measured Angular Neutron Energy Spectrum in the Positive "Z" Direction in the Interior of a 25.4 x 25.4 x 50.8 cm Beryllium Assembly, 20.3 cm from the Source Plane (re 30.5 cm)

E(eV)	Ø(E)	E(eV)	Ø(E)	E(eV)	Ø(E)
0.20268	0.000437	0.02376	0.042963	0.00403	0.140502
0.18911	0.000697	0.02266	0.042965	0.00391	0.132461
0.17687	0.001028	0.02162	0.046259	0.00380	0.134586
0.16577	0.001526	0.02066	0.047415	0.00369	0.129609
0.15569	0.002067	0.01976	0.047723	0.00359	0.118415
0.14650	0.002842	0.01892	0.048792	0.00349	0.119219
0.13810	0.003608	0.01813	0.048213	0.00339	0.116383
0.13040	0.004630	0.01739	0.046269	0.00330	0.109486
0.12333	0.005793	0.01669	0.043796	0.00321	0.107847
0.11682	0.007074	0.01604	0.043027	0.00313	0.102772
0.11081	0.008380	0.01542	0.044487	0.00305	0.097271
0.10525	0.010104	0.01470	0.043912		
0.10011	0.011506	0.01390	0.042131		
0.09533	0.013247	0.01316	0.039446		
0.09088	0.014995	0.01248	0.036710		
0.08674	0.016376	0.01185	0.034637		
0.08287	0.018485	0.01126	0.034747		
0.07926	0.020462	0.01072	0.033043		
0.07588	0.021983	0.01022	0.030153		
0.07271	0.023819	0.00975	0.029504		
0.06973	0.026107	0.00931	0.027990		
0.06694	0.028084	0.00891	0.026013		
0.06431	0.029523	0.00852	0.025013		
0.06183	0.031055	0.00817	0.023563		
0.05949	0.033110	0.00783	0.022193		
0.05728	0.033760	0.00751	0.020819		
0.05519	0.035133	0.00722	0.018364		
0.05322	0.036340	0.00694	0.020680		
0.05135	0.037231	0.00667	0.030646		
0.04957	0.038494	0.00643	0.035262		
0.04789	0.039713	0.00619	0.041514		
0.04629	0.040549	0.00597	0.039404		
0.04405	0.041451	0.00576	0.037571		
0.04129	0.043321	0.00556	0.036838		
0.03878	0.045529	0.00537	0.044056		
0.03650	0.047819	0.00519	0.108971		
0.03441	0.049511	0.00502	0.156145		
0.03249	0.049845	0.00485	0.158587		
0.03073	0.048719	0.00470	0.159145		
0.02911	0.047598	0.00455	0.155618		
0.02762	0.046066	0.00441	0.150096		
0.02623	0.044783	0.00428	0.145710		
0.02495	0.043960	0.00415	0.142706		

Table 29. Measured Angular Neutron Energy Spectrum in the Positive "Z" Direction in the Interior of a 25.4 x 25.4 x 50.8 cm Beryllium Assembly, 30.5 cm from the Source Plane (re 20.3 cm)

E(eV)	∅(E)	E(eV)	∅(E)	E(eV)	∅(E)
0.20318	0.000345	0.02455	0.043165	0.00415	0.413789
0.18964	0.000534	0.02339	0.042627	0.00403	0.399331
0.17741	0.000816	0.02232	0.042917	0.00391	0.380678
0.16632	0.001217	0.02131	0.045636	0.00380	0.377604
0.15625	0.001666	0.02038	0.046506	0.00369	0.364299
0.14706	0.002299	0.01950	0.047575	0.00359	0.349169
0.13866	0.003041	0.01868	0.048784	0.00349	0.335768
0.13096	0.003912	0.01791	0.047556	0.00340	0.320722
0.12388	0.004891	0.01719	0.044789	0.00330	0.312207
0.11736	0.006135	0.01651	0.043680	0.00322	0.297713
0.11134	0.007332	0.01586	0.042223	0.00313	0.286323
0.10578	0.008840	0.01526	0.043438	0.00305	0.278598
0.10062	0.010329	0.01455	0.043521		
0.09583	0.011811	0.01377	0.041681		
0.09137	0.013395	0.01304	0.039170		
0.08722	0.015080	0.01237	0.036771		
0.08334	0.016771	0.01176	0.034569		
0.07972	0.018812	0.01118	0.034655		
0.07633	0.020305	0.01065	0.033343		
0.07315	0.022430	0.01015	0.030780		
0.07016	0.024337	0.00969	0.029632		
0.06736	0.026410	0.00926	0.027356		
0.06471	0.027879	0.00886	0.025435		
0.06223	0.029928	0.00848	0.024836		
0.05988	0.030951	0.00813	0.023878		
0.05766	0.032874	0.00780	0.020396		
0.05556	0.033577	0.00749	0.019773		
0.05358	0.035659	0.00719	0.018760		
0.05170	0.036494	0.00692	0.019843		
0.04992	0.037626	0.00665	0.028677		
0.04823	0.038745	0.00641	0.037367		
0.04662	0.039618	0.00618	0.047889		
0.04509	0.040075	0.00595	0.047572		
0.04294	0.041583	0.00575	0.042884		
0.04030	0.043186	0.00555	0.041243		
0.03789	0.045366	0.00536	0.057258		
0.03570	0.047325	0.00518	0.254773		
0.03369	0.049503	0.00501	0.438148		
0.03184	0.048501	0.00485	0.454039		
0.03014	0.047779	0.00470	0.457025		
0.02858	0.046934	0.00455	0.441891		
0.02713	0.045528	0.00441	0.432467		
0.02579	0.044289	0.00428	0.427876		

Table 30. Measured Angular Neutron Energy Spectrum in the Positive "Z" Direction in the Interior of a 25.4 x 25.4 x 50.8 cm Beryllium Assembly, 40.6 cm from the Source Plane (re 10.2 cm)

E(eV)	∅(E)	E(eV)	∅(E)	E(eV)	∅(E)
0.20204	0.000266	0.02383	0.023568	0.00404	0.607459
0.18858	0.000358	0.02272	0.023234	0.00393	0.572054
0.17641	0.000572	0.02168	0.024980	0.00381	0.558603
0.16539	0.000835	0.02072	0.026361	0.00370	0.577396
0.15537	0.001153	0.01982	0.025833	0.00360	0.535643
0.14623	0.001583	0.01898	0.026701	0.00350	0.525049
0.13788	0.002008	0.01819	0.026873	0.00341	0.496910
0.13022	0.002639	0.01744	0.024884	0.00332	0.471314
0.12318	0.003147	0.01675	0.024043	0.00323	0.457940
0.11670	0.003874	0.01609	0.023040	0.00314	0.453600
0.11072	0.004591	0.01547	0.023985	0.00306	0.399807
0.10518	0.005492	0.01475	0.024070	0.00299	0.391278
0.10005	0.006361	0.01394	0.021889		
0.09529	0.007244	0.01320	0.020947		
0.09086	0.008111	0.01252	0.019094		
0.08673	0.009329	0.01189	0.018436		
0.08287	0.010503	0.01130	0.017581		
0.07927	0.011269	0.01076	0.017244		
0.07590	0.012127	0.01026	0.015200		
0.07274	0.013068	0.00979	0.014021		
0.06977	0.014734	0.00935	0.012827		
0.06698	0.015879	0.00894	0.012634		
0.06435	0.016334	0.00856	0.011327		
0.06188	0.017881	0.00820	0.010662		
0.05954	0.018750	0.00786	0.008249		
0.05734	0.019206	0.00754	0.007671		
0.05525	0.019804	0.00725	0.007205		
0.05328	0.020948	0.00697	0.008099		
0.05141	0.021022	0.00670	0.012479		
0.04964	0.021822	0.00645	0.017143		
0.04795	0.022707	0.00622	0.022531		
0.04636	0.023026	0.00599	0.024869		
0.04411	0.023563	0.00578	0.020032		
0.04136	0.024007	0.00558	0.019812		
0.03885	0.025385	0.00539	0.030484		
0.03657	0.026671	0.00521	0.271504		
0.03448	0.027786	0.00504	0.639876		
0.03256	0.027464	0.00487	0.695166		
0.03080	0.027068	0.00472	0.705841		
0.02918	0.026253	0.00457	0.681635		
0.02768	0.026058	0.00443	0.668261		
0.02630	0.024812	0.00429	0.652075		
0.02502	0.024264	0.00417	0.635450		

Table 31. Measured Energy Spectrum of Neutrons Leaking from the Center of the Front Face of a 25.4 x 25.4 x 50.8 cm Beryllium Assembly in the Positive "Z" Direction

E(eV)	Ø(E)	E(eV)	Ø(E)	E(eV)	Ø(E)
0.20480	0.000068	0.02467	0.005116	0.00416	0.628642
0.19112	0.000060	0.02351	0.005069	0.00404	0.598182
0.17877	0.000125	0.02243	0.005397	0.00393	0.570695
0.16757	0.000192	0.02142	0.005595	0.00381	0.570433
0.15740	0.000261	0.02048	0.005995	0.00371	0.594466
0.14813	0.000359	0.01960	0.006840	0.00360	0.559405
0.13965	0.000467	0.01877	0.006877	0.00350	0.533824
0.13188	0.000551	0.01800	0.006551	0.00341	0.503732
0.12474	0.000656	0.01727	0.006201	0.00332	0.483922
0.11817	0.000807	0.01658	0.006161	0.00323	0.468880
0.11210	0.001025	0.01594	0.005754	0.00315	0.438537
0.10648	0.001237	0.01533	0.005989	0.00307	0.425205
0.10128	0.001423	0.01462	0.006095		
0.09645	0.001617	0.01383	0.005687		
0.09196	0.001815	0.01310	0.005047		
0.08778	0.002134	0.01243	0.004915		
0.08387	0.002311	0.01181	0.004015		
0.08022	0.002504	0.01123	0.004347		
0.07680	0.002732	0.01070	0.004247		
0.07360	0.003077	0.01020	0.003786		
0.07059	0.003380	0.00974	0.004085		
0.06776	0.003545	0.00930	0.003755		
0.06510	0.004072	0.00890	0.002368		
0.06260	0.004104	0.00852	0.002617		
0.06023	0.004299	0.00816	0.002769		
0.05800	0.004508	0.00783	0.002317		
0.05589	0.004740	0.00752	0.002088		
0.05389	0.004794	0.00722	0.003198		
0.05200	0.004902	0.00695	0.003978		
0.05020	0.005103	0.00668	0.005035		
0.04850	0.005254	0.00644	0.007882		
0.04688	0.005212	0.00620	0.010164		
0.04534	0.005338	0.00598	0.010968		
0.04318	0.005522	0.00577	0.010613		
0.04052	0.005663	0.00557	0.009752		
0.03810	0.005876	0.00538	0.043171		
0.03589	0.006219	0.00520	0.359364		
0.03387	0.006688	0.00503	0.648937		
0.03201	0.006575	0.00487	0.691207		
0.03030	0.006179	0.00472	0.704558		
0.02872	0.006041	0.00457	0.679846		
0.02727	0.005767	0.00443	0.647962		
0.02592	0.005547	0.00429	0.640775		

BIBLIOGRAPHY

1. K. H. Beckurts and K. Wirtz, Neutron Physics, translated by L. Dresner. Springer-Verlag, New York (1964).

2. N. Corngold and P. Michael, "Some Transient Phenomena in Thermalization. II. Implications for Experiment," Nuclear Science and Engineering, 19, 91 (1964).

3. W. M. Andrews, "Measurement of the Temperature Dependence of Neutron Diffusion Properties in Beryllium Using a Pulsed Neutron Technique," UCRL-6803, University of California Radiation Laboratory (1960).

4. G. deSaussure and E. Silver, unpublished experimental work reported by K. H. Beckurts, Nuclear Instruments and Methods, 11, 144 (1961).

5. F. A. Kloverstrom and T. T. Komoto, "Diffusion Cooling in Beryllium and Graphite," Transactions of the American Nuclear Society, 1, 94 (1958).

6. I. F. Zhezherun, "Measurements of Neutron Pulse Drop in Small Slugs of Beryllium and Beryllium Oxide," in Neutron Thermalization and Reactor Spectra, pp. 179-98, IAEA, Vienna (1967). English translation, JPRS-43682.

7. M. M. R. Williams, "Space, Time and Energy Separability in the Pulsed Neutron Experiment," Nukleonik, 10, 252 (1967).

8. F. Ahmed and A. K. Ghatak, "On the Space-Energy Separability of the Fundamental Mode of the Neutron Transport Operator with Isotropic Scattering," Nucl. Sci. Eng., 33, 106 (1968).

9. M. M. R. Williams, "Time and Space Eigenvalues of the Boltzmann Equation with a Synthetic Thermalization Kernel," Nucl. Sci. Eng., 26, 262 (1966).

10. M. M. R. Williams, The Slowing Down and Thermalization of Neutrons, John Wiley and Sons, Inc., New York (1966).

11. N. Corngold, "Some Transient Phenomena in Thermalization. I. Theory," Nucl. Sci. Eng., 19, 80 (1964).

BIBLIOGRAPHY (Continued)

12. R. Conn and N. Corngold, "A Theory of Pulsed Neutron Experiments in Polycrystalline Media," Nucl. Sci. Eng., 37, 85 (1969).

13. R. Conn and N. Corngold, "Analysis of Pulsed Neutron Experiments in Polycrystalline Media Using a Model Kernel," Nucl. Sci. Eng., 37, 94 (1969).

14. D. J. Hughes and R. B. Schwartz, "Neutron Cross Sections," BNL-325, 2nd ed., Brookhaven National Laboratory (1959).

15. N. Corngold, P. Michael, and W. Wollman,, "The Time Decay Constants in Neutron Thermalization," Nucl. Sci. Eng., 15, 13 (1963).

16. J. Wood and M. M. R. Williams, "The Validity of the Buckling Concept and the Importance of Spatial Transients in the Pulsed Neutron Experiment," Journal of Nuclear Energy, 21, 113 (1967).

17. J. Wood, "Pseudo-Exponential Decay of a Neutron Pulse in Small Beryllium Systems," J. Nucl. Energy, 20, 649 (1966).

18. P. S. Grover and L. S. Kothari, "Equilibrium Spectra and Diffusion Lengths of Neutrons in Semi-Infinite Moderator Block," Nucl. Sci. Eng., 22, 366 (1965).

19. J. Wood, "The Decay of a Neutron Pulse in Low Temperature Beryllium," Nukleonik, 10, 3 (1967).

20. N. Corngold, "On the Maximum Absorption Theorem," Nucl. Sci. Eng., 24, 410 (1966).

21. M. M. R. Williams, "Existence of a Diffusion Length in a Finite Prism of Pure Moderator," in Neutron Thermalization and Reactor Spectra, pp. 27-43, IAEA, Vienna (1967).

22. M. M. R. Williams, "The Energy Dependent Diffusion Length Problem with Transverse Leakage," Nukleonik, 11, 219 (1968).

23. M. M. R. Williams, "Approximate Solutions of the Neutron Transport Equation in Two and Three Dimensional Systems," Nukleonik, 9, 305 (1967).

24. F. Ahmed, L. S. Kothari, and A. Kumar, "Effect of Transverse Dimensions on the Diffusion Length of Neutrons in Crystalline Moderator Assemblies," Nucl. Sci. Eng., 46, 203 (1971).

BIBLIOGRAPHY (Continued)

25. M. M. R. Williams, "Comments on the Effect of Transverse Dimensions on the Diffusion Length in Crystalline Moderator Assemblies," Nucl. Sci. Eng., 47, 498 (1972).

26. M. T. Rainbow and A. I. M. Ritchie, "Measurements in Pulsed BeO Assemblies with Decay Constants in the Region of Corngold's Limit," J. Nucl. Energy, 22, 735 (1968).

27. A. Graffstein, T. Rzeszot, and E. Warda, "Pulsed Neutron Measurements for Beryllium in the Range of Large Bucklings," J. Nucl. Energy, 22, 433 (1968).

28. N. N. Hanna and M. J. Harris, "Decay of a Thermalized Neutron Pulse in Graphite," J. Nucl. Energy, 22, 587 (1968).

29. V. I. Mostovoi, I. P. Sadikov, A. A. Chernysohov, S. N. Ishamev, M. S. Yudkevich, and V. Z. Nozik, "Experimental Study of the Neutron Thermalisation Process in Time in Graphite and Beryllium," in Pulsed Neutron Research, pp. 623-41, IAEA, Vienna (1965). English translation, AERE-Trans-1084.

30. I. C. Goyal, L. S. Kothari, and A. K. Ghatak, "Study of Transient Neutron Spectra in Beryllium Assemblies," Procedings of the National Institute of Science (India), Part A, 33, 38 (1967).

31. B. V. Joshi, V. R. Nargundkar, and K. Subbarao, "A Critical Study of BeO by Pulsed Neutron Method," J. Nucl. Energy, 21, 883 (1967).

32. I. C. Goyal and L. S. Kothari, "The Decay of Equilibrium Neutron Flux Inside Beryllium Blocks at Different Temperatures," Nucl. Sci. Eng., 23, 159 (1965).

33. L. S. Kothari, "Decay Constant of a Neutron Pulse Inside a Finite Solid Moderator Assembly," Nucl. Sci. Eng., 23, 402 (1965).

34. P. S. Grover and L. S. Kothari, "Equilibrium Spectra and Diffusion Lengths of Neutrons in Semi-Infinite Moderator Block--Part II: Effect of 'Trapped' and Cold Neutrons," Nucl. Sci. Eng., 23, 167 (1965).

35. G. deSaussure, "A Note on the Measurement of Diffusion Parameters by the Pulsed-Neutron Source Technique," Nucl. Sci. Eng., 12, 433 (1962).

36. N. Corngold, "Decay Constant of a Neutron Pulse," Nucl. Sci. Eng., 23, 403 (1965).

BIBLIOGRAPHY (Continued)

37. J. Wood, "An Interpretation of the Numerical Solution of the Neutron Pulsed Source Problem," J. Nucl. Energy, 22, 525 (1968).

38. J. A. DeJuren and V. A. Swanson, "Cold Neutron Effects in Graphite Diffusion Measurements," J. Nucl. Energy, 20, 905 (1966).

39. N. Corngold and K. Durgun, "Analysis of Pulsed-Neutron Experiments in Moderators via a Simple Model," Nucl. Sci. Eng., 29, 354 (1967).

40. J. Wood, "The Existence of a Discrete Decay Constant Exceeding $(v\Sigma(E))_{min}$ in the Pulsed Neutron Experiment," British Journal of Applied Physics (J. Phys. D.), 2, 149 (1969).

41. M. Sohrabpour and S. R. Bull, "Pulsed-Source Measurements in Small BeO Assemblies," Trans. Am. Nucl. Soc., 12, 675 (1969).

42. R. Conn and N. Corngold, "Pulsed Neutron Decay Constants in Crystalline Moderators," Trans. Am. Nucl. Soc., 10, 628 (1967).

43. E. R. Gaerttner, P. B. Daitch, R. R. Fullwood, R. R. Lee, and R. E. Slovacek, "The Effects of Coherent Scattering on the Thermalization of Neutrons in Beryllium," in Pulsed Neutron Research, pp. 483-99, IAEA, Vienna (1965).

44. P. S. Grover and L. S. Kothari, "Transient Neutron Spectra and the Slowing Down Relaxation Time in Beryllium," J. Nucl. Energy, 20, 835 (1966).

45. R. R. Lee and P. B. Daitch, "An Analysis of Neutron Thermalization in Beryllium," Nucl. Sci. Eng., 28, 247 (1967).

46. J. D. Jain, "Asymptotic Distribution of Thermal Neutron Flux in an Infinite Medium of Beryllium Containing a Constant Plane Source," Nucl. Sci. Eng., 17, 551 (1963).

47. J. U. Koppel and J. A. Young, "Scattering Kernel for Beryllium," Nucl. Sci. Eng., 19, 367 (1964).

48. G. M. Borgonovi and D. Sprevak, "A Calculation of the Coherent Neutron Scattering from Polycrystalline Beryllium," Nucl. Sci. Eng., 42, 137 (1970).

49. "Safety Analysis Report for the 5 Mw Georgia Tech Research Reactor," W. W. Graham, III and D. M. Walker, Eds., p. 60, Georgia Institute of Technology, Atlanta, Unpublished (1967).

BIBLIOGRAPHY (Continued)

50. S. W. Porembka, H. D. Hanes, and P. J. Gripshover, "Powder Metallurgy of Beryllium," DMIC-239, Defense Materials Information Center, Battelle Memorial Institute (1967).

51. B. S. Hickman, "Radiation Effects in Beryllium and Beryllium Oxide," in Studies in Radiation Effects, Vol. 1, G. J. Dienes, Ed., Gordon and Breach, New York (1966).

52. Specifications Sheet, Beryllium Block-High Purity Grade N-50-C, Brush Wellman Inc., Cleveland, Ohio (1972).

53. H. Pih, "A Survey of Beryllium Technology and Nuclear Applications," ORNL-4421, Oak Ridge National Laboratory (1969).

54. E. Fermi, J. Marshall, and L. Marshall, "A Thermal Neutron Velocity Selector and Its Application to the Measurement of the Cross Section of Boron," Physical Review, 72, 167 (1947).

55. T. Brill and H. V. Lichtenberger, "Neutron Cross-Section Studies with the Rotating Shutter Mechanism," Phys. Rev., 72, 583 (1947).

56. F. G. P. Seidl, H. Palevshy, R. F. Randall, and W. Thorne, "Thermal Neutron Time-Of-Flight Velocity Selector," Phys. Rev., 82, 345 (1951).

57. T. L. Isenhour and G. H. Morrison, "Modulation Technique for Neutron Capture Gamma Ray Measurements in Activation Analysis," Analytical Chemistry, 38, 162 (1966).

58. "Beryllium and Its Compounds," in Hygienic Guide Series, American Industrial Hygiene Association (1964).

59. H. E. Stokinger, "Recommended Hygienic Limits of Exposure to Beryllium," in Beryllium-Its Industrial Hygiene Aspects, H. E. Stokinger, Ed., Academic Press, New York (1966).

60. A. J. Vorwald, "Medical Aspects of Beryllium Disease," in Beryllium-Its Industrial Hygiene Aspects, H. E. Stokinger, Ed., Academic Press, New York (1966).

61. N. Bolton, Consultant in Industrial Hygiene, Private Communication to Dr. J. M. Kallfelz (June, 1970).

62. H. Etherington, Ed., Nuclear Engineering Handbook, McGraw-Hill Book Co., Inc., New York (1958).

BIBLIOGRAPHY (Continued)

63. P. R. Bevington, Data Reduction and Error Analysis for the Physical Sciences, McGraw-Hill Book Co., Inc., New York (1969).

64. W. R. Burrus, "Radiation Transmission Through BORAL and Similar Heterogeneous Materials Consisting of Randomly Distributed Absorbing Chunks," ORNL-2528, Oak Ridge National Laboratory (1960).

65. R. S. Stone and K. E. Slovacek, "Reactor Spectrum Measurements Using a Neutron Time-Of-Flight Spectrometer," KAPL-1499, Knowles Atomic Power Laboratory (1956).

66. J. Spalek, "Neutron Time-Of-Flight Spectrometry," ANL-6990, Argonne National Laboratory (1965).

67. V. F. Turchin, Slow Neutrons, Moscow (1963), translated by the Israel Program for Scientific Translations, Ltd. (1965).

68. A. Erdelyi, et al., Higher Transcendental Functions, Vol. 2, ch. 7, McGraw-Hill Book Co., Inc., New York (1953).

69. G. Arfken, Mathematical Methods for Physicists, pp. 396-406, Academic Press, New York (1966).

70. Handbook of Mathematical Functions, M. Abramowitz and I. Stegun, Eds., AMS-55, U. S. Dept. of Commerce, National Bureau of Standards, Applied Mathematics Series, pp. 495-502 (1964).

71. M. J. Poole, "Review of the Applications of Pulsed Sources to the Measurement of Neutron Spectra in Moderator and Reactor Lattices," in Pulsed Neutron Research, 1, pp. 430-1, IAEA (1965).

72. F. McGirt and M. Becker, "The Influence of a Reentrant Hole on Measurements of Fast and Thermal Neutron Spectra," Nucl. Sci. Eng., 39, 56 (1970).

73. L. E. Krejci and L. D. Scheel, "The Chemistry of Beryllium," in Beryllium-Its Industrial Hygiene Aspects, H. E. Stokinger, Ed., Academic Press, New York (1966).

74. B. I. Shamasundar, unpublished, Georgia Institute of Technology, Atlanta (1971).

75. M. M. R. Williams, "Diffusion Lengths and Criticality Problems in Two- and Three-Dimensional, One-Speed Neutron Transport Theory. I. Rectangular Coordinates," Journal of Mathematical Physics, 9, 1873 (1968).

BIBLIOGRAPHY (Concluded)

76. M. M. R. Williams, Private Communication (1971).

77. R. Kladnik and I. Kuscer, "Milne's Problem for Thermal Neutrons in a Nonabsorbing Medium," Nucl. Sci. Eng., 11, 116 (1961).

78. P. S. Grover and L. S. Kothari, "Comments on Michael's Criticism of the Use of Diffusion Theory for the Study of Thermal Neutrons in Beryllium," Nucl. Sci. Eng., 24, 94 (1966).

79. P. S. Grover, L. S. Kothari, and A. K. Ghatak, "Comparison of Neutron-Transport and Diffusion Theories of Isotropic Scattering," Nucl. Sci. Eng., 31, 314 (1968).

80. E. Browning, "Beryllium," in Toxicity of Industrial Metals, ch. 6, Butterworths, London (1961).

81. A. J. Breslin, "Exposures and Patterns of Disease in the Beryllium Industry," in Beryllium-Its Industrial Hygiene Aspects, H. E. Stokinger, Ed., Academic Press, New York (1966).

82. H. L. Hardy, "The Character and Distribution of Disease in American Industries Using Beryllium," Procedings of the Royal Society of Medicine, 44, 257 (1951).

83. K. H. Beckurts, unpublished (1960).

VITA

James Alan Lake was born on December 16, 1943 in Gary, Indiana. He attended public schools in Gary and graduated from Lew Wallace High School in 1961. Mr. Lake attended Hanover College in Hanover, Indiana where he received a Bachelor of Arts degree in 1965 with a major in Physics and minors in Mathematics and Chemistry.

During the summer of 1965, Mr. Lake was employed as a Metallurgical Analyst, testing automatic gaging equipment at United States Steel Corporation in Gary, Indiana.

Mr. Lake subsequently attended Miami University at Oxford, Ohio where he received a Master of Arts degree in Physics in 1967 with a thesis entitled "Internal Conversion in Ba-137". Throughout the course of his graduate work, Mr. Lake was employed as a Graduate Teaching Assistant with responsibilities for planning and teaching a series of Nuclear and General Physics laboratories.

During the summer of 1967, Mr. Lake was employed as a Nuclear Laboratory Scientist at Donald W. Douglas Laboratories in Richland, Washington.

Mr. Lake continued his graduate studies toward a Doctorate in Nuclear Engineering at Georgia Tech in Atlanta, Georgia where he received a Master of Science degree in 1969. His thesis work was supported in part by National Science Foundation and Atomic Energy Commission Traineeships.

Mr. Lake is married to the former Sharon Marie Hall of Louisville, Kentucky. He is a member of the American Nuclear Society and the Society of Sigma Xi.